

Process engineering of functional metakaolin based geopolymers

by

Matteo Pernechele

M.Sc., Università degli Studi di Padova, 2012

A THESIS SUBMITTED IN PARTIAL FULFILLMENT OF

THE REQUIREMENTS FOR THE DEGREE OF

Doctor of Philosophy

in

The Faculty of Graduate and Postdoctoral Studies

(Materials Engineering)

THE UNIVERSITY OF BRITISH COLUMBIA

(Vancouver)

April 2018

© Matteo Pernechele, 2018

Abstract

Geopolymers (GPs) are a class of inorganic materials which can be used as construction and refractory cements and as functional materials for environmental applications. GPs are low CO₂ emissions binders with high durability that can replace traditional cementitious materials. However the effects and interactions of processing parameters on the different stages of GP setting (“geopolymerization”) are still under scrutiny and the molecular mechanisms and rate limiting steps controlling the setting kinetics are unknown. The crystallization in GPs, which ultimately controls their performance in advanced applications such as water purification and toxic waste encapsulation, is a poorly investigated topic.

This dissertation provides new experimental evidences on the role of chemical composition and curing process on metakaolin-based GPs. Steady state and dynamic rheological studies, contact angle tests, microstructural (SEM), structural (XRD and FTIR) and mechanical analyses lead to better understanding of the fundamental transformations occurring during geopolymerization. GPs were seeded with different oxides and zeolites to determine the rate limiting step, increase the reaction rate and control the crystallization. This work contributes to clarification the complex effects of soluble silica on the geopolymerization process. It is shown that soluble and colloidal silicates (such as Na₄SiO₄ and Na₂SiO₃) can act as seeding agents, changing the geopolymerization rate limiting step at temperatures $T \geq 35^{\circ}\text{C}$. However, they also slow down the reaction rate, possibly by forming passivation layers on the metakaolin particles, thus producing a more chemically stable and mechanically stronger amorphous gel. Silicates also decrease the water requirement in GPs and thus the porosity. Under certain conditions silicates can increase the percentage of crystalline Faujasite in GPs, but the crystallization process requires higher curing temperatures and times ($T > 40^{\circ}\text{C}$ and $t > 4$ days, depending on the amount of silicates). The alkali metals have also a structure-directing role in crystallization of GPs in the form of zeolite, favoring Faujasite structure. Water has a templating effect in GPs, favoring the structure of zeolite LTA-type over hydrosodalite. This work also illustrates the compromises that need to be made when selecting appropriate processing parameters to tailor the rheology, structure and properties of geopolymers for specific applications.

Lay summary

This work studies reactions between inorganic clay-based materials with different alkaline solutions and additives to produce environmentally friendly cementitious materials, called “Geopolymers”. Such materials have both conventional and advanced applications, and in some areas may replace Ordinary Portland Cement. The characteristics of the resulting geopolymers were studied, in terms of their viscosity, chemical bonding, crystallinity and compressive strength. It was found that the chemistry of precursor solutions and the processing temperature have a profound effect on the reaction and on the nature of the final geopolymer materials. The use of processing additives brought light on the reaction mechanisms, thus enabling a deeper understanding of the resulting material. Guidelines were developed to tune the properties of the geopolymeric cement to specific applications.

Preface

This dissertation is original, unpublished, and independent work by the author. None of the text is taken directly from previously published articles. -M. Pernechele

Table of contents

Abstract.....	ii
Lay summary	iii
Preface	iv
Table of contents.....	v
List of tables	xi
List of figures.....	xiii
List of abbreviations and symbols	xxii
Acknowledgements.....	xxv
Dedication.....	xxvi
1. Introduction.....	1
1.1. Role of geopolymers in sustainable development	1
1.2. Inorganic binders	2
1.3. Motivation.....	7
2. Literature review.....	8
2.1. Introduction to geopolymers	8
2.1.1. Geopolymers and their terminology.....	8
2.1.2. Types of aluminosilicate geopolymers.....	12
2.1.3. Geopolymers properties and applications	15
2.2. Metakaolin - based geopolymers (MK-based GP).....	20
2.2.1. Historical perspective	20
2.2.2. The solid precursors to GP: metakaolin	23
2.2.3. The alkaline solutions.....	24
2.2.4. Geopolymerization reactions.....	28

2.2.4.1. Conceptual models for geopolymerization reactions	29
2.2.4.2. Dissolution and precipitation reactions in cementitious systems	32
2.2.4.2.1. Thermodynamic and kinetic of complex reactions.....	32
2.2.4.2.2. Heterogeneous reactions.....	34
2.2.4.3. Metakaolin dissolution.....	36
2.2.4.4. Aluminosilicates condensation in solutions	40
2.2.4.5. Kinetic models of geopolymerization.....	43
2.2.4.6. Additives and Seeding	46
2.2.5. GP technology development: composition and properties optimization.....	48
2.3. Zeolites.....	51
2.3.1. Synthesis, structure and applications.....	51
2.3.2. Induction time and kinetics of crystallization of zeolites.....	55
2.3.3. Synthesis of zeolites from metakaolin.....	57
2.4. Advanced GP applications and geopolymer crystallinity	59
3. Objectives	63
4. Approach and methodology.....	64
4.1. Materials, synthesis and preparation methods	64
4.1.1. Raw material and metakaolin characterization	64
4.1.2. Geopolymer synthesis	67
4.2. Analysis methods	67
4.2.1. Rheological characterization	67
4.2.1.1. Viscosity	68
4.2.1.2. Steady-state measurements.....	68
4.2.1.3. Dynamic oscillatory measurements.....	72
4.2.1.4. Empirical tests	73

4.2.2. Contact angle measurements	75
4.2.3. Mechanical and microstructural analysis	76
4.2.4. Structural analysis - XRD.....	76
4.2.5. Structural analysis - FTIR	79
4.2.6. Factorial design and Analysis of Variance (ANOVA).....	81
5. Analysis of MK-based GP formulations.....	84
5.1. Formulation in Metakaolin-based GP	84
5.1.1. Constraints in the GP formulations	84
5.1.2. Soluble silicate MK-based GP	89
5.2. Effects of Si/Al on the GP.....	92
5.2.1. Optimum H ₂ O/solid for NaOH/MK-based GP	92
5.2.2. Sample preparation and slurry properties.....	94
5.2.3. Activating solutions.....	96
5.2.4. Sample curing and unconfined compressive strength (UCS).....	98
5.2.5. Structural characterization.....	99
5.3. Summary	103
6. Seeded geopolymers	105
6.1. Seeds selection and processing	105
6.1.1. Seeded geopolymers.....	105
6.1.2. Oxide seed selection.....	106
6.1.2.1. Mechanochemical activation of zeolites.....	109
6.1.3. Bottom-up approach: synthetic zeolites	112
6.1.3.1. Conventional synthesis: LTA, FAU	112
6.1.3.2. Colloidal zeolite seeds	113
6.1.4. Summary	116

6.2. Seeds effect on NaOH/MK-based GPs	118
6.2.1. Effects of commercial oxide seeds	118
6.2.1.1. Seeded-GP synthesis and analyses	118
6.2.1.2. GPs setting times, GPs mechanical and physical properties	120
6.2.1.3. Structural reorganization of seeded GPs.....	123
6.2.2. Effect of synthetic zeolites seeds.....	127
6.2.2.1. Seeded-GP synthesis and analyses	127
6.2.2.2. GPs physical and mechanical properties	127
6.2.2.3. Structural characterization of the GPs	129
6.2.3. Discussion: strength of interlocked GP crystals.....	131
6.2.4. Summary	132
7. Rheology and reaction kinetics of GPs.....	134
7.1. Introduction and hypothesis	134
7.2. Metakaolin wettability in activating solution.....	136
7.2.1. Contact angle measurement.....	136
7.2.2. Result and discussion	138
7.3. Rheology of MK-based GP	139
7.3.1. Introduction to concentrate suspensions and clays materials	139
7.3.2. Flow curve and thixotropy of NaOH/MK-based GP.....	142
7.4. Dynamic rheology and crossover time.....	144
7.4.1. Materials and experimental set-up	145
7.4.2. Results and discussion.....	146
7.5. Dynamic rheology and rate limiting steps	151
7.5.1. Materials and experimental set-up	152
7.5.2. Results and discussion.....	152

7.6. Summary and conclusions	156
8. Geopolymer phase transformations and crystal engineering.....	158
8.1. Rationale	158
8.2. Design of experiments	159
8.3. Response quantification	165
8.3.1. ATR-FTIR spectra deconvolution.....	166
8.3.1.1. Precision and accuracy	168
8.3.2. QXRD and Rietveld refinement	169
8.3.2.1. Precision and accuracy	172
8.4. Results.....	173
8.4.1. Setting time.....	173
8.4.2. ANOVA analysis.....	174
8.4.3. FTIR	178
8.4.3.1. FTIR: GP peak position	178
8.4.3.2. FTIR: GP%	179
8.4.3.3. FTIR: GP peak FWHM	179
8.4.3.4. FTIR: peak area ratio solid/H ₂ O	180
8.4.4. QXRD.....	180
8.4.4.1. XRD: zeolite conversion %	180
8.4.4.2. XRD: LTA%	181
8.4.4.3. Long term stability: Oswald rule of successive transformations.....	182
8.4.5. SEM images	183
8.5. Discussion	186
8.5.1. Reaction extent and kinetics.....	186
8.5.2. Geopolymer gel nature and reorganization	191

8.5.3. Crystallinity and crystal engineering.....	193
8.6. Summary	197
9. Conclusions and future work	199
References.....	204
Appendices	233

List of tables

Table 1.1 Main mineralogical phases in Portland cement clinker, their shorthand notation and weight percentage [17].	5
Table 2.1 Geopolymer nomenclature [38].	12
Table 2.2 Chemical compositions of geopolymers according to [35]	21
Table 2.3 Physical and thermodynamic values for cations of interest in GP [11]. pKa values are quoted from Baes [93].	25
Table 4.1 Materials adopted in GP and zeolite synthesis, and various oxides used as seeds.	64
Table 4.2 some empirical tests to measure the rheological response of cementitious materials.	74
Table 4.3 Precursors and geopolymers infrared characteristic bands [38].	81
Table 5.1 Measured compressive strengths and calculated GPs ratios ($H_2O/solid$, Si/Na , $solution/solid$) extracted from Rowles work on metakaolin-based GPs [62].	90
Table 5.2 Pearson correlation coefficient obtained from Rowles [62].	90
Table 5.3 NaOH/MK-based GPs prepared to optimize the activating solution/MK mass ratio (m_{AS}/m_{SP}) and $H_2O/solid$ ratio. Φ is the volume fraction of solids.	92
Table 5.4 Setting times of geopolymer pastes with different water content at 3 different temperatures. Error percentage is approximately 20%.	94
Table 5.5 Geopolymer compositions, slurry flow (determined using a flow table) and activating solution properties. AS: Activating solution.	95
Table 6.1 Codes for the geopolymers containing different nanoparticles. MOR=mordenite, Fau= faujasite, m.=milled ; Fau-H = hydrogen faujasite, Fau-Na =sodium faujasite.	119
Table 6.2 Values of bulk density and unconfined compressive strength at 3 days and 7 days for the 9 different samples. The values of pH and conductivity were measured on samples cured for 7 days, after 24 hours of soaking in distilled water.	121
Table 6.3 Unconfined compressive strength of unseeded GP and seeded with synthetic zeolite type P at different curing conditions.	128
Table 6.4 Zeolite weight % of different GPs as determined by QXRD using internal TiO_2 standard. LTA: zeolite type A. FAU: zeolite type X. HS: hydroxisodalite.	130

Table 7.1 Parameters of Papo's model obtained by NLSF of the complex viscosities for different GP pastes.....	155
Table 8.1 Geopolymers formulas for samples A, B, C, D and E.....	161
Table 8.2 List of all geopolymer compositions used in this study. Geopolymer parameters are fixed and derived ratios calculated based on the real metakaolin content in Powerpozz. MK stands for metakaolin, WG-N for sodium silicate type N, WG-Ms for molar ratio $\text{SiO}_2/\text{Na}_2\text{O}$ of the activating solution	163
Table 8.3 List of quantifiable responses (obtained from the deconvolved ATR-FTIR spectra and QXRD) and the main information they carry.	165
Table 8.4 Setting time of GPs type A, B, C, D, E (refer to Table 8.1 for their compositions) vs curing temperature	174
Table 8.5 The p-values obtained from the Analysis of Variance (ANOVA) of GP samples A,B,C and D (see Table 8.2).....	175
Table 8.6 The p-values obtained from the Analysis of Variance (ANOVA) of GP samples A, E and D. (see Table 8.2)	176
Table 8.7 Attribution of the response variation to the appropriate factor (Na/Al , $\text{H}_2\text{O}/\text{solid}$ or $[\text{NaOH}]$)by comparing the p-values of Na/Al , $\text{H}_2\text{O}/\text{solid}$ and solution/MK.....	177
Table 8.8 QXRD results of 1 year old samples compared with their initial phase content. The selected samples were the unseeded GP with composition A, E and D cured at 60deg for 7 days.	182
Table 8.9 Results of the QXRD for the different geopolymers analyzed with SEM. “Saturation” refers to the zeolite content of the geopolymers compared to the values obtained for the same geopolymers at 7 days curing.	185
Table A.1 Fractional coordinates, isotropic thermal parameters (100\AA^2), occupancies, unit cell parameters, for the refined LTA [287] ICSD 24901 and NaX [288] - ICSD 15568 phases using respectively the diffractograms E-60-7 and Cs-40-7.	233
Table B.1 Responses obtained from the multifactorial design in Chapter 8.	235

List of figures

Figure 1.1 Left: Pantheon “temple of every god” in Rome built using roman cement 2000 years after its construction. Right: Schematic structure of the C-S-H, main hydration product of roman and modern cements: A 2-D sheet of 7-coordinated Ca ions share oxygen’s with depolymerized "dreierketten”chains of SiO ₄ tetrahedra. Qn represents the connectivity “n” of the silica tetrahedra [15].	4
Figure 1.2 Left: CaO–Al ₂ O ₃ –SiO ₂ ternary diagram of cementitious materials [18]. Right: Main oxide weight % of selected materials used as inorganic binders.	6
Figure 2.1 Number of scientific papers using the geopolymer terminology since 1991 [37].	11
Figure 2.2 Classification of AAMs according with RILEM [4]. GPS are considered a subgroup of AAMS with low calcium and high alumina content.	14
Figure 2.3 Names, structures and applications of geopolymer at different Si/Al ratio [38]...	16
Figure 2.4 Comparison between selected properties of inorganic binders: Ordinary Portland Cement (OPC), geopolymer based on slag, metakaolin and soluble silicate (GP Slag), geopolymer based on fly ash and soluble silicate (GP Slag), geopolymer based on metakaolin and soluble silicates (GP MK-WG), and geopolymer based on metakaolin and alkali hydroxides (GP MK-MOH). The data are compiled from [4], [32], [38], [57]–[60].....	18
Figure 2.5 Effects of increasing Si/Al ratio through the use of sodium silicate in metakaolin-based GPs. Left: Effects on compressive strength and young modulus [58]. Right: phase diagram of nepheline-albite, corresponding to a GPs with Si/Al ratio of 1 and 3 respectively [64].....	20
Figure 2.6 On the left: ²⁹ Si MAS NMR experimental distribution of the different species of silicates in a water-based solution as a function of the alkali oxide content in lithium (Δ), sodium (□) and potassium (○) silicates [103]. On the right: a qualitative interpretation of sodium silicate speciation in solution [104].	28
Figure 2.7 Representation of the five ortho-sialate species isolated in KOH solution by North [115]; these molecules are the precursors of both zeolites and geopolymers [38]......	30
Figure 2.8 Mechanism of hydrolysis of silicon alkoxides in basic environment (from [117]).	31

Figure 2.9 Normalized reaction rate as a function of chemical affinity according to the transition state theory.....	38
Figure 2.10 Simplified representation and interpretation of isothermal calorimetry of geopolymerization. Reaction steps are taken from [100], see Figure 2.11.....	44
Figure 2.11 Scheme of an empirical kinetics model of geopolymerization [100].....	45
Figure 2.12 SEM images of MK-based GP cured at 40 C (left) and 85 C (right). Left: microstructure of GP with Si/Al ratio and UCS of (a) 1.15 and 18 MPa, (b) 1.40 and 40 MPa, (c) 1.65 and 56 MPa, (d) 1.90 and 73 MPa (e) 2.15 and 63 MPa (from [58]). Right: microstructure of GP with Si/Al ratio and UCS of 1.25 and 2.7MPa, 1.5 and 29 MPa, 1.75 and 48 MPa and 1.9 and 48 MPa (from [57]).....	50
Figure 2.13 The contours of the constant compressive strength [MPa] of metakaolin geopolymers, cured at 75°C for 24 h; the compressive strength was measured after subsequent aging for 7 days at room temperature [62].....	51
Figure 2.14 Secondary building unit (SBU) used to classify zeolites from Newsam [24].....	52
Figure 2.15 Progressive construction of a zeolites structure. The (Si,Al)O ₄ tetrahedra condense to form a truncated octahedral, also called a “sodalite” or “β-cage”, made of 4-members and 6-members rings. The sodalite cage is found in different zeolite frameworks, such as in sodalite (SOD), faujasite (FAU), linde type A (LTA) and EMT frameworks. From Newsam [24].....	53
Figure 2.16 Zeolite A (region I) and zeolite X (region III) crystallization diagram for a 2M aqueous solution. In region II these phases coexist, in region IV there are no stable zeolites. (from [174]).	54
Figure 2.17 Mechanism of LTA crystallization from MK and 5M NaOH (from [193]). Solid lines represent observed reaction steps, dashed lines represent other possible reaction pathways.	58
Figure 2.18 Top view (left) and cross section (right) of self-sustaining zeolite A membrane obtained via geopolymerization route for seawater desalination [198].....	61
Figure 4.1 SE-SEM analysis of Powerpozz (metakaolin).	65
Figure 4.2 Top: X-rays diffractogram of Powerpozz. Blue line: quartz; red line: anatase; peak at 2θ=8.8° belong to halloysite. Bottom: ATR-FTIR spectra of kaolin and metakaolin.....	67
Figure 4.3 Shear stress vs shear rate according to the Bingham model [170], [212].	69

Figure 4.4 Cross section of a concentric cylinder rheometer	70
Figure 4.5 Left: schematic representation of the Haake Rotovisco vt550 rotational viscometer. Right: experiment program commonly used to obtain a steady state flow curve [213]......	71
Figure 4.6 Thixotropic measurements. Left and middle: hysteresis loop method. Right: constant shear rate method [213]......	72
Figure 4.7 Left: schematic representation of the Anthon Paar Rheometer. Right: stress-strain response of a viscoelastic material during dynamic rheology tests [209].	73
Figure 4.8 Sessile drop (left) and captive bubble (right) schematic diagrams [219]......	75
Figure 4.9 Left: Geopolymer bar during demolding operation. Right: GP cube and head of the Instron machine during UCS test.	76
Figure 4.10 Schematic representation of diffractograms in Bragg-Brentano geometry, from [225]	79
Figure 5.1 Left: Sodium soluble silicate diagram $\text{SiO}_2\text{-Na}_2\text{O-H}_2\text{O}$ (from [101]) with compositions of some commercially available chemicals . Region 9 is the most stable region of soluble silicate solutions and most of commercial solutions are located within this region. Right: Viscosity of sodium silicate as a function of silica modulus at constant solid contents. From [234], adaptation from Vail [101].	88
Figure 5.2 Calculated $\text{H}_2\text{O/solid}$ and solution/MK ratios of GPs with different Si/Al ratio studied by Duxson [58].	89
Figure 5.3 SEM images of NaOH/MK-based GP with different activating solution/MK ratio ($m_{\text{AS}}/m_{\text{MK}}$) cured at 55°C for 20 hours	93
Figure 5.4 Flow table apparatus and flow of the GP with $\text{Si/Al}=1.35$	95
Figure 5.5 Activating solutions intended for the synthesis of GPs with different Si/Al . Sample in the middle is a colloidal dispersion.	96
Figure 5.6 In red: Measured X-rays diffractograms of the gel precipitate by centrifuging the activating solution intended for GP with $\text{Si/Al}=1.35$. In blue: Peak position of sodium silicate hexa-hydrate $\text{Na}_2\text{SiO}_3\cdot(\text{H}_2\text{O})_6$, ICSD code 9171.	96
Figure 5.7 $\text{Na}_2\text{O-SiO}_2\text{-H}_2\text{O}$ diagram for the GP activating solution. Red triangles: activating solutions used by Duxson [58]. Black squares: Activating solution adopted in this current work.	97

Figure 5.8 UCS of GP with different Si/Al. Left: constant H ₂ O/solid GP prepared in this work. Right: constant SiO ₂ /Na ₂ O prepared by Duxson [58].	98
Figure 5.9 SE-SEM images of the fracture surfaces of the three GPs cured at 40°C for 20 hours at different magnification.	100
Figure 5.10 SE-SEM images of the fracture surfaces of the three GPs cured in autoclave at different magnification.	101
Figure 5.11 XRD patterns of GPs with different Si/Al cured at 40°C for 20 hours with and without autoclave treatment rutile internal standard was used for all samples. s=silica (ICSD 90145, quartz), an=anatase (ICSD 63711), r=rutile (ICSD 34372), a=zeolite type A (ICSD 24901).	103
Figure 6.1 SE-SEM images of the silica (top left), alumina (top right), zirconia (bottom left) and Faujasite-H (bottom right) seeds used in this study.	107
Figure 6.2 XRD of the different seeds: silica, alumina, zirconia, mordenite-Na, faujasite-H and faujasite-Na.	108
Figure 6.3 ATR-FTIR peaks for two pure crystalline faujasite type-Y, one in its hydrogen form and the other in its sodium form. Note the shoulder at 1100 cm ⁻¹ which overlaps with the metakaolin peaks, Figure 4.2. Note also the peak shift due to the different cations, from 976 cm ⁻¹ to 1023 cm ⁻¹ when sodium is substituted by hydrogen.	108
Figure 6.4 Particle size distributions of the faujasite-Na seeds determined by laser scattering.	109
Figure 6.5 SE-SEM image of mordenite (top left), milled mordenite (top right), faujasite-Na (bottom left) and milled faujasite-Na (bottom right)	110
Figure 6.6 Left: XRD of mordenite and milled mordenite. Right: FWHM ratio of the XRD peaks.	111
Figure 6.7 ATR-FTIR spectra of mordenite before and after milling.	111
Figure 6.8 Left: X-rays diffractograms of the synthetic zeolite type A (LTA) and zeolite type Y (FAU). Right: ATR-FTIR spectra of the aforementioned synthetic zeolites.	112
Figure 6.9 Left: digital picture of the zeolite precursor solution aged for 45 hours at different temperatures. Right: XRD of the colloidal particles obtained after aging at 50° for 45 hours.	115

Figure 6.10 BSE-SEM image of colloidal nanocrystalline faujasite. Air-dried precipitate obtained after curing at 50° for 45 hours of the zeolite precursor solution.	115
Figure 6.11 X-rays diffractograms of the zeolite obtained by autoclave curing of precursor solution and diffractogram of the database structure of Gismondine (ICSD 9550).	116
Figure 6.12 SE-SEM images of Gismondine zeolites obtained after autoclave treatment...	116
Figure 6.13 Unconfined Compressive Strength (UCS) of the seeded geopolymers compared with the non-seeded geopolymer (sample 1) at the same aging time.	122
Figure 6.14 pH and conductivity values of the geopolymers soaked in distilled water for 24 hours.	122
Figure 6.15 XRD diffractograms of metakaolin, milled-mordenite-seeded geopolymer at 3 hours, 3 days and 7 days. Zeolite type X (x), Linde type A (a), silica (s), anatase (an).	123
Figure 6.16 Zeolite content expressed in term of sums of XRD integrated intensities of 200) reflection of zeolite A and the (111) reflection of zeolite X over the (011) reflection of SiO ₂ at 3 days and at 7 days.	124
Figure 6.17 Integrated intensity ratios of the (200) reflection of zeolite A over the (111) reflection of zeolite X at 3 days and at 7 days in the XRD patterns.	124
Figure 6.18 ATR-FTIR spectra for the GP seeded with SiO ₂ (left) and mordenite (right), at 3 hours, 3 days and 7 days.	125
Figure 6.19 SEM images at 3 days (left) and 7 day (right) for the alumina-seeded geopolymer, sample 3. A: zeolite type A; X: zeolite type faujasite-X.	126
Figure 6.20 SE-SEM images after 7days curing at 45°C of GP with FAU-Na seeds (sample 6, left) and milled-FAU-Na seeds (sample 7, right).	126
Figure 6.21 Curing procedures of the unseeded and seeded geopolymers.	127
Figure 6.22 Selected X-Ray diffractograms of the seeded and unseeded GPs with different curing conditions. Letters indicate the peak position of faujasite (X), zeolite type A (A), hydrosodalite (H), silica (S), and Anatase (An).	129
Figure 6.23 SE-SEM images of the unseeded (left) and zeolite-P1-seeded (right) GPs cured for additional 24 hours at 45°C and RH=0%.....	131
Figure 7.1 Schematic of the method to determine the rate limiting step by seeding.	135
Figure 7.2 SE-SEM images of the surface of the metakaolin pellet.....	137

Figure 7.3 Left: photo of the MK pellet immersed in the liquid and the needle dispensing an air bubble. Right: image of the contact angle θ_c measured by the software; in yellow the Young-Laplace fitting of the bubble shape.	138
Figure 7.4 Contact angles between different solutions and metakaolin. WG-N stands for soluble silicate type N, in bracket the water dilution.....	139
Figure 7.5 House of card structure observed in kaolinite suspension (from [265]).	141
Figure 7.6 Flow curve (left) and apparent viscosity (right) of a NaOH/MK-based GP.	143
Figure 7.7 Hysteresis loop of a NaOH/MK-based GP. Left: shear rate program. Right: experimental hysteresis loop.....	144
Figure 7.8 Left: picture of the rheometer. Left: schematic of the parallel plate geometry...	146
Figure 7.9 Left: moduli and complex viscosity measured during a time sweep test for the unseeded GP at 30°C. Right: complex viscosity for an unseeded GP at 30 °C measured during a delayed time sweep test.	147
Figure 7.10 Time sweep tests for unseeded GP at 30°C (top left), unseeded GP at 40°C (top right), faujasite seeded GP at 40°C (bottom left) and zirconia seeded GP at 40°C (bottom right).	148
Figure 7.11 Repeated time sweep test for unseeded GP cured at T=40°C to assess the reproducibility of the method to determine the crossover point. Crossover points are marked in green.	149
Figure 7.12 Arrhenius plot of the crossover times at different temperatures for seeded and non-seeded GP.	150
Figure 7.13 Geopolymer activation energies for unseeded and seeded GPs obtained from the Arrhenius plot of the crossover points in time sweep experiments.	151
Figure 7.14 Complex viscosity measured during time sweep tests for unseeded NaOH-based GP (top left), faujasite seeded NaOH-based GP (top right, note different scale), unseeded WG-based-GP (bottom left) and faujasite seeded WG-based GP (bottom right).	153
Figure 7.15 Time sweep tests performed on GPs. Solid lines represent the measured viscosity, dashed lines represent the NLSF using Papo's model. Left: effect of temperature on unseeded NaOH-based GP. Right: effect of faujasite seeding on NaOH-based GP cured at 35°C.	154

Figure 7.16 Setting times t_r (left) and kinetic factors N (right) obtained by NLSF of the rheograms using Papo's model.	156
Figure 8.1 Representation of the GP compositions and GP codes in the adopted 2^2 factorial design with a central point.	161
Figure 8.2 Representation of the 180 characterized GPs: 5 compositions, 4 temperatures and 3 curing times (left), and 3 seeding conditions (right; each of the three systems in this graph is the time-temperature system copied form the left figure).	163
Figure 8.3 ATR-FTIR measured spectra (in black) and NLSF fitting lines (in blue) of the metakaolin and selected geopolymer samples: sample Bs cured at 20°C for 4 day and sample Bs cured at 60°C for 4 days. Deconvolved peaks of the metakaolin are in red and fuchsia, deconvolved peak of geopolymer is in green.	168
Figure 8.4 SEM image of the XRD internal standard rutile. Particles are below 2 μm providing a good standard for QXRD in term of count statistic.	170
Figure 8.5 Measured diffraction patterns of selected geopolymers seeded with colloidal faujasite, and cured for 7 days at 60°C. Symbols in the image represents the position of the more intense peak zeolite type LTA (A), zeolite type X (X), rutile (R), silica (S), anatase (An).	172
Figure 8.6 GPs setting time measured according with ASTM C807.	174
Figure 8.7 SEM images showing the effects of the different compositional, seeding and curing factors on the geopolymer morphology. Sample C_60_4 is taken as baseline.	184
Figure 8.8 SEM images of C_60_4 (top-left) and Belviso's GP [204] (top-right) showing the ZK-5 zeolite. Octahedral crystals observed in the Cw_60_4 (bottom left). Crystal growth of a FAU-X and LTA crystals in Cs_60_4 (bottom-right).	186
Figure 8.9 Simplified representation of the kinetics of the geopolymer formation and zeolite conversion at different curing temperatures using an Avrami-type expression [146]. Dashed lines represent the times when the responses were collected.	187
Figure 8.10 Effect of solution/MK on GP% (left) and on zeolite conversion% (right) for unseeded GPs. The central values (red bars) represents a GP with Na/Al=1, i.e. GP type E.	188

Figure 8.11 GP% responses obtained from ATR-FTIR deconvoluted spectra of GP seeded with colloidal faujasite after 7 days of curing. Samples cured at 5°C (top left), 20°C (top right), 40°C (bottom left) and 60°C (bottom right).	189
Figure 8.12 Percentage of the geopolymer gel that was converted in crystalline zeolite for all the crystallized GPs. The maximum value of 94.7% was obtained for a GP seeded with colloidal faujasite seeds Ds-60-7.	190
Figure 8.13 Effect of seeding on the zeolite conversion % for GP with Na/Al=1.25, H ₂ O/solid=1.06 and curing temperature 60°C.	191
Figure 8.14 Effect of seeding on the GP peak position (left) and GP% (right) for a geopolymer with Na/Al=1 and H ₂ O/solid=0.84 cured at 40°C.	193
Figure 8.15 Left: effect of solution/MK, and indirectly of Na/Al, on the LTA% for GP cured at 60°C with different seeding type. Right: effect of temperature and H ₂ O/solid on the LTA% for GP with Na/Al=1.25 seeded with colloidal FAU.	194
Figure 8.16 Effect of curing time and temperature on the LTA% of a GP with Na/Al=1.25, H ₂ O/solid=0.66 seeded with colloidal FAU.	196
Figure A.1: Observed (in red) and calculated (in blue) diffraction patter of the sample E-60-7 with 25% of rutile as internal standard. On top of the diffractograms peak positions: rutile ICSD 34372 as aqua bars, anatase ICSD 63711 as black bars, quartz ICSD 90145 as green bars, zeolite LTA ICSD 24901 as fuchsia bars. GOF=6.0.	234
Figure A.2: Observed (in red) and calculated (in blue) diffraction patter of the sample Cs-40-7 with 25% of rutile as internal standard. On top of the diffractograms peak positions: rutile ICSD 34372 as aqua bars, anatase ICSD 63711 as black bars, quartz ICSD 90145 as green bars, zeolite NaX ICSD 155683 as fuchsia bars. GOF=5.1.	234
Figure C.3 FTIR peak positions associated with GP: effect of Na/Al (top left), H ₂ O/solid (top right), solution/MK (bottom left) and interaction between curing time and seeding (bottom right).	238
Figure C.4 GP% obtained from the deconvolution of the FTIR spectra: effects of Na/Al (top left), curing temperature (top right), curing time (mid left), seeding (mid right) and solution/MK (bottom).....	239
Figure C.5 GP% obtained from the deconvolution of the FTIR spectra: interaction between curing temperature and time (top left), curing temperature and seeding (top right), curing	

temperature and H ₂ O/solid (bottom right) and curing temperature and Na/Al (bottom right)	240
Figure C.6 FWHM of the FTIR peak associated with GP: effects of Na/Al (top left), temperature (top right) and solution/MK (bottom).....	241
Figure C.7 FWHM of the FTIR peak associated with GP: interaction between Na/Al and seeding (left) and H ₂ O/solid and seeding (right).	241
Figure C.8 Area ratio of FTIR peaks associated with solids and H ₂ O: effect of H ₂ O/solid.	242
Figure C.9 Zeolite conversion % of GP as determined by QXRD: effects of curing temperature (top left), curing time (top right), Na/Al (mid left), seeding (mid right) and solution/MK (bottom).....	243
Figure C.10 Zeolite conversion % of GP as determined by QXRD: interaction between curing temperature, curing time and Na/Al. Na/Al=0.75 (left) and Na/Al=1.25 (right).	244
Figure C.11 Zeolite conversion % of GP as determined by QXRD: interaction between curing temperature, curing time and seeding. GP without seeds (top left), GP with waterglass seeds (top right) and GP with colloidal Faujasite (bottom).....	244
Figure C.12 LTA% of GP as determined by QXRD: effects of Na/Al (left), interaction between seeding and Na/Al (top right), interaction between curing temperature and Na/Al (mid left), interaction between H ₂ O/solid , seeding (mid right) and effect of solution/MK (bottom).	245

List of abbreviations and symbols

Abbreviations

2SIP	solvent separated ion pairs
AAM	alkali activated materials
ANOVA	analysis of variance
AS	activating solutions
BSE-SEM	back scattered electrons - scanning electron microscope
CBC	chemically bonded ceramic
CIP	contact ion pairs
C-S-H	calcium silicate hydrates
DMA	dynamic mechanical analysis
DOE	design of experiment
DoF	degrees of freedom
DSC	differential scanning calorimetry
DTA	differential thermal analysis
EDX	energy dispersive X-ray spectroscopy
FA	fly ash
FAU	faujasite zeolite
FD	framework density
FI	factors interaction
FT-IR	Fourier transform infrared spectroscopy
FTIR-ATR	Fourier transform infrared spectroscopy - attenuated total reflectance
FWHM	full width at half maximum
GP	geopolymer
ICSD	inorganic crystal structure database
LTA	Linde type A zeolite
MK	metakaolin
Ms	silica modulus: molar ratio $\text{SiO}_2/\text{Na}_2\text{O}$
NLSF	nonlinear least-squares data fitting

NWF	network former
OPC	ordinary portland cement
QXRD	quantitative X-ray diffraction
RH	relative humidity
SBU	secondary building units
SEM	scanning electron microscope
SE-SEM	secondary electrons - scanning electron microscope
SIP	solvent shared ion pairs
SS	sum of squares
SS MAS NMR	solid state magic angle spin nuclear magnetic resonance
TEOS	tetraethyl orthosilicate
TGA	thermogravimetric analysis
UCS	unconfined compressive strength
WG	waterglass, alkali silicates
XRD	X-ray diffraction

Symbols

α	reaction degree
β	reaction activity quotient and the equilibrium solubility product ratio
γ	interfacial energy
$\dot{\gamma}$	shear rate
ΔG	Gibbs energy change
ΔH	enthalpy change
δ	phase angle
ε	extinction coefficient
η	viscosity
$[\eta]$	intrinsic viscosity
Θ_{SL}	contact angle
ϑ	diffraction angle
λ	wavelength

v_i	stoichiometry coefficient
ρ	density
τ	shear stress
Φ	solid volume fraction
ω	angular frequency
a_i	species activity
E_{att}	activation energy
G	dynamic modulus
GP%	geopolymer conversion percentage
I	radiation intensity
J	Nucleation frequency
k	kinetic constant
k_B	Boltzmann constant
K_{eq}	equilibrium solubility product
LTA%	percentage of Linde type A zeolite
m	mass
m_{AS}	mass of activating solution
m_{SP}	mass of solid precursor
pK_a	acid dissociation constant
r	reaction rate
R	gas constant
S	surface area
t	time
T	temperature

Acknowledgements

I would like to express my deepest gratitude and respect to my supervisor Prof Tom Troczynski for his patience and continual encouragement throughout the completion of this work. My appreciation also goes to my supervising committee members: Prof Marek Pawlik for his constant support and availability and Prof Lee Groat and Prof Wenying for their valuable suggestions and ideas.

I also thank the faculty and staff at the material engineering department of the University of British Columbia: Michelle Tierney, Gary Lockhart, Fiona Webster, Ross McLeod, Mary Jansepar, Norma Donald, Sherry Legislator. Special thanks go to Kim Wonsang, Sally Finora and Jacob Keibel for sharing their time and expertise with me.

Many thanks are also owed to the colleagues at the University of British Columbia for their help and support: Carmen Oprea, Azadeh Goudarzi, Hamidreza Zargar, Hamed Karimi, Tirdad Nickchi, Ryan Grutze, Megan Ho, Shubham Jain, Xin Lin, Mostafa Samadzadeh, Antonio Natale, Mattia Bacca, Cristina Zanotti and Alberto Baltelli. I also would like to thank Gilberto Artioli, Danilo Pedron, Joanna Mastalska-Popławska, Christophe Gadea, the UBC Composite Research Network and Savvas Hatzikiriakos.

I am extremely grateful for all the sacrifices endured by my family, for their understanding, for their love and their guidance. Grazie Ugo, Giovanna, Marco, Severino, Margherita, Carlo, Margaret, Mattia, Nicca, Alberto, Andrea, Nicoletta, Marta, Gabriele. Thanks to all my dear friends who accompany me in this journey: Thalia, Oscar and Marilu, Luis and Patricia, Tirdad and Maryam, David and Gabi, Baseer, Pooya and Azadeh, Rory and Matt Roik, Abdulrahman, Nick and Shannon, the Black Aces and A La Mode, Friday hockey and everyone who showed up at McBride park.

Dedication

To my family,
for their unconditional love and support

“It is change, continuing change, inevitable change that is the dominant factor in society today. No sensible decision can be made any longer without taking into account not only the world as it is, but the world as it will be.” - Isaac Asimov

“Al di là di sei fiumi e tre catene di montagne sorge Zora, città che chi l’ha vista una volta non può più dimenticare. Ma non perché essa lasci come altre città memorabili un’immagine fuor del comune nei ricordi. Zora ha la proprietà di restare nella memoria punto per punto, nella successione delle vie, e delle case lungo le vie, e delle porte e delle finestre nelle case, pur non mostrando in esse bellezze o rarità particolari. Il suo segreto è il modo in cui la vista scorre su figure che si succedono come in una partitura musicale nella quale non si può cambiare o spostare una sola nota. L’uomo che sa a memoria com’è fatta Zora, la notte quando non può dormire immagina di camminare per le sue vie e ricorda l’ordine in cui si succedono l’orologio di rame, la tenda a strisce del barbiere, lo zampillo dai nove schizzi, la torre di vetro dell’astronomo, la edicola del venditore di cocomeri, la statua dell’eremita e del leone, il bagno turco, il caffè all’angolo, la traversa che va al porto. Questa città che non si cancella dalla mente è come un’armatura o reticolo nelle cui caselle ognuno può disporre le cose che vuole ricordare: nomi di uomini illustri, virtù, numeri, classificazioni vegetali e minerali, date di battaglie, costellazioni, parti del discorso. Tra ogni nozione e ogni punto dell’itinerario potrà stabilire un nesso d’affinità o di contrasto che serva da richiamo istantaneo alla memoria. Cosicché gli uomini più sapienti del mondo sono quelli che sanno a mente Zora. Ma inutilmente mi sono messo in viaggio per visitare la città: obbligata a restare immobile e uguale a se stessa per essere meglio ricordata, Zora languì, si disfece e scomparve. La Terra l’ha dimenticata.” - Italo Calvino

1. Introduction

1.1. Role of geopolymers in sustainable development

The history of human progress has been a succession of challenges, discoveries, innovations, mistakes and improvements. This inexorable progress has not been a linear process and the foundation of its latest flare was laid in the scientific revolution, initiated by Kopernik, Newton and Galileo in the 16th and 17th centuries. Driven by the scientific method and intellect rather than tradition and reverence, human knowledge and capabilities increased until a breaking point: the discovery of steam engine and the sequential widespread use of coal [1].

Suddenly an unprecedented supply of power was accessible to mankind and it triggered a chain reaction of inventions and innovations: the industrial revolution. Power allowed mankind to scale up mining operations and extract and process different minerals. Electric power stations could be built without the need of dams thanks to coal, which also propelled other industrial sectors, such as the chemical industry. It also made economically and practically viable processes such as the synthesis of Portland Cements and the whole iron industry which are energetically expensive. Also pre-existing industries, such as the manufacture of textiles, were affected and manual labour was gradually replaced by machinery which led to an increase in production capacity.

Henceforward human condition changed dramatically and its development and progress has been linked with changes in the Earth's environment. Greenhouse gas emissions have increased ever since, and air and water pollution due to mineral and industrial activities has posed big challenges on population health. New challenges have been raised, such as recycling and/or disposal of by-products generated from the coal-power plants and the steel industries, mining industries - such as mine tailing and red mud - and energy industry - radioactive waste. Today, mankind needs to shift its focus from just social and economic development to sustainable development in all aspects, where decision-makers should take in consideration the repercussions on society and environment and not only on economy.

When seeking effective solutions to the abovementioned problems we need to develop technologies that can be easily implemented worldwide and can be tailored to adapt to different conditions. Among the main materials that fostered human development, silicon has had a key role and the complexity of its chemistry is second arguably only to carbon and iron [2]. The glass, semiconductor and construction industries are all based on silicon, thanks to its unique chemical and physical properties. In particular most of conventional ceramic materials are based on silicate and aluminosilicate materials. If we exclude oxygen, silicon and aluminum make approximately 2/3 of the total mass of the Earth's crust, thus any technological solution based on aluminosilicates can be easily implemented in large scale worldwide at relatively low cost [3].

In particular, a new class of materials named GeoPolymers "GPs" have shown great potential to substitute Portland Cement as inorganic binder in construction applications, cut CO₂ emissions generated during calcination of raw materials, recycle large quantities of industrial and mineral waste, while allowing encapsulation of toxic and radioactive waste materials [4]. Additionally, GPs can be used in advanced environmental and industrial applications, such as water purification [5], [6], production of membranes [7] etc. This work focuses on developing functional metakaolin based geopolymers which can address many of the abovementioned challenges. The principal objective of this work is the identification of the main processing parameters that control the synthesis and structure of advanced geopolymers. Particular attention is given to develop a better understanding of the interrelations between processing, structure, properties and performance of GP.

1.2. Inorganic binders

This section is not intended to be a complete review of all inorganic binders, but to introduce the reader to this class of material, also called cements. GP science and cement science have many aspects in common and ultimately GP performances need to be compared to ones of other cementitious systems (Section 2.2.4.2). Binders are usually mixed with a liquid to form viscous slurry that hardens over time to form an artificial "stone". Inorganic binders are the core materials of construction industry and they are seldom used by themselves: they are rather combined with sand to form mortar or with sand and aggregate to produce concrete.

Concrete is the second most used material by man after water: 33Gt of concrete were poured in 2010 [1]. It has brought numerous benefits to human society, for instance parasitic diseases are reduced in residential areas where concrete flooring is used, while economic activities and value of land and rental increase [1].

The pursuit of alternative inorganic binders stems from the high CO₂ impact that the cement production is associated with. Around 5% of the total anthropogenic CO₂ emissions come from cement production, with an approximate ratio of 0.815 t CO₂ / t OPC: 0.425 t from raw materials calcination (e.g. $\text{SiO}_2 + 3\text{CaCO}_3 \rightarrow 3\text{CaO} \cdot \text{SiO}_2 + 3\text{CO}_2$) and 0.390 t from fuels [8]. Nonetheless, the embodied energy of OPC, i.e. 1MJ/kg, and its CO₂ emission per ton of material is among the lowest compared with other construction materials. Steel and aluminum emit approximately 3 and 5 times more CO₂ on a weight base, while their embodied energies are roughly 21.5 MJ/kg and 240 MJ/kg [8]–[11]. It is the sheer amount of OPC production that causes the problem: 82.8x10⁶ ton only in US during 2015 worth \$10 billion in sales [12]. Thus, any small improvement can have a huge effect in terms of energy savings and CO₂ emissions reduction.

The first binder discovered by mankind over 5000 years ago was gypsum and it is based on the hydration reaction of calcium sulfate hemihydrate $\text{CaSO}_4 \cdot 0.5\text{H}_2\text{O}$ with water to produce calcium sulfate hydrate $\text{CaSO}_4 \cdot 2\text{H}_2\text{O}$. The calcium sulfate hemihydrate is obtained by calcining gypsum at approximately 120°C. Another historic inorganic binder is obtained by calcining calcium carbonate at 900°C to produce lime CaO, a binder that upon reaction with water forms hydrated lime $\text{Ca}(\text{OH})_2$, which with time reverts back to CaCO_3 , by picking up atmospheric CO₂. Both gypsum and lime are non-hydraulic binders as they cannot be exposed for prolonged amount of time to moisture or water [11]. Another type of non-hydraulic binder was invented in 1867 by Sorel [13]: the magnesia cement, based on the reaction of magnesia MgO and magnesium chloride $\text{Mg}(\text{Cl})_2$ with water to produce solid magnesium chloride hydrates which are fairly soluble in water [14].

The first hydraulic binder was discovered by the Romans and reported in 1 year of BC by Vitruvius in the book “De Architectura”. Romans added volcanic silica-rich ashes from Pozzuoli, an Italian city near Naples, to a lime binder. The reaction between the amorphous

silica SiO_2 in the ash and the lime Ca(OH)_2 produced calcium silicate hydrates, also called C-S-H, Figure 1.1 [15]. This cement had the ability to set and harden under water and showed improved properties in term of flexural strength and durability. Because of these characteristics Roman cement structures such as the Colosseum, the Aqua Claudia aqueduct and the Pantheon have lasted 2000 years until nowadays, and likely will last for thousands years more, Figure 1.1.

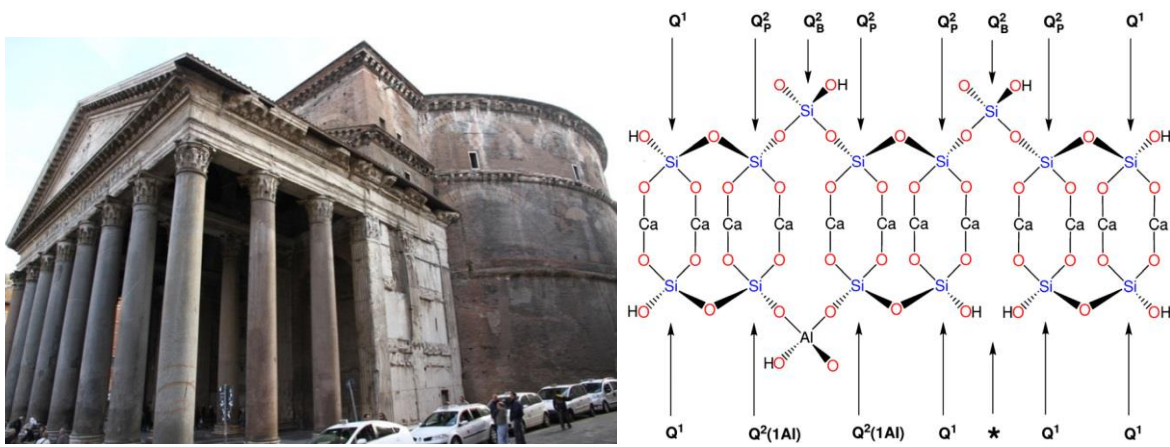


Figure 1.1 Left: Pantheon “temple of every god” in Rome built using roman cement 2000 years after its construction. Right: Schematic structure of the C-S-H, main hydration product of roman and modern cements: A 2-D sheet of 7-coordinated Ca ions share oxygen’s with depolymerized “dreierketten” chains of SiO_4 tetrahedra. Q_n represents the connectivity “n” of the silica tetrahedra [15].

For the modern cement as we know it we had to wait until the 1786 AD (Parker cement) and 1824 AD (Portland cement patent by Joseph Aspdin) [16]. The invention consisted in calcining a precise amount of ground limestone and clay at a temperature of about 1400°C - 1500°C to produce the “clinker” and by grinding the clinker to obtain a highly reactive fine powder. The main phases in the Ordinary Portland cement (OPC) are the tricalcium and dicalcium silicates, which produce C-S-H and hydrated lime Ca(OH)_2 upon hydration, Table 1.1. ASTM C150 specifies the different types of OPCs, ASTM C595 described different blended cements and ASTM C1157 divides the cements based on their performances. Similarly in Canada the CAN/CSA-A3000 Cementitious Material Compendium describes in details the different classes of cementitious materials. Blended cements are obtained when Portland cement is mixed with different supplementary cementitious materials (SCMs) which have pozzolanic properties and react with the Ca(OH)_2 to produce even more C-S-H. The most common pozzolanic materials used in OPC are fly ashes class F (low in CaO), natural

pozzolanas, silica fumes and metakaolin [17]. Compared with OPC, SCMs are richer in SiO_2 and Al_2O_3 , Figure 1.2.

Table 1.1 Main mineralogical phases in Portland cement clinker, their shorthand notation and weight percentage [17].

Shorthand notation	Chemical name	Mineral name	chemical formula	weight % in clinker
C_3S	Tricalcium silicate	Alite	Ca_3SiO_5	50-70
C_2S	Dicalcium silicate	Belite	Ca_2SiO_4	15-30
C_3A	Tricalcium aluminate	Celite	$\text{Ca}_3\text{Al}_2\text{O}_6$	5-10
C_4AF	Tetracalcium aluminoferrite	Brownmillerite	$\text{Ca}_4\text{Al}_2\text{Fe}_2\text{O}_{10}$	5-15

Another type of inorganic binder is calcium aluminates cement, CAC, obtained from calcination of limestone with bauxite at 1450-1600°C. The resulting powder hydrates quickly, it has a better resistance to sulfate solutions than OPC and it can be used as refractory cement, a heat-resistant type of binder used to produce refractory castables [17]. All those binders have in common is the high percentage of calcium which makes the cement basic and has the ability to form almost insoluble salts at high pH with most anions, such as SO_4^{2-} , OH^- and CO_3^{2-} , and oxyanions, such as $[\text{SiO}_x(\text{OH})_{4-x}]^{-x}$ and $[\text{AlO}_x(\text{OH})_{4-x}]^{-x-1}$. The presence of calcium is also the weak characteristic of those binders, which is the sensitivity to attack by acidic solutions. Moreover, since limestone CaCO_3 is used as raw material for their production, these binders emit a significant amount of carbon dioxide: CO_2 accounts for 44% of the molecular mass of CaCO_3 which adds up to emissions generated by the fossil fuels burnt in the kilns.

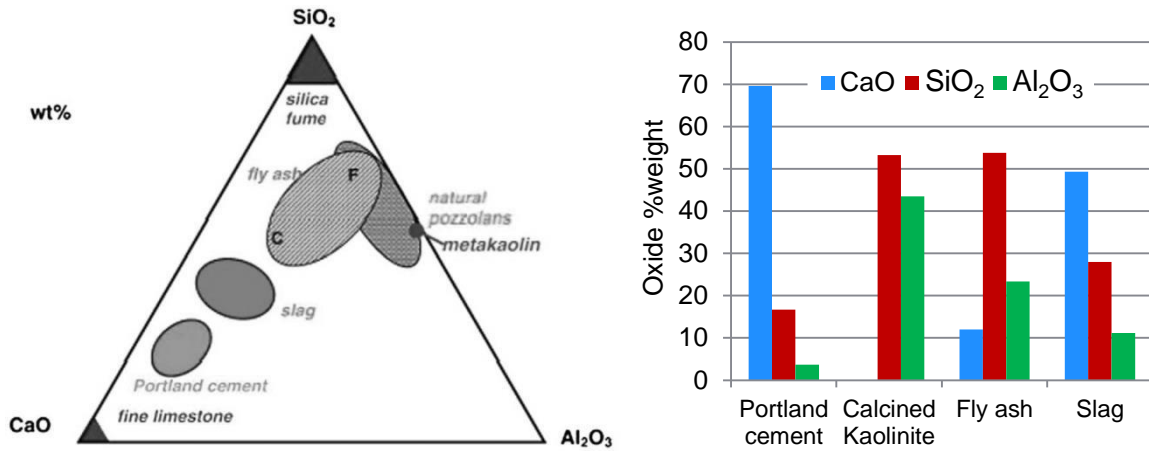


Figure 1.2 Left: $\text{CaO}-\text{Al}_2\text{O}_3-\text{SiO}_2$ ternary diagram of cementitious materials [18]. Right: Main oxide weight % of selected materials used as inorganic binders.

A different class of inorganic binders is the Chemically Bonded Ceramics (CBCs) which are obtained by the reaction of two components, one acidic and one alkaline. GPs belong to this class of material: the solid aluminosilicate powder is the acidic component and the hardener is the alkaline component. Other CBCs also exist, for example polyalkenoate, oxy-chloride, and oxy-sulfate cements [19]. Another large class of CBCs are the phosphate chemically bonded ceramics extensively described by Wagh [19]. In this case the acidic component is the liquid phosphate (e.g. diluted phosphoric acid), while the basic component is an oxide powder such as zinc oxide ZnO , magnesium oxide MgO , calcium oxide CaO , wollastonite CaSiO_3 , magnetite Fe_3O_4 , wustite FeO and alumina Al_2O_3 [19], [20].

The CBCs can be considered as an intermediate class of materials between ceramics and conventional hydraulic cements. Conventional ceramic materials are crystalline materials stable at high temperatures but their synthesis requires sintering at high temperatures i.e. $T > 1000^\circ\text{C}$, and elevated pressures. Hydraulic binders are mainly amorphous materials that can be prepared at room temperature and they lose their structural integrity at relatively low temperature, i.e. $T = 100-300^\circ\text{C}$. CBCs can be processed at near room temperature and retain their cohesion at temperatures up to 1000°C and beyond. Their applications span from construction materials to refractory cements, dental cements, corrosion and fire protection coatings, material for toxic and radioactive wastes encapsulation [20].

1.3. Motivation

In this dissertation the transformations which occur during the synthesis of metakaolin based geopolymer were investigated in term of processing parameters. While much work was done in the field of constructional cements, there was no fundamental understanding of the reactions that can lead to the production of functional materials which exploit the zeolitic properties of the geopolymer. The knowledge gap led to inconsistent GP properties which hindered their uses in advanced technologies. This research aimed to advance the knowledge in this field and to produce geopolymers with tunable structures and properties for industrial and environmental applications. While Chapters 6 and 8 focus mostly on functional NaOH-based geopolymers, Chapters 5 and 7 provide important insights on both constructional and advanced GPs.

2. Literature review

2.1. Introduction to geopolymers

2.1.1. Geopolymers and their terminology

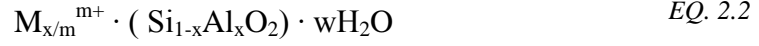
Geopolymerization is a technology that converts aluminosilicates to advanced inorganic binders, i.e. geopolymers (GPs), which show performance advantages in respect to traditional binders e.g. Ordinary Portland Cement (OPC). The advantages span from better resistance to acid and sulfate attack, thermal stability, possibility of heavy metals encapsulation, durability, etc. Geopolymers are also attracting increasing attention due to two additional factors: the need to lower the CO₂ emissions during processing of cementitious binders, such as OPC, and to recycle industrial waste otherwise intended for disposal in landfills. The properties and applications of geopolymers will be further covered in Section 2.1.3.

From a structural point of view GP consists of the atomic lattice of condensed silica and alumina tetrahedra with alkali cations balancing the negative charge on aluminum [21]–[23]. In fact the main difference between geopolymers and OPC lays on the nature of the network former (NWF): in OPC the main NWF is calcium (see Figure 1.1), while in GP is silicon and aluminum. Calcium can also be present in GP, but in this case it has a charge-balancing role. As calcium is a metal with electronegativity 1.00, it forms mostly ionic bond with oxygen. Silicon and aluminum instead are semimetals with electronegativity 1.90 and 1.61 respectively, thus they form mostly covalent bonds with oxygens. The general empirical formula of a geopolymer can be expressed as in EQ. 2.1 [22]:

$$M_n \cdot ((SiO_2)_z \cdot (AlO_2))_n \cdot wH_2O \quad EQ. 2.1$$

where “M” is an alkali metal cation such as K⁺ or Na⁺, “n” is the degree of polycondensation, “z” usually varies between 1 and 3 and “w” is the water content. This formula explicitly expresses the alumina in tetrahedral coordination, i.e. AlO₂⁻, and the correct stoichiometry of a charge-balanced composition.

This formula closely resembles the one of zeolites, a class of hydrous aluminosilicate frameworks which will be later described and their formula can be written as in EQ. 2.2 [24]:



EQ. 2.3 represents an alternative way to express the chemical formula of geopolymer independently from the degree of polycondensation, where x , y , z , and w are the moles of alkaline oxide, silica, alumina and water [25]. This chemical formula will be used within this manuscript to identify and compare different geopolymer compositions. The GP compositions can then be expressed in a contracted form by indicating the oxides moles separated by a hyphen, e.g. 1-1-2-11 stands for $1M_2O \cdot 1Al_2O_3 \cdot 2SiO_2 \cdot 11H_2O$.

Most GPs are prepared from 2-components systems which include a solid aluminosilicate powder and an alkaline solution often referred as activating solution, alkaline solution or hardener. Upon mixing the flowable slurry polymerizes (“hardens”) at temperatures ranging from $T \approx 0^\circ C$ up to $T = 85^\circ C$ [22]. One-component geopolymers have also been investigated but will not be covered in this work. The suitable aluminosilicate powders for geopolymerization can be roughly divided into two classes: 1) Thermally activated aluminosilicates, including especially but not exclusively clay minerals containing kaolin [26]; 2) Industrial by-products in which the alumina and silica bearing wastes have been subjected to high temperature and then abruptly cooled to room temperature. The two most used industrial by-products in GP applications are ground granulated blast furnace slag (GGBFS) and fly ash (FA) generated by coal-fired power plants [27]. On the contrary of OPC, the solid components of geopolymer do not require the calcination of carbonate-bearing minerals associated with CO_2 emissions. Kaolin does not contain calcium and can be calcined at lower temperature (i.e. $T = 750^\circ C$) compared with OPC (i.e. $T = 1450^\circ C$). Fly ash and GGBFS can be considered as already thermally activated due to the high-temperature processes that generate them.

The first conceptual mechanism for geopolymerization was elaborated in 1959 by Glukhovsky in order to explain the reactions involved in the formation of the new binders he

was developing. It was named “soil cement” and obtained from ground aluminosilicate and rich alkalis industrial wastes [28]. Glukhovsky model described the geopolymerization reactions in three steps:

1. destruction - coagulation
2. coagulation - condensation
3. condensation - crystallization

These stages are so defined because they cannot be isolated; for example the dissolution reaction proceeds simultaneously with the gel formation and the polycondensation setting reactions. In other words, the first step represents the hydrolysis of the Si-O-Al bonds of the powder and the release of small oligomers in the alkaline solution, while the second step represents the condensation of those small oligomers to form a 3D network of silica and alumina [29].

Many researchers refer to geopolymers as “alkali activated aluminosilicates” and thus geopolymerization could be defined as “alkali activation of aluminosilicates”. However, the precise definition of geopolymer and the boundaries between geopolymers and non-geopolymers are still a matter of debate nowadays among GPs scientists. Additionally, several other denominations have been given to this class of materials [30]: alkaline cements, alkali-activated materials, alkali-bonded ceramics, geopolymer cements, geopolymeric cementitious compounds, geocements, poly(sialates), mineral polymers, inorganic polymer concretes, hydroceramics, etc. [4], [21], [28], [31]–[33]. Some authors used the term geopolymer only when the reaction product is a zeolite with amorphous to semi-crystalline characteristic [34]. Further confusion arises when geopolymerization is compared with pozzolanic reactions, which is the acid-base reaction between calcium hydroxide and reactive silica [34].

The term geopolymer was coined by Joseph Davidovits. He initially defined them as polysialates in his first patent related to GPs: Polymère Minéral FR 79.22041, later translated as “Mineral polymers and method of making them” [35]. Later on he renamed this class of material as geopolymers [22], [23], [36]: *“For the chemical designation of geopolymer based on silico aluminates we suggested poly(sialate). [...] Poly(sialates) have this empirical*

formula: $M_x(-(SiO_2)_z-Al_2O)_n \cdot wH_2O$ wherein “z” is 1,2 or 3;...” [22]. In 1979 he cofounded with his family the French private research company “Cordi-Géopolymère” and in 1979 he founded the Geopolymer Institute focused on GP science communication and this certainly helped the diffusion of his terminology. Since then the number of scientific papers using the term geopolymers increased exponentially, Figure 2.1.

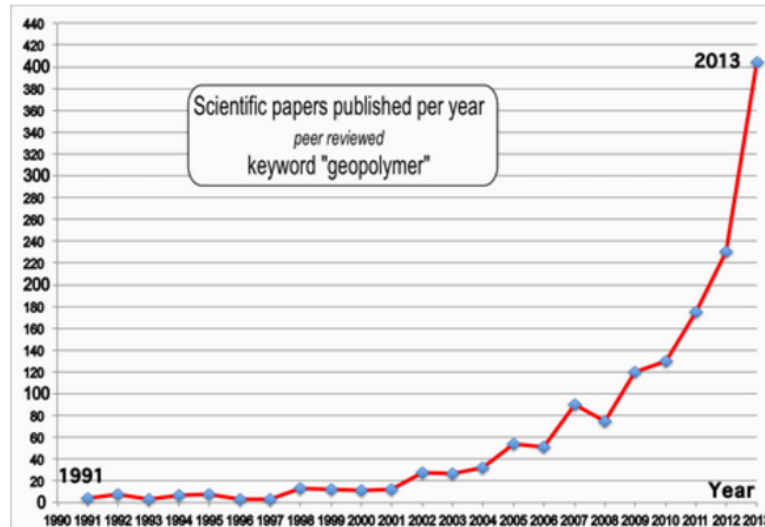


Figure 2.1 Number of scientific papers using the geopolymer terminology since 1991 [37].

Davidovits then proposed that geopolymer is not an alkaline activated aluminosilicate but rather a mineral compound consisting of repeating units created through the process of geopolymerization [38]. This definition shifted the attention on the geopolymerization process itself, which in turn he defined as the process of combining small molecules, i.e. oligomers, in basic or acid medium into a covalent bonded network. This more general definition allows the inclusion of phosphate-based geopolymers, which are the products of the acid-base reactions between inorganic oxide and an acid phosphate.

Table 2.1 compiles the nomenclature used to describe various components of geopolymer systems [38]. When the chemical unit blocks form small chains or rings the name of the compound has the prefix “oligo” followed by the name of the building block (e.g.

oligosialate). When the unit blocks form big macromolecules the name of the compound has the prefix “poly” followed by the name of the building block, e.g. poly(sialate-disiloxo).

Table 2.1 Geopolymer nomenclature [38].

Chemical unit	Nomenclature
-Si-O-Si-O-	siloxo
-Si-O-Al-O-	sialate
-Si-O-Al-O-Si-O-	sialate siloxo
-Si-O-Al-O-Si-O-Si-O-	sialate disiloxo
-P-O-P-O-	phosphate
-P-O-Si-O-P-O-	phospho siloxo
-P-O-Si-O-Al-O-P-O-	phospho sialate
-R-O-Si-O-Si-O-R-O-	organosiloxo
-Al-O-P-O-	alumino phosphate
-Fe-O-Si-O-Al-O-Si-O-	ferro sialate

There is an ongoing debate about GP terminology. In this work, unless otherwise specified, geopolymer will be considered as a low-calcium alkali activated aluminosilicate cement with a $\text{Si/Al} \leq 3$ [4], consisting of condensed silica and alumina tetrahedra with alkali cation balancing the negative charge on aluminum. Thus it is the four-fold coordination and tetravalence of aluminum that defines geopolymers, as specified in [21], [23].

2.1.2. Types of aluminosilicate geopolymers

Aluminosilicate GPs are Chemically Bonded Ceramics (CBC) and they are processed using two components: the solid component is acidic and typically composed of silica and alumina whereas the liquid component is alkaline and can be referred to as hardener (or “activating solution”). In principle all materials containing silica and alumina are suitable for geopolymerization. In practice the silica and alumina must be sufficiently reactive for the geopolymerization reaction to be significant; the more reactive the component containing

alumina and silica is the more and faster they will be converted into a geopolymer. For this reason chemical analysis of the raw materials is not enough and X-ray diffraction techniques should be used to determine the amount of amorphous, and thus more reactive, phases in the aluminosilicate solid precursors [39]. Crystalline materials are more resistant to the geopolymerization reactions [40].

Activating solutions mainly consist of concentrated alkaline metal hydroxides solutions, such as sodium hydroxide NaOH and potassium hydroxides KOH, or concentrated soluble silicate solutions of sodium or potassium (further described in Section 2.2.3.)

As previously mentioned, defining the boundary between GPs and non-GPs systems is often not straightforward and once again calcium is at the center of the discussion. According with the RILEM technical committee [4] GPs are a subcategory of AAMs (Alkali Activated Materials) with low calcium content and high alumina content, Figure 2.2. Davidovits did not agree with this classification and according to him: geopolymers are not gels or precipitates but polymers, and thus the scientific community should follow the polysialate nomenclature [22]; AAMs leach sodium while GPs do not. He also stressed that “GP is a concept, not a product” [37]. The debate is complicated by Davidovits not actively publishing in scientific journals but rather communicating through the Geopolymer Institute’s medias [37].

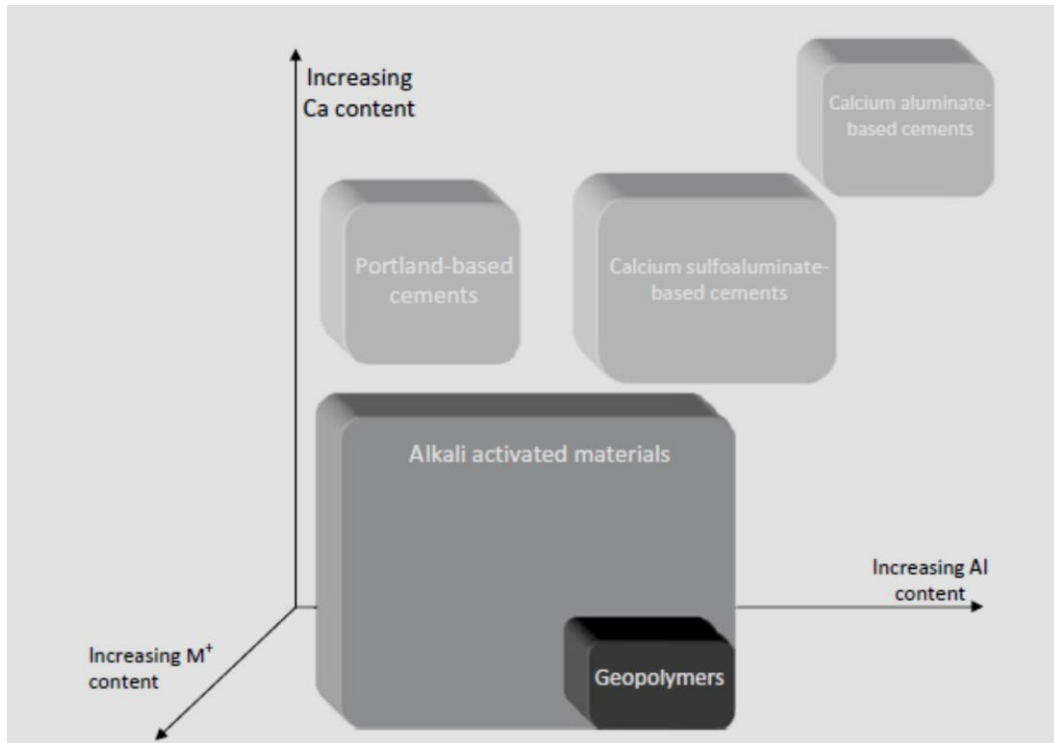


Figure 2.2 Classification of AAMs according with RILEM [4]. GPS are considered a subgroup of AAMS with low calcium and high alumina content.

Davidovits further suggested that the difference between an alkali activate slag and a GP based on slag is that the second material includes metakaolin $\text{Al}_2\text{Si}_2\text{O}_7$, which increases the alumina content and decreases the overall calcium content. This is essentially the same as the description given by RILEM committee, Figure 2.2. While most of AAMs have C-S-H as reaction product, GPs reaction products are made of a 3D network of aluminosilicates, Figure 1.1 and Figure 2.15. The leaching of sodium from AAMs is equivalent to the cation exchange properties of GPs containing crystalline zeolite: the higher the alumina content the higher the AAMs ability to exchange Na^+ with H^+ in solution [41]. Poly(sialate) based on NaOH and MK belongs to this category of low Si/Al geopolymers.

Several exhaustive reviews on AAMs are available [4], [42]–[45]. For instance Shi [45] described these systems complexity and the possible permutations of raw materials. Many other types of geopolymers have been studied which adopts different industrial waste as raw materials [46]: rice husk ashes, palm oil fuel ashes, incineration products of sludges, coal bottom ashes, silico-manganese slag, mineral processing tailings such as red mud and mine

tailings, catalyst residues from petroleum refineries, waste glasses and ceramics. In his book [38] Davidovits classified the GPs based on kaolinite, metakaolin, metakaolin with slag, rock based geopolymer (based on calcined clays containing Fe_2O_3), silica based geopolymers (based on rice-husk or silica fume), fly ash based geopolymers and phosphate based geopolymers.

The reason why many researchers prefer not to use the term AAM is to avoid the association with the alkali silica reactions, including a reaction in OPC concrete between the aggregate and calcium hydroxide which leads to expansion, crack formation and concrete degradation [17]. However, alkali silica reactions with the aggregate do not occur in AAM and GP concrete [38]. The advantage of having a soluble silicate over the alkaline hydroxides lies in the relatively lower pH which makes the materials easier to handle. Based on this concept the AAMs can be divided into user-friendly (pH = 11 to 13) or user-hostile (pH = 13 to 14.2). On this topic a recent patent “Geopolymeric cement based on fly ash and harmless to use” [47] on GPs using soluble silicates with a ratio $\text{SiO}_2/\text{Na}_2\text{O} > 1.28$ has been granted.

In this manuscript we will consider alkali-activated metakaolin as GPs: *“In general, aluminosilicate binder materials activated by alkali hydroxides or silicates under high-pH conditions are classified as being geopolymers,...”* [30]; *“The activator will usually be an alkali metal hydroxide or silicate”* [4].

2.1.3. Geopolymers properties and applications

The wide range of the reported GP compositions and processing conditions reflects their possible wide range of applications. GP can be cheap, fire resistant, emit during processing low amount of CO_2 compared with OPC, can quickly set and develop high compressive strength at room temperature, have low permeability and low leaching, low thermal conductivity, be acid resistant, have low shrinkage, have high cation exchange capacity [38]. Nonetheless, the composition and preparation of GP needs to be tailored in order to maximize the desired properties based on the application and often compromises need to be made. As Duxson observed: *“Inorganic polymers should not be considered a universal panacea for all material selection problems, but rather a solution that may be tailored by correct mix and processing design”* [29].

According with Davidovits the main parameter regulating the properties of the geopolymers is the ratio silica over alumina [38], [48]. Geopolymers with a Si/Al between 1 and 2 find applications as alternative construction materials such as low and high strength concrete, bricks and tiles, fire and acid resistant coating and binders for mining and nuclear waste encapsulation [38]. Higher Si/Al ratio leads to geopolymer with high temperature and fire stability with application such as ceramic for molding, fire proofing and heat resistant composite [49].

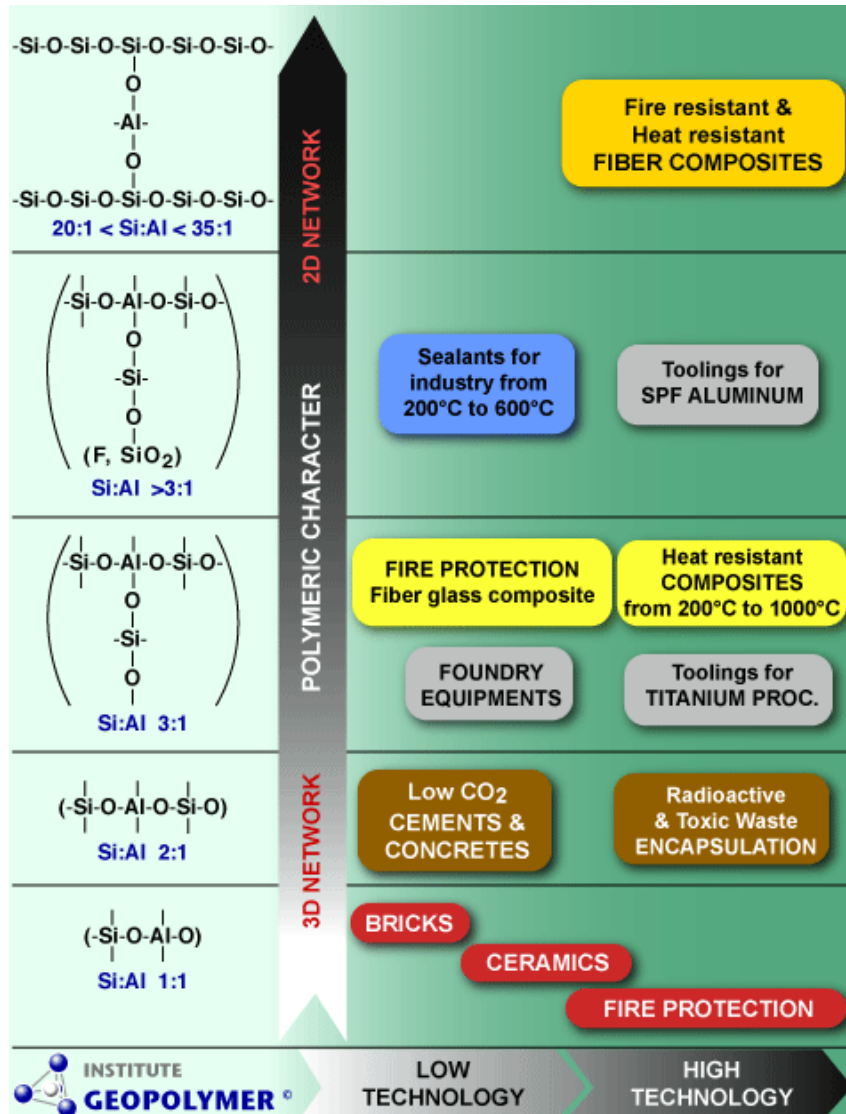


Figure 2.3 Names, structures and applications of geopolymer at different Si/Al ratio [38].

For instance, GPs based on metakaolin, slag and potassium silicates can be used in the following applications [48]: fire resistant wood panels; insulated panels and walls; decorative stone artifacts; foamed (expanded) geopolymer panels for thermal insulation; low-tech building materials; energy low ceramic tiles; refractory items; thermal shock refractory; aluminum foundry application; geopolymer cement and concrete; fire resistant and fire proof composite for infrastructures repair and strengthening; fireproof high-tech applications and coatings, aircraft interior, automobile and high-tech resin systems.

The geopolymer technology has great potential in connection with the recycling of industrial by-products such as red mud and mine tailings. Hazardous industrial by-product containing clay minerals can be calcined and activated at moderate temperatures to produce a precursor material [50] for stabilization purpose or to be used as a binder for cemented paste backfill [51], [52]. Finally GPs can substitute Portland cement also in future technologies, such as 3D printing of geopolymer structures and artifacts [53], [54]. Geopolymer foams have good thermal insulation properties [55]; additionally, they can be also used to remove copper and ammonia from wastewater [56]. Other advanced applications will be covered in Section 2.4.

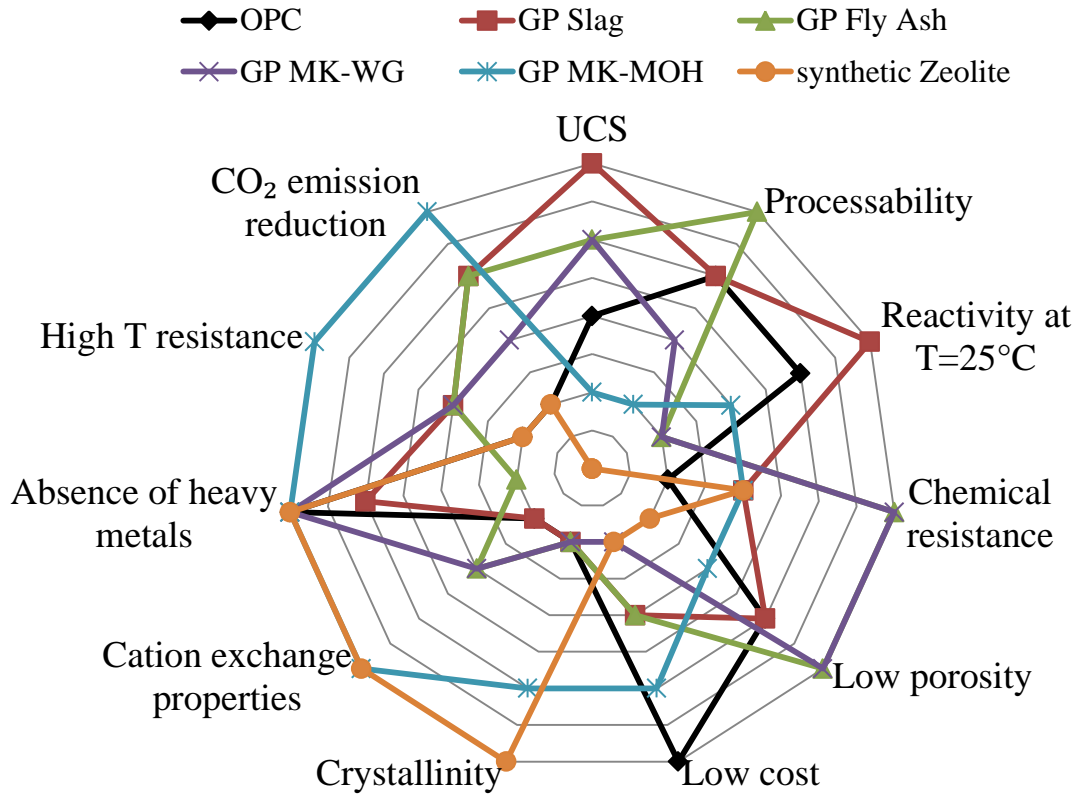


Figure 2.4 Comparison between selected properties of inorganic binders: Ordinary Portland Cement (OPC), geopolymer based on slag, metakaolin and soluble silicate (GP Slag), geopolymer based on fly ash and soluble silicate (GP Slag), geopolymer based on metakaolin and soluble silicates (GP MK-WG), and geopolymer based on metakaolin and alkali hydroxides (GP MK-MOH). The data are compiled from [4], [32], [38], [57]–[60]

Figure 2.4 illustrates selected properties of GPs and different binders obtained using different raw materials; high values in the web chart are desirable. The data, compiled based on [4], [32], [38], [57]–[59], are not quantitative but an indication of material performance when compared with each other. The main advantages of OPCs are their low cost, processability and low temperature reactivity; per contra they have low durability and chemical resistance in comparison with GPs [61] and relatively low temperature resistance [17].

GPs based on slags can quickly harden at room temperature and have relatively high unconfined compressive strength (UCS), typically in the range of 30 to 70 MPa [60]. Their chemical resistance is however inferior to low calcium GPs and they have no important functional properties [4]. Their main application is low CO_2 cement and concrete and companies such as Wagner developed and successfully implemented this material,

trademarked as “Earth Friendly Cement” [37]. GPs using industrial waste product such as slag and fly ash are usually cheaper than GPs using thermally activated clays since there is no calcination operations involved.

The highest cost of GP raw materials are usually activating solutions, in particular sodium silicate is much more expensive than sodium hydroxide (i.e. typically \$800/t vs \$125/t), and its synthesis is associated with higher values of CO₂ emissions [32]. Although soluble silicates can retard the setting reaction at low temperatures compared with sodium hydroxides [25], it is widely accepted that they lead to a denser microstructure and higher UCS of the resulting GP [58], [62] and increase its chemical resistance [41], Figure 2.5. On the other hand, using soluble silicate decreases the crystallinity of GPs, reduces their cation exchange capacity, and decreases their melting point from about 1256°C to 1065°C, Figure 2.5. Usually geopolymers do not contain albite and nepheline crystalline phases, they are amorphous or they crystallize as zeolites. Nonetheless these two phases can form when geopolymers are heated at elevated temperatures, $T \approx 800^\circ\text{C}$.

Fly ashes based GPs are usually the easiest to process due to FA spherical morphology, while metakaolin based GPs have higher viscosity and thus require additional water or solution to be processed (e.g. cast), which usually increases the porosity and weakens the final product [63]. Synthetic zeolites are not cements since they are prepared in highly diluted solutions and thus have no binding characteristics.

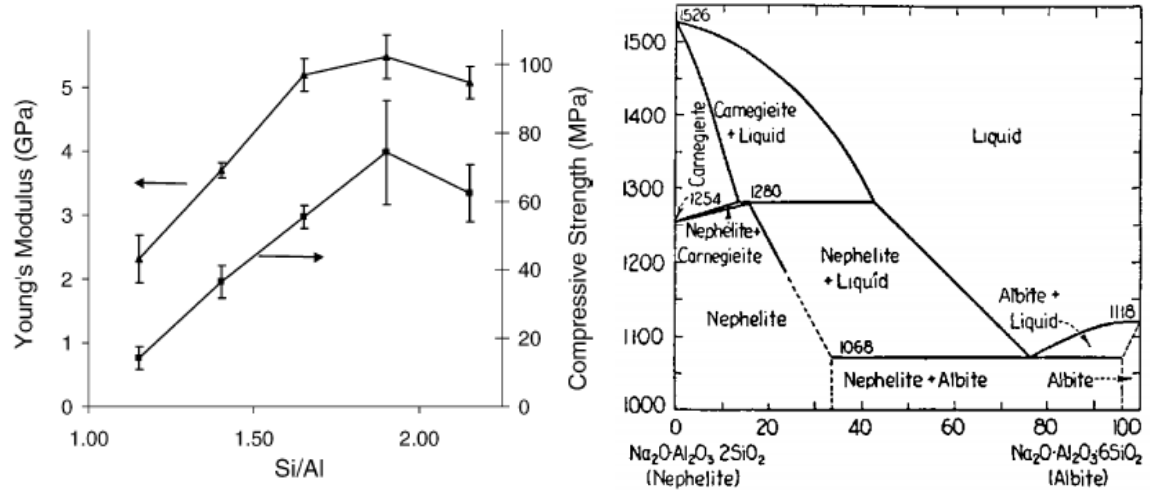


Figure 2.5 Effects of increasing Si/Al ratio through the use of sodium silicate in metakaolin-based GPs. Left: Effects on compressive strength and young modulus [58]. Right: phase diagram of nepheline-albite, corresponding to a GPs with Si/Al ratio of 1 and 3 respectively [64].

One of the main obstacles to the widespread use of GPs cements and concretes as a low CO₂ alternative to OPC is coming from regulatory bodies, i.e. the prescriptive nature of the standard ASTM C150 and ASTM C595, which makes the use of Portland Cement mandatory. This is also the case in Europe with the standard EN 206-1 and EN 197-1. The only current standard that permits the use of GPs and AAMs is the performance based ASTM C1157 [10], which is only accepted in 5 out of 50 states in the US [4].

2.2. Metakaolin - based geopolymers (MK-based GP)

2.2.1. Historical perspective

The dawn of AAMs as alkali activated slags lays in the work of Purdon in 1940 [65] and Glukhovski in 1959 [28], nevertheless slags were already used in combination with lime and as supplementary cementitious material in OPC during the 19th century [66].

The birth of geopolymers is associated instead with metakaolin (MK), when Davidovits was developing fire-proof binders in response to a series of catastrophic fires in Paris [48]. In 1974 Davidovits developed decorative ceramic panels bonded by organic polymers [67], and then he worked on the production of ceramic plates from clays and sodium hydroxide by hot-pressing at 150°C [68]. According to him the first geopolymer patent dated back in 1982 and

was based on geopolymerization of MK at low temperatures [35]. Also his following papers in regard to geopolymers were focused on this material [22], [23], [49]. The main difference between AAMs based on slag and a GPs based on slag seems to rely on the addition of MK to the latter. A subcategory of geopolymers made of metakaolin, waterglass and sodium hydroxide are described in the patent [35] where the composition range is expressed as follows:

Table 2.2 Chemical compositions of geopolymers according to [35] .

ratio	min	max
$\text{Na}_2\text{O} / \text{SiO}_2$	0.20	0.28
$\text{SiO}_2 / \text{Al}_2\text{O}_3$	3.5	4.5
$\text{H}_2\text{O} / \text{Na}_2\text{O}$	15	17.5
$\text{Na}_2\text{O} / \text{Al}_2\text{O}_3$	0.8	1.2

The resulting paste had the viscosity of a resin and should be cured at temperature between 25°C and 120°C. The higher the temperature the shorter the curing time required: at $T=25^\circ\text{C}$ the setting takes more than 15 hours, while at $T=85^\circ\text{C}$ the setting takes about 1.5 hours. The use of fly ash in geopolymer started only in the 1994 with Wastiels [69].

Davidovits's work was followed by Palomo in 1992 who studied chemically bonded cements based on MK [70]. In 1996 Rahier extensively investigated geopolymers 1.0-1.0-3.4-10.0 (nomenclature in Section 2.1.1) which he named "Low Temperature Inorganic Polymer Glass" LTIPG. By using NMR, DSC, DMA (dynamic mechanical analysis) and other techniques he proved that a unique reaction stoichiometry exists, in which 1 mole of Na_2O is needed for each mole of Al_2O_3 . Different stoichiometry resulted in unreacted metakaolin or in an excess of solution that is entrapped in the geopolymer [59–62].

In 1998 Granizo et al. used isothermal calorimetry to investigate the reaction kinetics between metakaolin and sodium hydroxide for geopolymer with high solution/solid and a $\text{Na}/\text{Al} > 1$ [75]. The geopolymerization reactions were found to be exothermic: after a rapid exothermic peak associated with MK dissolution an induction period was detected, followed by an intense and asymmetric exothermic peak associated with polymerisation and crystallization. The duration of the induction period increased by increasing solution content or ionic strength, i.e. sodium hydroxide concentration [75].

The first experimental evidence of the superior sulfate resistance and durability of geopolymer mortar over OPC was experimentally determined by Palomo *et al* in 1999: the flexural strength of metakaolin activated with soluble silicates at 85°C for 2 hours did not decrease after 270 days exposure to aggressive liquids [61].

Barbosa and Kriven focused on the thermal stability of GP [76]–[80]. In 2000 Barbosa [76] performed a statistical analysis of the effects of the processing parameters including $\text{Na}_2\text{O}/\text{SiO}_2$, $\text{SiO}_2/\text{Al}_2\text{O}_3$, $\text{H}_2\text{O}/\text{Na}_2\text{O}$ on the properties of geopolymers with $\text{Si}/\text{Al} > 1.6$ cured at 65°C for 2.5 hours. Although the aluminum in each variant of such geopolymers was mainly IV-coordinated, ^{29}Si NMR data revealed that the soluble silicates did not react with the MK when an excess of water was used. For those samples the formation of sodium carbonates was also observed.

Barbosa then compared the high temperature stability of their best sample of the composition 1.00-1.21-3.99-10.00 with a poorly-formulated sample which had an excess in sodium and water: 1.00-0.88-3.33-17.50. Small shrinkage ($\Delta L/L \approx 3\%$) was observed for both samples at temperature of $T=200^\circ\text{C}$ due to water evaporation and at 800°C due to crystallization and densification. The onset of melting of GP 1.00-1.21-3.99-10.00 was $T=1300^\circ\text{C}$. An excess of sodium induced nepheline NaSiAlO_4 crystallization at 800°C and reduced the onset of melting to 1100°C [77]. A similar study on potassium-based GPs revealed that these GP are stable up to 1400°C and that crystallization of nepheline and kalsilite KSiAlO_4 are favorable at low Si/Al [78].

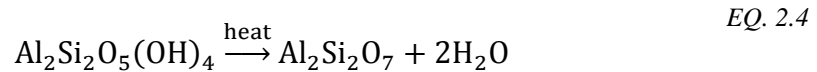
In 2003 Kriven explored sodium GP with composition 1.00-1.00-3.33-11.00 and potassium GP with composition 1.00-0.83-3.34-11.00 adopting different curing routes [79]. Fully

reacted GP were obtained by autoclave curing at 85°C and 20MPa for 24h. The GPs were made of nanoparticulates and nanopores of approximately 10nm size which were stable up to 1000°C [79]. The bending strength of the potassium GP was improved 5-fold by using basalt fibers reinforcement, to 10.3 MPa; the work of fracture also increased dramatically (to 21.8 J/m²) due to fibers pullout from the GP matrix. A successive research proved that potassium geopolymer mold can endure multiple pouring cycles of molten diferrous silicide Fe₂Si at 1450°C [80].

About the same time period the Melbourne research group started its research as well, focusing on the geopolymerization potential of different minerals, fly ashes and metakaolin [39], [81], [82]. Many fundamental studies were done by this team and they will be presented in the following Sections.

2.2.2. The solid precursors to GP: metakaolin

Metakaolin, also called metakaolinite, is an amorphous reactive aluminosilicate obtained by calcination (heat treatment at 600 to 750°C [83]) of kaolin, also called kaolinite. The de-hydroxylation reaction has the following form:



The reaction kinetics depends both on the kiln technology and the operating temperature. The de-hydroxylation of kaolin has been studied with TGA-DTA and the reaction has a maximum rate at 530°C; however XRD analysis suggests that kaolinite fully reacts when temperature is higher than 650°C. Specific surface area reaches a maximum at 750°C, thereafter sintering of metakaolin particles occurs and thus their reactivity decreases [83]. If the calcination temperature is higher than 980°C, the metakaolin decomposes into alumina-silica spinel Al₄Si₃O₁₂, mullite Al₆Si₂O₁₃ and silica [84]. Thus the optimum calcination temperature for good metakaolin reactivity is 750°C ± 100°C; the use of lower or higher temperature leads to lower-reactivity materials and to poorer quality geopolymers.

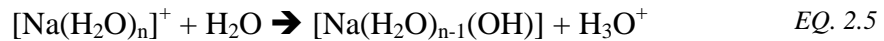
The different reactivity of metakaolin can be explained based on the coordination of the aluminum atoms. During dehydroxylation the octahedral aluminum can assume two different configurations, it can be either tetra-coordinated or penta-coordinated, depending on the dehydroxylation mechanism. The existence of a minor percentage of tricoordinated aluminum atoms was also observed [85][86]. X-ray and neutron pair distribution function data and density functional modelling have also shown how the buckled alumina layer induce a distortion in the silica layer [85] [86] . The hydrolysis of metakaolin with aluminum atom in V-fold coordination is faster than metakaolin with tetracoordinated aluminium [38].

Most of mineral deposits of kaolinite contain at least a 5% of impurities, mostly quartz SiO_2 , halloysite $\text{Al}_2\text{Si}_2\text{O}_5(\text{OH})_4$ and anatase TiO_2 . Synthetic metakaolin can be prepared in order to minimize the effect of impurities during the process of geopolymerization. This can be obtained through sol-gel route using TEOS and aluminum nitrate [87] or aluminum isopropoxide [88], [89], and by steric entrapment method [90], [91]. Further advantages of these approaches allow to have MK with different stoichiometry and a morphology that requires less water for casting. Nonetheless synthetic MK contained themselves by-products, so most studies on MK-based GP include impurities; their effects are unknown but considered negligible since they should not dissolve in alkaline solutions.

2.2.3. The alkaline solutions

The alkaline solutions used in geopolymer synthesis can roughly be divided into two classes: alkali metal hydroxides or soluble silicate solutions. They can also be further divided based on the alkali metal type, i.e. typically sodium and potassium.

Alkali metals exist in solution as cation and form hydrated species called aquacations which have a typical pK_a of 11 to 14.5 [92]. For example, Na^+ has a $\text{pK}_a=14.2$ after the following hydration reaction:



Different ions have different hydration enthalpies and pK_a . Potassium has a higher pK_a than sodium; thus potassium hydroxide is more basic than sodium hydroxide and it can better dissolve geopolymer precursors such as MK, Table 2.3. The enthalpy of hydration depends on the bond strength between the cation and the water's oxygen. Potassium has a lower hydration enthalpy than sodium, it can lose water more easily and as a result its negative charge is less screened. Because of this it is easier for potassium than for sodium to form ion pairs with anions: this can decrease the condensation rate between aluminosilicates (Section 2.2.4.4 for more details). The lower hydration enthalpy is also the reason why potassium silicates are less viscous than sodium silicates [38]: less water is needed to solvate the cations and there is more free-water between the silicate species.

The pK_a for $\text{Ca}(\text{OH})_2$ is 12.8 and above $\text{pH} \approx 11$ condensation occurs due to the presence of the species $[\text{Ca}(\text{H}_2\text{O})_5\text{OH}]^+$. For this reason, the presence of calcium in GP precursors, such as in slag, lowers the pH of the activating solution and its reactivity. On the other end, the precipitation of lime and relatively depolymerized C-S-H lowers the setting time of GP and increases the early strength.

Table 2.3 Physical and thermodynamic values for cations of interest in GP [11]. pK_a values are quoted from Baes [93].

ion	radius [Å]	Z/r [$\text{C}\text{\AA}^{-1}$]	ΔH° hydration [kJmol^{-1}]	pK_a
K^+	1.33	0.75	-322	14.5
Na^+	0.97	1.03	-406	14.2
Li^+	0.68	1.47	-519	13.6
Ca^{++}	0.99	2.02	-1577	12.8
Mg^{++}	0.66	3.03	-1921	11.4

In solution sodium is solvated by water molecules and its hydration number varies between 4 and 8; the radius of cations in solution varies with their coordination numbers [94]. The hydroxyl ion instead is solvated by approximately 5 molecules of water and it is hyper-coordinated: the hydroxyl's oxygen accepts 4 hydrogens from 4 different water molecules

and the hydroxyl's hydrogen bonds with the oxygen of another water molecule [95]. Thus for every NaOH moles, approximately 11 H₂O molecules are needed in order to form complete first hydration shells; the NaOH concentration of such solution is approximately 4.7M, which is way too low compared with sodium hydroxide solution used in metakaolin-based geopolymers (i.e. 8 to 12 M). This solution would produce a geopolymer with formula 1.0-1.0-2.0-22.0, solution/solid=2.1 and H₂O/solid=1.5 (see Chapter 5 for more information). In such GP slurry the low alkalinity may not dissolve the MK and the high water content would make the material extremely porous, weak and prone to shrinkage and cracking.

This means that alkaline solutions for geopolymer are usually concentrated and ions are in poorly solvated conditions; they likely form different ion-pairs based on the concentration: solvent-separated ion pairs 2SIP, solvent shared ion pairs SIP, contact ion pairs CIP [96]. In highly alkaline solution the sodium and hydroxide can form SIP and CIP and the hydrogen bonded structure of water is completely destroyed. Solutions of 7.5 M NaOH are expected to be composed of distorted dimeric octahedral complex anions $[(OH)_2(H_2O)_{10}]^{2-}$ [96]. The activating solutions are more similar to ionic liquids (e.g. molten hydrated salts) than conventional solutions. This creates challenges both in modelling, e.g. determining activity coefficients, and experimentally. Ion pairing in this highly concentrate solution are expected [29] and it complicates the detailed deconvolution of aluminosilicate FTIR spectra [97] thus precluding the study of the evolution of different oligomers and structures during the geopolymerization reactions. Concentrated sodium hydroxide solutions are also used in the Bayer process for the refining of alumina in information can be found in this field. For example it has been suggested that strong ion pairing between Na⁺ and aluminates is the reason for the lack of aluminate dimers or polymeric structure.

Thermodynamic values of solution are not based on the concentration of species, but on their activities a . The activity coefficient γ needed to calculate a can be obtained from the Debye-Hückel equation for ionic strength values $\mu < 10^{-1}$. This equation cannot be used in geopolymer due to the high ionic strength of activating solutions, i.e. 7.5M sodium hydroxide solutions have $\mu=7.5$. The activity of concentrated solution can be described using Specific Ion Interaction theory SIT or the Pitzer model which use a linear combination of parameters to express the interaction ion-solvents and ion-ion and can calculate mixed-ion

activity coefficient [98]. This approach has been used by Provis to model ion exchange in multicomponent solutions and in concentrated soluble silicate solutions [99]. The silicate speciation thus obtained was used in a kinetic model of geopolymerization [100] that will be summarized in Section 2.2.4.5.

Soluble silicates, also called waterglasses (WG), are mixtures of silica, alkali metal oxides and water [101] and their general formula is $x\text{SiO}_2 \cdot M_2\text{O} \cdot z\text{H}_2\text{O}$, where x is called molar mass M_s , z the number of water molecules and M is an alkali metal such as sodium or potassium. They are usually classified based on the ratios of silica SiO_2 to soda Na_2O in the system: the weight ratio $WR = \text{wt}\%_{\text{SiO}_2} / \text{wt}\%_{\text{Na}_2\text{O}}$ and the molar ratio $M_s = WR \cdot M_{\text{Na}_2\text{O}} / M_{\text{SiO}_2}$, where M is the molar mass. For sodium silicates the ratios are similar since the molecular masses of SiO_2 and Na_2O are respectively 60 and 62 g/mol. Although the silica and metal oxide can be combined in all proportions, the commercially available silicates are usually restricted to some specific ratios due to manufacturing reasons [19,90]. For example commercial sodium silicates have usually the following molar ratios: sodium orthosilicate $M_s=0.5$, sodium metasilicate $M_s=1$, sodium disilicate $M_s=2$, sodium polysilicate $M_s=3.3$.

These ratios are particularly important because they regulate the speciation of silicates in solution, Figure 2.6. The notation for the different silica tetrahedral is Q^x , where x represents the number of oxygens that a silicon atom shares with other silicon atoms, e.g. quartz SiO_2 is made of Q^4 . A more comprehensive notation that is valid also for aluminosilicates in a solution is $Q^x(m\text{Al})$, where x is the number of oxygen atoms that the silica shares with other tetrahedra, while m represents the number of aluminum atoms that occupy those tetrahedra (for this reason $m \leq x$). This notation was introduced by Engelhardt in 1982 [102].

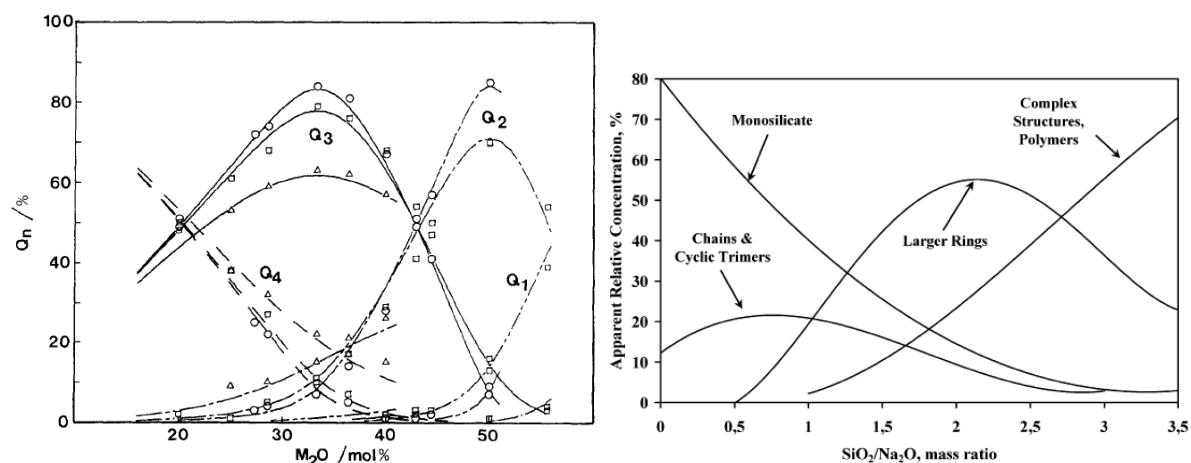


Figure 2.6 On the left: ^{29}Si MAS NMR experimental distribution of the different species of silicates in a water-based solution as a function of the alkali oxide content in lithium (Δ), sodium (\square) and potassium (\circ) silicates [103]. On the right: a qualitative interpretation of sodium silicate speciation in solution [104].

When solid metal silicates contact water, the ionic bonds between alkali and oxygen break, siloxo groups Si-OH form and pH of the solution increases. The silicates then swell and cleavage in alkaline solution of the siloxo bonds Si-O-Si occurs until equilibrium is reached [38]. The solubility of the different soluble silicates depends both on the Ms, water temperature and on the initial degree of hydration of the silicate [101]. Many studies have been done on the speciation of soluble silicates solution and glasses [99], [103], [105]–[108] using different techniques. Some of these works are in disagreement, in particular ^{29}Si NMR gives different results than spectroscopy analyses: in particular according to Raman [107] waterglass with $\text{SiO}_2/\text{Na}_2\text{O}$ between 1 and 3.22 are made of Q^1 and Q^2 , but no Q^3 was measured. In the solid state anhydrous sodium metasilicate contained exclusively Q^1 , while the solid sodium metasilicate nonahydrate has only Q^0 [109]. Indeed silicates with similar Ms are more dissociated when they are in diluted form, as also observed with Raman spectroscopy [107].

2.2.4. Geopolymerization reactions

The modelling of geopolymeric reactions that produce a strong solid monolith from the initial slurry is a complicated, relatively unexplored but extremely important aspect of GP processing science and technology. In fact modelling can help in interpreting experimental data and provide additional information, such as the nature of intermediate transient species,

that cannot be obtained due to experimental limitations. In order to effectively model the GP reactions it is necessary to properly describe the starting materials, which are the inorganic precursors and the alkaline solutions. Their accurate modelling is a complex task itself since the solid precursors are amorphous and often inhomogeneous and the concentrated activating solutions contain poorly solvated species, difficult to model from a thermodynamic point of view, Section 2.2.3. Compared with fly ash and slag, MK is by far the least complex inorganic precursor due to relatively homogeneous distribution of silica and alumina in MK.

2.2.4.1. Conceptual models for geopolymerization reactions

The understanding and modelling of geopolymerization reactions is based both on vast literature data on aluminosilicate research in similar fields, i.e. sol-gel science, zeolite science, mineral weathering and cement science, and on few studies delving directly into geopolymers themselves. It is therefore quite tempting to borrow the GP reaction model concepts from other fields, but only direct experimental evidences can confirm their validity for geopolymers.

The first attempt to model the alkali activation of slag was done by Glukhovsky [28] who divided the process into three steps: destruction, condensation and crystallization. The “destruction reactions”, as defined by the author, represent the dissolution of the inorganic precursors. At molecular level this consist in the hydrolysis of Si-O-Al and Si-O-Si bonds in the alkaline solutions which produce Si-O⁻, Si-OH, Al-O⁻ and Al-OH groups. Condensation reactions between these groups create new bonds and finally an inorganic amorphous polymer is obtained. During the first step water is consumed, while in the second it is regenerated.

This conceptual model was then expanded by Provis by adding details about other phenomena occurring during the geopolymerization reactions. He included the work of Swaddle [98,99] on the speciation of aluminosilicate and added a step of equilibration reaction between the silicate, aluminate and aluminosilicate species generated by the dissolution of metakaolin. After gelation caused by the condensation of aluminosilicate oligomer, the gel undergoes reorganization reactions in which the tetrahedrals connectivity, and thus also geopolymer strength, increase over time.

When talking about gel reorganization, some authors refer to the structural rearrangement in zeolite precursors that precedes the formation of crystalline nuclei [112], while others refers to a transition from an initial Al-rich gel to a Si-rich gel [113], [114]. The latter-stage gel transformation is due to the slower condensation reaction between silicate species compared with condensation between silicate and aluminate species. Since the overall geopolymerization reaction is a complex series of interconnected and simultaneous reactions, it is hard to label every single step and isolate it from the others; however these conceptual models are useful to approximately identify and compare different stages of geopolymer structural and microstructural evolution.

Davidovits proposed a reaction mechanism for the dissolution of metakaolin based on a covalent concept [38]. He rejected the idea of monomeric release of $\text{Si}(\text{OH})_4$ and $\text{Al}(\text{OH})_4^-$ in solutions and suggested the release of orthosialate molecule $\text{Si}(\text{OH})_3\text{OAl}(\text{OH})_3$. This claim was supported by the existence of this species in the solution [115], Figure 2.7, and by the congruent dissolution of kaolinite in KOH solutions [116]. The dissolution is a linear function of log of time and can be explained in terms of chemical affinity [116]. This argument assumes that dissolution mechanisms of octahedral Al (kaolin) and tetrahedral Al (metakaolin) are similar.

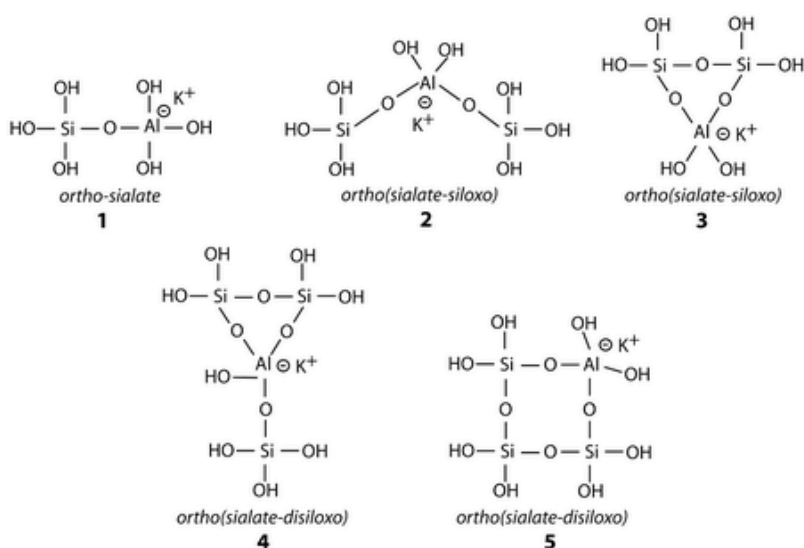


Figure 2.7 Representation of the five ortho-sialate species isolated in KOH solution by North [115]; these molecules are the precursors of both zeolites and geopolymers [38].

Thus the alkalization of metakaolin leads to the release of the soluble ortho-sialate molecules $(OH)_3 - Si - O - Al - (OH)_3$. The first step is the addition of a hydroxyl group to the aluminum, which become tetravalent. The attachment of another hydroxyl to the silicon induces it into a highly reactive penta-covalent state which leads to the cleavage of the siloxane oxygen and the formation of a silanol group $-Si-OH$ and a siloxane group $-Si-O^-$, with a balancing alkali metal. The final ortho-sialate is obtained through the full cleavage of the siloxane oxygens, molecule 1 in Figure 2.7 [38]. The idea of a penta-covalent silicon is widely used in sol-gel chemistry to describe the basic-catalyzed hydrolysis of silicon alkoxides [117] although it has not been confirmed in the case of geopolymers,

Figure 2.8.

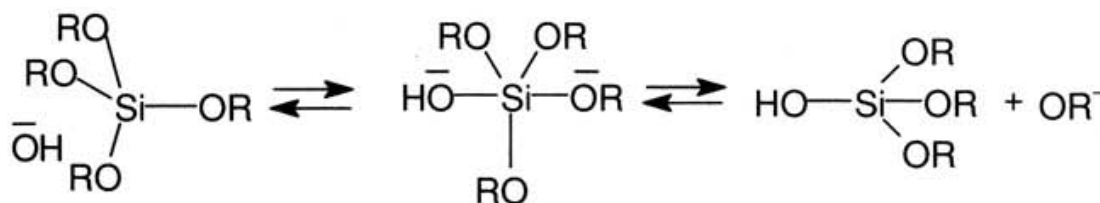


Figure 2.8 Mechanism of hydrolysis of silicon alkoxides in basic environment (from [117]).

The fate of the ortho-sialate molecule depends on the presence of additional soluble silicates among the reactants. If there is no additional soluble silicates, three ortho-sialate molecules condense forming a tri-cyclo-diasialate; further polycondensations can lead to a nepheline framework [38]. If the ortho-sialate reacts with monomeric orthosiloxonate in solution, the linear ortho-sialate-siloxo molecule is formed (molecule 2 in Figure 2.7); further polycondensations can lead to phillipsite framework [38]. If the ortho-sialate reacts with a di-siloxonate in solution, two ortho-sialate-disiloxo cyclic structures are obtained (molecules 4 and 5 in Figure 2.7); further polycondensations can lead to albite framework [38]. This conceptual reaction model is highly simplified as these phases are not the only structures found in GPs, which are often highly disordered materials, i.e. amorphous.

The fact that also in unreacted metakaolin the VI-Al and V-Al fully transform into IV-Al supports the idea that the first step of dissolution is the formation of tetravalent aluminum

[71]. The first intense exothermic peak measured during isothermal calorimetry [74], [118]–[120] can perhaps be assigned to this step instead of the whole MK dissolution.

2.2.4.2. Dissolution and precipitation reactions in cementitious systems

The dissolution and precipitation reactions that occur during geopolymerization also occur in other inorganic binders. For this reason it is possible to make some thermodynamic and kinetic analogies with them, although many competing phenomena can occur which need to be experimentally proven.

2.2.4.2.1. Thermodynamic and kinetic of complex reactions

Let's define a chemical reaction with a fixed stoichiometry and without volume change:



The reaction is spontaneous only if the Gibbs free energy of reaction $\Delta G_{\text{REACTION}}$ is negative and the chemical affinity A is positive:

$$\Delta G_{\text{REACTION}} = -A = RT \ln \left(\frac{Q}{K_{\text{EQUIL.}}} \right) < 0 \quad \text{EQ. 2.7}$$

Chemical affinity A is positive when $Q < K_{\text{EQUIL.}}$, where $K_{\text{EQUIL.}}$ is the equilibrium solubility product and Q is the reaction activity coefficient, which is a function of species activities a_i and stoichiometry coefficients v_i .

$$Q = \prod_i^n a_i^{v_i} = \frac{a_Z^{12}}{a_A^6 a_B^{12} a_C^{21}} \quad \text{EQ. 2.8}$$

On the other hand, the rate of reaction is not defined by the activities but by the actual species concentrations [121]:

$$r = \frac{1}{v_i} \frac{d[n_i]}{dt} = -\frac{1}{6} \frac{d[A]}{dt} = -\frac{1}{12} \frac{d[B]}{dt} = -\frac{1}{21} \frac{d[C]}{dt} = \frac{1}{12} \frac{d[Z]}{dt} \quad \text{EQ. 2.9}$$

The rate equation or rate law can be defined as

$$r = k[A]^\alpha[B]^\beta[C]^\gamma[Z]^\delta$$

where k is the kinetic constant, and α , β , γ and δ are the partial order of reaction which sum gives the overall order of reaction, also called molecularity [121]. The partial order of reactions differ from the stoichiometry coefficients and they are usually determined phenomenologically using the isolation method, that is by measuring how the reaction rates vary by changing the concentration of one reagent at the time.

The kinetic constant k can be expressed in term of the Arrhenius equation which shows its dependence with temperature [122]:

$$k = Ae^{(-E_{att}/RT)}$$

where A is a pre-exponential factor, E_{att} is the activation energy of the reaction and R and T are the gas constant and temperature. The rate equation is a function of concentrations and not of activities because the reaction depends on the molecular collision of reagents.

Describing the geopolymerization reaction stages that lead to a hardening of GP is complex task. The overall reaction is a series of sequential reaction where intermediate species are produced and consumed.

During geopolymerization there may also be parallel reactions, where the same reagent can react to form different products, e.g. condensation of a silicate monomer with another silicate monomer or with an aluminate monomer. For sequential reactions the overall rate is controlled by the rate limiting step, and this is controlled by the free energy difference between the reagents and the transition state complex, the highest energy barrier to overcome [121]. Transition state complexes and reaction intermediates are two different entities and only the latter can be experimentally measured. This energy barrier is the activation energy of reaction and can be determined by measuring the reaction rate at different temperature. Nonetheless changing the temperature may change rate limiting step, or can change the transition state complex and the reaction mechanism. $E_{act} \approx 5\text{kcal/mol}$ is typical of reactions limited by diffusive transfer, while $E_{act} \approx 20\text{kcal/mol}$ by reactions limited by bond-breaking. For example at low temperature the rate limiting step for mineral dissolution is usually an

interfacial reaction, while at high temperature the mechanism change and diffusion become the limiting factor: thus one expect to see a change in slope in the Arrhenius plot [121].

Complex reaction rate can usually be expressed as a function of the elementary reaction rate (the rate limiting one), activity coefficients and equilibrium constants. Activity correction factors are required because the rate is a function of concentration but the equilibrium constants are a function of activity coefficients [122]. Even if the mechanism is assumed, it is not easy to determine all those parameters.

2.2.4.2.2. Heterogeneous reactions

Since geopolymer slurry is a multiphase system, geopolymerization is a heterogeneous reaction. Thus the rate equation should include the active surface area of the solid component, and any kinetic model should take into account variation of these surfaces due to dissolution or precipitation reactions. Another heterogeneous reaction is the hydration of Portland Cement which involves at least two solid phases and a liquid phase: the anhydrous phases dissolve in water and then hydrates species precipitate from solution. Both reactions are interfacial reactions and their rates can be expressed as the product of interfacial reaction rate $r_{interface}$ and interfacial area S between solid and liquid. Since the pore solution chemistry varies with time, also the driving forces ΔG and the interfacial rates $r_{interface}$ vary with time. The reaction rate for precipitation and dissolution can be written as [18]:

$$R(t) = r_{interface}(\Delta G(t), [ions], ...) * S(t) \quad EQ. 2.12$$

$$\Delta G(t) = RT \ln(\beta(t)) \quad EQ. 2.13$$

where $\beta(t)=Q(t)/K_{EQ}$ is the ratio between the reaction activity quotient and the equilibrium solubility product. If $\beta>1$ precipitation occurs, if $\beta<1$ dissolution occurs. The dissolution and precipitation reactions are coupled, meaning that the former provide the reactants for the second, and the second provide the driving force for the first to continue. The reason is that the pore solution is over-saturated respect to the final hydration product, which nucleates and grows, but under-saturated respect to the anhydrous reagents, which dissolves. After an

initial induction period in which the hydrates have not formed yet, the hydration rate equals the dissolution and precipitation reaction $R_{HYDRAT.} = R_{DISSOL.} = R_{PRECIP.}$, thus [18]:

$$r_{precip.} * S(t)_{hydrates} = r_{dissol.} * S(t)_{anydr.} \quad EQ. 2.14$$

In the early stages S_{anydr} and r_{precip} are large and the solution is closer to equilibrium with the anhydrous phases. In the later stages $S_{hydrates}$ and r_{dissol} become dominant and the solution is closer to equilibrium with the hydrated species. According with this model the maximum hydration rate is observed approximately when the surface area of the dissolving and precipitating phases are similar [18].

At the time of mixing EQ. 2.14 does not hold because the surface of hydrates is null. The initial decrease in hydration rate is explained in term of classical nucleation theory which defines the nucleation frequency J ($m^{-3}s^{-1}$) and the induction time for homogeneous nucleation t_{ind} (s) as follows:

$$J = K_0 \exp \left(- \frac{f \Omega^2 \gamma^3}{(k_B T)^3 \ln^2 \beta} \right) \quad EQ. 2.15$$

$$\ln(t)_{ind} = \frac{f \Omega^2 \gamma^3}{(k_B T)^3 \ln^2 \beta} - \ln K_0 \quad EQ. 2.16$$

where K_0 ($m^{-3}s^{-1}$) is a kinetics constant, f is a form factor, Ω (m^3) is the molecular volume, γ (Jm^{-2}) is crystal-solution interfacial energy, β is the ratio between the ionic activity product and equilibrium solubility product, k_B (JK^{-1}) is Boltzmann constant and T (K) is temperature. Before nucleation occurs, the dissolution of anhydrous particles slow down since the solution is almost at equilibrium with the dissolves species ($\beta = Q/K_{EQ} \approx 1$) and the driving force $\Delta G_{DISS} \approx 0$.

In the latest stages of OPC hydration the reaction slows down because the hydrates phases coalesce and their surface areas diminish. Moreover, most reagents particles are covered by products and the limiting rate mechanism becomes the diffusion of species through this shell. Similarly, the formation of a metastable shell on the surface of reagents has also been invoked to explain the induction period. This metastable phase has an intermediate solubility between the initial reagents and the final products, thus it reduces the dissolution and

precipitation reaction driving forces [123]. The reduction in reaction rate due to a low-solubility coating was also observed in the case of magnesium phosphate ceramic in which boron has been added as a retardant additive [19]. Another alternative explanation of the induction period rely on the idea that a semipermeable membrane forms on the surface of the reagents which will later on burst due to the osmotic pressure between the inner and outer solution [17].

All the aforementioned thermodynamic and kinetics considerations are also applicable to the geopolymerization reactions. They were used throughout this dissertation to explain and interpret experimental data on the surface properties of metakaolin, the geopolymerization activation energy, the effect of seeding and on the determination of the GP rate limiting step.

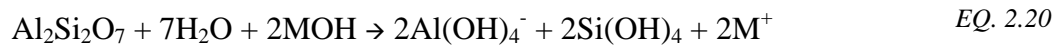
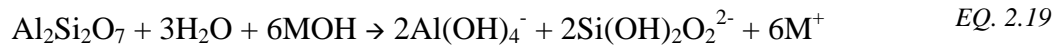
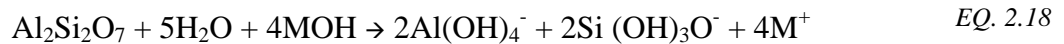
2.2.4.3. Metakaolin dissolution

An accurate model of condensation reactions, polymerization and hardening of geopolymer requires as input characteristics the species in solution generated over time by the metakaolin dissolution. Additionally, it is important to know if the dissolution is incongruent since a solution that change composition over time will generate different type of gels.

Kaolinite dissolution in basic solution can be schematically written [82] as:



Similarly, the dissolution of metakaolin can be written as:



These equations represent some of the possible geopolymerization reaction stoichiometries. They reflect different possible dissolution mechanisms, depending on the pH, on the

deprotonation and polymerization degree of the detached species. In particular the last 2 equations represent the reactions suggested by Davidovits [38] already described in Section 2.2.4.1. Extra H_2O and NaOH could be involved in intermediate species and be consumed and regenerated during the dissolution process, thus acting as catalyst.

The dissolution of aluminosilicates is a vast topic itself. Several challenges complicate the determination of the mechanism and the rate of MK dissolution: the structure of metakaolin is quite complex and it has only recently being modeled [124]; metakaolin is amorphous thus it is not possible to determine its dissolution by using QXRD as it is done for Portland cement and its phases [125]; the dissolved species tend to precipitate so the analysis of species in solution can be misleading and the first exothermic peak detected in calorimetry cannot be unequivocally assigned to hydrolysis reactions.

Most studies on the dissolution of aluminosilicate have focused on acidic conditions due to their higher solubility at low pH. In this case preferential dissolution of aluminum in acidic pH is generally accepted, although it may depend based on the dissolving aluminosilicate and the experimental conditions such as pH, temperature, ions in solutions, etc. [126], [127].

The dissolution itself is a multistep process and its kinetic depends on the rate-limiting step that can be: 1) diffusion of species to the surface to initiate the dissolution; 2) diffusion of species away from the dissolving surfaces; 3) surface-control formation of an activated complex (or transition state complex); 4) diffusion through a low solubility phase that covers the dissolving phase; 5) nucleation and growth of a low solubility precipitate that increases the dissolution driving force. For MK dissolution, mechanism 3 and 5 are likely to be the rate limiting step and mechanism 4 is also possible for concentrated slurries [121], [128]. MK in diluted and concentrated solution may have different kinetics of dissolution due to different rate limiting step, so it can be dangerous to extrapolate kinetics data.

If the limiting step of dissolution is the interfacial reaction the rate needs to be normalized by the mineral surface area. Nevertheless the rate normalized by area can also decrease over time with a parabolic kinetics $r=kt^{0.5}$ because of an initial faster dissolution of highly energetic surfaces [121]. This behaviour was also observed in the dissolution of Alite in Portland Cement [18]. In certain cases the dissolution rate decrease with the logarithm of

time [116] and this can be explained in term of chemical affinity and transition state theory: the higher the concentration of dissolved species the lower the driving force for dissolution. The transition state theory is usually valid for elementary reaction, but it can be applied for complex reaction if an elementary reaction is the rate-limiting mechanism, in this case the formation of the activated complex. This theory assumes equilibrium between the reagents and the activated complex or transition state complex and the rate equation can be written as [121] :

$$r_{net} = -k_+ \prod a_j^{m_j} \left(1 - e^{\left(\frac{n_1 \Delta G}{RT} \right)} \right) \quad EQ. 2.23$$

where k_+ is the reaction rate for the dissolution reaction, a_j represents the activities of the species involved in the formation of the activated complex, m_j and n_l are constants and ΔG can be expressed as in EQ. 2.7. In Figure 2.9 the normalized rate is shown to be constant when system is far from equilibrium and roughly proportional to ΔG near equilibrium. The transition state theory can also explain the faster dissolution of aluminosilicate at increasing temperatures [129].

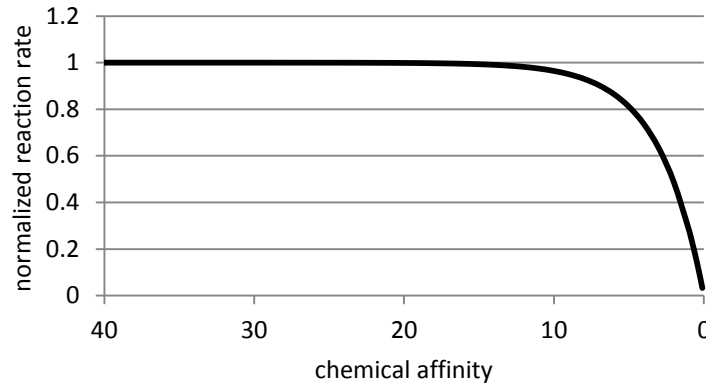


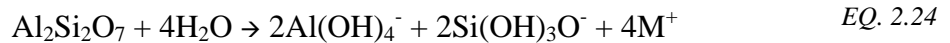
Figure 2.9 Normalized reaction rate as a function of chemical affinity according to the transition state theory.

Since the reaction rate is observed to decrease by increasing aluminum in solution but stay constant when silica concentration is varied, the activated complex for many aluminosilicate minerals relies on the aluminum species. The presence of aluminum in solution has an effect on the chemical affinity but can also act as an inhibitor by adsorption on the mineral surfaces [121].

As previously mentioned, Davidovits covalent concept [38] supported EQ. 2.21 and it is based on the works of Bauer [116], [130] that indicate congruent dissolution of kaolinite in alkaline solution. Nonetheless in the same paper Bauer wrote: *“At the high pH of the solutions in our experiments, it is likely that the initial dissolution of kaolinite is dominated by the detachment of Al. [...] A preferential Al release cannot be observed in our experiments given the great amount of dissolved material”* [116]. Moreover the solutions were only analyzed after 2 days of dissolutions at 35°C or after 12 hours at 80°C. The dissolution rate increased with the KOH concentration, and different activation energies were found for different KOH concentrations, suggesting the existence of different dissolution mechanisms. Congruent dissolution for kaolinite at pH>11 was also found by Xie [126].

Sagoe-Crentsil [118] found for dissolving metakaolin that there is more alumina than silica in solution when the concentration of NaOH is below 6M, and vice versa when the concentration is above 8M. According with Granizo [131] there is an initial release of alumina from MK, followed by congruent dissolution of Si and Al; if the alkali concentration and temperature are high enough there is also a third stage of preferential Si dissolution at longer times.

The dissolution of MK in alkaline solution is highly exothermic $\Delta H_r = -134.3$ kJ/mol according with calculation base on the heat of formation of metakaolin, Si(OH)₄ and Al(OH)₄ [132].



Other studies have supported the idea that the dissolution-hydrolysis reactions of MK are endothermic [133] and generally the dissolution of oxides in acidic or alkaline solutions absorbs heat [19]. The initial high exothermic peak observed in calorimetry [119], [120] may be associated with the alkalination of the MK and the formation of Al^{IV} on the surface, while the formation of alumina and silica monomers is probably endothermic [19]. This idea is supported by the tetrahedral coordination of aluminum atoms even for samples that did not fully react and are still part of the MK particles [71]. An endothermic dissolution reaction could indeed explain why geopolymerization reactions are favored at elevated temperatures. Other investigations suggested that there is a residual of Al^{VI}, especially when silicates are

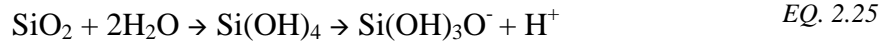
already present in the activating solutions [134]. Also, SEM images on geopolymers obtained with alkaline silicate solutions revealed unreacted MK [57].

Although the hypothesis that initial preferential release of aluminum from MK seems to be increasingly accepted, the descriptions of alkaline solution and MK dissolution mechanism and kinetics is still incomplete and much work is still needed on this topic, both from an experimental and modelling point of view.

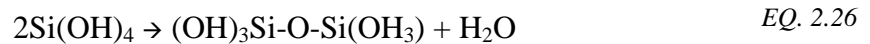
The determination of the unreacted MK in GP is challenging since both materials are mostly amorphous and intermixed at the micron scale. Williams introduced four methods to calculate the residual amount of MK based on XRD and SEM analyses which showed good agreement. For sodium silicate based GP cured at 70°C he found the percentage of unreacted MK varied between 25% to 90%, depending on the GP composition [135].

2.2.4.4. Aluminosilicates condensation in solutions

As silicon is a semimetal, it does not exist in aqueous solution as cation but as oxide or hydroxide and it can form oxoanion. Silicon acts as a weak Lewis acid and increases the polarity of the O-H bond which becomes easier to break [136]:



Depending on the conditions, hydroxide and oxoanions tend to form hydroxo bridges which can results in condensation reactions and the formation of oxo-bridges:



Aluminum oxide is amphoteric and can act as an oxocation in acidic solution or as oxoanion in basic solution. Since we are focusing on geopolymers synthetized with alkaline solutions we will consider the aluminum as a weak Lewis acid [136]:



The silanol bond Si-OH and aluminol bond Al-OH can be deprotonated to form different aqueous monomeric species: $[\text{AlO}_n(\text{OH})_{4-n}]^{(1+n)-}$ and $[\text{SiO}_n(\text{OH})_{4-n}]^{n-}$. In the case of aluminum the deprotonation occurs only in extremely alkaline solution, i.e. pH>14. These deprotonated

anions can form ion pairs with cations: contact ion pairs, solvent shared ion pairs or solvent separated ions pairs. Ions pairs can inhibit condensation between oxoanions and thus retard the coagulation reaction in geopolymer. Since larger ions form stronger ion pairs [137], geopolymers based on sodium have usually faster condensation rates compared with potassium geopolymers. Thus, non-bridging oxygens can be in three states: protonated, deprotonated, deprotonated and ion-paired with a cation. Similarly, silanol and aluminol in aluminosilicate oligomers can also be deprotonated and form ion-pairs.

Let us consider a condensation reaction between two non-bridging oxygens:

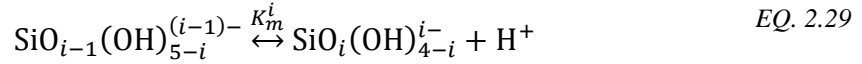


where T_1 and T_2 can be either Al or Si and X and Y can be either a hydrogen H, a metal cation M or a negative charge. Without making any assumptions the author of this dissertation consider the condensation reaction rates to depend on:

- type of network former: silica or alumina;
- degree of condensation of the network former: Q^0 , Q^1 , Q^2 , Q^3 ; for example, Q^2 means that two oxygens are shared with other tetrahedra to form linear chains $(-O-T(OH)_2-)_n$;
- type of the bonded network formers, for example for Q^3 there are 4 possibilities: $Q^3(0Al)$, $Q^3(1Al)$, $Q^3(2Al)$, $Q^3(3Al)$; e.g. $Q^3(2Al)$, means that three-out-of-four oxygen are shared with other tetrahedra, two of which are aluminum tetrahedra;
- status of the non-bridging oxygen: protonated, deprotonated, or deprotonated and forming ion pairs;
- status of the other non-bridging oxygens bonded to the same network former.

Without considering the molecular weight of the oligomers (for species Q^2 and Q^3), the cyclization in species Q^2 , the ionic strength of the solvent, the different type of ion pairings and excluding Al-O-Al bonds to obey the Loewenstein's rule we obtain 2628 types of non-bridging oxygens. Since we expect the condensation rate to depend on both oxygens, we should expect $2628^2 \approx 7 \cdot 10^6$ reactions rate.

This simple mathematical exercise can explain why it can be quite complex to model the condensation reaction in geopolymers, fortunately many of those 2628 oxygen species do not exist. First of all, in alkaline solution with $\text{pH} > 11$ the aluminate monomer is never deprotonated, so the only possible species is $\text{Al}(\text{OH})_4^-$ [138]. However, less is known on the status of aluminol when it is a part of a larger oligomer. Instead, the degree of deprotonation for silica monomer depends on the solution pH:



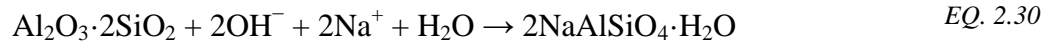
Selfcik [139] found that $\text{pK}_m^1=9.5$, $\text{pK}_m^2=12.6$, $\text{pK}_m^3=15.7$ and $\text{pK}_m^4=18.8$. Since alkaline solutions in geopolymers have a $\text{pH} \approx 11-15$ we expect most of the monomers to be mono or dideprotonated: $\text{SiO}(\text{OH})_3^-$ and $\text{SiO}_2(\text{OH})_2^{2-}$. The pK values vary based on the connectivity of the silicate species [139], and a good review of these values can be found in [140].

One of the most cited study regarding the kinetics of condensation in geopolymer involves the modelling of oligomerization and cyclization of monomeric silicate using density functional theory DFT [141]. Water was simulated as a continuum by using a COSMO (COnductor-like Screening MOdel) solvation approach to determine the interaction between solvent and oligomers. The pH effects were accounted by considering different protonation level. This work was initially intended for the nucleation and growth of zeolite species but many concepts can be adopted to explain condensation reactions in geopolymers. Dimerization was found to be energetically favorable when occurring between the $\text{SiO}(\text{OH})_3^-$ and $\text{Si}(\text{OH})_4$ ($\Delta G = -28 \text{ kJmol}^{-1}$) and $\text{SiO}_2(\text{OH})_2^{2-}$ and $\text{Si}(\text{OH})_4$ ($\Delta G = -53 \text{ kJmol}^{-1}$), but it is energetically unfavorable between two negative $\text{SiO}(\text{OH})_3^-$ monomers ($\Delta G = +13 \text{ kJmol}^{-1}$). For the former reaction the change in enthalpy overcomes the negative change in entropy as the reactions are exothermic. This work has often been used to explain the non-monotonic dependence of the geopolymerization rate with the Na/Al ratio [63,127]. If the alkalinity is too high (e.g. $\text{pH} > 13$) most monomers in solution are negatively charged [139] and their condensation rate is slow. In a following work [143] some water molecules and the counterions Na^+ were explicitly included, deprotonation energies were calculated and similar results for the condensation reactions were found.

Using a similar approach White included the aluminum species and the effect of the pH by varying the dielectric constant: $\epsilon_r=78.54$ at pH=7 and $\epsilon_r=56$ at pH=11 [144]. At high pH the most energetically favorable dimerization reactions occurs between $\text{Al}(\text{OH})_4^-$ and $\text{Si}(\text{OH})_4$ ($\Delta G=-21.2 \text{ kJmol}^{-1}$), $\text{Si}(\text{OH})_4$ and $\text{SiO}_2(\text{OH})_2^{2-}$ ($\Delta G=-12.1 \text{ kJmol}^{-1}$), $\text{Al}(\text{OH})_4^-$ and $\text{SiO}(\text{OH})_3^-$ ($\Delta G=-9.7 \text{ kJmol}^{-1}$), $\text{Si}(\text{OH})_4$ and $\text{SiO}(\text{OH})_3^-$ ($\Delta G=-9.3 \text{ kJmol}^{-1}$), $\text{Si}(\text{OH})_4$ and $\text{Si}(\text{OH})_4$ ($\Delta G=-1.8 \text{ kJmol}^{-1}$), and $\text{SiO}(\text{OH})_3^-$ and $\text{SiO}(\text{OH})_3^-$ ($\Delta G=-0.9 \text{ kJmol}^{-1}$). Varying the dielectric constant has a big impact on deprotonation and dimerization calculation, thus differences in condensation rate for different geopolymers could be due to both different species involved in the reaction and different dielectric constants. Unfortunately the dependence of the dielectric constant on the concentration of alkali aluminosilicate in solution is unknown and more work is needed in this field.

2.2.4.5. Kinetic models of geopolymerization

Few comprehensive approaches have been used to model the overall reaction kinetic in geopolymer materials and most of them focused on metakaolin [100], [114], [119], [120]. Calorimetry has been widely adopted to monitor the reaction kinetics of geopolymers and the extent of reaction can be calculated as the measured heat-release divided by the theoretical maximum heat release. This last quantity is approximated by different authors using different enthalpies of reaction calculated from different reaction stoichiometries and enthalpies of formation. For example Zhang [119], [120] studied the effect of NaOH concentration, soluble silicate, temperature from 20°C to 40°C. He adopted the enthalpy of formation of analcime $\text{NaAlSi}_2\text{O}_6 \cdot \text{H}_2\text{O}$ for the geopolymer gel, reaction stoichiometry in EQ. 2.30 and he found an enthalpy of reaction of -358.2 kJ/mol .



Although the individual reaction steps, Figure 2.10, were interpreted using a single overall enthalpy of reaction, precious semi-quantitative information could be obtained and confirmed by deconvolution of the FTIR spectra. For instance, increasing the NaOH concentration and temperature increased the reaction kinetics. Temperature had no significant effect on the total reaction extent α , (where α is the ratio of the heat release to the theoretical maximum heat release) especially when $\text{Na}/\text{Al} \geq 1$; adding soluble silicate

decreased α while increasing Na/Al increased it. Adding silicates also suppressed the third exothermic peak associated with gel transformation and crystallization.

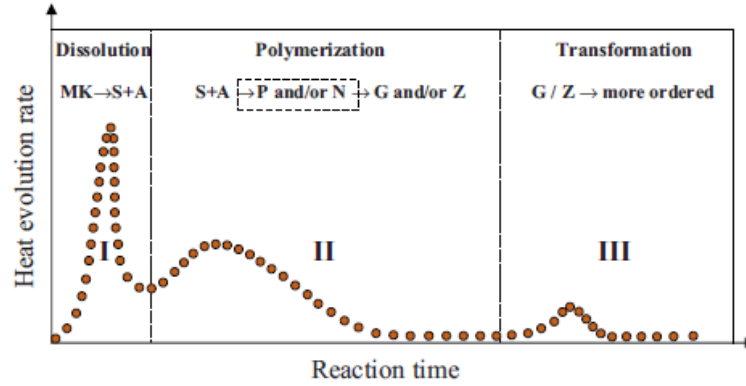


Figure 2.10 Simplified representation and interpretation of isothermal calorimetry of geopolymerization. Reaction steps are taken from [100], see Figure 2.11.

A system of differential equations [145] was developed to fit calorimetry DSC data obtained by Rahier [74]; the model was then refined [100] to describe energy-dispersive X-Ray Diffractometry EDXRD data [146]. This empirically-based reaction kinetics framework is an adaptation of Faimon [147] model of aluminosilicate weathering, Figure 2.11. Metakaolin generates silicate monomers and aluminate monomers with a rate $r_1=k_1*M$; the kinetics constant k_1 decreased when water is added to the activating solution. Aluminosilicate oligomers are formed with rate $r_2=k_2*A*S^n$ and they grow into amorphous aluminosilicate polymers: this last step represented both nucleation, $r_4=k_4*O^2$, and autocatalytic growth, $r_5=k_5*P^2*O^2$. The autocatalytic step was initially assumed by Faimon to explain non-linear oscillation of concentration of dissolving mineral. Autocatalysis can explain the increase of reaction kinetics, and so heat release in calorimetry data [74], over time. Nonetheless this is a common phenomenon in heterogeneous reaction and autocatalysis in zeolites processing is not used to describe precursor gel precipitation but the crystallization kinetics [148].

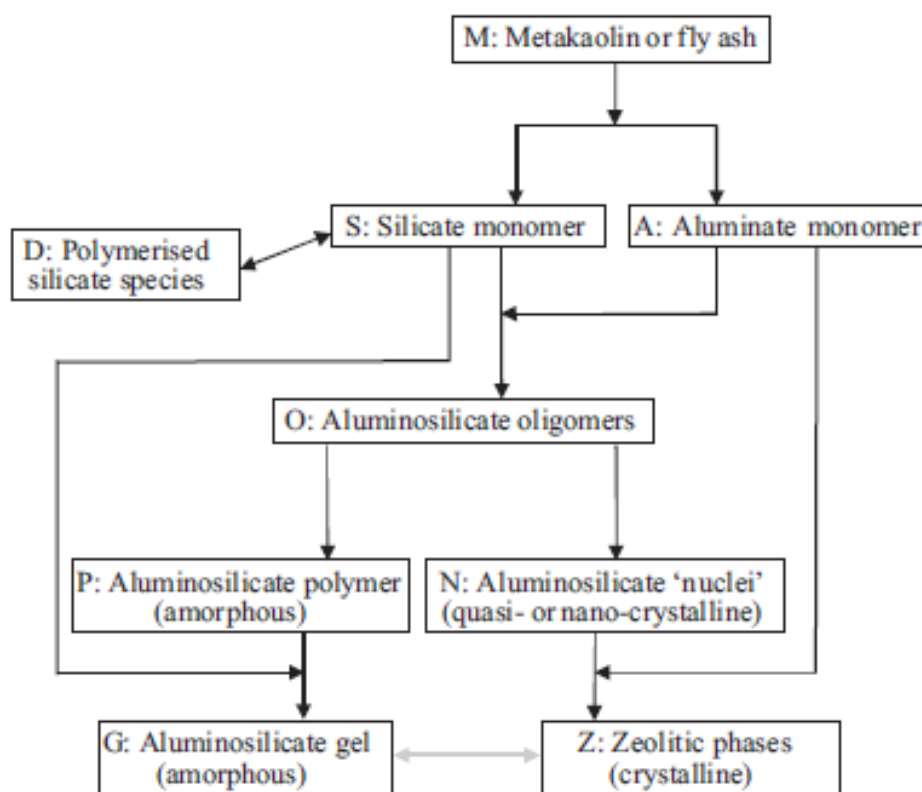


Figure 2.11 Scheme of an empirical kinetics model of geopolymerization [100].

This model was successfully implemented to determine the effects on kinetics of different solid precursors with different particle sizes, Si/Al ratio, additional water and alkaline cations type which influence the silicate speciation. The kinetics constants were not obtained from fundamental studies and they were not optimized according with a least-squares refinement [149], but rather picked arbitrarily to better match the experimental data. Further, the crystallization of geopolymer, although included in the model, had no impact on the reaction kinetics. The model did not take in account mass transport and incongruent dissolution of solid particles. All things considered, it represents a good starting point and it can be improved by focused kinetics studies on rate limiting steps and rate constants of individual reactions. Research on these individual reactions encounters intrinsic difficulty as they are all coupled and rate constants obtained in other conditions, such as in dilute systems or at high temperatures, may be associated with different reaction pathways.

A different approach was adopted by White to describe the evolution of aluminosilicate clusters which represents the growth of the aluminosilicate gel [114], [150]. Coarse grained Monte Carlo was adopted, dissolution reactions were modelled by a “swap event” and condensation reactions by a “bond” event. The dimerization energies obtained by DFT were used as condensation energies. The swap event also assured that the minimum energy configuration could be achieved. This investigation could match and explain many experimental observations, although many approximations were implemented, i.e. simplified MK structure, speciation and condensation energies calculated for constant pH=11, etc. . In particular it could better show the differences between geopolymers activated with alkali hydroxides and alkali silicate solutions. Metakaolin was completely consumed in the alkali hydroxide system but not in the waterglass solutions, in agreement with results obtained with ^{27}Al MAS NMR [134], SEM images [57] and X-ray pair distribution function analysis [151]. The geopolymer gel nucleates in the solution when activated in NaOH and on the MK surface when activated by waterglass. Finally the geopolymer gel undergoes Ostwald ripening, i.e. small clusters are consumed by the larger clusters, but only when silicates are present in solutions.

Much more work has to be done to create acceptable geopolymerization models that can help engineers to better formulate geopolymer mix designs based on the available raw materials. Some of the obstacles are the lack of systematic studies on these materials, the computational costs of creating multiscale models that can link molecular reactions to GP structure and microstructure and then properties, and the intrinsic limitations of some experimental techniques that cannot directly verify the model outputs. The work will help by providing to GP scientists involved in modelling with experimental data on GP reaction kinetics, structure and properties that are not presently available in the literature.

2.2.4.6. Additives and Seeding

Understanding the kinetics of GP reaction is not just important from a processing point of view, i.e. setting time and pumpability/castability, but also from an application and performance perspective since altering the reaction pathway can result in different final crystalline structures, phenomena already observed in geopolymers [142]. Controlling the

kinetics and the reaction products in dissolution - precipitation reactions can be challenging without fully understand the reaction mechanism and rate limiting step.

Similar problems are faced by the Portland cement industry, where there are still many open questions [18], e.g. if the rate limiting step associated with the induction period is due to a metastable barrier layer covering the cement particles or due to the saturation of the solution (slow dissolution step) [152]. However recent works worth-to-be-mentioned have improved the knowledge on the hydration kinetics of Alite, the main component of cement [125]. It has been demonstrated that the C-S-H, the main precipitation product of cement, nucleates heterogeneously on the Alite surface. The use of PCE superplasticizer which adsorb on the Alite surface change the nucleation mechanism to homogeneous and it produces a delay in the hydration kinetics of cement.

Adding synthetic C-S-H to this system provides an alternative pathway for C-S-H nucleation and growth, decrease the induction time, increase overall reaction kinetics and improve yield. More importantly it was possible to modify the silicate connectivities Q^2/Q^1 and thus to tailor the structure and properties of the C-S-H [153], [154]. Investigating the effects of seeds can bring light to the rate limiting step and improve transformation kinetics when the nucleation of the new phase is the rate limiting step [155]–[158], as opposed to precursor dissolution. Using zeolite seeds is a common practice in the zeolite synthesis, where the outcome of zeolite synthesis in term of crystalline phase can be modified by seeds-gel interaction: it promotes and direct crystallization, and reduce induction time associated with crystallization [159]–[162].

The effect of different seeds such as silica, alumina and zirconia on geopolymers has been studied using spectroscopic and diffraction techniques on fly ash based geopolymers [163]–[165] and on one-part geopolymer [166]. In general the seeds fasten the dissolution of geopolymer precursor by acting as heterogeneous nuclei inducing further nucleation and by reducing surface passivation due to gel precipitation on the precursors, Chapter 6.

2.2.5. GP technology development: composition and properties optimization

The practical development of geopolymers technology was driven mostly by civil engineers aiming to replace OPC. Thus, most of the studies performed on GP included the optimization of GP formulation and curing operation to: maximize unconfined compressive strength UCS of the consolidate material, minimize shrinkage, cracking and efflorescence, and optimizing slurry viscosities and setting times [38].

In order to obtain a strong crack-free binder, evaporation of water needs to be prevented and this is often achieved by curing in 100% relative humidity chambers or by sealing the molds [167]. The reason is that the dissolution of aluminosilicate in alkaline solution needs water to occur. Furthermore, concentrated solutions of soluble silicates can turn into viscous gel when water evaporates, thus reducing the diffusion of species in the slurry. On the other hand too much water can hinder polycondensation. Similar trend has been observed for alkali hydroxides and there is a concentration optimum: small concentration of MOH slowed down dissolution while high [MOH] reduced polycondensation kinetics [75], [142], [167]. This last observation has often been associated with the speciation of silicates in high pH and their dimerization: condensation between two negatively charged silicates $\text{SiO}(\text{OH})_3^-$ is slower compared with a condensation between $\text{SiO}(\text{OH})_3^-$ and $\text{Si}(\text{OH})_4$ [144].

Setting time of GP is usually determined according to ASTM C 191 - 08 “Time of Setting of Hydraulic Cement by Vicat Needle” and it depends on the formation of geopolymer gel, which in turn depends on the dissolution of inorganic precursor. At room temperature MK-based GPs may need up to several days to set, while it only takes few hours at mild curing condition, i.e. 40°C. For this reason the use of metakaolin as GP precursor limits its use to precast application, unless slag or other calcium sources are added. Curing conditions above room temperature can improve the reaction kinetics since the reactivity of material toward activating solution increases with the curing temperature [50], [119]. De Silva [25] found that the addition of soluble silicates can delay the setting time of MK-based geopolymers up to 5 times at 40°C, in accordance with calorimetry studies [120]. A different research on fly ash geopolymers analyzed deconvolved FTIR spectra and confirmed that the addition of

soluble silicate slow the overall reaction, unless the activating solution had a $\text{SiO}_2/\text{Na}_2\text{O} < 0.2$; if the soluble silica is added in small quantities then it accelerate the reaction kinetics [168].

Although soluble silicates decrease the reaction kinetics and crystallinity of geopolymers, they reduce the porosity of the consolidated material and thus increase their compressing strength and Young Modulus. Duxson studied the microstructure of different MK-based GPs cured at 40°C for 20 hours at different Si/Al and with constant $\text{H}_2\text{O}/\text{Na}_2\text{O}=11$ [58]. When GP had a $\text{Si}/\text{Al} < 1.4$ the microstructure was porous and composed of micron-sized clustered particulates and large pores, when $\text{Si}/\text{Al} > 1.65$ the microstructure is homogeneous made of 10nm clusters and the pore volume decreased from 0.206 to 0.082 cm^3/g . The compressive strength correlated with the homogeneity and porosity of the GPs: higher Si/Al increased the compressive strength from 10MPa to 30 MPa and more. There seems to be an optimum of Si/Al in MK-based geopolymer around $\text{Si}/\text{Al}=1.8\text{-}2.2$ [25], [57], [58], [62], [90], [169], higher values decrease the mechanical properties probably due to the lower pH of the activating solution which cannot dissolve the MK particles. This optimum is not well defined also because most researchers improperly consider the silica impurities in the metakaolin as part of the geopolymer stoichiometry. This can be also seen by SEM, in fact the higher the Si/Al the more unreacted metakaolin is observed [57], [58]. While GP with Si/Al is formed by coagulation of small particulates, higher Si/Al GP can be considered as a composite material made of dense amorphous gel and unreacted metakaolin.

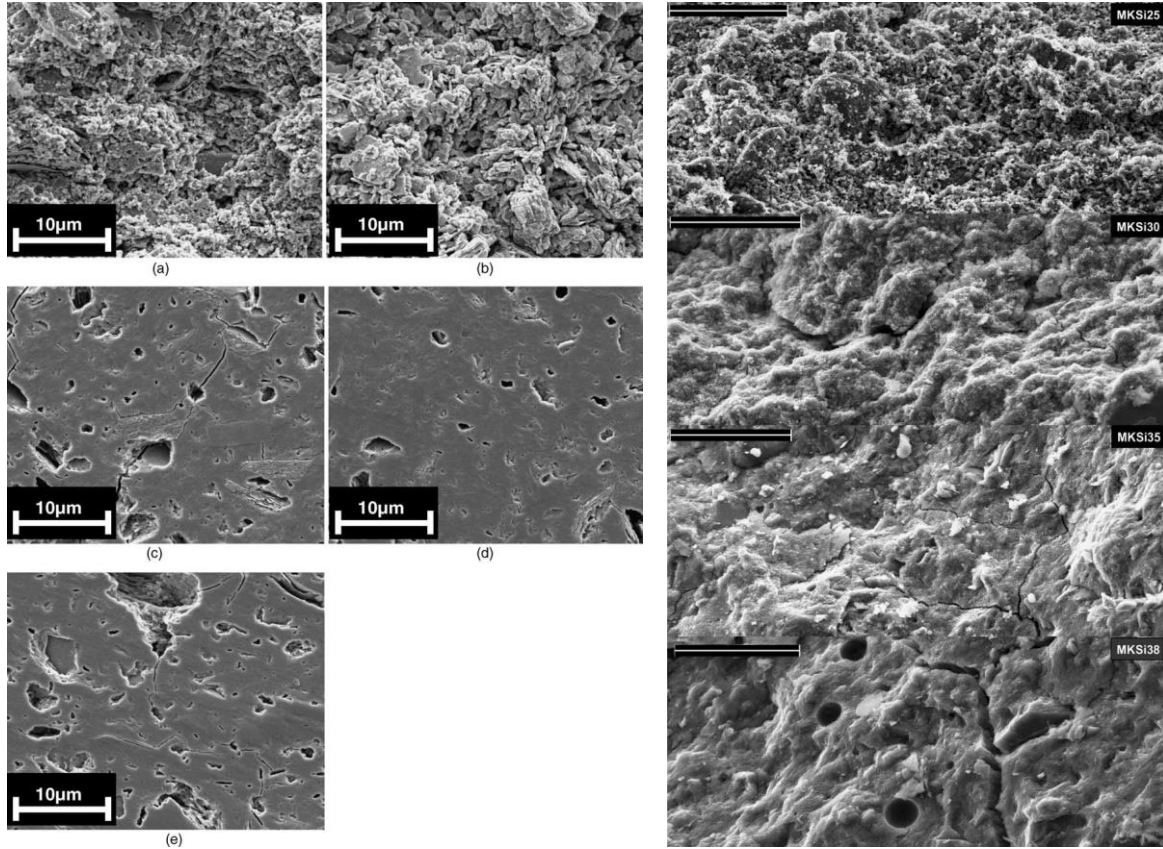


Figure 2.12 SEM images of MK-based GP cured at 40 C (left) and 85 C (right). Left: microstructure of GP with Si/Al ratio and UCS of (a) 1.15 and 18 MPa, (b) 1.40 and 40 MPa, (c) 1.65 and 56 MPa, (d) 1.90 and 73 MPa (e) 2.15 and 63 MPa (from [58]). Right: microstructure of GP with Si/Al ratio and UCS of 1.25 and 2.7MPa, 1.5 and 29 MPa, 1.75 and 48 MPa and 1.9 and 48 MPa (from [57])

Additional water can decrease viscosity and increase workability of the GP slurry [170], but it also increases the total porosity of the set material and it lowers the compressive strength. When all the other parameters are kept constant, the effect of alkali cations (potassium or sodium) on the compressive strength of GP is less pronounced than the Si/Al: only at $\text{Si/Al} > 1.5$ mixed cations Na/K-geopolymers shows higher strength than pure Na-GP and K-GP [90]. Potassium silicates are known to have lower viscosity than sodium silicate [38], thus it is possible to obtain GP with similar viscosity and workability with less water which result in less porous and stronger GPs.

The chemical composition of metakaolin-based geopolymer cured at 75°C has been optimized to produce high strength material with compressive strength above 60 MPa, Figure 2.13.

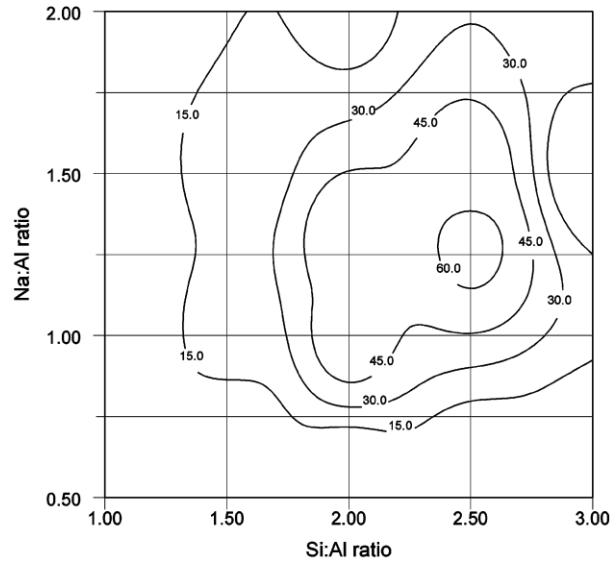


Figure 2.13 The contours of the constant compressive strength [MPa] of metakaolin geopolymers, cured at 75°C for 24 h; the compressive strength was measured after subsequent aging for 7 days at room temperature [62].

In order to properly link the geopolymers formulation and curing condition to their final structure and properties it is necessary to know the effects of the parameters on the geopolymer reaction. Understanding of the reaction mechanisms help interpret, predict and eventually control the effect of different reagents on the development of geopolymer performance.

2.3. Zeolites

2.3.1. Synthesis, structure and applications

Zeolites are hydrous aluminosilicate frameworks with a metal-to-oxygen atomic ratio equal to 2 and can be found both in nature and are made synthetically mainly in hydrothermal conditions [24]. In 2015 approximately 71,100 tons of natural zeolites were consumed in US at a cost of approximately \$100-230/ton [12]. Natural zeolites main uses are in oil and gas absorption and filtration operations, they can be used as catalysts, as fertilizer or pesticide carriers and as desiccants; their widest applications are in animal feed, wastewater treatment and purification, pet litter and odor control. The worldwide mine production of natural zeolites in 2015 was 2.8×10^6 tons and they consisted mostly in chabazite, clinoptilolite, erionite, mordenite and phillipsite, while the most common synthetic zeolite are zeolite type

A, X, Y and ZSM-5. The applications of synthetic zeolites span from petroleum refining for the production of fuels, petrochemicals processing for aromatics, olefins and detergents production, separation and purification processes, manufacturing industries, consumer products and environmental protection applications [171].

Numerous zeolitic materials exist, i.e. 232 different framework types were identified as in 2016 [172] and each framework can have different stoichiometries. The large range of zeolite structures is due to the bond angle between tetrahedral cation-oxygen-cation (T-O-T) which can assume a wide range of values between 125° and 180° . The tetrahedra can form different “secondary building units” (SBU), Figure 2.14. The same SBU can assume different configuration based on different orientation of the tetrahedral. The majority of zeolites is formed by a single type of SBU [24].

Different Archimedean polyhedra can form based on the SBUs they are made of, and different polyhedra can interlink in different ways leading to a large number of different zeolite frameworks, Figure 2.14. Different zeolites with the same frameworks are characterized by specific bond length and angles and by different non-framework species.

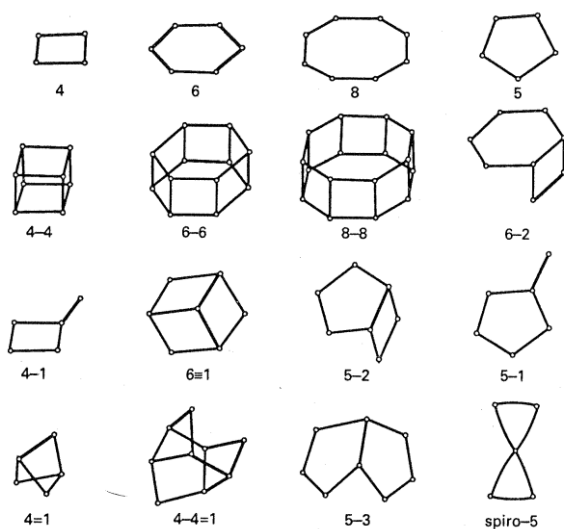


Figure 2.14 Secondary building unit (SBU) used to classify zeolites from Newsam [24].

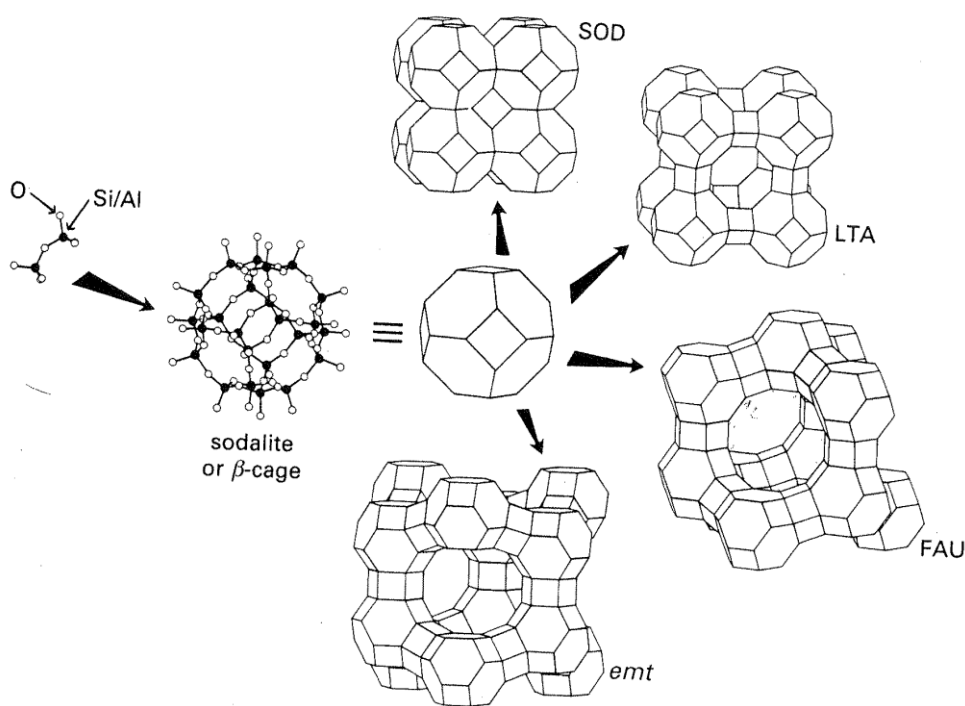


Figure 2.15 Progressive construction of a zeolites structure. The $(\text{Si,Al})\text{O}_4$ tetrahedra condense to form a truncated octahedral, also called a “sodalite” or “ β -cage”, made of 4- members and 6-members rings. The sodalite cage is found in different zeolite frameworks, such as in sodalite (SOD), faujasite (FAU), linde type A (LTA) and EMT frameworks. From Newsam [24].

The synthesis of zeolites involves inclusion in the water-based precursors solution of a source of alumina, a source of silica and an inorganic base, usually a group I or group II metal hydroxide. When these components are combined in diluted aqueous environment, they form a gel or a viscous liquid which entails amorphous aluminosilicate materials. Crystallization under hydrothermal condition of this gel, usually performed under autogenous pressure at $T=100\text{-}200^\circ\text{C}$, leads to a zeolite or a combination of different crystalline zeolites. The initial kinetics control of the crystal nucleation implies that the type of framework obtained also depend on the crystallization time, on seeds and impurities [24]. The debate if the zeolite structure formation is controlled by kinetic or thermodynamic is still open [173]. Using thermodynamic analysis, Sefcik [174] calculated the solubility of zeolite type A and zeolite type X assuming pseudo-equilibrium and obtained a crystallization diagram considering stable steady state, Figure 2.16. He found that zeolite type X had similar solubility in respect to zeolite type A when Si/Al approach to 1, thus these phases can coexist in this region.

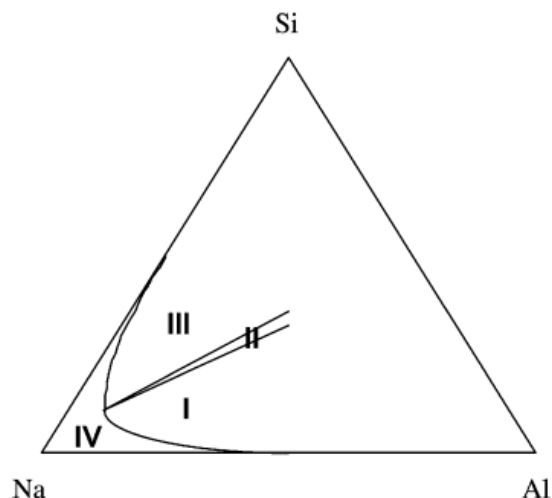


Figure 2.16 Zeolite A (region I) and zeolite X (region III) crystallization diagram for a 2M aqueous solution. In region II these phases coexist, in region IV there are no stable zeolites. (from [174]).

It should be remembered that the SBU concept is useful to describe the structure of zeolites, but the mechanism of zeolite formation does not involve the condensation of different SBUs. Instead the framework is built based on a progressive addition to the growing surface of small aluminosilicate units, such as dimers and tetramers [111]. This is the hypothesis of crystallization occurring via a solution-mediated mechanism, where the gel is dissolved and growth of the zeolite framework occurs by Oswald ripening. This explains the accelerated kinetics of zeolite growth at higher pH, when smallest aluminosilicate species are preferred to cages and cycles [111]. Another crystallization theory consists in a solid-state transformation, and some researchers suggested that both crystallization mechanisms are possible [159].

Zeolites frameworks are characterized by an open pore structure and the pore dimension is determined by the number of atoms forming the rings. The catalytic properties of zeolites are caused by the large effective surface area, usually between 300 and 700 m²/gram. Therefore all atoms of a zeolite are within few angstroms from the internal surface. The catalytic activity is associated with the aluminum tetrahedra which form acid sites [24]. Since the charge balancing cations have access to the pore system in zeolites, they can readily be exchanged with other ions in the solution. The maximum exchange capacity depends on the number of framework aluminum tetrahedral [24]. This property has led to several

commercial applications of zeolites as cation exchange materials for water purification, radioactive wastewater treatment and agricultural horticultural and medical uses [175]. On the other hand the aluminum sites are also more readily attacked by acid solutions which can promote the cleavage of the Al-O-Si bonds and, for low Si/Al zeolites, the collapse of the framework. For some zeolites the same framework can be prepared synthetically with different Si/Al. Higher Si content produces adsorbents with higher hydrophobicity, acid catalytic activity and hydrothermal stability, whereas higher Al content produces hydrophilic adsorbent with higher cation exchange capacity CEC [171]. The water used during the synthesis is adsorbed within the pore system and, in contrast to hydrated salts, thermal dehydration of zeolites does not provoke structural changes within the framework and zeolites are usually thermally stable.

Since geopolymers can be considered as amorphous-nanocrystalline zeolites [34], [38], studying zeolites help to understand the structure of geopolymers. Also, zeolites they can potentially be used as seeds in GP processing, as investigated in this work. No previous research has been published on zeolite seeding of geopolymers. The main difference between geopolymers and zeolites is not in their final chemical constituents, but in the precursor materials, processing and applications. Zeolites are usually synthesized adopting the molar ratios $\text{H}_2\text{O}/\text{SiO}_2=10\text{-}100$ and $\text{OH}^-/\text{SiO}_2=2\text{-}20$ in hydrothermal conditions: $T= 60^\circ$ to 200°C under autogenous pressure [24], [176]. On the contrary, geopolymers are formed in systems with $\text{H}_2\text{O}/\text{SiO}_2=2\text{-}10$ and $\text{OH}^-/\text{SiO}_2=0.1\text{-}0.5$ at relatively lower temperatures of $T= 25$ to 110°C , at approximately ambient pressure $p \approx 1\text{ atm}$ [177]–[179].

2.3.2. Induction time and kinetics of crystallization of zeolites

In the previous Section we described the crystallization process of zeolites either in solution or as a solid-state transformation. From zeolites synthesis standpoint, silicate and aluminate solutions are mixed at room temperature, an amorphous gel precipitate forms and it is left to age until hydrothermal treatment. It is generally accepted that before the crystallization occurs, the gel slowly undergoes structural rearrangement [112]. The initial amorphous gel precipitated from the precursor solutions evolves over time to form a secondary amorphous gel, which has a more similar structure to zeolite than the former. This mechanism seems to

follow the Ostwald's rule of stages: the first product (the primary gel) is more similar to the previous state of the system (the aluminosilicate solution) and it gradually evolves to its more favorable thermodynamic state: secondary gel and then crystalline zeolite. This gel transformation was captured by White using Coarse Grain Monte Carlo simulations [140] and is similar to the gel transformation observed in geopolymers [114].

Studies on zeolites crystallization kinetics are based on experimental data obtained by XRD. The zeolite crystallization is a nucleation and growth process, where the formation of nuclei can be associated with the cyclization reaction of tetramers and hexamers [141]. An induction period is always associated with crystallization of zeolite and this could be explained by the Kelvin effect [180]: smaller crystalline nuclei have lower solubility due to their higher surface area and thus lower growth rate. The induction time depends on several factors, such as temperature, gel composition, aging time of gel, presence of seeds, solution chemistry [112].

If the crystallization is a solid state transformation it can be expressed with the Kohnogorov-Johnson-Mehl-Avrami (KJMA) equation:

$$\frac{m_z(t)}{m_z(t_\infty)} = 1 - e^{[-K(t-\tau)^n]} \quad \text{EQ. 2.31}$$

$$\ln\left(-\ln\left|1 - \frac{m_z(t)}{m_z(t_\infty)}\right|\right) = \ln(K) + n * \ln(t - \tau) \quad \text{EQ. 2.32}$$

where $m_z(t)$ is the volume of crystalline zeolite at the time t , $m_z(t_\infty)$ is the final crystalline volume, n and K are constants. The value of n can be obtained by fitting experimental data and provides insight into the mechanisms of nucleation and growth. Time τ is the induction period and it is the sum of three different times [112]: the relaxation time, the time to form stable nuclei and the time needed by the nuclei to reach a detectable dimension.

Since the Avrami equation described solid-state transformation, a population balance approach is preferred by the advocated of solution-mediated mechanism [181]. A simplified equation can be written as:

$$\frac{m_z(t)}{m_z(t_\infty)} = K t^q$$

where the constant q identify the nucleation mechanism: For $q=3$ the nucleation is heterogeneous, for $q=4$ it is homogeneous and for $q>4$ it is autocatalytic [182], [183]. Autocatalytic nucleation is explained in terms of larger solubility of the amorphous gel compared with the quasi-crystalline nuclei: as the crystals growth and the gel dissolves, nuclei that were covered by gel are released into the solution and begin to grow resulting in an “*explosive rate of nuclei formation*” [182], [183]. Successive investigations have identified three components of autocatalytic nucleation: nuclei formed during gel precipitation, nuclei formed during gel aging process and nuclei added as seeds [184].

In GP the idea of an autocatalytic formation of the amorphous geopolymer gel was borrowed by this phenomenon found in zeolites processing. The formation of geopolymer is more similar to the precipitation of the initial amorphous gel in zeolite synthesis rather than its crystallization in hydrothermal condition. The first study to support the idea of autocatalytic geopolymerization is the historical work of Rahier on calorimetry data [74] where an increase of the reaction rate was observed with time. Nonetheless no factor $q>4$ was provided and the increase in reaction rate can be explained in other terms [18], [148].

2.3.3. Synthesis of zeolites from metakaolin

Kaolinite and metakaolinite have been used in the past as aluminosilicate source to synthesize zeolite [185]. These syntheses have higher crystallization temperatures, water content and Na/Al ratio as compared to geopolymer synthesis. The main reaction products are zeolite LTA, zeolite X, hydrosodalite, zeolite type P and cancrinite [148], [186], [187].

Metakaolin and NaOH at 90°C initially form zeolite LTA and hydrosodalite HS and at longer crystallization time zeolite type P [188]. The calcination of kaolinite had in impact on the zeolite produced. At 93°C and solution/solid ≈ 50 , kaolinite reacted with NaOH 4.25M and 10.75M to give hydrosodalite, while different metakaolin produce zeolite type A and minor amount of zeolite type X [186]. Youssef found similar results at 70°C using solution/MK=25; moreover the use of LTA seeds could increase the crystallinity of the

product [189]. Zeolite type A, hydrosodalite and cancrinite were instead found at higher temperature, i.e. $T = 100^{\circ}\text{C}$ [190].

Besides changing kaolinite calcination process, crystallization temperature and time, amount of water and alkali, different crystalline phases can be obtained by addition of silica to increase the ratio Si/Al above 1 [187]. Kaolinite and 1.33M NaOH at 100°C gave LTA, HS and cancrinite, while zeolite type X could also form when an extra source of SiO_2 was added [187]. The addition of colloidal silica could increase the amount of zeolite type X also when metakaolin was used instead of kaolinite; the synthesis was carried at 93°C , solution/MK ≈ 8 and Si/Al = 1.5 and the crystallization induction time increased when the colloidal silica was used [191]. Also at lower temperature of $T = 68^{\circ}\text{C}$ and 4.4 M NaOH the crystallization of zeolite type X was preferred to LTA when soluble silicates were added; at longer curing times hydrosodalite and zeolite type P forms [192].

As in geopolymer, Rocha suggested that the first step of reaction is the conversion of Al^{V} and Al^{VI} into Al^{IV} on the MK surface followed by the initial preferential dissolution of aluminate species which condense with silicate to form an amorphous gel [193]. In the last stage this gel undergoes a solid-state rearrangement to produce crystalline LTA, but he could not completely rule out a solution-based mechanism.

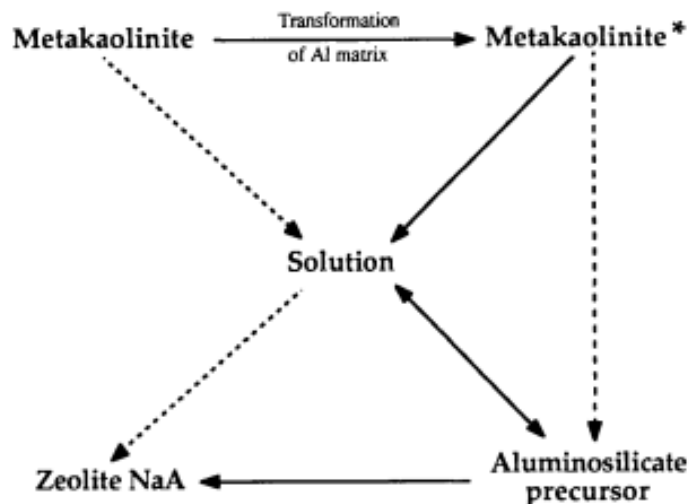
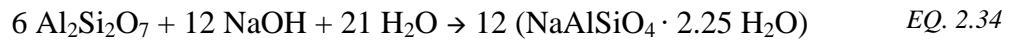


Figure 2.17 Mechanism of LTA crystallization from MK and 5M NaOH (from [193]). Solid lines represent observed reaction steps, dashed lines represent other possible reaction pathways.

The concentration of alkali had an effect on the crystallization kinetics, as it reduces the crystallization time and increases the product crystallinity [194]. Gualtieri studied the kinetics of crystallization of zeolite type A from metakaolin, 4M NaOH and solution/MK=2 in the temperature range $T=70-110^{\circ}\text{C}$. The crystallization behaviour supported an autocatalytic mechanism, i.e. $q>4$ in EQ. 2.33. At higher temperature hydrosodalite was preferred to zeolite type A, however Oswald rule of successive transformation was not observed but secondary nucleation of HS on the surface of LTA. The overall reaction can be expressed as in EQ. 2.34 and this stoichiometry was used as an example in Section 2.2.4.2.1.



2.4. Advanced GP applications and geopolymer crystallinity

The applications of GPs are manifold, it can be used as a low CO_2 emission / early strength replacement for Ordinary Portland Cement (OPC) and concrete [32], or as a binder to prepare refractory composites [195], as containment for toxic (heavy metals) and radioactive waste, and for water filtration and purification [6], [196]–[198]. The potential of geopolymers in these different fields arises from the two characteristics of the material: a) it is a chemically-bonded-ceramic based on covalent bonding, thus it has better fire and heat-resistant properties compared to the hydrogen-bonding based materials such as OPC [19], [38]; b) it has a zeolitic nature [38], [199] which provides it with the functional properties such as ion exchange.

The main current applications of GPs include high early-strength constructional cements. As for now there are no commercialized geopolymers that exploit their zeolitic properties. The main reason is that most researchers have focused on the consolidation kinetics and mechanical properties of geopolymers and not on their functional properties. The properties of these materials highly depend on their structure; controlling and tailoring the formation of crystalline phases in geopolymer will allow to engineer the properties of functional geopolymers. Unfortunately GP crystallization phenomena are still not fully understood, and this prevents the widespread of functional geopolymers and more work is needed in this

field. The present work attempts to address some of these gaps of knowledge of GP systems processing and crystallization.

According to Rahier [73] the crystallinity of geopolymers depends on the $\text{SiO}_2/\text{Na}_2\text{O}$ of the activating solution: if this ratio is larger than 0.8 the geopolymer is completely amorphous. This ratio represents a soluble silicate without Q^3 and Q^4 species and with $\text{pH} > 13.5$ [200], Figure 2.6. When the silicates concentration in the activating solution is low or null the crystallinity seems to increase with increasing water content in the geopolymer mix [75], [201]; this suggests that the crystallization in geopolymers could be a solution-mediated mechanism. MK-based geopolymers prepared at 40°C are still amorphous after 3 days but crystallized at longer curing time to produce zeolite type X, A, P and chabazite [202]. The addition of soluble silicates delayed the crystallization of zeolite, while the increase of sodium hydroxide increased the overall crystallinity [202]. Ferone obtained zeolite type A and zeolite type X at room temperature using metakaolin and 10M NaOH [169]. Zhang [203] studied the effect of Si/Al and NaOH/MK ratios on geopolymers cured at 40°C from 2 hours to 10 days. Adding soluble silicates suppressed crystallization, while increasing NaOH/MK increased the kinetics of zeolite type A and X formation. Synthesis of MK-based geopolymer at 45°C with the alkali fusion method gave hydrosodalite at short and long time, and zeolite type A and X at intermediate curing times, between 12 and 144 hours [204]. Unfortunately most of these analyses were qualitative and did not quantify the crystallinity and the relative percentages of different frameworks. According to Provis, GPs with $\text{Si}/\text{Al} > 1$ contain crystals which are not detectable by XRD but are by HRTEM. The addition of soluble silicates caused rapid nucleation of zeolites in the proximity of the metakaolin particles and the agglomeration of these nanocrystals produced the final geopolymer gel [98].

Promising studies have shown that geopolymers can be adopted as adsorbent of heavy metals for water treatment: Pb^{2+} , Cd^{2+} , Zn^{2+} , Cr^{3+} , NH_4^+ could be successfully adsorbed [6], [196], [197]. This relies on the high cation exchange capacity of geopolymers, for instance GPs based on MK and soluble silicates have $\text{CEC} = 129.5 \text{ meq}/100\text{g}$ [196]. Moreover, geopolymers can be used to encapsulate radioactive isotopes such as Sr^{2+} and Cs^+ which fit into the sodalite cage of faujasite [205].

An advantage of geopolymers over zeolites is their superior mechanical properties, in fact some investigations have already looked into the use of LTA-containing geopolymers to substitute self-supporting zeolite membranes for seawater desalination through pervaporation [198] and FAU-containing geopolymer to separate alcohol/water mixtures [7]. Another advantage is the GPs flexibility in term of processing: GP can be poured, cast, extruded, sprayed, 3D printed, contour crafted, etc. [195] and in this context some comprehensive rheological studies on metakaolin-based geopolymer have been conducted [170]. The particular zeolitic nature of GP determines the geopolymers performance in environmental applications [132], e.g. different zeolite structures have different channels and cages sizes [24]. Thus engineering and controlling the crystallisation of zeolite in geopolymer is required to achieve its full technical and commercial potential as functional material and not just as a mere low CO₂ binder.

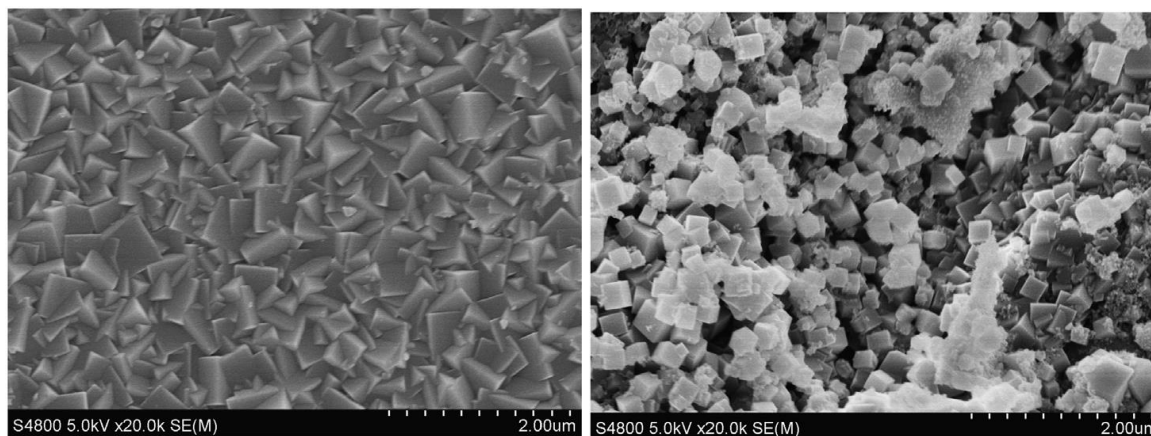


Figure 2.18 Top view (left) and cross section (right) of self-sustaining zeolite A membrane obtained via geopolymerization route for seawater desalination [198]

In this work we focus on “model”, well-defined chemistry geopolymers processed through metakaolin reacting with metal hydroxides and soluble silicates. This GPs subclass usually needs curing at mild temperature (~40°C) and thus cannot be used to replace OPC on job-site, but rather in precast applications. On the other side the zeolitic nature of these GPs provides new properties that can be exploited in solving environmental applications and in industrial catalysis. The chemical formulations of these metakaolin-based geopolymers have been explored and different oxides were selected to study and improve the setting kinetics and to engineer their crystal structure. This work contributes both to the advancement of

fundamental science of geopolymer reactions kinetic and to the control and optimization of GP properties for industrial and environmental applications.

3. Objectives

More than 20 years of research have been done on geopolymers, focusing especially on the development of a binder with low CO₂ emission that can substitute OPC in the construction industry. In recent years more efforts were given to understand the mechanism of geopolymerization, especially in MK-based geopolymer, and to explore the advanced properties of GP stemming from their zeolitic nature. Some critical aspects remained however unexplored or understudied, in particular the rate limiting mechanism of geopolymerization, the complex role of soluble silicates in the activating solution and the nucleation and growth of crystalline zeolite within the material. This work provides new insights on these three aspects which can be implemented into geopolymerization models to better predict and tailor their final properties. Practical guidelines on GP processing science developed in course of this work could help manufacturers and researchers to control the crystallinity in GPs and tailor their properties to obtain the desired functionality. A more complete understanding of the processing parameters that control the geopolymerization reaction may lead to more reliable products and a wider acceptance of this relatively new class of material.

The objectives of this work are as follows:

1. Assess and isolate the multi-faceted effects of soluble silicates on the compressive strength, microstructure and crystallinity of metakaolin-based geopolymers obtained in alkaline solutions.
2. Study the geopolymerization reactions, and identify the step that limits the overall reaction kinetics and assess the effects of seeding to enhance the reaction rate and control the final structure of the resulting GP.
3. Identify geopolymer compositions, additives and processes that lead to advanced functional materials for ceramic membranes, waste encapsulation and catalysis.
4. Provide experimental observations of the molecular events occurring during geopolymerization for the development of more sophisticated kinetic models, especially in regard to the reorganization and crystallization of geopolymers.

4. Approach and methodology

In this Chapter we present the different analytical techniques used to achieve the aforementioned objectives. In Chapter 5 we delved into the chemical constraints in MK-based GPs and into the effects of soluble silicates on the mechanical properties and structure of GPs. Based on such investigations a subgroup of GPs was selected and the effect of seeding was investigated in terms of the compressive strength, microstructural and structural development in seeded GPs, and reported in Chapters 6 and 6.2. Chapter 7 reports studies of the early stages of GP setting reactions, using rheological techniques. The setting rate limiting step of different GPs was determined by observing the effects of seeding. Finally, in Chapter 8 a multifactorial design was adopted to identify the processing parameters that control the gel formation and the crystallization of different zeolites.

4.1. Materials, synthesis and preparation methods

4.1.1. Raw material and metakaolin characterization

Table 4.1 lists the materials used in this work and their suppliers.

Table 4.1 Materials adopted in GP and zeolite synthesis, and various oxides used as seeds.

Material	Supplier
Powerpozz metakaolin (Advanced cement technologies)	Starpatch Concrete Products, Canada, Burnaby (BC)
Caustic soda NaOH	Alfa Aesar, Ward Hill, US (MA)
Sodium orthosilicate Na_4SiO_4	Alfa Aesar, Ward Hill, US (MA)
Sodium metasilicate Na_2SiO_3	Alfa Aesar, Ward Hill, US (MA)
Sodium aluminate NaAlO_2	Alfa Aesar, Ward Hill, US (MA)
Sodium silicate type N (PQ corporation)	Univar, Canada, Richmond (BC)
Colloidal silica (HS-50 Ludox)	Alfa Aesar, Ward Hill, US (MA)
Zeolite mordenite	Alfa Aesar, Ward Hill, US (MA)
Zeolite faujasite-H	Alfa Aesar, Ward Hill, US (MA)
Zeolite faujasite-Na	Alfa Aesar, Ward Hill, US (MA)
5 MIN-U-SIL fine ground silica SiO_2	U.S. Silica, Chicago, US (IL)
$\alpha\text{-Al}_2\text{O}_3$ Nano Powder	Inframat Advanced Material, Manchester, US (CT)
Fully stabilized zirconia ZrO_2 (8% Y_2O_3)	Lida, China

Powerpozz from Advanced Cement Technologies [Blaine, WA, United States] was used as source of metakaolin (MK). MK particles had the platelet-like structure typical of the clay, maximum diameter of approximately 1 μm and they formed 1-5 μm aggregates, see Figure 4.1. The chemical composition, determined with SEM equipped with energy-dispersive X-ray spectroscopy (EDX), included 53.3% SiO_2 , 43.5% Al_2O_3 , 1.9% Fe_2O_3 , and 1.3% TiO_2 .

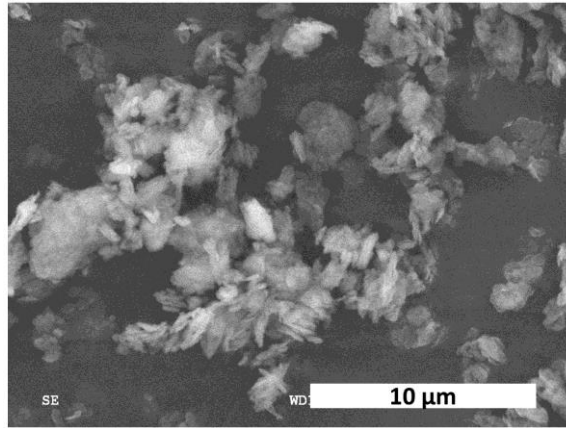


Figure 4.1 SE-SEM analysis of Powerpozz (metakaolin).

Powerpozz was mostly amorphous, Figure 4.2 top, there were no traces of residual kaolinite and the detected impurities were quartz SiO_2 (ICSD: 90145), anatase TiO_2 (ICSD: 63711) and halloysite $\text{Al}_2\text{Si}_2\text{O}_5(\text{OH})_4$ (ICSD: 26716). The broad peak associated with the amorphous phase was centered at $2\theta=23^\circ$ as expected [206]. The proper calcination (typically at 600°C to 850°C , for 1 to 12 hours [207]) which promotes transformation kaolinite-metakaolin was also confirmed by FTIR spectroscopy, Figure 4.2 bottom. The bands between 400 and 550 cm^{-1} corresponded to Si-O bending, peak at 636 cm^{-1} to Si-O-Si stretching, the bands at 752 and 785 cm^{-1} to surface hydroxyl Al-OH vibrations, the peaks at 915 and 936 cm^{-1} to in-plane hydroxyl vibration, bands at 1014, 1036 and 1108 cm^{-1} to perpendicular Si-O vibrations [208]. For MK, the main peak at 1080 cm^{-1} was associated with asymmetric Si-O-Al stretching, the shoulder at 1200 cm^{-1} with the asymmetric Si-O-Si stretching, the peak at 790 cm^{-1} with the Al(IV)-O stretching and the peak at 460 cm^{-1} with the Si-O bending [84]. It is evident that the calcination removed the surface hydroxyls, induced the formation of Al in tetrahedral coordination and destroyed the order of the Si-O Al layers [124].

In this work the effects of metakaolin surface area and calcination temperature were not investigated and these parameters were kept constant by adopting Powerpozz for both kinetics and structural investigations.

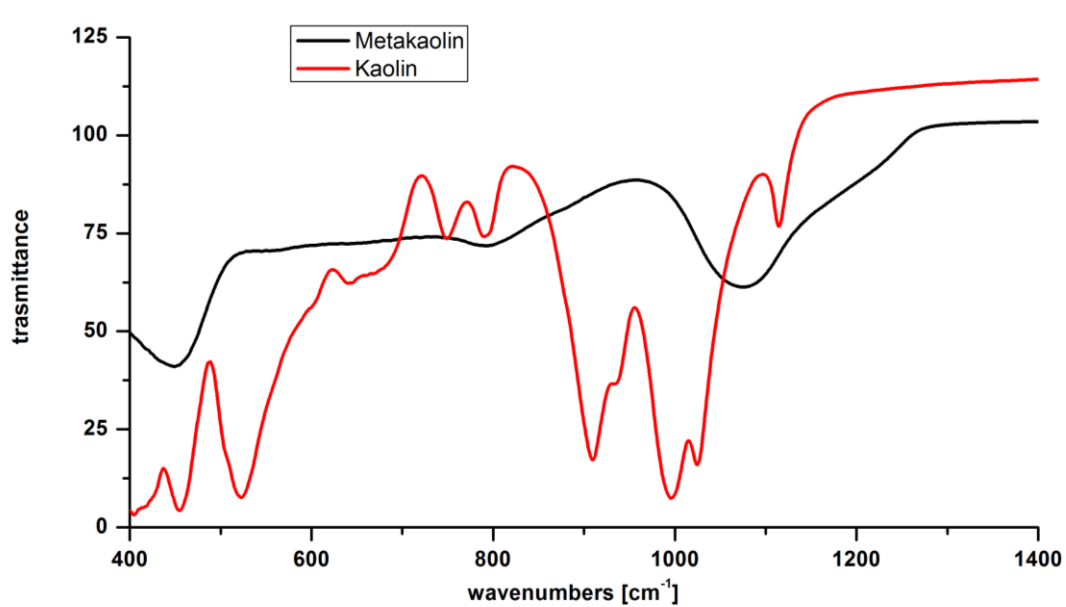
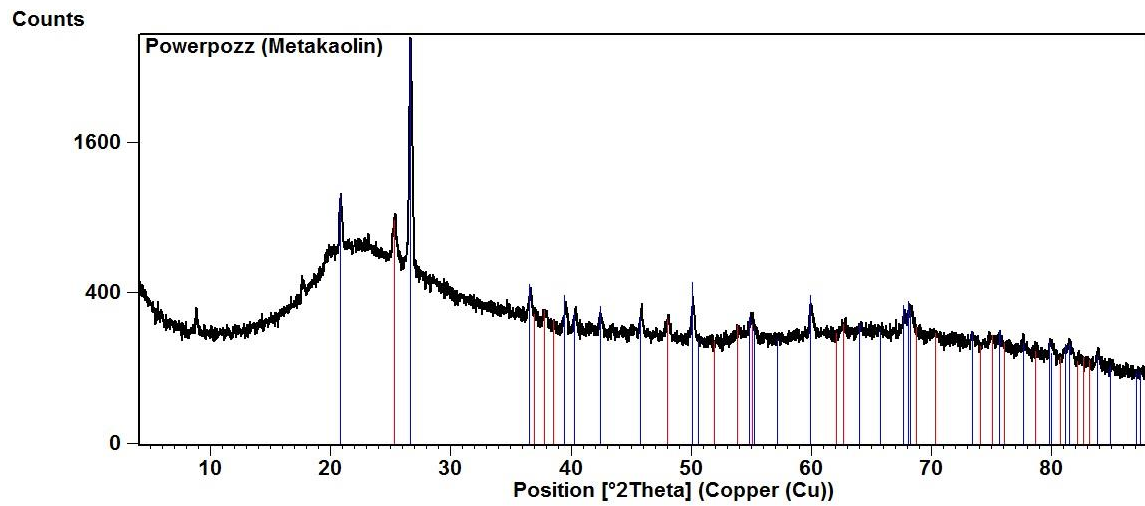


Figure 4.2 Top: X-rays diffractogram of Powerpozz. Blue line: quartz; red line: anatase; peak at $2\theta=8.8^\circ$ belong to halloysite. Bottom: ATR-FTIR spectra of kaolin and metakaolin.

4.1.2. Geopolymer synthesis

Sodium hydroxide solutions were prepared by mixing sodium hydroxide NaOH pellets (Alfa Aesar, 98%) in distilled water for 24 hours using magnetic stirrer. The concentration of NaOH solution was determined by titration and then the desired NaOH concentration obtained by proper dilution. When silicates were needed in the activated solutions, sodium silicate type N or sodium metasilicate were added to the NaOH solutions and mixed for 48 hours. The activating solution was then added to MK and mixed for 5 minutes with an impeller at approximately 2700 rpm. The impeller was made of stainless steel 18mm x 30mm cross blades. The GP slurries were then cast into molds. The compaction operations were performed using a vibrating table for 2 minutes to remove the entrapped air; this duration was considered adequate as no macroscopic air bubbles formed after 1 minute of compaction. After 15 minutes from the initial mixing the molds were covered by a rubber sheet, placed in sealed plastic bags and left in a dryer for the required time at the required curing temperatures.

4.2. Analysis methods

4.2.1. Rheological characterization

All inorganic cements were obtained by mixing a solid component with a liquid component to obtain a dispersion which can be plastically deformed under the stress delivered by the rheometer. Chemical reactions (e.g. hydroxyl condensation) and physical processes (e.g. coagulation) transformed progressively during the test the fluid slurry to a solid monolith. The main difference between the (i) initial viscous and the (ii) final elastic material lays in their response to the applied stress: the first undergoes a deformation proportional to the stress τ , time t and inversely proportional to the viscosity coefficient, while the second undergoes an instant deformation proportional to the stress and inversely proportional to the

modulus of elasticity. In reality most materials have a mixed viscoelastic response to stress, which will be further described in Sections 5.1.1 and 7.3.

The branch of science studying the deformation and flow of matter is called rheology and it is particularly important in cement and geopolymer science for two reasons. First, the manufacture processes for cementitious materials, e.g. casting, extrusion and spraying, require a detailed characterization and control of their rheological properties. Second, as the viscoelastic response of suspension depends on the interactions between its components, it is possible to study the nature and kinetic of the geopolymerization reaction by rheological techniques.

4.2.1.1. Viscosity

The simplest fluids in term of rheological properties are the Newtonian fluids. When a shear stress τ is applied to this material a velocity gradient called shear rate $\dot{\gamma}$ is observed within the material [209]. For an ideal Newtonian material those quantities are directly proportional and the constant that links them is called viscosity η . The viscosity is independent of the shear rate and the shear history of the material. Sodium hydroxide and sodium silicate solution are Newtonian fluids, especially at low shear rates, i.e. 0.1 s^{-1} [210].

$$\eta = \frac{\tau}{\dot{\gamma}} \quad \text{EQ. 4.1}$$

The viscosity of solution can be measured using a rotational viscometer in which a spindle rotates in a single direction at different angular velocities and the shear stress is measured [211]. In this work a “Brookfield Digital Viscometer, Model: LVDV-E” was used to study the viscosity of selected activating solutions. The mechanical bearing of these viscometers are not designed for high viscosity pastes such as cements and geopolymers.

4.2.1.2. Steady-state measurements

Cementitious materials, such as geopolymers, differ in many aspects from ideal Newtonian fluids. If the stress is too low no flow is observed in normal observation times, e.g. hours; the threshold stress above which material starts flowing is called yield stress τ_0 . Once the yield

stress is exceeded the proportionality between stress and strain rate is restored. “Self-compacting cement” term usually refers to a particular mix-design including additives that reduce the cement yield stress. The shear rate $\dot{\gamma}$ vs shear stress τ line is defined as flow curve and it defines the rheological properties of viscous materials. There are several models that describe this rheological behavior and the Bingham equation [170], [212] is one of them, as expressed in EQ. 40.

$$\tau = \tau_0 + \eta\dot{\gamma} \quad \text{EQ. 4.2}$$

As first approximation, most of the OPC and geopolymer cements can be represented by the Bingham model including these two parameters: yield stress and plastic viscosity.

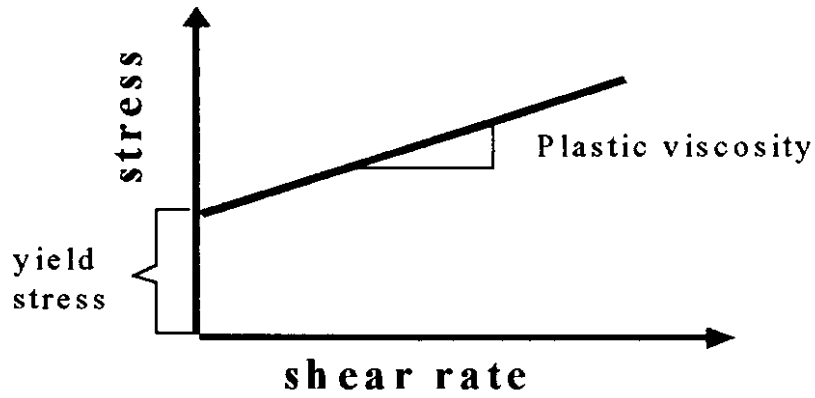


Figure 4.3 Shear stress vs shear rate according to the Bingham model [170], [212].

There are shear rate and time-dependent effects that can alter the Bingham response. If the plastic viscosity decreases at higher shear rate the material is defined as pseudo-plastic (or shear-thinning), if the opposite is observed the material is defined as dilatant (or shear-thickening). These behaviours can be correctly described with the Herschel and Bulkley equation [212], where K is the consistency index and n is the flow index.

$$\tau = \tau_0 + K\dot{\gamma}^n \quad \text{EQ. 4.3}$$

Thixotropy is another property of pastes and slurries that become less viscous over time when shaken, agitated, or otherwise stressed. The shear stresses gradually break the inter-particle bonds and the particles can move more freely within the material; those bonds are restored once the paste is left at rest and the viscosity increases. For this reason the rheological properties of the material are time and history dependent [212]. The increase of

viscosity that is observed after the cement is cast has positive effects such as the reduction of formwork pressure and the stability of the extruded material. Thixotropy can be exploited in specific applications such as 3D printing of geopolymeric materials [195].

In this work the rheological properties of the geopolymeric pastes (such as viscosity coefficient vs shear rate) were probed using a Haake Rotovisco vt550 rotational rheometer equipped with grooved rotor to reduce slippage at the surface. The pastes were placed between the sensor (the external cylinder) and the rotor (the internal cylinder) and the motor set the rotor at a pre-determined speed. The resistance of the fluid to flow generated a torque on the shaft that was recorded. The test can be performed controlling the shear rate and measuring the shear stress or vice versa. The shear rate and the shear stress can be obtained from the torque, the angular velocity and the geometry parameters of the rheometer, as follows [211]:

$$\tau = \frac{T}{2\pi r_a^2 H} \quad \dot{\gamma} = \frac{r_a \Omega}{r_2 - r_1} \quad \text{EQ. 4.4}$$

where T is the torque, r_1 is the inner cylinder radius, r_2 is the external cylinder radius, r_a is the average radius between r_1 and r_2 , Ω and H are respectively the angular velocity and the height of the rotor, Figure 4.4.

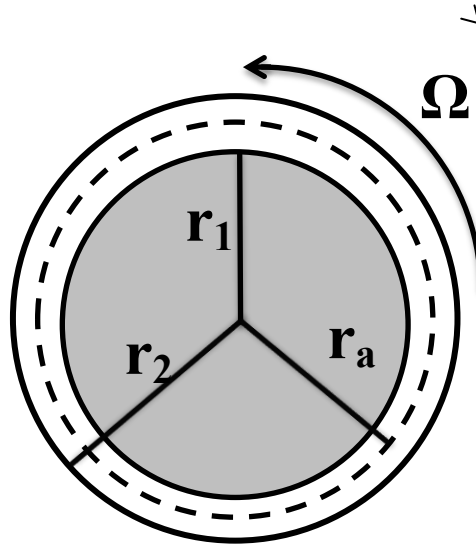


Figure 4.4 Cross section of a concentric cylinder rheometer

In order to obtain the flow curve and determine the nature of the paste a steady state must be achieved. The steady state was obtained by keeping the shear rate constant for each step and shear stress was measured after equilibrium was reached. In Figure 4.5 the shear stress as a function of time is displayed for each of the programmed shear rates. Once equilibrium is obtained the shear stress value was stored and the result represented data point in the flow curve.

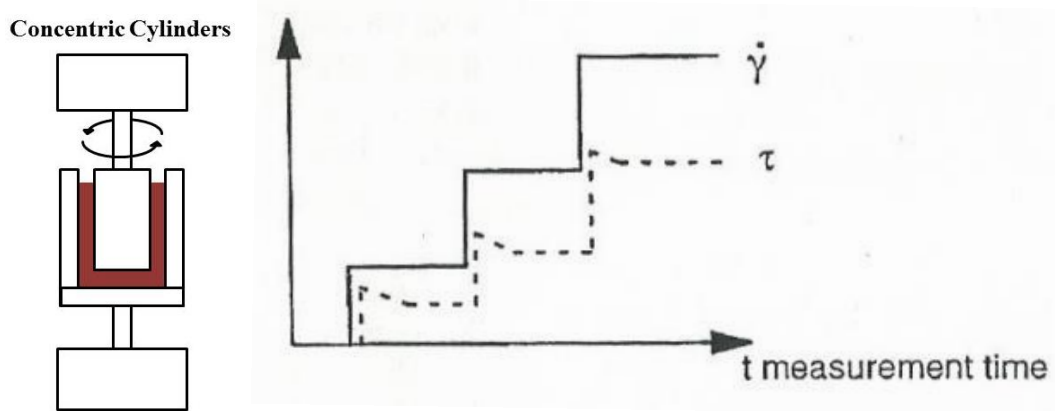


Figure 4.5 Left: schematic representation of the Haake Rotovisco vt550 rotational viscometer. Right: experiment program commonly used to obtain a steady state flow curve [213].

There are several experiments available for measuring and characterizing the thixotropy. One method consists of measuring the area between the up and down flow curve, Figure 4.6 [206]: the shear rate increases from zero up to a pre-determined point, it then decreases back to zero and the shear stresses versus shear rates are plotted. The two curves define a hysteresis loop and area within the hysteresis loop represents the energy required to breakdown the structure of the thixotropic suspensions. The measurement of the variation of thixotropy vs time after mixing GP reactants provides useful information on structural rebuilding within the mix. Unfortunately this method is relative since it strongly depends on the testing procedures and equipment.

Another method to determine thixotropy is based on keeping the shear rate constant and measuring the shear stress over time [213]. Two parameters are obtained with this method, one is called the initial stress “ τ_i ” and depends on the initial structural condition of the mixture, and the other is called equilibrium stress “ τ_{eq} ” and indicates a balance between the structural breakdown and rebuilding. In this work the hysteresis loop method was adopted.

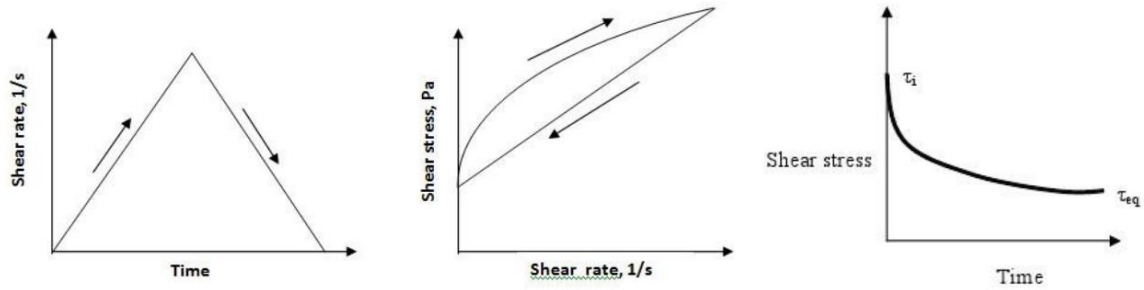


Figure 4.6 Thixotropic measurements. Left and middle: hysteresis loop method. Right: constant shear rate method [213].

4.2.1.3. Dynamic oscillatory measurements

At the early time of mixing, cementitious materials are not purely viscous or elastic but are viscoelastic [170]. A portion of the energy is stored elastically within the material, while the rest is dissipated during the viscous flow. Rheological measurements in which the viscosity is measured at a constant shear rate cannot distinguish the viscous from the elastic component of the response. Tests where the shear rate is varied linearly also cannot separate the two contributions. Instead, during dynamic rheology the sample is subject to a sinusoidal strain $\gamma = \gamma_0 \sin(\omega t)$ and the sinusoidal stress $\tau = \tau_0 \sin(\omega t + \delta)$ is measured, or vice versa [211]. The elastic component of the response is in phase ($\delta = \omega \cdot \Delta t = 0^\circ$) with the strain, while the viscous component is out-of-phase ($\delta = 90^\circ$). In this work the Anton Paar Rheometer MCR502 was used with parallel plate geometry in dynamic rheology experiments.

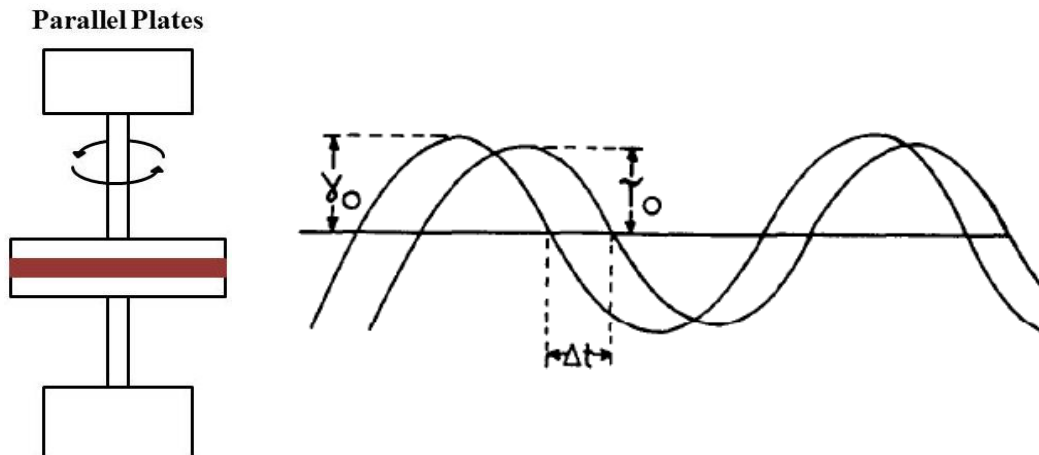


Figure 4.7 Left: schematic representation of the Anthon Paar Rheometer. Right: stress-strain response of a viscoelastic material during dynamic rheology tests [209].

The response of the material can be described by the complex modulus $G^*=G'+iG''$, which is obtained experimentally by measuring the amplitude of stress and strain, and the phase angle δ [209], [211]. The storage modulus G' and the loss modulus G'' represent the energies store elastically or dissipated viscously during one oscillation cycle. The complex viscosity $\eta^*=\eta'+i\eta''$ can be calculated from the dynamic viscosity η' and out-of-phase viscosity η'' .

$$|G^*| = \sqrt{G'^2 + G''^2} = \frac{\tau_0}{\gamma_0} \quad \text{EQ. 4.5}$$

$$\delta = \omega \Delta t \quad \text{EQ. 4.6}$$

$$G' = |G^*|\cos(\delta) \quad \text{EQ. 4.7}$$

$$G'' = |G^*|\sin(\delta) \quad \text{EQ. 4.8}$$

$$\eta' = \frac{G''}{\omega} \quad \text{EQ. 4.9}$$

$$\eta'' = \frac{G'}{\omega} \quad \text{EQ. 4.10}$$

4.2.1.4. Empirical tests

Most of the aforementioned rheological tests cannot be used practically for quality control in the field. Moreover, most rheometers have intrinsic limitation: in coaxial cylinder geometry, the maximum diameter of particles must be at least 10 times smaller than the gap size. Thus mortar and concrete cannot be studied.

For this reason several empirical tests have been developed [212], [214]. In the construction field terms like workability, consistency, plasticity and flowability are often adopted, but their definitions are mostly descriptive. Empirical quantitative terms were developed in connection with particular test that aims to measure the particular response of the paste (e.g. Ve-be, slump, compaction factor). Albeit these tests are useful as quality control tools, they

are one-point tests and cannot describe the complex rheological behaviour of cementitious materials. The appropriate parameters to characterize the flow of the paste include fundamental quantities such as the viscosity and the yield stress that regulate the rheological behaviour of the material. Most of the empirical tests give a single number which is a complex function of those two fundamental rheological parameters; therefore it is not possible to derive the accurate yield stress and the viscosity from such tests [215]. In this work the empirical flowability was determined using a flow table [216]: the geopolymer was poured in a bottomless mold placed on a surface; the mold is removed, the surface is dropped several times and the percentage of lateral spread of the slurry is measured.

Table 4.2 some empirical tests to measure the rheological response of cementitious materials.

Test name	main rheological parameter determining the response	application of stress	standard
slump	yield stress	gravity	ASTM C143
Ve-Be time	yield stress	external vibration	ASTM C1170
flow cone	yield stress	gravity	ASTM C939
turning tube viscometer	viscosity	gravity	ASTM C360

The transformation of the viscoelastic suspension into an elastic solid is usually determined by an empirical test, i.e. Vicat test (ASTM C 191 “Standard method for time of setting of hydraulic cement by Vicat needle” [217]). During the test a specific load is applied to the cement via a needle and the material is said to have set when the needle leave no mark on the surface. This method was adopted in this work to measure the setting times of the geopolymers as there is not ad-hoc test for geopolymer. The GP setting times were more difficult to measure compared with Ordinary Portland Cement (OPC) pastes due to their thixotropic behavior. Moreover some GPs composition did set but had low initial mechanical strength and hardness, and the needle left a mark on the surface. For this reason the GPs were considered set when the penetration values were less than 0.5mm.

4.2.2. Contact angle measurements

The wettability of a solid towards a certain liquid can be quantified as the tangential contact angle between the solid surface and a liquid drop. This angle depends on the solid-liquid γ_{SL} , liquid-gas γ_{LG} and solid-gas γ_{SG} interfacial energies. Young's equation is a fundamental equation that expresses the contact angle based on the three boundary conditions that are present at equilibrium [218].

$$\gamma_{SG} = \gamma_{LG} \cos \theta_{SL} + \gamma_{SL} \quad \text{EQ. 4.11}$$

Experimentally the contact angle can be measured with two different set-ups: sessile drop or captive bubble [218]. Sessile drop test involves producing a droplet of the testing fluid which is deposited on top of the solid. Instead, in a captive bubble test the substrate is immersed in the testing fluid and an air bubble is placed underneath the submerged substrate and the contact angle is measured. In this work most tests were carried out adopting the captive bubble method, see Section 7.2.1 for more details. The contact angle measurements were performed using a First Ten Angstroms (FTA) 1000 B Class contact angle goniometer, equipped with a microliter syringe, Leur-Lok needles, Navitar 2x magnification camera. The fluid was dispensed and the images analyzed by using a custom software.

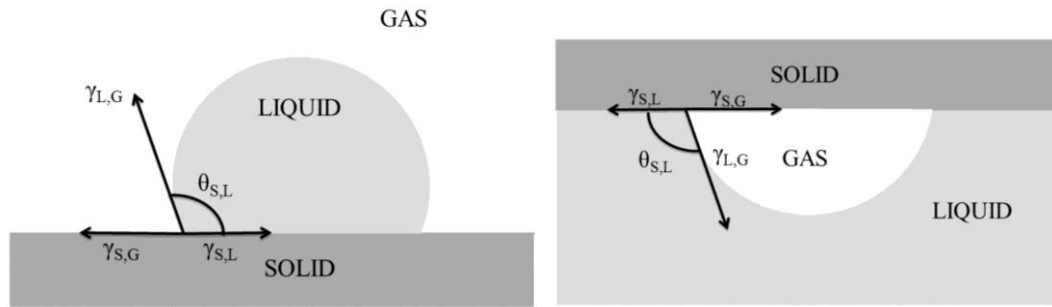


Figure 4.8 Sessile drop (left) and captive bubble (right) schematic diagrams [219].

4.2.3. Mechanical and microstructural analysis

Most geopolymer samples prepared in this work were cast in mold with dimension 1 by 1 by 7 inches (0.025 x 0.025 x 0.178 m). The GP bars were cut in 1 inch cubes using a diamond saw. The unconfined compressive strength (UCS) of the GP was tested using a INSTRON 3369 test machine equipped with a 50 kN load cell and using a crosshead speed of 0.5mm/min. Efforts were made to assure that the samples were as close as possible to perfect cubes with parallel surfaces; inaccuracies were compensated by testing larger numbers of samples (e.g. 9 cubes per composition) to improve statistical analysis.

The microstructure of the raw materials, the reaction products and the fractures surfaces were analyzed without polishing using a Hitachi S-570 scanning electron microscope (SEM) with a tungsten filament that can operate either in high vacuum mode or in variable pressure. Gold-palladium coating and carbon coating were applied with a sputtering machine for samples analyzed in high vacuum mode to make them conductive and minimize charging effects. Semi quantitative elemental chemical analysis and maps were obtained by EDX.



Figure 4.9 Left: Geopolymer bar during demolding operation. Right: GP cube and head of the Instron machine during UCS test.

4.2.4. Structural analysis - XRD

X-Ray diffraction analysis is used to identify and quantify crystalline structures, study the crystals dimensions, shapes and their orientations within a material [220]. The electrons act as secondary sources of X-Rays and constructive interference occurs when they belong to an

ordered lattice, i.e a crystals. The Bragg law, EQ. 4.12, links the interatomic distances d of the crystal to the experimental angles $2\theta^\circ$ at which the interference occurs [220]. The intensities of the Bragg peaks of a crystalline phase Y_{ph} depend on many factors, but most importantly on the atomic content of the crystal unit cell, EQ. 4.13. The X-ray diffraction intensity y_{ic} can be calculated by adding the Y_{ph} contributions of all phases and the background contributions I_b , EQ. 4.14. Finally, the size of the crystals has an impact on the shape of the Bragg peaks and the Sherrer equation describes this relation, EQ. 4.15 [220].

$$2 d_{hkl} \sin(\theta_{ph}) = n \lambda \quad \text{EQ. 4.12}$$

$$Y_{ph} = F_{ph} H(\theta - \theta_{ph}) K_{ph} \quad \text{EQ. 4.13}$$

$$y_{ic} = I_b + S_h \sum_p Y_{ph} S_{ph} \quad \text{EQ. 4.14}$$

$$L = \frac{K\lambda}{\beta \cos\theta} \quad \text{EQ. 4.15}$$

d_{hkl} is the interatomic plane in the crystal, θ is the diffraction angle, n is an integer number, λ is the X-ray wavelength, F_{ph} is the structure factor of the crystalline phase, H represents the shape of the diffracted peak, K_{ph} is the product of several intensity correction factors, I_b is the background intensity, S_h is the scale factor, S_{ph} is the phase scale factor, K is the shape factor and β represents the crystal contribution to the FWHM of the diffraction peaks.

The information contained in diffractograms can be extracted by using a least-square refinement between the experimental function y_{io} and a model y_{ic} that describes the source of XRD, the diffractometer instrumental configuration and the sample. This method is named after its inventor, the Rietveld refinement [221], and practical aspect and guidelines of this technique can be found in [222] . The Rietveld method is particularly important for phases quantification because of the whole-pattern fitting approach which guarantees a much greater accuracy and precision compared with other methods, such as the Reference Intensity Ratio (RIR) Methods.

By using the Rietveld method it is possible to perform quantitative phase analysis (QPA) [223]: the phase weight percentage w_i can be obtained from the phase scale factors S_i and the unit cell mass M_i and volume V_i , EQ. 4.16. Since amorphous phases do not contribute to the Bragg intensity, a Rietveld refinement of a partially crystalline material overestimates the weight fractions of the crystalline phases. Adding a known amount of crystalline material $X_{s,c}$ and comparing it with its weight percentage obtained by Rietveld refinement X_s allows the quantification of the amorphous content w_a (EQ. 4.17) and normalization of the weight percentage of the crystalline phases w_i .

$$w_i = \frac{S_i M_i V_i}{\sum_j S_j M_j V_j} \quad \text{EQ. 4.16}$$

$$w_a = \frac{100}{(100 - w_s)} \left(1 - \frac{X_s}{X_{s,c}} \right) \quad \text{EQ. 4.17}$$

Graphical observation of the measured and calculated diffractograms is usually adopted to understand how the model can be improved or if the refinement is good enough [224], e.g. a mismatch between measured and calculated peak positions can be associated with incorrect unit cell parameters. R -factors quantify those differences and the Goodness of Fit (GOF) is calculated to determine if the model is appropriate: the lower the GOF, the better the refinement. Unfortunately there are no strict guidelines on the acceptable threshold value for GOF.

$$R = \sum_i w_i (y_{io} - y_{ic})^2 \quad \text{EQ. 4.18}$$

$$R_{wp} = \left[\frac{\sum_i w_i (y_{io} - y_{ic})^2}{\sum_i w_i (y_{io})^2} \right]^{1/2} \quad \text{EQ. 4.19}$$

$$R_{exp} = \left[\frac{N - P}{\sum_i w_i (y_{io})^2} \right]^{1/2} \quad \text{EQ. 4.20}$$

$$GOF = \frac{R_{wp}}{R_{exp}} \geq 1 \quad \text{EQ. 4.21}$$

where w_i depends on the estimated standard deviation, N is the data point numbers and P is the number of parameters in the model [224].

In this work X-ray powder diffractograms were obtained using a Rigaku Model MultiFlex with Cu-K $_{\alpha}$ ($\lambda=1.5418\text{\AA}$) in Bragg Brentano theta-theta geometry with 1 cm receiving slit, 1° soller slit, 0.3° divergence slit and graphite monochromator. The scans were set to run at 40 kV and 30 mA with the step size ranging from 0.5 to 2 degree/min depending on the tested samples. Rietveld analyses were carried using the software X'Pert Highscore Plus.

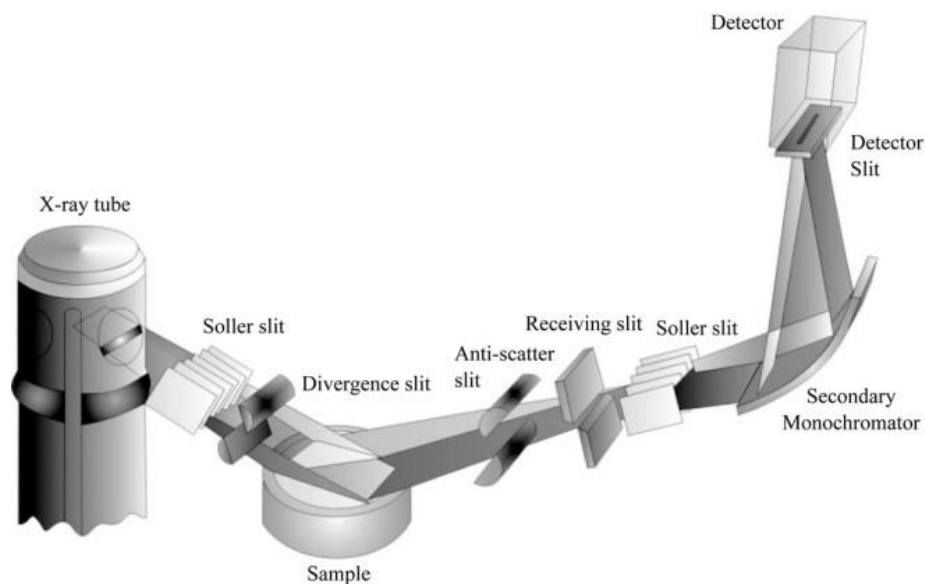


Figure 4.10 Schematic representation of diffractograms in Bragg-Brentano geometry, from [225].

4.2.5. Structural analysis - FTIR

Fourier-Transformation Infrared spectroscopy (FTIR) is based on the energy quantization of internal vibrations of atoms and molecules within a material [226]. Since the energy gap between the fundamental and excited vibrational state corresponds to the energy of infrared (IR) light, the selective absorption of photons in this frequency region by the material reveal the presence of particular functional groups, such as hydroxyl groups -OH. This technique probes the interatomic bonds of the material, thus it does not require the material to be crystalline.

FTIR can be performed using different geometries, both in transmission and in reflection, e.g. attenuated total reflectance ATR. An FTIR spectrum usually consists of transmittance values (in percentages) over different wavenumbers (cm^{-1}). Transmittance T is calculated as the ratio between the signal intensity of the sample I over the intensity of the previously collected background I_0 . The molar concentration c of a molecule is assumed to be proportional to the absorbance A of the sample, which is calculated from the transmittance, EQ. 4.22 [226]. Quantitative analysis thus requires the absorbance to be normalized by the molar extinction coefficient ε and the interaction distance between the IR light and the sample (see penetration depth l in EQ. 4.23). Since the penetration distance in the FTIR-ATR depends on the wavelength λ of the infrared light, ATR spectra need to be corrected using EQ. 4.24 when quantitative analyses are performed.

$$A = \log_{10} \left(\frac{I_0}{I} \right) = -\log_{10}(T) \quad \text{EQ. 4.22}$$

$$A = \varepsilon c l \quad \text{EQ. 4.23}$$

$$l = \frac{\lambda}{2\pi n_1 (\sin^2 \Phi - n_{21})} \quad \text{EQ. 4.24}$$

where Φ is the incidence angle of the IR light, n_1 is the refractive index of the ATR crystal and n_{21} is the ratio of the sample refractive index over n_1 [226], [227]. ATR-FTIR analyses were performed using a Perkin Elmer spectrum 100 - FTIR machine with a Tl-Br-I ATR plate (diamond coated). The resolution adopted was 1 cm^{-1} and the spectra were acquired from 4000 cm^{-1} to 250 cm^{-1} averaging 25 scans. In the following table the typical frequencies for geopolymeric material are listed.

Table 4.3 Precursors and geopolymers infrared characteristic bands [38].

chemical group	frequency [cm^{-1}]	type of vibration
Si-O	1080-1100	symmetrical vibration
Si(Al)-O	1008	asymmetrical vibration
Al-OH	914	6-coordinated Al-OH stretching vibration
Si-OH	840	bending vibration
Al-O	798	4 coordinated Al-O stretching vibration
Si-O	694	symmetrical stretching vibration
Si-O-Al	540	bending vibration
Si-O	469	in-plane bending vibration

4.2.6. Factorial design and Analysis of Variance (ANOVA)

In material engineering there is a relation between materials processing, structure, properties and performance. In order to determine if a synthesis parameter has an effect on a certain material property we need to quantify it and assess if the differences are due to a real effect or due to random variation. This can be accomplished by the analysis of variance ANOVA, which is a statistical method particularly useful when a factorial design of experiment is adopted [228]. The latter consists of testing multiple processing parameters at the same time instead of performing multiple single-parameter (one-at-the-time) experiments. Factorial design in combination with ANOVA allows a more efficient investigation of the parameter effects and, more importantly, the identification of interactions between multiple processing parameters.

The Design of Experiment (DOE) has its own terminology, where the parameters are named *Factors*, the different values assumed by each factor are called *Levels*, the measured data is named *Response*, the combination of factor levels is named *Treatment* and their effects are to be compared with other treatments. In Chapter 8 ANOVA analyses were performed in order to study the effects and interactions of different factors, each with multiple different levels, on different responses, following the methodology and software provided by StatEase [229].

Factors included both GP chemical compositions and processing parameters, i.e. curing time and temperature, and the responses were chosen and calculated to quantify the transformations occurring during the geopolymerization reactions.

For simplicity, let's assume a full factorial design consisting of 4 factors, each with 3 levels, i.e. $4^3 = 64$ data points. If we ignore interactions between the factors, each factor has $n_t = 4^{3-1} = 16$ replicates (wherein the inspected factor is kept constant while the others are changed) and $k=3$ treatments (i.e. setting different levels of the inspected factor while other factors are kept constant). In this case \bar{y} represents the mean of all data, \bar{y}_t represent the means of the replicates for the 3 different inspected factor levels and y_{ti} represents the individual data point. If the response varies more between treatments than within treatment the factor is said to have a statistical significant effect on the response. In order to quantify this we need to introduce the sum of squares SS : SS_{tot} represents the total sum of squares calculated based on the overall mean \bar{y} ; SS_w represent the sum of squares calculated from the individual treatment means y_t ; SS_b represent the sum of squares calculated between the treatment means y_t and the overall means \bar{y} . DoF_b and DoF_w are respectively the degree of freedom between groups and within groups, k is the number of treatments and n_t is the number of replicates. EQ. 4.28 links these three different SS values to each other [228].

$$SS_{tot} = \sum_{t=1}^k \sum_{i=1}^{n_t} (y_{ti} - \bar{y})^2 \quad EQ. 4.25$$

$$SS_w = \sum_{t=1}^k \sum_{i=1}^{n_t} (y_{ti} - \bar{y}_t)^2 \quad EQ. 4.26$$

$$SS_b = \sum_{t=1}^k n_t (\bar{y}_t - \bar{y})^2 \quad EQ. 4.27$$

$$SS_{tot} = SS_b + SS_w \quad EQ. 4.28$$

$$DoF_b = k - 1 \quad EQ. 4.29$$

$$DoF_w = n_t - 1 \quad EQ. 4.30$$

Once these quantities are calculated it is possible compute the F -ratio, EQ. 4.31. The calculated F ratios are then compared with the F -distribution tables to obtain the p -values α . α represents the probability that the difference in y_t values can be attributed to random errors, i.e. the null hypothesis. It is usually accepted that for $\alpha < 0.05$ the null-hypothesis is rejected and the factor is said to have a statistically significant effect on the response.

$$F(DoF_b, DoF_w) = \frac{SS_b / DoF_b}{SS_w / DoF_w} \quad \text{EQ. 4.31}$$

In a similar manner we can calculate the sums of squares and degrees of freedom for different parameters interaction, compute the F -ratio and determine the p -values. Each treatment need to have the same sample size, in this case the design is said to be balanced. In this work we consider the combination of different factor levels. For example, if X_1, X_2, X_3 and Y_1, Y_2 and Y_3 are the different levels of a 2^3 factorial design, the treatments are: $X_1Y_1, X_1Y_2, X_1Y_3, X_2Y_1, \dots$. Thus it is possible to identify higher order interactions for multifactorial designs; this analysis was adopted in Chapter 8. Further information is available in [228]. ANOVA analyses were performed using the software Design-Expert® Version 8 [229].

5. Analysis of MK-based GP formulations

5.1. Formulation in Metakaolin-based GP

5.1.1. Constraints in the GP formulations

The geopolymer can be expressed as in EQ. 5.1 below, where X, Y, Z and W are respectively the total moles of alkali, alumina, silica and water. Since most GPs are 2-parts GPs (i.e. solid + solution), both the solid precursor SP (such as metakaolin) and the activating solution (AS) contribute to the final molar composition. Thus the geopolymer formula can be obtained by adding the contributions of solid precursor SP and activating solution AS as follows: $X_{GP}=X_{SP}+X_{AS}$; $Y_{GP}=Y_{SP}+Y_{AS}$; $Z_{GP}=Z_{SP}+Z_{AS}$ and $W_{GP}=W_{SP}+W_{AS}$. The GP formula is usually normalized over the total number of alkaline moles, EQ. 5.4, so that the first term cancels to 1. Henceforth lowercase symbols refer to normalized quantities, i.e. $x_{SP}=X_{SP}/(X_{AS}+X_{SP})=1$. Geopolymers physical parameters, which are significant for their rheological and microstructural properties, can be calculated accounting for the molecular weight of those oxides, EQ. 5.5 and EQ. 5.6.

$$\text{GP:} \quad X_{GP} \text{ M}_2\text{O} \cdot Y_{GP} \text{ Al}_2\text{O}_3 \cdot Z_{GP} \text{ SiO}_2 \cdot W_{GP} \text{ H}_2\text{O} \quad \text{EQ. 5.1}$$

$$\text{SP:} \quad X_{SP} \text{ M}_2\text{O} \cdot Y_{SP} \text{ Al}_2\text{O}_3 \cdot Z_{SP} \text{ SiO}_2 \cdot W_{SP} \text{ H}_2\text{O} \quad \text{EQ. 5.2}$$

$$\text{AS:} \quad X_{AS} \text{ M}_2\text{O} \cdot Y_{AS} \text{ Al}_2\text{O}_3 \cdot Z_{AS} \text{ SiO}_2 \cdot W_{AS} \text{ H}_2\text{O} \quad \text{EQ. 5.3}$$

$$\text{GP:} \quad \frac{X_{SP}+X_{AS}}{X_{SP}+X_{AS}} \text{ M}_2\text{O} \cdot \frac{Y_{SP} + Y_{AS}}{X_{SP}+X_{AS}} \text{ Al}_2\text{O}_3 \cdot \frac{Z_{SP} + Z_{AS}}{X_{SP}+X_{AS}} \text{ SiO}_2 \cdot \frac{W_{SP} + W_{AS}}{X_{SP}+X_{AS}} \text{ H}_2\text{O} \quad \text{EQ. 5.4}$$

$$\frac{H_2O}{total_solid} = \frac{(W_{SP} + W_{AS}) * 18.08}{(X_{SP} + X_{AS}) * 61.98 + (Y_{SP} + Y_{AS}) * 101.96 + (Z_{SP} + Z_{AS}) * 60.98} \quad \text{EQ. 5.5}$$

$$\frac{m_{AS}}{m_{SP}} = \frac{X_{AS} * 61.98 + Y_{AS} * 101.96 + Z_{AS} 60.98 + W_{AS} * 18.02}{X_{SP} * 61.98 + Y_{SP} * 101.96 + Z_{SP} 60.98 + W_{SP} * 18.02} \quad \text{EQ. 5.6}$$

The ratio “ $H_2O/total_solid$ ” is important because it controls the porosity of the set binder: the more water is added, the higher the porosity and therefore the lower the compressive strength of set GP.

The GP mix rheology is controlled by the ratio of the activating solution content to the solid precursor content, m_{AS}/m_{SP} , as defined in EQ. 75. In fact the relative viscosity of GP mix, $\eta_r =$

η_{GP}/η_{AS} is a function of the volume fraction $\Phi = \frac{m_{SP}/\rho_{SP}}{m_{SP}/\rho_{SP} + m_{AS}/\rho_{AS}} = \frac{\frac{m_{SP}}{m_{AS}} \cdot \frac{\rho_{AS}}{\rho_{SP}}}{\frac{m_{SP}}{m_{AS}} \cdot \frac{\rho_{AS}}{\rho_{SP}} + 1}$ according

with the Dougherty-Krieger equation [230]:

$$\eta_r = \left[1 - \left(\frac{\Phi}{\Phi_p} \right) \right]^{-[\eta]\Phi_p} \quad EQ. 5.7$$

where Φ is the volume fraction, Φ_p is the maximum packing fraction of the solid precursor, $[\eta]$ [Pa·s] is the intrinsic viscosity [209], ρ_{AS} and ρ_{SP} [g·cm⁻³] are respectively the activating solution and solid precursor densities.

According to EQ. 5.4, EQ. 5.5 and EQ. 5.6 for a fixed total amount of geopolymer there are maximum 7 degrees of freedom (DoF) available to change the GP composition, porosity and viscosity. We can independently fix only as many GP parameters, e.g. Na⁺/H₂O, SiO₂/Na₂O, Si/Al, as there are available degrees of freedom.

Different geopolymer reagents introduce different constraints which can reduce the number of degrees of freedom available. For example, when the solid precursor SP is metakaolin, there are no alkalis or water in SP: $X_{MK}=0$, $W_{MK}=0$ and the DoF decrease to 5. In metakaolin the number of moles of silica are twice the moles of alumina, thus $Z_{MK} = 2Y_{MK}$ and the DoF decrease to 4. Moreover, the activating solution AS usually has no alumina, hence $Y_{AS}=0$ and the DoF decrease to 3. The equations can thus be rewritten for MK-based GPs as follows (WG-GP stands for GP activated with waterglass, NaOH-GP stands for GP activated with NaOH) :

$$\text{WG-GP:} \quad 1 \text{ M}_2\text{O} \cdot y_{MK} \text{ Al}_2\text{O}_3 \cdot (2y_{MK} + z_{AS}) \text{ SiO}_2 \cdot (w_{AS}) \text{ H}_2\text{O} \quad EQ. 5.8$$

$$\text{WG-GP:} \quad \frac{H_2O}{total_solid} = \frac{w_{AS} * 18.08}{x_{AS} * 61.98 + y_{MK} * 101.96 + (2y_{MK} + z_{AS}) * 60.98} \quad EQ. 5.9$$

$$\text{WG-GP:} \quad \frac{\text{activating solution}}{MK} = \frac{x_{AS} * 61.98 + z_{AS} * 101.96 + w_{AS} * 18.08}{y_{MK} * 101.96 + 2y_{MK} * 60.98 + z_{SP}} \quad \text{EQ. 5.10}$$

$$\text{NaOH-GP:} \quad 1 \text{ M}_2\text{O} \cdot y_{MK} \text{ Al}_2\text{O}_3 \cdot (2y_{MK}) \text{ SiO}_2 \cdot (w_{AS}) \text{ H}_2\text{O} \quad \text{EQ. 5.11}$$

$$\text{NaOH-GP:} \quad \frac{\text{H}_2\text{O}}{\text{total_solid}} = \frac{w_{AS} * 18.08}{x_{AS} * 61.98 + y_{MK} * 101.96 + 2y_{MK} * 60.98} \quad \text{EQ. 5.12}$$

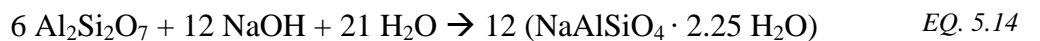
$$\text{NaOH-GP:} \quad \frac{\text{activating solution}}{MK} = \frac{x_{AS} * 61.98 + z_{AS} * 101.96 + w_{AS} * 18.08}{y_{MK} * 101.96 + 2y_{MK} * 60.98 + z_{SP}} \quad \text{EQ. 5.13}$$

For instance, when MK (formula 0-1-2-0, refer to the notation introduced in Section 2.1.1) is mixed with a sodium waterglass with formula 1-0-2-11 with a mass ratio $m_{AS}/m_{SP}=1.7$, it produces a WG-GP with formula 1-1-4-11, $H_2O/\text{total_solid}=0.49$ and $\Phi=0.26$. A NaOH-GP prepared with 11.2M NaOH and $m_{AS}/m_{SP}=1.1$ has formula 1-1-2-10, $H_2O/\text{total_solid}=0.63$ and $\Phi=0.32$.

According to Rahier [71], the optimum stoichiometry of GPs requires $y_{MK}=1$, i.e. Na/Al=1 and if this condition is adopted the DoF are now 3. For a balanced NaOH/MK-based GP only one degree of freedom remains, i.e. w_{AS} , because there is no silica in the activating solution: $z_{AS}=0$. So if we want to decrease the set GP porosity, the viscosity of the mix will inevitably increase and all other ratios will decrease, including H_2O/solid , H_2O/SiO_2 , $H_2O/\text{Al}_2\text{O}_3$, $H_2O/\text{Na}_2\text{O}$. Determining the real contribution of a single factor on the GP properties can therefore become complicated since separating its contribution from the other factors is not always possible.

The increase in strength by decreasing w_{AS} can thus be associated with the decrease in concentration of NaOH (related to the ratio $\text{Na}_2\text{O}/\text{H}_2\text{O}$), or with the increase in the solid content $\text{solid}/\text{H}_2\text{O}$. Fortunately in this case there are plenty of studies on the effects of $\text{H}_2\text{O}/\text{solid}$ on cement paste for OPC, thus the predominant effect of $\text{solid}/\text{H}_2\text{O}$ can be assumed. In particular the compressive strength of OPC concrete follow the Abram's law: $\sigma=A/B^{w/c}$, where σ is the compressive strength, A and B are constants and w/c is the water to cement ratio [17], [231]–[233].

The transformation of metakaolin to zeolite type LTA during GP setting and crystallization can be expressed using the following equation [148]:



According to this equation the concentration of NaOH is 22M (i.e. saturated sodium hydroxide solution) and the mass ratio solution/metakaolin=0.64, a value too small to achieve a homogeneous paste. In conventional zeolite synthesis using MK in dilute condition, the solution/MK can be as low as 2 [148] or as high as 5 [187], while in geopolymer the ratio solution/MK \approx 1-2 is usually adopted [58], depending on the particle size of the MK. As a consequence only part of the water in the final GP is zeolitic (i.e. is part of the zeolite structure) and the water excess increases the material porosity.

For a WG/MK-based GP there are 3 degrees of freedom, or only 2 degrees in case Na/Al=1 is fixed. However the waterglass solution itself is not stable within the entire SiO₂-Na₂O-H₂O compositional diagram and stable commercially available solutions are confined to the Region 9 (refer to Figure 5.1 left). This region roughly ranges from 40% to 68% H₂O, 6% to 26% Na₂O, and 21% to 40% SiO₂. Sodium silicates in Region 9 have also the lowest viscosity (Figure 5.1 right); in particular solutions with Ms=1.8 have the lowest viscosities when compared at constant solid fraction [210]. By decreasing the H₂O content (Region 8) their viscosity η increases dramatically so it is unpractical to prepare and use such solutions. Further water reduction produces semisolids (Region 7), hydrated glasses (Region 5) and glasses (Region 4). Increasing the SiO₂ content produces highly polymerized silica and phase separation: formation of colloidal micelle and gel (region 11). Increasing the Na₂O content also induces phase separation: precipitation of crystalline alkaline silicates (Region 3). The triangular Region 2 is defined by the composition of crystalline NaOH, crystalline anhydrous sodium metasilicate Na₂SiO₃ and crystalline sodium metasilicate nonahydrate Na₂SiO₃·9H₂O. Thus, although an unbalanced WG-MK geopolymer has three degrees of freedom, constraints in the WG can reduce them to only two degrees.

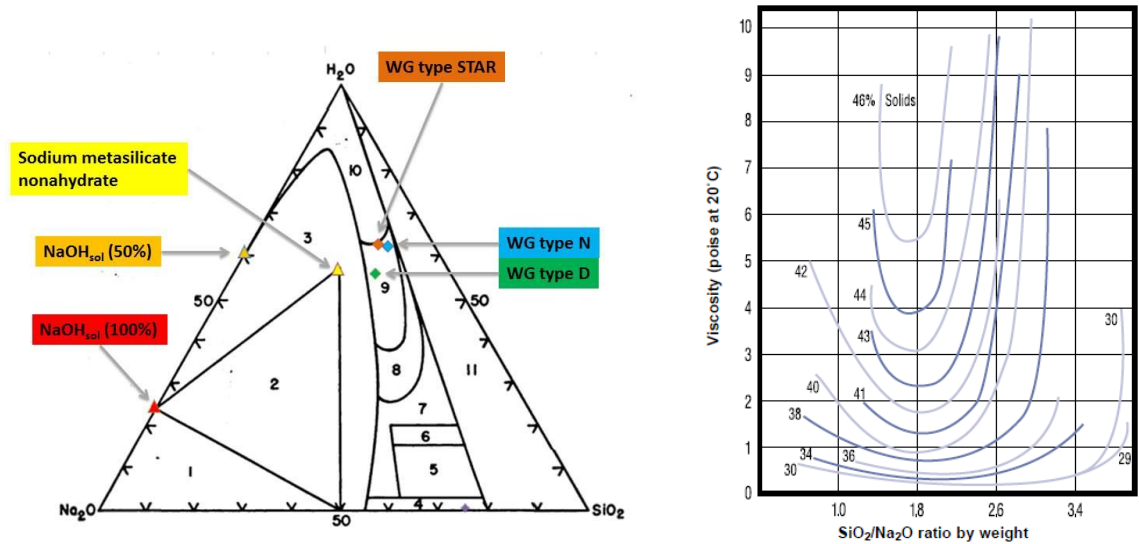


Figure 5.1 Left: Sodium soluble silicate diagram SiO_2 - Na_2O - H_2O (from [101]) with compositions of some commercially available chemicals. Region 9 is the most stable region of soluble silicate solutions and most of commercial solutions are located within this region. Right: Viscosity of sodium silicate as a function of silica modulus at constant solid contents. From [234], adaptation from Vail [101].

The most available and cheapest type of soluble silicate is the type N (close to interface between Region 9 and Region 10), which contains 8.9% of Na_2O , 29.9% of SiO_2 , 62.4% of H_2O ; it has a $\text{Ms}=3.22$ and it is the commercial silicate with the highest silica content. It has a $\text{pH}=11.3$ and $\eta=180$ cP [234]. WG-type N has also relatively high water content and low Na_2O and its formula can be expressed as $1\text{Na}_2\text{O} - 3.22\text{SiO}_2 - 23.53\text{H}_2\text{O}$. A balanced GP prepared with MK and this silicate would have formula 1.00-1.00-5.22-23.53 (refer to the notation introduced in Section 2.1.1), mass ratios water/solid ≈ 0.89 and solution/solid ≈ 3.1 , and $\Phi=0.38$. Such geopolymer paste would be highly diluted and its relatively low $\text{pH}=11$ to 11.5 can hardly dissolve the metakaolin particles. Since metakaolin dissolution consumes water, EQ. 2.18, WG-N slowly turns into a highly viscous gel which further limits the diffusion of reagents, thus increasing the setting time of the GP. Therefore, if the geopolymer mix is not properly sealed during the curing operation, water evaporation may induce a fake setting process due to gelation of WG; in this case the gel is made of sodium silicate and it is not a geopolymeric alkali aluminosilicate.

5.1.2. Soluble silicate MK-based GP

Several studies [58], [62] have been done to identify the GP compositions that maximize materials compressive strength. For example, in Figure 2.5 the compressive strengths of balanced MK-based GP prepared by Duxson [58] showed how the UCS of GPs increases with the ratio Si/Al until the optimum GP composition of 1.00-1.00-3.80.11.00 and Si/Al=1.90. The ratios Na/Al=1 and Si/Al=1.15,1.40,1.65, 1.90 and 2.15 were fixed. The last degree of freedom was chosen to be the ratio Na₂O/H₂O=11, which was kept constant for all compositions. The ratios H₂O/solid and solution/MK varied across the materials, Figure 5.2. In particular, a higher Si/Al resulted in a higher solution/MK (which reduced the paste viscosity and facilitate the degassing operations) and decreased the H₂O/solution, which decreases the overall porosity of the binder. Thus, it is complicated to determine if the increase in strength was due to a difference in gel type or due to an increase in gel volume.

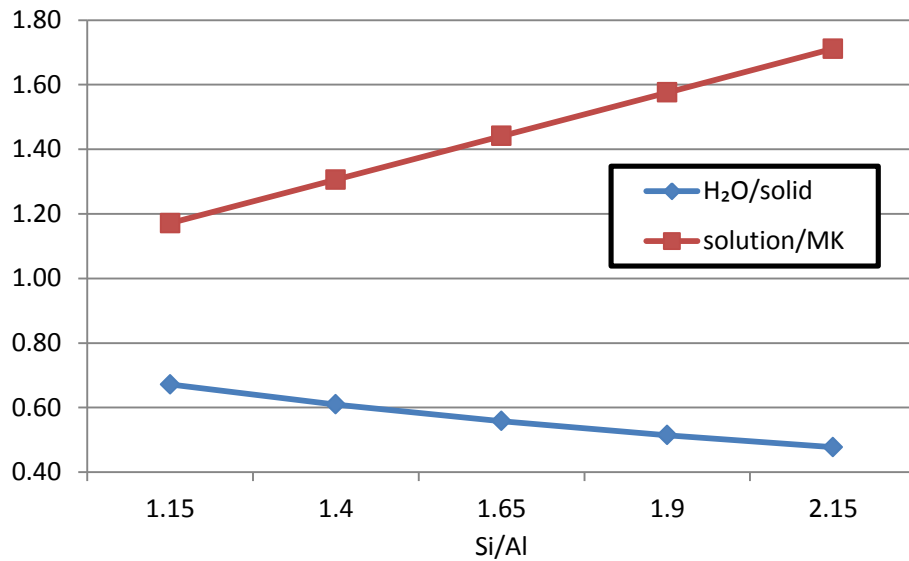


Figure 5.2 Calculated H₂O/solid and solution/MK ratios of GPs with different Si/Al ratio studied by Duxson [58].

Similar considerations are also valid in the research conducted by Rowles [62], where all the parameters of the MK-based GPs were varied but the results were presented in terms of Si/Al and Na/Al ratio, Figure 2.13. We calculated the Pearson correlation coefficients (EQ. 5.15) between each factor and the UCS (Table 5.2) and the most important parameter was

H₂O/solid, followed by Si/Al and solution/MK. Factors Si/Na and Na/Al, on the contrary, had a relatively smaller effect.

$$\rho_{X,Y} = \frac{cov(X,Y)}{\sigma_X \sigma_Y} \quad EQ. 5.15$$

Table 5.1 Measured compressive strengths and calculated GPs ratios (H₂O/solid, Si/Na, solution/solid) extracted from Rowles work on metakaolin-based GPs [62].

		Si:Al							Si:Al				
		1.08	1.50	2.00	2.50	3.00			1.08	1.50	2.00	2.50	3.00
		compressive strength [Mpa]							H ₂ O/solid				
Na:Al	0.52	0.40					Na:Al	0.52	0.85				
	0.71	2.20	6.20					0.71	0.82	0.75			
	1.00	4.40	23.40	51.30				1.00	0.79	0.73	0.67		
	1.29			53.10	64.00			1.29			0.66	0.62	
	1.53		19.80		49.00	2.60		1.53		0.69		0.61	0.64
	2.00			11.80		19.90		2.00			0.62		0.62
		Si/Na							solution/solid				
Na:Al	0.52	1.92					Na:Al	0.52	1.12				
	0.71	1.41	2.00					0.71	1.18	1.50			
	1.00	1.00	1.42	1.92				1.00	1.29	1.60	1.97		
	1.29			1.49	1.88			1.29			2.08	2.45	
	1.53		0.93		1.58	1.91		1.53		1.79		2.54	3.05
	2.00			0.96		1.46		2.00			2.33		3.22

Table 5.2 Pearson correlation coefficient obtained from Rowles [62].

Pearson correlation coefficient (with the UCS)				
Si/Na	H ₂ O/solid	Na/Al	Si/Al	Solution/MK
0.21	-0.61	0.21	0.41	0.34

Unfortunately no H_2O /solid iso-lines are available in the literature for GP formulations, so it is not possible to separate the contribution of water content from the Si/Al. Therefore we addressed this problem analytically and experimentally in the following Section.

5.2. Effects of Si/Al on the GP

5.2.1. Optimum H₂O/solid for NaOH/MK-based GP

WG-based GPs benefit from the dissolved silica in the activating solutions and it is possible to obtain a small solids volume fraction Φ and low GP viscosity η_{GP} even when the total solids content is relatively high compared with NaOH-based GP, Figure 5.2. At constant H₂O/solid, NaOH-based GPs have lower solution/MK ratios which results in more viscous slurries. In order to compare GP with different Si/Al but similar H₂O/solid, the latter needed to be optimized to produce a flowable NaOH-based GP with Si/Al=1.

Three different GPs were prepared with Na/Al=1, Si/Al=1 and different solution/MK following the procedure presented in Section 4.1.2, and cured the material at 25, 40 and 55°C for 20 hours. The best composition was selected based on visual observation of the slurry rheological response (ability to compact the paste using a vibration table) and by SEM analyses of the set GPs (Figure 5.3): mass ratio between activation solution and MK of 1.1 and mass ratio H₂O/solid=0.64. Lower m_{AS}/m_{SP} values resulted in a viscous paste which cannot be successfully degassed: the entrapped air created 200-300 μ m pores which can reduce the compressive strength (UCS). Higher m_{AS}/m_{SP} values increased the percentage of small pores originated from the extra water and could also reduce the UCS.

Table 5.3 NaOH/MK-based GPs prepared to optimize the activating solution/MK mass ratio (m_{AS}/m_{SP}) and H₂O/solid ratio. Φ is the volume fraction of solids.

m_{AS}/m_{SP}	H ₂ O/solid	NaOH concentration	GP formula	Φ
1.00	0.56	12.50	1.0-1.0-2.0-8.9	0.35
1.10	0.64	11.06	1.0-1.0-2.0-10.1	0.32
1.20	0.72	9.90	1.0-1.0-2.0-11.4	0.30

Higher magnification SEM images reveled the cubic crystals of zeolite type A (also called zeolite LTA) and octahedral crystals of zeolite type X (also called faujasite-X), according to XRD data presented in Section 6.2.1.3. Geopolymers with higher H₂O/solid appear more

crystalline and the crystals were larger. The water excess seemed to facilitate the formation of zeolite and this can be due to two reasons: 1) the crystallization is a solution-based transformation that requires H_2O to occur; 2) the crystallization of the amorphous gel is associated with a volume change. The effect of H_2O /solid are further investigated in details in Chapter 8.

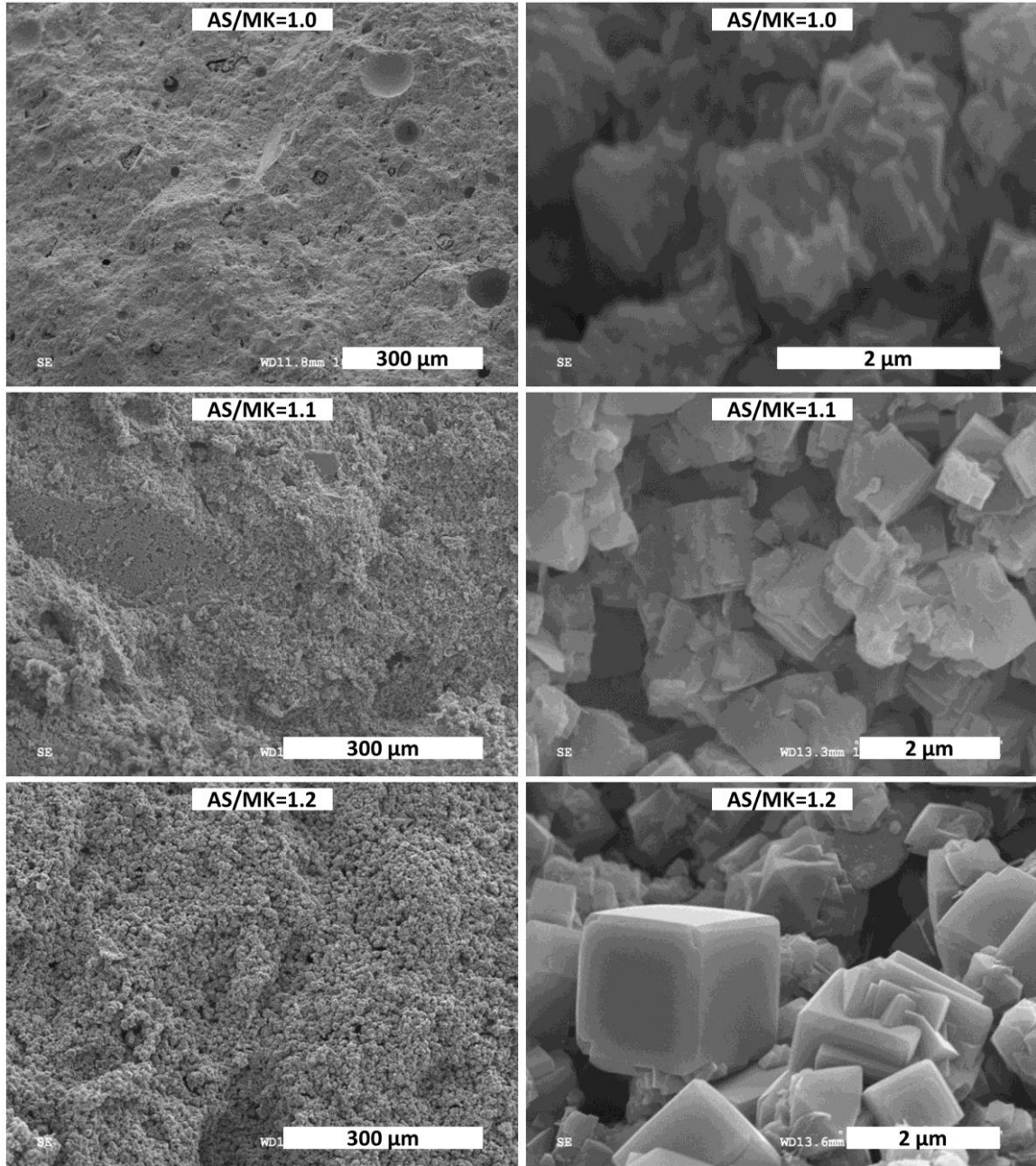


Figure 5.3 SEM images of NaOH/MK-based GP with different activating solution/MK ratio (m_{AS}/m_{MK}) cured at 55°C for 20 hours .

The setting times of these GPs were determined using the Vicat needle according to ASTM standards [217] and the results are shown in Table 5.4. Additional water delayed the setting time especially at room temperature. Curing at mild temperatures reduced the setting time and the effect of additional water became negligible.

Table 5.4 Setting times of geopolymer pastes with different water content at 3 different temperatures. Error percentage is approximately 20%.

Geopolymer setting time [minutes]			
GP formula	Curing temperature		
	25°C	40°C	55°C
1-1-2-8.9	130	40	30
1-1-2-10.1	200	50	30
1-1-2-11.4	280	70	40

5.2.2. Sample preparation and slurry properties

A different set of three MK-based geopolymers was prepared with constant $H_2O/solid=0.634$, $Na/Al=1$ and Si/Al respectively 1, 1.34 and 1.68, in order to determine the effects of Si/Al at constant $H_2O/solid$. The activating solutions were prepared starting from sodium silicate type N, sodium hydroxide pellets and water. After the pellets were fully dissolved in water, WG-type N was slowly added and the activating solutions were mixed at 40°C for 2 days with a magnetic stirrer. Samples were prepared following the procedure described in Section 4.1.2 and cured at 40°C for 20 hours. The same curing condition used by Duxson [58] were adopted to directly compare the unconfined compressive strength UCS of the set GPs, presented later in Figure 5.8, Section 5.2.4. The GPs formulations and other details can be found in Table 5.5 below.

Table 5.5 Geopolymer compositions, slurry flow (determined using a flow table) and activating solution properties. AS: Activating solution.

Geopolymer					Activating solution	
Si/Al	H ₂ O/solid	m_{AS}/m_{MK}	GP formula	flow [%]	η_{AS} [cP]	ρ_{AS} [g/cm ³]
1	0.634	1.09	1.0-1.0-2.0-10.0	63±2	41±2	1.35±2
1.35	0.634	1.39	1.0-1.0-2.7-11.5	113±2	1200±6	1.42±1
1.68	0.634	1.69	1.0-1.0-3.4-12.9	>256	73±1	1.46±2

Higher Si/Al values resulted in higher mass ratio between the activating solution and the MK m_{AS}/m_{MK} , and lower viscosity of the GPs. The flowability of the GPs was determined using a flow table, Figure 5.4, according to ASTM-C1437 [216] and the results can be found in Table 5.5. The consistency of GP with Si/Al=1 was previously optimized to be comparable with OPC based binders. GP with Si/Al=1.35 was twice as flowable as the previous sample, while GP with Si/Al=1.68 was a liquid slurry with a flow that exceeded the limits of the apparatus.



Figure 5.4 Flow table apparatus and flow of the GP with Si/Al=1.35.

5.2.3. Activating solutions

The three activating solutions were named after the Si/Al ratios of the geopolymers they were intended for, Figure 5.5. The solution for GP with Si/Al=1 was an 11.2 molar hydroxide solution. The Si/Al=1.35 activating solution was a soluble silicate with Ms=0.7 and 66.5 wt% water content. The Si/Al=1.68 solution was a soluble silicate with Ms=1.36 and 61.9 wt% water content. The viscosities of the activating solutions were determined using a “Brookfield Digital Viscometer, Model: LVDV-E” and their densities using a pycnometer. The activating solution for GP with Si/Al=1.35 was not homogeneous but it was an opaque colloidal dispersion, Figure 5.5. A portion of this solution was centrifuged at 6000 rpm for 20 minutes and the precipitate was directly analyzed by XRD (Figure 5.6).

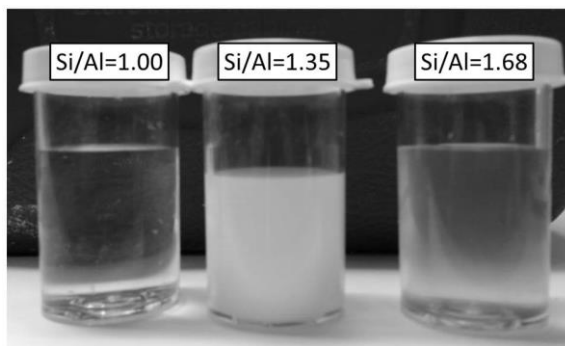


Figure 5.5 Activating solutions intended for the synthesis of GPs with different Si/Al. Sample in the middle is a colloidal dispersion.

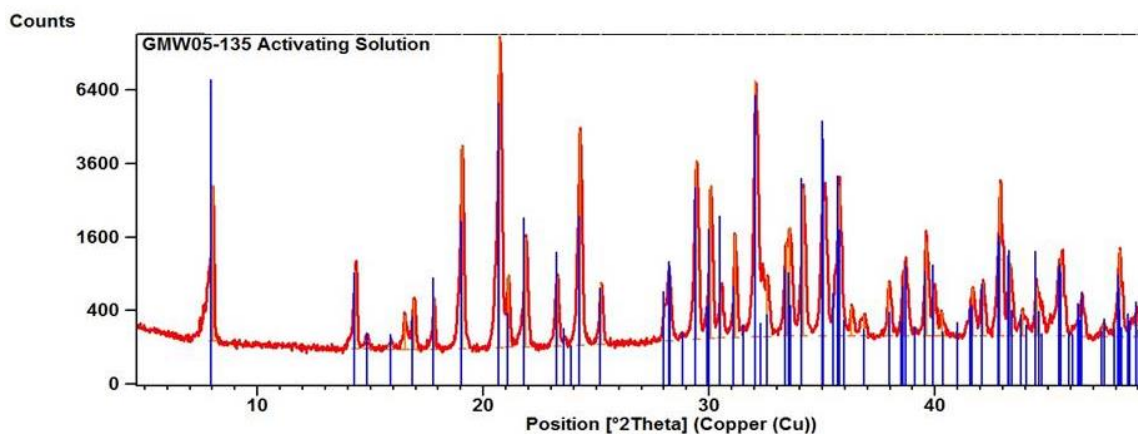


Figure 5.6 In red: Measured X-rays diffractograms of the gel precipitate by centrifuging the activating solution intended for GP with Si/Al=1.35. In blue: Peak position of sodium silicate hexa-hydrate $\text{Na}_2\text{SiO}_3 \cdot (\text{H}_2\text{O})_6$, ICSD code 9171.

The colloidal precipitate was found to be crystalline sodium metasilicate hexa-hydrate. All sodium metasilicate hydrates $\text{Na}_2\text{O} \cdot \text{SiO}_2 \cdot n\text{H}_2\text{O}$ ($n = 9, 8, 6, 5$) contain discrete silica tetrahedra monomers $[\text{SiO}_2(\text{OH})_2]^{2-}$ and sodium in octahedral coordination [109], [235]–[237]. Depending on the hydration degree, the sodium atoms can form sheet with octahedrals alternatively sharing faces and corners (for $n=6$ [236]) or helical chains of corner sharing octahedrals (for $n=9$ [235]). Instead, anhydrous sodium metasilicate Na_2SiO_3 is composed of chains of corner sharing tetrahedral $(\text{SiO}_3)^{2-}$ [109]; this crystal is not expected to be formed in the solution but it can be used as an extra source of silica for certain just-add-water geopolymers. The hydration degree of the sodium metasilicate has an effect on the $\text{Na}_2\text{O} \cdot \text{SiO}_2 \cdot n\text{H}_2\text{O}$ structure and solubility and probably on its interaction with the liquid phase of the activating solution and the monomers and oligomers generated by the MK dissolution. Provis [238] found that the partial substitution of sodium with potassium can suppress or delay the crystallization of the metasilicate.

The location in the SiO_2 - Na_2O - H_2O diagram of the activating solution adopted in this study can be found in Figure 5.7. The AS for GP with $\text{Si}/\text{Al}=1.35$ was in fact in the metastable Region 3, as described in Figure 5.1 (left). The AS used by Duxson [58] are also represented in the same diagram and some of them probably contained colloidal sodium metasilicate hydrates.

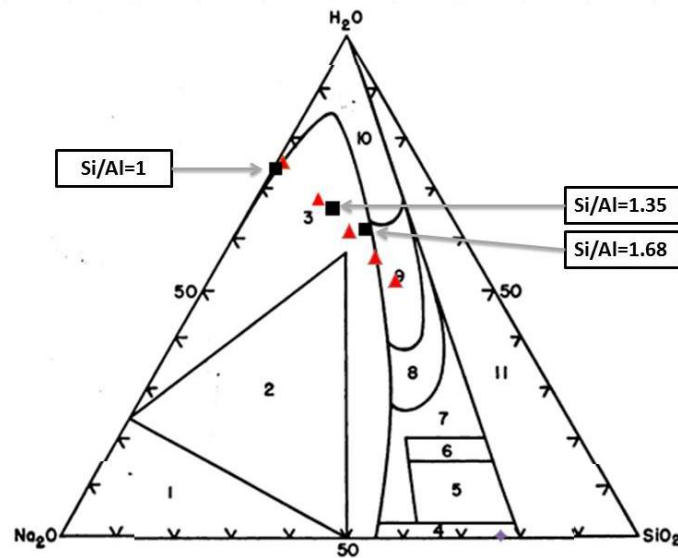


Figure 5.7 Na_2O - SiO_2 - H_2O diagram for the GP activating solution. Red triangles: activating solutions used by Duxson [58]. Black squares: Activating solution adopted in this current work.

5.2.4. Sample curing and unconfined compressive strength (UCS)

Nine samples for each composition were tested for UCS after 20 hours of curing, in order to obtain a good statistic. The samples cured at 40°C set within 1 to 3 hours, as tested according to ASTM [217], nonetheless it is still not certain if the GPs had fully reacted and achieved their maximum strength after 20 hours of curing. For this reason additional nine samples for each composition were autoclaved for 6 hours at 125°C in autogenous pressure (i.e. 30 psi) to produce fully cured GP. A similar procedure to obtained fully-reacted GP was used by Kriven [79]. The unconfined compressive strength UCS values are shown in Figure 5.8.

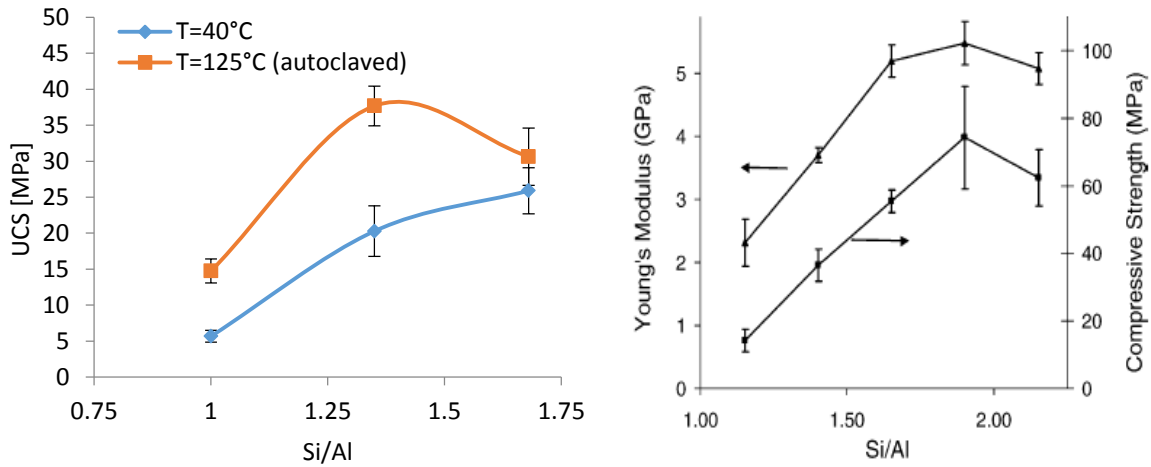


Figure 5.8 UCS of GP with different Si/Al. Left: constant H₂O/solid GP prepared in this work. Right: constant SiO₂/Na₂O prepared by Duxson [58].

T-tests were performed to compare both the effect of Si/Al and the effect of autoclaving. The null-hypotheses were rejected for all the tests. It is obvious that autoclaving had a larger role at low Si/Al. In particular the accelerated curing autoclave increased the UCS of GPs with Si/Al=1.0, 1.35 and 1.68 respectively by 160%, 86% and 18% (as compared to 40°C for 20 hours non-autoclave curing). This suggests that curing beyond 20 hours at 40°C is needed to obtain the maximum achievable strength. The strongest samples in compression after normal curing was the GP with Si/Al=1.68, but the strongest fully-cured autoclaved GP had the largest UCS=38 MPa at Si/Al=1.35.

In his work Duxson obtained higher UCS values for samples with Si/Al>1; the reason lies in lower H₂O/solid used in that work [58]. The difference he found between GP with Si/Al=1.4

and 1.65 was more pronounced than what observed in this study. Thus the Si/Al ratio appears to play an important role especially at low Si/Al, but at higher ratios the increase in compressive strength observed by previous studies [58], [62] was due to a lower water content in the GPs.

5.2.5. Structural characterization

The fracture surfaces of the GPs were coated with carbon and observed in high-vacuum SEM using secondary electrons. The microstructures of GPs cured at 40°C for 20 hours (Figure 5.9) and fully-reacted GP (Figure 5.10) were studied to better understand the mechanical properties of the GPs.

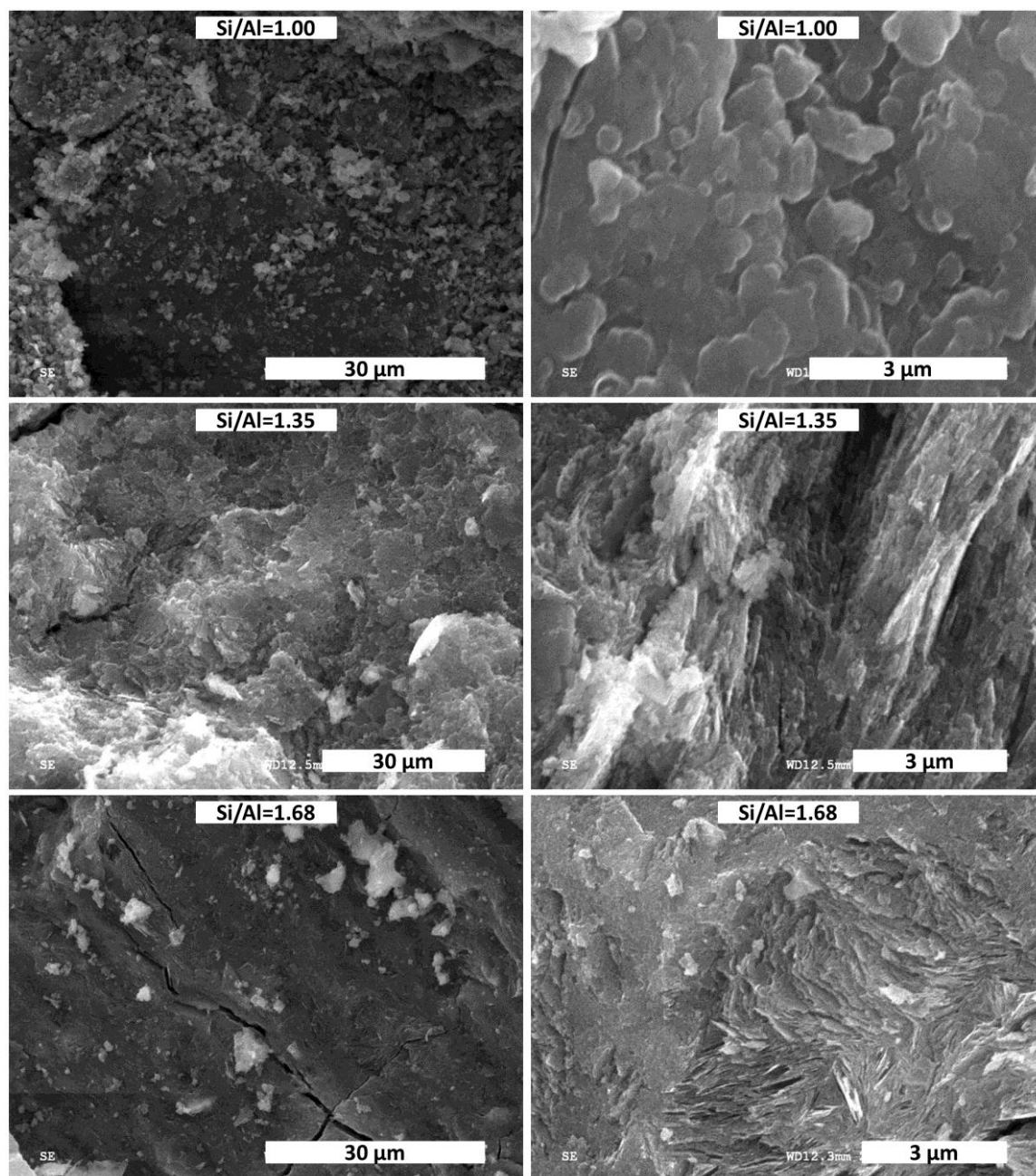


Figure 5.9 SE-SEM images of the fracture surfaces of the three GPs cured at 40°C for 20 hours at different magnification.

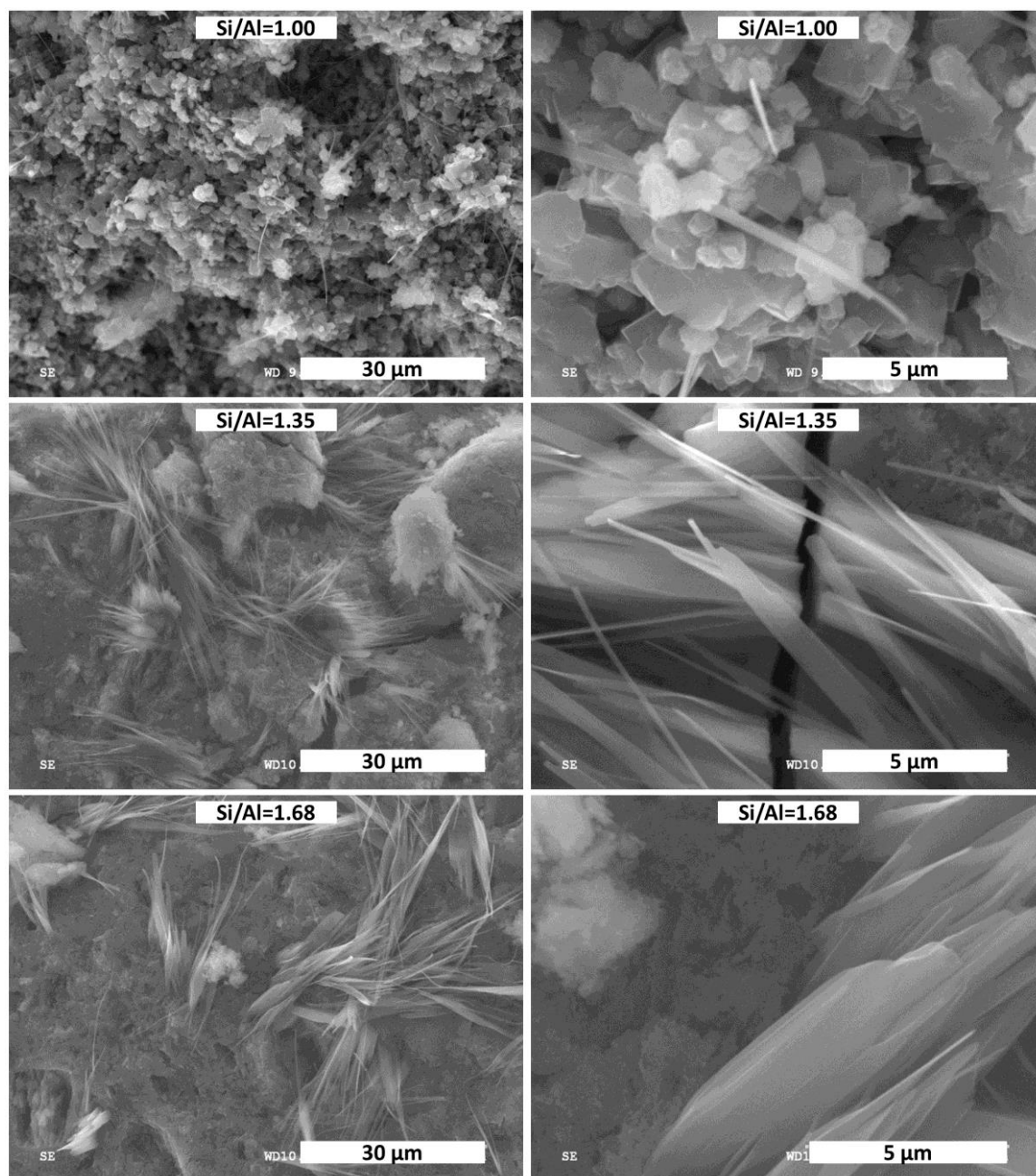


Figure 5.10 SE-SEM images of the fracture surfaces of the three GPs cured in autoclave at different magnification.

All samples cured at 40°C (Figure 5.9) had a dense microstructure; conversely the samples with smaller Si/Al prepared by Duxson [58] were more porous due to the higher H₂O/solid ratio. GP with Si/Al=1.00 was a dense binder made of coagulated colloidal particles of micron and submicron size. Geopolymer gels with Si/Al=1.35 and 1.68 were made of smaller units with submicron size that bound the unreacted MK particles together. In

particular the GP with the highest UCS=26MPa and Si/Al=1.68 had the largest amount of unreacted MK. It is thus possible that the higher UCS values were also related to the composite nature of GPs with high Si/Al ratio, in which the unreacted MK particles deflected the crack propagating through the gel.

When cured in autoclave the fully reacted GP (Figure 5.10) underwent prominent transformations. Samples with Si/Al=1 formed cubic crystals which correspond to zeolite type A. This observation was confirmed by XRD, Figure 5.11. The crystallization was probably associated with a change in volume since the GP appeared more porous as compared to one cured at 40°C. The strength of this GP increased by 160%: although the sample was more porous, the intergrowth of crystals provides a better binding than the weak interaction between the amorphous lumps observed for samples cured at 40°C. Moreover some long fibrous structures of 200 nm diameter were also detected; these fibers may also help the GP to redistribute the stress when cracks are propagating, effectively increasing its fracture toughness.

The amount of fibrous structures increased with the increase of Si/Al; however their aspect ratios decreased with Si/Al ratio. Fully cured GP with Si/Al=1.35 had fibres with 0.5-1.0µm diameter, while GP with Si/Al=1.68 had both fibrous and tabular structures. These fibrous and tabular structures have not been observed for MK-based GP, but they were detected in NaOH/fly-ash based GP cured above 40°C [239]. The nature of these amorphous fibers is unknown, and their lack of crystallinity complicates the identification (Figure 5.11). The lack of crystallinity excluded the possibility that they were made of thermonatrite $\text{Na}_2\text{CO}_3 \cdot \text{H}_2\text{O}$, which is known to form acicular crystals, thus they were probably aluminosilicate fibers. Detailed analysis of the fractured surface indicated a strong bond between the fibers and the geopolymer gel, as no fibers pull-out was observed and the crack did not change direction when reaching the fibers. Due to the heterogeneity of the GPs it was hard to assess if all the MK was dissolved, nonetheless the autoclaved curing undoubtedly decreased the amount of unreacted MK.

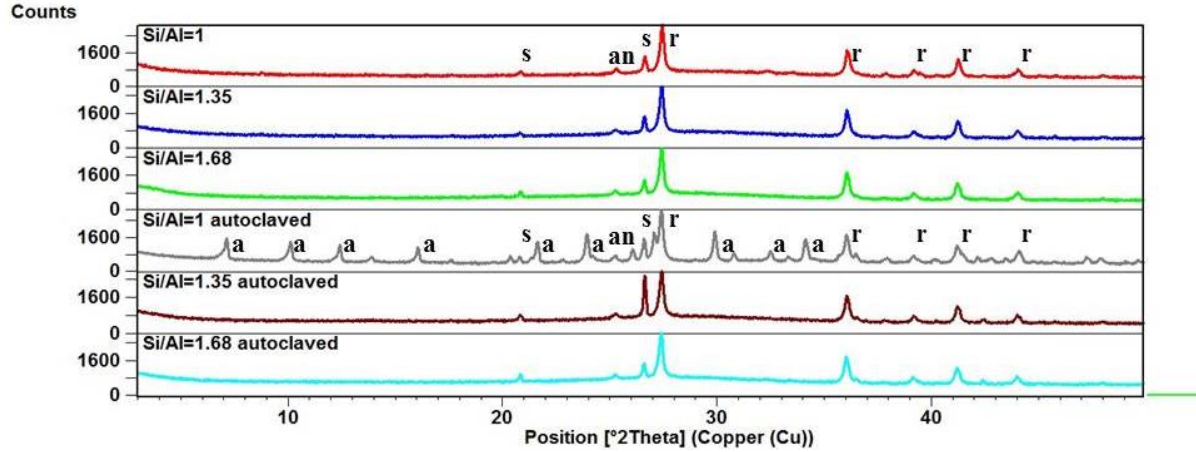


Figure 5.11 XRD patterns of GPs with different Si/Al cured at 40°C for 20hours with and without autoclave treatment rutile internal standard was used for all samples. s=silica (ICSD 90145, quartz), an=anatase (ICSD 63711), r=rutile (ICSD 34372), a=zeolite type A (ICSD 24901).

As previously mentioned, all the GPs cured at 40°C for 20 hours were amorphous, and crystalline zeolite type A was detected only for the autoclaved GP with Si/Al=1. These findings are in agreement with the research conducted by Yan [59] on geopolymers obtained by sol-gel route and cured at different conditions. After curing at 60°C for 24 hours geopolymers with Si/Al=1.0 and Si/Al=1.5 were still amorphous; additional curing at 90°C for 6 hours induced partial crystallization only for the GP with Si/Al=1. The sample with Si/Al=1.5 crystallized only after additional curing at 180°C for 6 hours. In the current study the autoclaved samples were subjected to T=125°C which was still too low to induce crystallization in GP with high Si/Al ratios. Independently from the nature of the binder, it is commonly observed [240] that strength is enhanced by amorphous rather than crystalline structures. It is believed that the crystal interlocking is rigid and it cannot accommodate residual stresses [240]. On the contrary amorphous binders are more flexible, thus they can sustain residual stresses and better conform to aggregate roughness to improve adhesion.

5.3. Summary

In this Chapter the composition of MK-based GPs was investigated in terms of the number of degrees of freedom of the process parameters, and the resulting mechanical properties, microstructure and structure. Balanced NaOH/MK-based GP possess only one degree of freedom so compromises need to be made between NaOH concentration, slurry viscosity and

GP porosity. On the other hand, balanced WG/MK-based GPs have more degrees of freedom and the soluble silica in the activating solution allows the preparation of flowable pastes with low water content which produces GPs with relatively low porosity. WG/MK-based GPs with intermediate values of $\text{Si}/\text{Al} \approx 1.35$ had a heterogeneous activating solution containing colloidal particles of sodium metasilicate hydrate which can act as heterogeneous nucleation centers. Thus, any predictive model of geopolymerization needs to properly describe the $\text{Na}_2\text{O} \cdot \text{SiO}_2 \cdot n\text{H}_2\text{O}$ crystals in solution and their role in the GP reactions.

By comparing the UCS of GPs processed in this work with the values found in the literature it is possible to conclude that both $\text{H}_2\text{O}/\text{solid}$ and Si/Al have an effect on strength. Soluble silicates in the activating solution increase the intrinsic strength of gel at $1 < \text{Si}/\text{Al} < 1.35$ and also the gel content. At $\text{Si}/\text{Al} > 1.35$ the increase in strength is mostly due to an increase of $\text{solid}/\text{H}_2\text{O}$ and the gel has comparable properties. New GP amorphous fibrous morphologies were found when samples were cured in autoclave.

6. Seeded geopolymers

6.1. Seeds selection and processing

6.1.1. Seeded geopolymers

When dealing with heterogeneous reactions, seeding is a common practice used to increase the reaction kinetics and also to control the reaction products, as previously mentioned in Section 2.2.4.6. While several studies have already been done on the seeded GP system, however none of them focused on pure MK-based GPs [163], [165], [166], [177]. Additional original contribution of the present work is the selection and processing of seeds, including zeolite seeds.

When GP based on fly ash and 6M NaOH was seeded with Al_2O_3 [177] the silicate monomers quickly reacted with the liberated Al in solution, reducing the surface passivation and allowing more rapid fly ash dissolution. The faster consumption of monomers by the growing gel also decreased their concentration in the solution and enhanced the total yield of the reaction. In a different study on geothermal silica and sodium aluminate geopolymers the effect of Al_2O_3 , ZnO and ZrO_2 seeds was investigated [166]. It was claimed that the seeds had multiple effects: induced nucleation of geopolymer gel in the initially Al-rich reaction mixture; prevented surface passivation of the silica particles due to alumina adsorption on their surfaces; and enhanced the dissolution of silica. Different results were however reported in [163], where ZrO_2 seeds did not improve the reaction kinetics and did not induce zeolite crystallization in a GP based on MK, fly ash, NaAlO_2 and soluble silicates. The effect of amorphous nanosilica and nano α -alumina on the compressive strength of GPs based on rice husk ash, fly ash, sodium hydroxide and waterglass was investigated at different temperatures [165]. Silica seeds had a positive influence on the mechanical strength, apparently by acting as heterogeneous nuclei and accelerator and promoter of the geopolymerization reaction. On the other hand alumina seeds did not increase the compressive strength of the GP. The silica and alumina were sometimes considered as reagents and sometimes as seeds in research literature, thus complicating the understanding of the nucleating and growth of the geopolymer gel. On one hand they changed the solution

chemistry and on the other they just provided nucleation sites for the growth and crystallization of the geopolymer.

In this work we undertook the task to explore the effects of seeds on MK-based GP in a way not reported before. To the best of our knowledge none has ever investigate the role of seeding on only-metakaolin based GP, zeolites were never included in GP seeding experiments and the effects of mechanical activation on the zeolite seeds has never been inspected. Two different types of seeds were selected: 1) oxides already studied in other GP types; and 2) different zeolite seeds. As the final crystalline products of the geopolymer are zeolites, such as faujasite, the use of these mineral phases was a natural choice. It is however common both in zeolite synthesis and in Portland cement hydration to use seeds that resemble the final reaction products [154], [159], [160], [162]. Zeolite phases that are not commonly found in GP were also selected in this part of our research (mordenite) or synthesized (zeolite type P), to determine if seeds could affect the nucleation and growth of different products in set GP.

6.1.2. Oxide seed selection

Six different types of particles were used to seed the geopolymers in this work, including: (1) SiO_2 [U.S. Silica, United States], (2) $\alpha\text{-Al}_2\text{O}_3$ [Inframat Advanced Materials, United States], (3) ZrO_2 [Lida, China]. Three different zeolites used as seeds were purchased from Alfa Aesar, and included: (4) mordenite ($\text{Si}/\text{Al}=6.5$ and $\text{Na}/\text{Al}=0.92$), (5) sodium faujasite type Y ($\text{Si}/\text{Al}=2.5$ and $\text{Na}/\text{Al}=0.96$) and (6) hydrogen faujasite type Y ($\text{Si}/\text{Al}=2.5$ and $\text{Na}/\text{Al}=0.21$). More information on these seed materials is available in Table 4.1. All the seeds had isoelectric point (IEP) below 12, thus it is expected that the surface of the seed is negatively charged when dispersed in the highly alkaline geopolymer activating solutions [241]. Nonetheless high ionic strength can change the IEP. In some cases there is no IEP and the particles are positively charged, but their behaviour is highly dependent on the nature of the particle and solute [242]. SEM images of the seeds are shown in Figure 6.1 and Figure 6.5. Since most oxides had agglomerates, different deagglomeration methods were used in this work: mechanochemical activation (Section 6.1.2.1), dispersion in the activating solution (Chapter 7) or alternative method (Section 6.1.3.2).

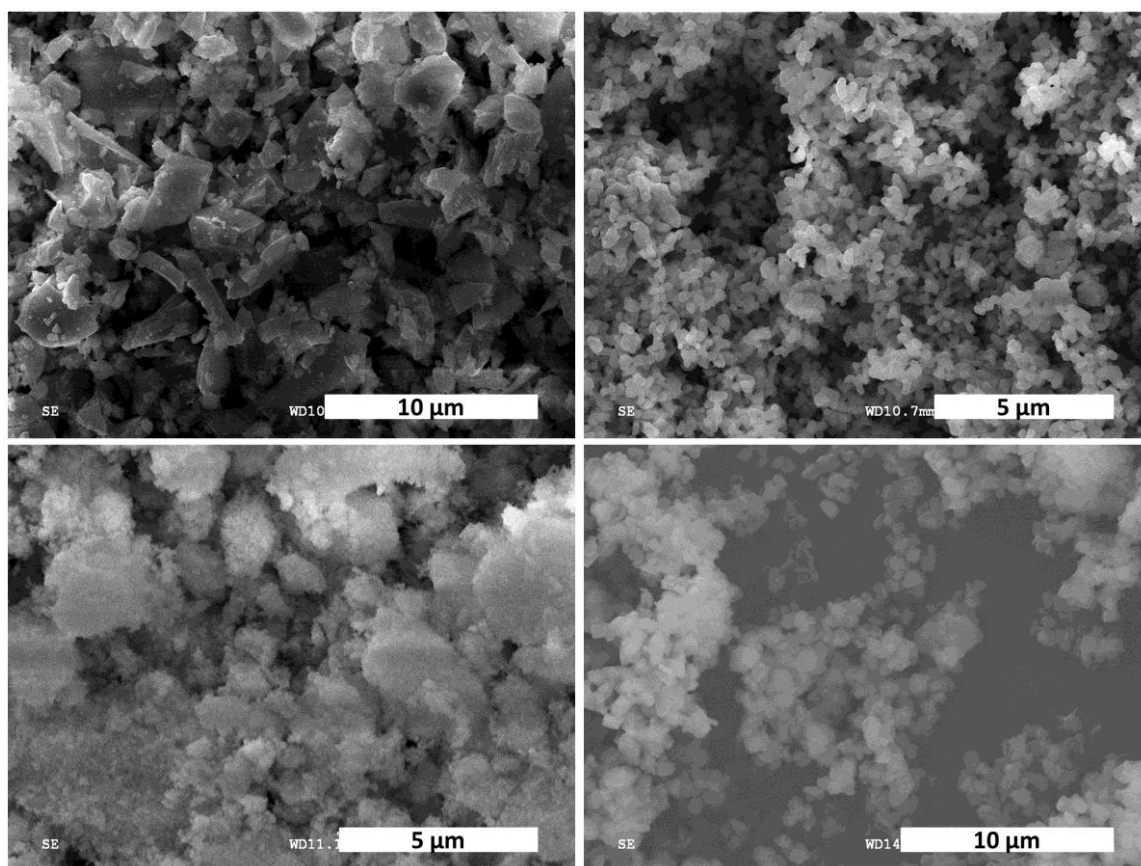


Figure 6.1 SE-SEM images of the silica (top left), alumina (top right), zirconia (bottom left) and Faujasite-H (bottom right) seeds used in this study.

XRD and FTIR analyses were performed on each seed and no detectable impurities were found. Mordenite and faujasite had distinct X-ray diffraction patterns characterized by peaks with different positions. On the contrary, faujasite-H and faujasite-Na shared the same XRD peak positions but had slightly different peak intensity ratios. These similarities limit the ability of the XRD to distinguish the two phases and justify the adoption of a single faujasite phase to describe these zeolite crystals in geopolymer in Chapter 8. Silica seeds were made of quartz (ICSD 90145), alumina was mostly α -alumina with small impurities of γ -alumina (ICSD 60419 and ICSD 82504), while zirconia seeds were pure tetragonal phase (ICSD 70014).

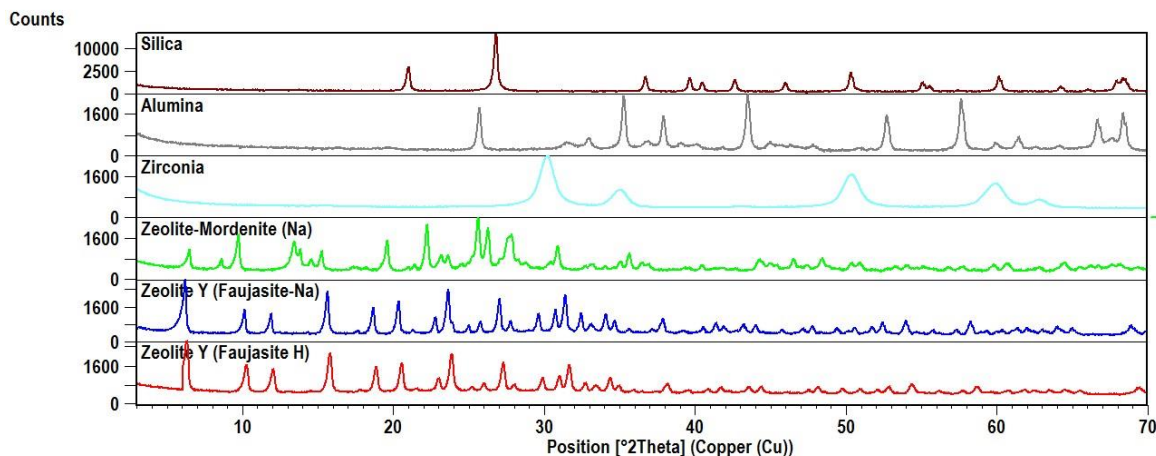


Figure 6.2 XRD of the different seeds: silica, alumina, zirconia, mordenite-Na, faujasite-H and faujasite-Na.

The substitution of Na ions with H ions could instead be detected with ATR-FTIR analysis. The main asymmetric stretching band around 1000cm^{-1} is usually associated with the Si/Al ratio, but in Figure 6.3 it is evident how the faujasite-Na peak was located at 975cm^{-1} . This observation confirmed the dependence of the peak position on charge balancing cation, and not only on the Si/Al ratio and gel connectivity, i.e. bridging or non-bridging oxygens [243].

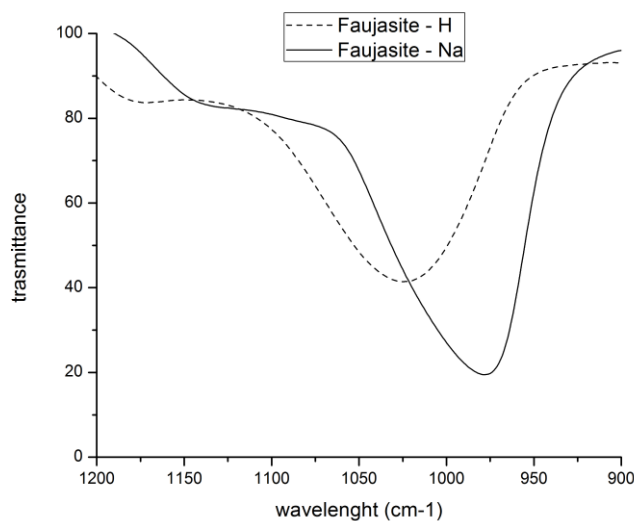


Figure 6.3 ATR-FTIR peaks for two pure crystalline faujasite type-Y, one in its hydrogen form and the other in its sodium form. Note the shoulder at 1100 cm^{-1} which overlaps with the metakaolin peaks, Figure 4.2. Note also the peak shift due to the different cations, from 976 cm^{-1} to 1023 cm^{-1} when sodium is substituted by hydrogen.

6.1.2.1. Mechanochemical activation of zeolites

According with IUPAC [244] a mechanochemical reaction is a “*chemical reaction that is induced by mechanical energy*”. It is known that high energy milling results in the partial collapse of the zeolite structure, amorphization and reduction of the Bronsted acid sites [245]. Also, the kinetics of zeolite crystallization can be accelerated when zeolite seeds were milled [246]. Mechanochemical activation was performed of the three different zeolite seeds used in this study, i.e. mordenite, faujasite-Na and faujasite-H. The effect of the activation in term of increase surface area and modification of the surface site was investigated in Section 6.2.

The zeolites underwent high intensity ball milling using a “Spex 8000 mixer mill”. The grinding media consisted of 3 mm zirconia balls, a ratio ball/powder of 50 and a milling time of 15 minutes were adopted since longer milling time resulted in amorphization of the material. The effects were studied using a Mastersizer 2000 laser diffraction particle size analyzer, FTIR, XRD and SEM. The particle size distributions presented in Figure 6.4 show how the milling procedure increased the fraction of submicron particles, as also revealed by SEM analysis, Figure 6.5. The particle dimensions measured by laser scattering were larger than the sizes observed by SEM due to the instrument limit to detect submicron sizes and to the persistence of aggregates despite the use of TritonTM X-100 surfactant and sodium hexametaphosphate defloculant.

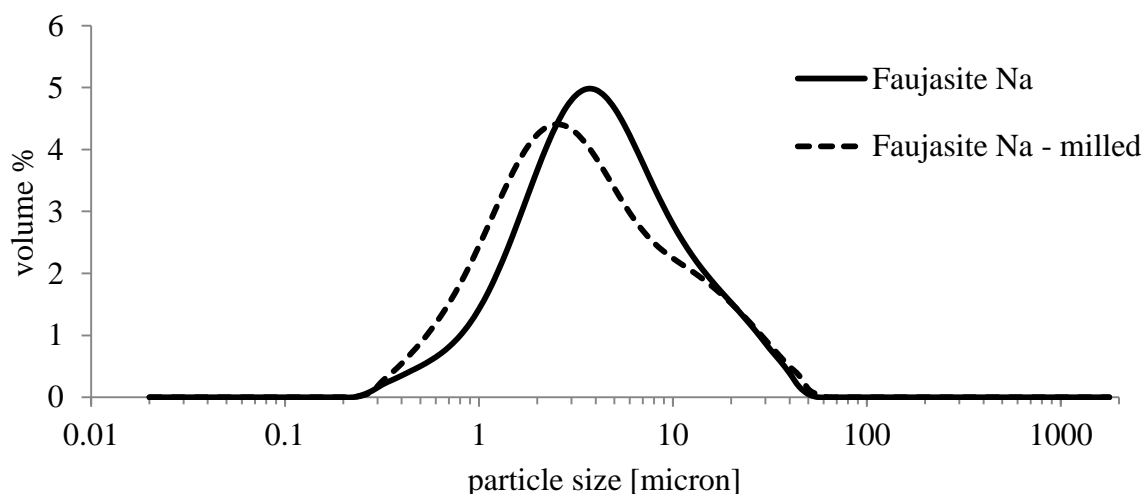


Figure 6.4 Particle size distributions of the faujasite-Na seeds determined by laser scattering.

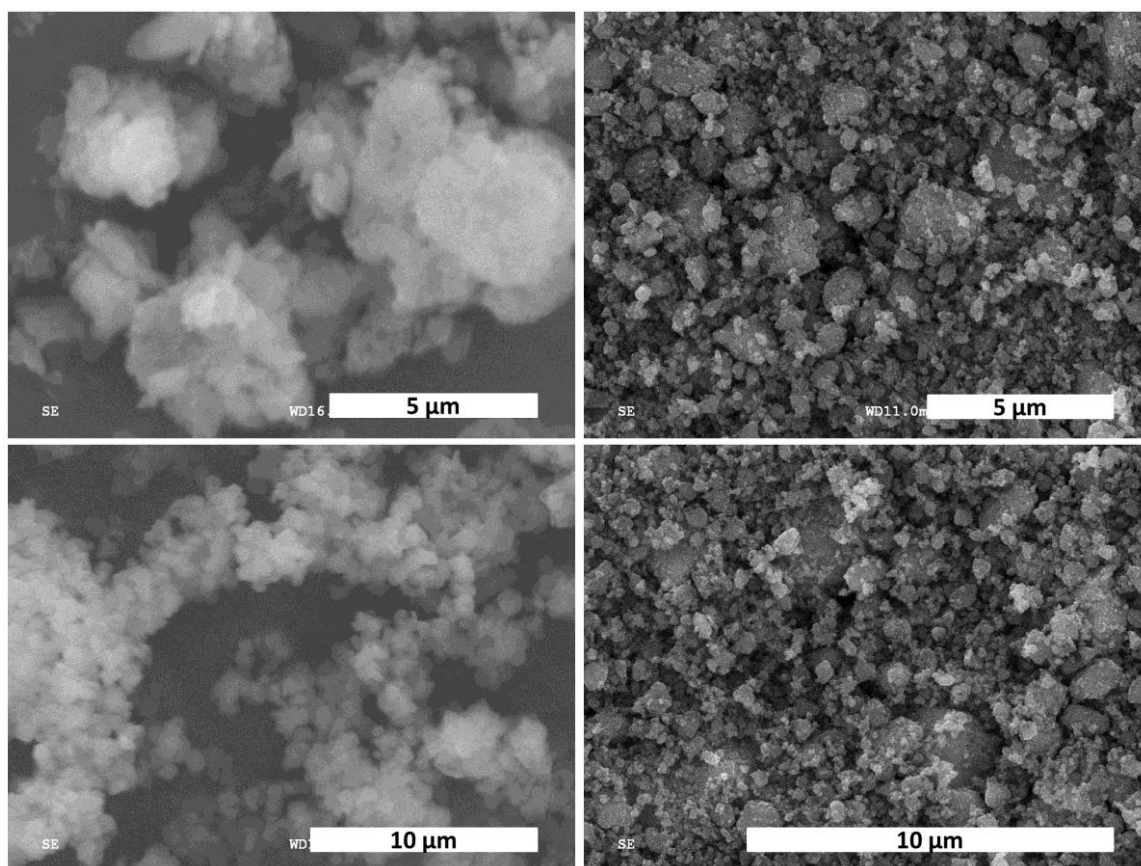


Figure 6.5 SE-SEM image of mordenite (top left), milled mordenite (top right), faujasite-Na (bottom left) and milled faujasite-Na (bottom right)

All the milled zeolite specimens had broader peaks, both in the FTIR and in XRD spectra. The peak broadening in XRD was due to decrease in crystal sizes and due to the introduction of strains in the crystals. Figure 6.6 (right) shows the XRD full width half maximum (FWHM) ratios of ball milled mordenite over as-received mordenite. Size strain analyses were performed on diffractograms acquired from 3° to 120° 2θ and the instrumental peak broadening was subtracted using the software X'Pert Highscore Plus. The peaks were fitted using pseudo-Voigts and the sample broadenings were analyzed using the Caglioti formula [220]. The crystal sizes and strains of the as received and ball milled sodium faujasite type Y were respectively 120 nm and 0.05%, 300nm and 0.14%. The results for the hydrogen faujasite type Y were 150nm and 0.18%, 490nm and 0.23%. The mordenite samples results were 2400 nm and 0.21%, 110 nm and 0.19%. The low intensities of the peaks at $2\theta > 50^\circ$ made it difficult for the algorithm to discern the contribution of size and strain and the increases in size of the crystals due to ball milling is likely a refinement artifact, Figure 6.5.

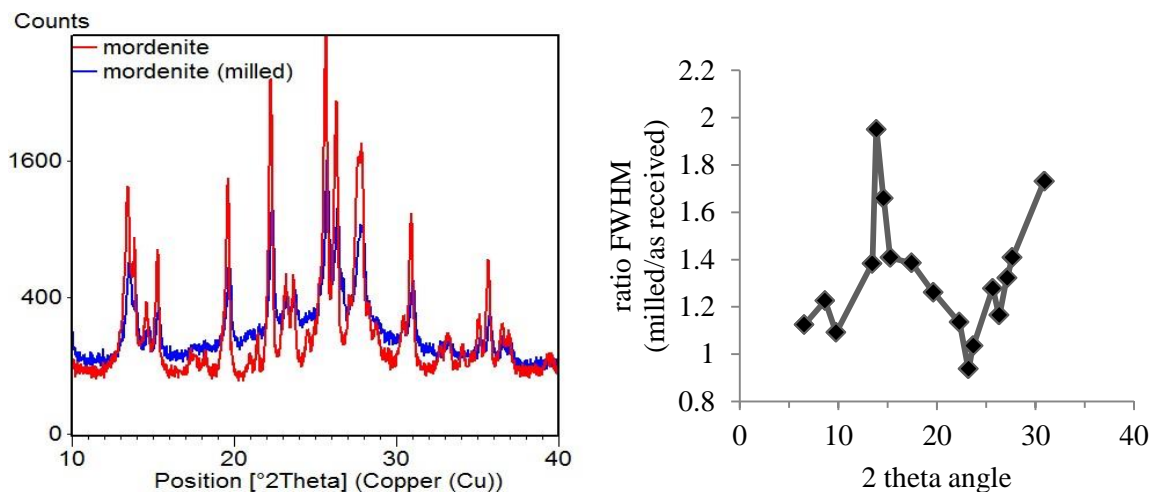


Figure 6.6 Left: XRD of mordenite and milled mordenite. Right: FWHM ratio of the XRD peaks.

An increase of the FWHM was also observable for the FTIR peak of mordenite, Figure 6.7, which indicates a larger distribution of bond lengths and angles probably due to the strain induced by ball milling: “It is known that phases of non-ordered structure cause the increase in the band width due to the existence of significant fluctuations of geometric parameters, i.e. bond lengths and angles” [247]. This trend was common for all the zeolites used in this work.

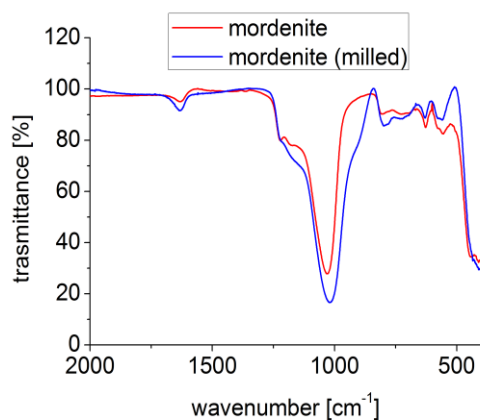


Figure 6.7 ATR-FTIR spectra of mordenite before and after milling.

6.1.3. Bottom-up approach: synthetic zeolites

Zeolites size cannot be easily reduced without altering their crystallinity. Thus an alternative approach, i.e. bottom up approach, was used to control their particle dimensions. Initially a conventional method using high temperatures aging was adopted, whereas a novel approach at mild temperatures resulted in a stable suspension of monocrystalline zeolites.

6.1.3.1. Conventional synthesis: LTA, FAU

Zeolite type A (LTA) and Zeolite Type Y (FAU) with a Si/Al=2.42 were synthesized based on the procedure from the International Zeolite Association [172]. The synthesis consisted in the preparation of aluminosilicate precursor solutions which were then cured at 100°C for approximately 4-5 hours in sealed polypropylene bottles. The precipitates were washed with distilled water and dried at 110°C for 24 hours before analysis. For more detailed information the reader can refer to the IZA website [172] and other references [185], [248].

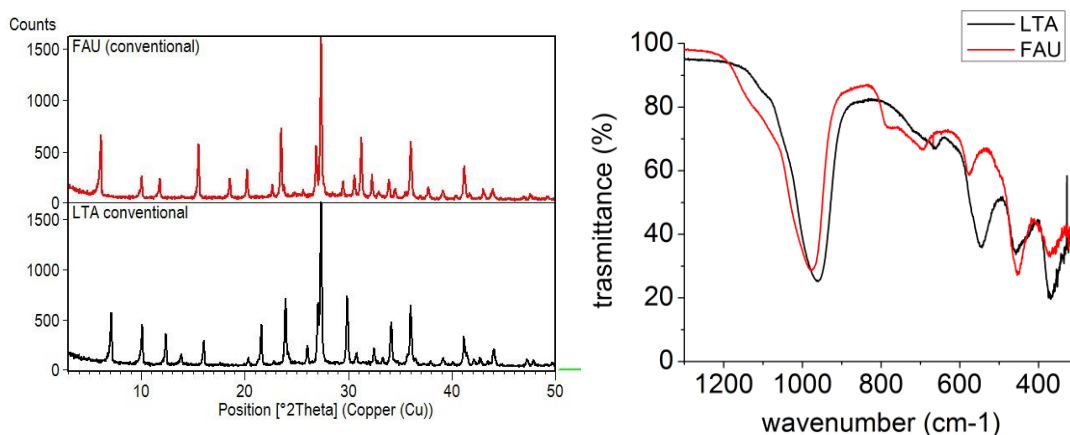


Figure 6.8 Left: X-rays diffractograms of the synthetic zeolite type A (LTA) and zeolite type Y (FAU). Right: ATR-FTIR spectra of the aforementioned synthetic zeolites.

The XRD peak positions corresponded to those of ICSD 24901 (zeolite type A) and ICSD 155683 (zeolite type Y). Also, the FTIR peak positions had the same wavenumbers of the zeolites obtained by Novembre [192]. The bands in the region 1200 and 950 cm⁻¹ represented the asymmetric stretching of the Si-O-T bonds; the larger shoulder at high wavenumber denoted the higher Si/Al ratio of FAU compared with LTA. Si-O-T symmetric stretching for LTA was located at 660 cm⁻¹, while for FAU there were multiple bands in the spectral region

690-750 cm^{-1} . Zeolite double ring vibrations were located at 560 cm^{-1} for FAU and at 550 cm^{-1} for LTA. Finally, T-O bend vibration appeared at 458 cm^{-1} for FAU and 464 cm^{-1} for LTA.

6.1.3.2. Colloidal zeolite seeds

Synthesis of nanocrystalline zeolites with narrow size distribution usually requires the assistance of organic template, such as tetramethylammonium (TMA) cations, around which developing zeolite cages form [249]. However, these organic cations are non-recyclable and expensive, reduce the reaction yields and cannot be extracted from the zeolites without causing aggregation [250]. The effect of TMA on the geopolymerization reactions could be of scientific and industrial interest but it was not the focus of this dissertation, thus a different synthesis procedure was needed. Nanosized zeolites are also difficult to produce using a top-down approach since they are susceptible to amorphization [251]. Addition of dry particles into solution often results in nanoparticles agglomeration: composite material and cement manufacturers struggle to obtain a stable dispersion of nanosize additives in cements and other resin-like or paste-like materials. For instance Kawashima [252] found that CaCO_3 nanoparticles agglomeration in fly-ash cement system could only be partially reduced if the particles were strongly sonicated in the presence of surfactant.

A relatively new organic-template-free method to produce highly disperse crystalline zeolite was adopted in this work according to Awala [250]. He prepared a water-clear precursors solution $9\text{Na}_2\text{O}:0.7\text{Al}_2\text{O}_3:10\text{SiO}_2:160\text{H}_2\text{O}$ by slowly adding an aluminate solution to a silicate solution kept in an ice-bath to decrease the kinetics of polymerization. The solution was aged at room temperature for 24 hours. According to the author: “*the formation of precursor particles of similar size with identical growth kinetics drastically limits Ostwald ripening of the resulting nanocrystals, ensuring a much narrower particle size distribution*” [250]. Homogenous distribution of monomeric aluminate and low molecular weight silicate species during gel preparation was identified as a key factor in controlling particle size. Curing at mild temperatures (i.e. 50°C for 45 hours) induced crystallization of the particles without decreasing their surface areas.

In this work the aluminate solution was obtained by mixing 7.86 g of sodium aluminate, 23.52 g of sodium hydroxide and 61.47 g of water. The silicate solution was prepared using 90 g of colloidal silica (HS-50 Ludox), 111 g of water and 24 g of sodium hydroxide. The two solutions were stored at 60°C until clear solutions were obtained; they were then cooled at 0°C and mixed, followed by aging at 25°C for 24 hours. The aged solution was separated in 9 containers which were then cured respectively at 40°C, 50°C and 60°C for 40 hours, 45 hours and 50 hours. One last sample was autoclaved at 125°C and 30 psi for 6 hours.

We have found that the control of curing temperature is of paramount importance as only synthesis at 50°C produced colloidal solutions. Higher temperatures induced particles growth and precipitation, while lower temperatures resulted in clear solutions, Figure 6.9 left. To separate the particles from the solutions the samples were centrifuged at 6000 rpm for 30 minutes. No precipitate was observed at 40°C and no zeolite particles were present in the solution. On the other side, a white gel precipitated from solution cured at 50°C upon flocculants addition (polyacrylamide, MW=5000000-6000000, Polyscience Inc.) and centrifuging. The precipitated white gel was dried at T=25°C in a desiccator with silica gel for 3 days to minimize sample alteration. It was then characterized by XRD, Figure 6.9 right, and SEM, Figure 6.10. The XRD peaks corresponded to crystalline faujasite, ICSD 155683. SEM analysis revealed that the zeolite particles were smaller than 200 nm. It was not possible to obtain higher resolution images as we had to adopt relatively high vacuum level, i.e. 50 kPa, during SEM analysis due to residual water content in the sample. Removal of this water would have required higher temperatures which could result in Oswald ripening.

In conclusion, the synthesis method invented by Awala [250] was successfully reproduced by using sodium aluminate instead of metallic aluminum; the resulting stable colloidal nanocrystalline faujasite was used as seeds for the processes reported in Chapters 7 and 8. Zeolite crystals represented the 10.5 wt% of the suspension, and the remaining solution was made of sodium silicate with a Ms=0.79 and 75 wt% H₂O.

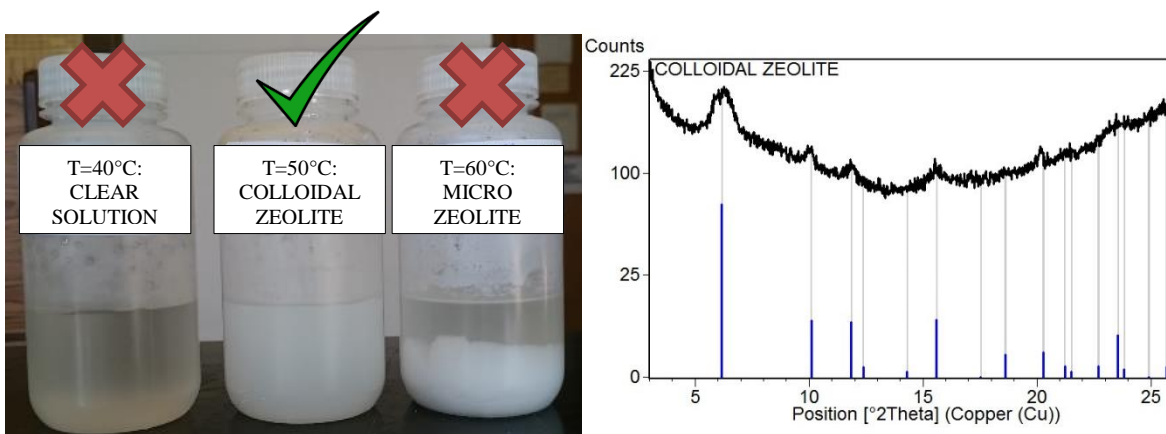


Figure 6.9 Left: digital picture of the zeolite precursor solution aged for 45 hours at different temperatures. Right: XRD of the colloidal particles obtained after aging at 50° for 45 hours.

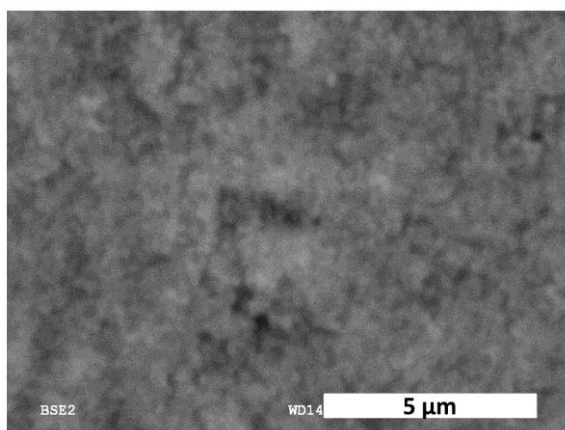


Figure 6.10 BSE-SEM image of colloidal nanocrystalline faujasite. Air-dried precipitate obtained after curing at 50° for 45 hours of the zeolite precursor solution.

The precursor solution aged in autoclave at 125°C resulted in a white precipitate and a supernatant solution. The precipitate was washed with distilled water and analyzed with XRD and SEM. The diffractograms corresponded to the ICSD 9550 belonging to zeolite type P, also referred to as Gismondine. The presence of this zeolite was in agreement with the literature: “*suspension of FAU crystals in growth solutions heated at elevated temperatures and/or for longer times can undergo a structural phase transformation to GIS-type zeolite*” [253]. The crystal morphology as observed by SEM was also tetragonal and the crystal size was approximately 5 μm. The Gismondine seeds were used in Section 6.2 to determine if

they could act as templates for the growth of Gismondine crystals and increase the mechanical properties of geopolymer.

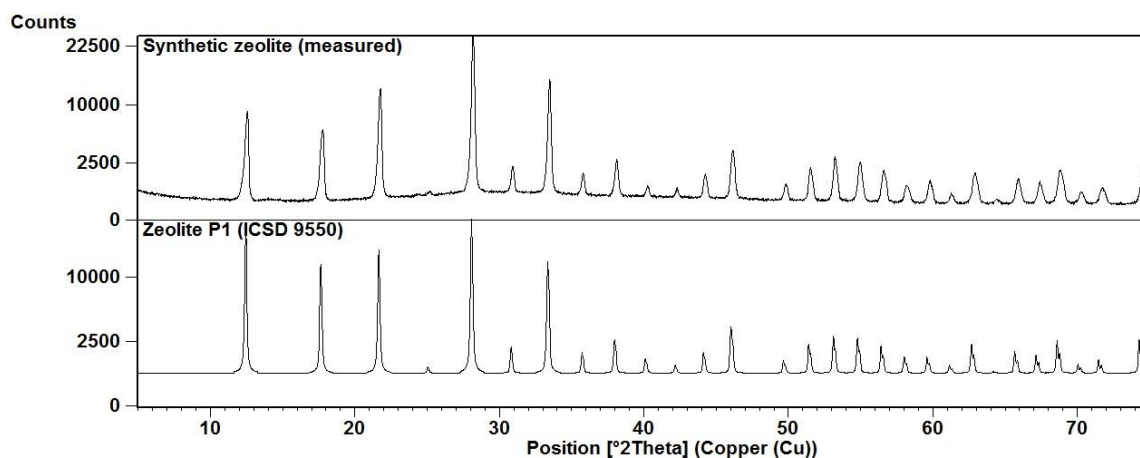


Figure 6.11 X-rays diffractograms of the zeolite obtained by autoclave curing of precursor solution and diffractogram of the database structure of Gismondine (ICSD 9550).

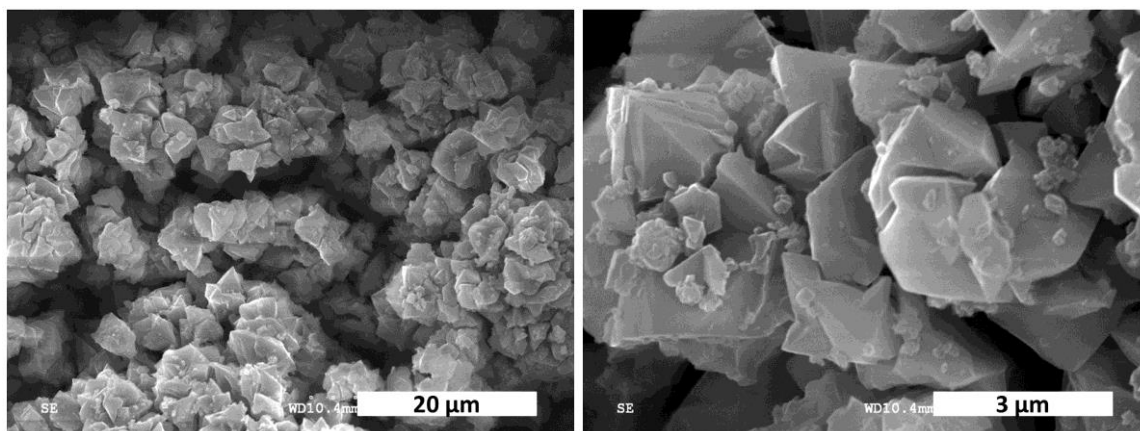


Figure 6.12 SE-SEM images of Gismondine zeolites obtained after autoclave treatment.

6.1.4. Summary

In this Chapter different commercial seeds were characterized, including SiO_2 , Al_2O_3 , ZrO_2 and three different zeolites: mordenite-Na, faujasite-H and faujasite-Na. The charge balancing cations had an effect on the FTIR peak position and on the intensity of the XRD peaks of faujasite. Mechanical activation of zeolites decreased both particle size and

crystallinity of the seeds. Zeolite type A, X and P were prepared according to conventional zeolite synthesis methods; the crystal had sizes of approximately 2 to 5 microns. A recently proposed method to produce dispersed colloidal nanocrystalline faujasite was successfully implemented. These particles were used in GP processing experiments to assess their potential as seeding agents in MK-based geopolymers.

6.2. Seeds effect on NaOH/MK-based GPs

In this Chapter the effect of different seeds on NaOH/MK-based GPs were investigated in term of consolidation kinetics, structure and microstructure evolution and development of compressive strength.

The results of Chapter 5 indicated that curing GPs at 40°C for 20 hours was not enough to obtain fully reacted geopolymer, thus longer curing times and/or higher curing temperatures were adopted. In Section 6.2.1 commercial seeds (SiO_2 , Al_2O_3 and different zeolites) were added to the MK prior to samples preparation. Subsequently GP mixes were prepared and cured at 45°C and RH=100% for 3 hours, 3 and 7 days. Synthetic zeolite seeds (Gismondine) were dispersed in the activating solution before mixing and casting operations; these results are presented in Section 6.2.2. Samples were cured at 45°C for 24 hours and the effects of additional curing at different temperatures and relative humidity condition were determined in terms of GP crystal structure and mechanical properties.

In all cases 2 wt% of seeds (of the mass of MK) was adopted, in line with many other studies on seeded cementitious binders. For example 2 wt% of C-S-H increased the hydration kinetics of tricalcium silicate [154]; 3 wt% of ZrO_2 improved the compressive strength of FA-based GP by 30% [163]; 0.5% of Al_2O_3 , ZnO and ZrO_2 increased the dissolution of GP solid precursors [166] ; 3 wt% of SiO_2 increased the compressive strength of FA-based GP. To the best of our knowledge no research has been done before on seeded MK-based GP, and none has studied the effects of zeolite seeds in any GP system.

6.2.1. Effects of commercial oxide seeds

6.2.1.1. Seeded-GP synthesis and analyses

GP samples were prepared following the procedure described in Section 4.1.2. The seeds were added directly to the metakaolin (MK) powder and mixed with a spatula for 30 seconds. The slurries were cast into cylindrical polymeric molds with height and diameter of ≈ 3 cm, and cured at $T = 45 \pm 3^\circ\text{C}$ and RH=100%.

The selected GP formula was $1.0\text{Na}_2\text{O}\cdot 1.0\text{Al}_2\text{O}_3\cdot 2.0\text{SiO}_2\cdot 10.1\text{H}_2\text{O}$, which is a polysialate according to Davidovits nomenclature [38] – refer to Section 2.1.1 for the notation details. In order to obtain this composition 11 M NaOH solution was added to the MK powder with a ratio of solution/metakaolin equal to 1.1. Thus the total molar ratios of the geopolymer were: $\text{Na}_2\text{O}/\text{SiO}_2=0.5$; $\text{Na}_2\text{O}/\text{Al}_2\text{O}_3=1$; $\text{SiO}_2/\text{Al}_2\text{O}_3=2$; $\text{H}_2\text{O}/\text{Na}_2\text{O}=10.1$. This formulation was adopted in order to avoid the templating effect of the soluble silicate, which directs and accelerate the condensation of $\text{Al}(\text{OH})_4$ monomers [203], thus to focus only on the seeding effects of oxides particles and zeolites. The water content was optimized according to Section 5.2, Table 5.3.

Two single-oxide seeds were used, 5 MIN-U-SIL Fine Ground Silica SiO_2 and $\alpha\text{-Al}_2\text{O}_3$ Nano Powder, and three pure synthetic zeolite, namely mordenite and sodium and hydrogen faujasite. These zeolites were selected since they have different Si/Al ratio and different site acidity. Surface activation of the zeolite was achieved by high intensity ball milling using a “Spex 8000 mixer mill”. More information on the seeds is available in Chapter 6.

The codes for the different seeded geopolymers are shown in Table 6.1. The chemical composition and curing conditions resembled the ones used by Zhang [119] who, using isothermal calorimetry, detected three exothermic peaks associated with the immediate dissolution of metakaolin, the condensation of oligomers and the structural reorganization of the geopolymers which occurred between 36 and 84 hours.

Table 6.1 Codes for the geopolymers containing different nanoparticles. MOR=mordenite, Fau= faujasite, m.=milled ; Fau-H = hydrogen faujasite, Fau-Na =sodium faujasite.

sample code #	1	2	3	4	5	6	7	8	9
seed type	none	SiO_2	Al_2O_3	MOR	m.MOR	Fau-Na	m.Fau-Na	Fau-H	m.Fau-H

The time of setting measurements and unconfined compressive strength tests were performed on every formulation. A total of six specimens were tested to evaluate the 3 days and 7 days compressive strength for each formulation. The fractured surfaces were analyzed using SEM. Portions of the fractured samples were then pulverized using agate mortar and pestle and

analyzed using attenuated total reflectance Fourier transform infrared (ATR-FTIR) spectroscopy and powder X-ray diffraction (XRD). XRD and ATR-FTIR analyses were performed on each material at three different aging times: 3 hours, 3 days and 7 days. The geopolymer samples were kept in a sealed bag to avoid water evaporation, crushed using mortar and pestle and immediately analyzed without drying. This procedure was adopted in order to study the geopolymerization products in the bulk material without alteration due to water removal

Bulk density, moisture content and durability of the intact samples were also determined. Durability test were performed in accordance with Lancelotti [179]: undamaged samples were soaked for 24 hours in distilled water using solid/liquid ratio of 10 and the values of pH and conductivity were used to indirectly evaluate ions release and the stability of the geopolymeric matrix.

6.2.1.2. GPs setting times, GPs mechanical and physical properties

The seeds had no detectable effects on the setting time, which was 75 ± 15 minutes for all the samples. The low precision of the Vicat apparatus for GPs setting time precluded the determination of minor differences due to seeding. If seeds influenced the setting time, their contribution was probably lower than 20%. Dynamic rheological measurements were performed on the seeded and unseeded geopolymer slurries to establish if such a minor effect exists, Chapter 7.

Table 6.2 presents the results for unconfined compressive strength (UCS), bulk density and durability. The standard deviation of the UCS was approximately 20-30% due to differences in defects density, size and distribution. The compressive strength of these GPs is lower compared with OPC and they are not suitable for construction applications. Nonetheless they are still interesting from an environmental prospective as they can be used as functional material for encapsulation, filtration and purification applications.

The average moisture content of the geopolymers was $27 \pm 3\%$. Considering their average density of about 1.6 g/cm^3 , the dry bulk density was 1.17 g/cm^3 in accordance with the values obtained by Liew [201]; thus these geopolymers could possibly be used as light-weight materials. There was no correlation between the values of density and compressive

strength, which means that the difference in compressive strength cannot be ascribed to the variation in porosity introduced during the handling of the paste.

Table 6.2 Values of bulk density and unconfined compressive strength at 3 days and 7 days for the 9 different samples. The values of pH and conductivity were measured on samples cured for 7 days, after 24 hours of soaking in distilled water.

Sample Code #	Density [g/cc]		UCS [MPa]		pH	conductivity [milli MHO]
	3d	7d	3d	7d	7d	7d
1	1.62±0.02	1.59±0.04	4.7±1.3	5.8±1.2	12.44	15.5
2	1.53±0.01	1.59±0.04	8.2±0.5	6.0±0.2	12.42	13.0
3	1.64±0.03	1.58±0.02	4.1±0.3	6.0±1.0	12.35	11.0
4	1.67±0.02	1.66±0.03	6.3± 0.3	9.0±2.0	12.35	10.0
5	1.56±0.01	1.64±0.04	8.0±2.0	11.0±2.0	12.31	9.5
6	1.63±0.01	1.64±0.02	4.5±1.5	10.0±2.0	12.09	3.5
7	1.56± 0.02	1.60±0.02	5.2±0.2	6.1±1.3	12.41	14.0
8	1.64±0.01	1.66±0.01	5.3±1.3	10.0±3.0	12.3	8.5
9	1.58±0.09	1.56±0.02	5.2±1.3	8.3±7.0	12.39	11.0

The values of the compressive strength are displayed in Figure 6.13. The SiO₂ and Al₂O₃ seeds (samples 2 and 3) did not show significant improvements, while the zeolites seeded GP shown a significant (i.e. nearly double) increase in compressive strength. The samples seeded with mordenite zeolites had a higher compressive strength already at 3 days. The compressive strengths from 3 to 7 days for samples 1,2 and 3 did not significantly improve, while in the samples seeded with zeolite there was a continuous increase in compressive strength which indicates an ongoing geopolymerization process not present in the non-seeded paste. The effect of milling on zeolite was more difficult to explain since the milling operation improved the compressive strength for mordenite seeds and faujasite-H seeds, but it seemed to have no effect on the faujasite-Na. Further studies are required, in particular it is recommended to test a higher number of samples in order to have a better statistic. In fact the observed sample means are plus or minus roughly 2 standard deviations from the population

means with a 95% confidence, which means that with the current data it is hard to draw any definitive conclusions since most of the results overlap.

Previous work [58] on geopolymers with similar composition and cured at 40°C found a compressive strength of approximately 15 ± 3 MPa. This higher value is probably due to a more reactive MK or a denser matrix with less entrained air obtained by adopting 15 minutes long vibrating operations. The seeded samples had better durability, especially sample 6 seeded with faujasite-Na, Figure 6.14, and there was a good correlation between pH and conductivity values.

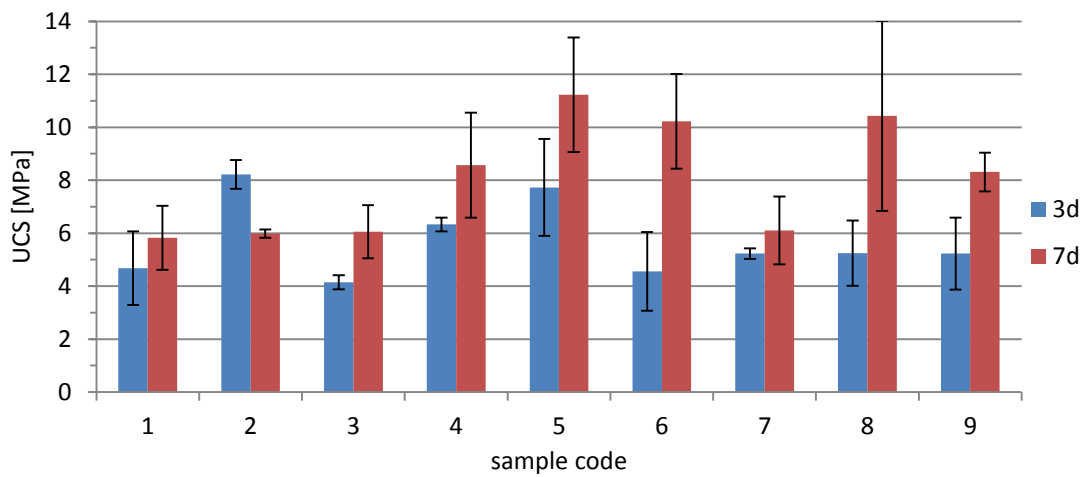


Figure 6.13 Unconfined Compressive Strength (UCS) of the seeded geopolymers compared with the non-seeded geopolymer (sample 1) at the same aging time.

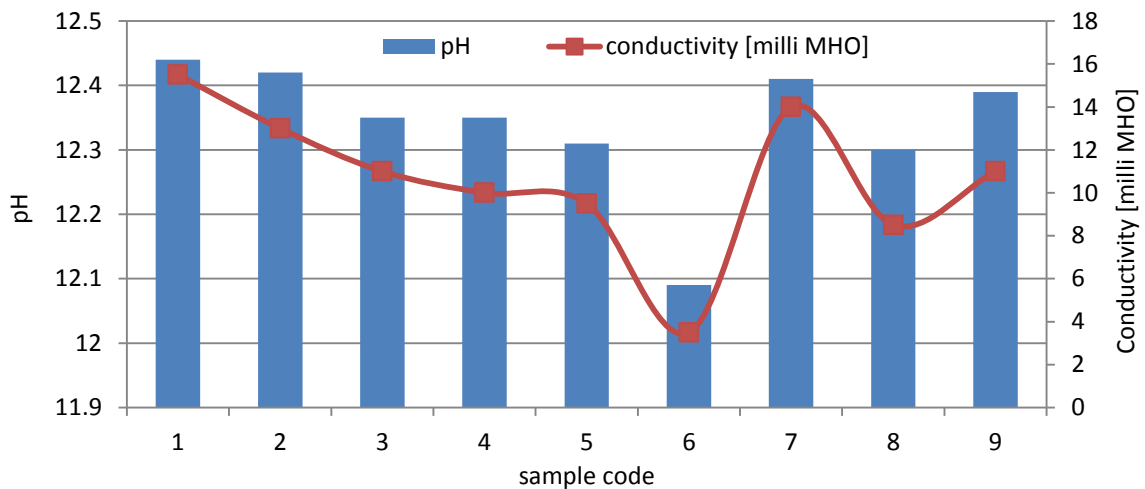


Figure 6.14 pH and conductivity values of the geopolymers soaked in distilled water for 24 hours.

6.2.1.3. Structural reorganization of seeded GPs

Although all the geopolymers did set in 75 minutes, the XRD diffractograms of the seeded geopolymers (Figure 6.15) did not display any crystalline phases except for the small impurities already present in the metakaolin, including anatase, silica and halloysite. At 3 days crystalline peaks of zeolite type A (Linde type A) and zeolite type X (faujasite-X) appeared. The samples seeded with zeolites had even stronger zeolites peaks at 7 days which means that there was continuous nucleation and growth of zeolites in the geopolymer gel. This increase was also present for the sample seeded with alumina while there was not such an increase of crystalline zeolites for the sample 1 and 2.

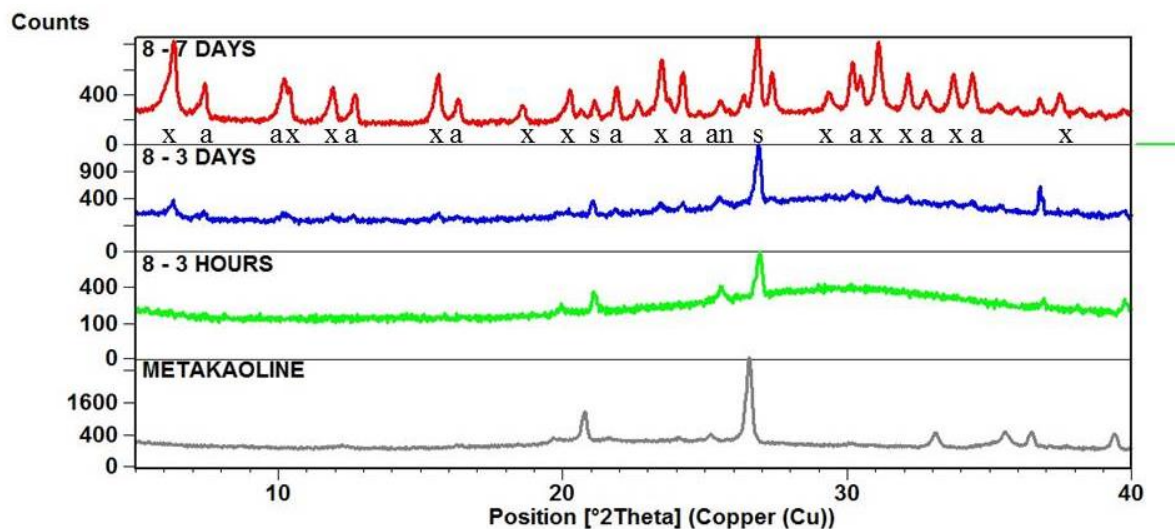


Figure 6.15 XRD diffractograms of metakaolin, milled-mordenite-seeded geopolymer at 3 hours, 3 days and 7 days. Zeolite type X (x), Linde type A (a), silica (s), anatase (an).

A semi-quantitative estimation of the zeolite content was obtained by normalizing the integrated intensities of the (200) reflection of zeolite A and (111) reflection of zeolite X by the intensity of the (011) reflection of the unreacted silica impurities. For unseeded GP and SiO₂-seeded GPs the crystallinity did not appreciably vary between 3 and 7 days (Figure 6.16). On the other hand, most of the other seeded-GPs displayed a lower crystallinity at 3 days but a higher final zeolite content at 7 days. The smaller zeolite content at 3 days may be due to a smaller size of the crystals which cannot be detected by XRD. This phenomenon was already observed in seeded FA-based GP and explained by Rees: “Adding more nucleating sites leads to smaller crystals as the nuclei compete for species in the solution”

[164]. The role of milling was not univocal as it had a negligible effect for mordenite seeds but it increased the crystallinity at 3 days for the two faujasite seeds, i.e. sample 7 and 9.

An interesting correlation exists between the GPs UCS, their durability and the main crystalline phase. The stronger samples, i.e. samples 4, 5, 6 and 8, were also the richer in faujasite (Figure 6.17). On the contrary sample 1, 2 and 7 contained a large amount of zeolite type A, their compressive strength was lower and they also had a smaller durability. The difference was particularly pronounced for the GPs seeded with FAU-Na (sample 6) and milled-FAU-Na (sample 7) which also possessed a distinct microstructure, Figure 6.20.



Figure 6.16 Zeolite content expressed in term of sums of XRD integrated intensities of 200) reflection of zeolite A and the (111) reflection of zeolite X over the (011) reflection of SiO₂ at 3 days and at 7 days.

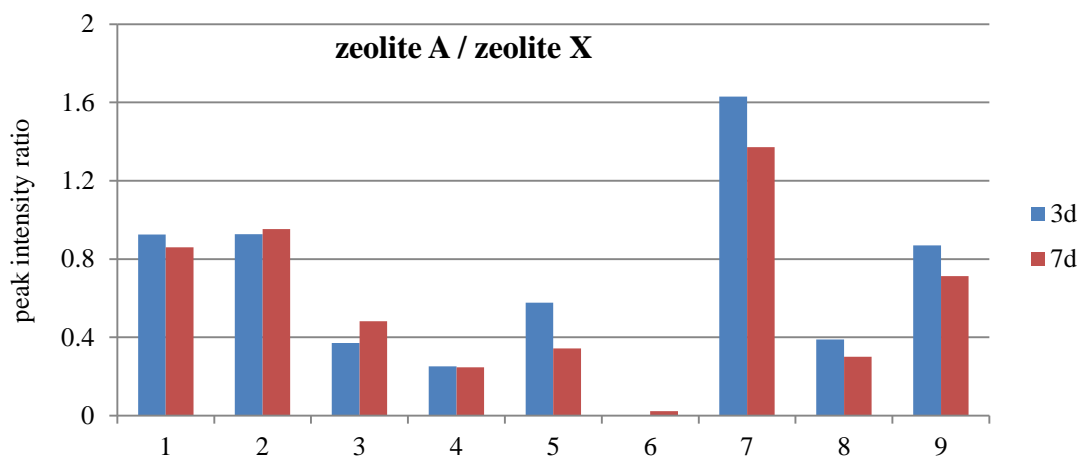


Figure 6.17 Integrated intensity ratios of the (200) reflection of zeolite A over the (111) reflection of zeolite X at 3 days and at 7 days in the XRD patterns.

This structural reorganization directly visible in the XRD and indirectly in the UCS values was seen in the FTIR spectra as well (Figure 6.18). The peaks associated with zeolite ring vibrations, which are located at low wavelengths (usually below 800 cm^{-1}) [254], increased in intensity and became sharper at 3 days of setting. For the samples 1, 2 and 7 there were no differences in the spectra between 3 and 7 days, while for all the other geopolymers the peaks became more intense and the FWHM decreased. These correlations between XRD, FTIR and UCS changes between 3 and 7 days are strong evidences that the seeds influenced the structural reorganization of the geopolymers.

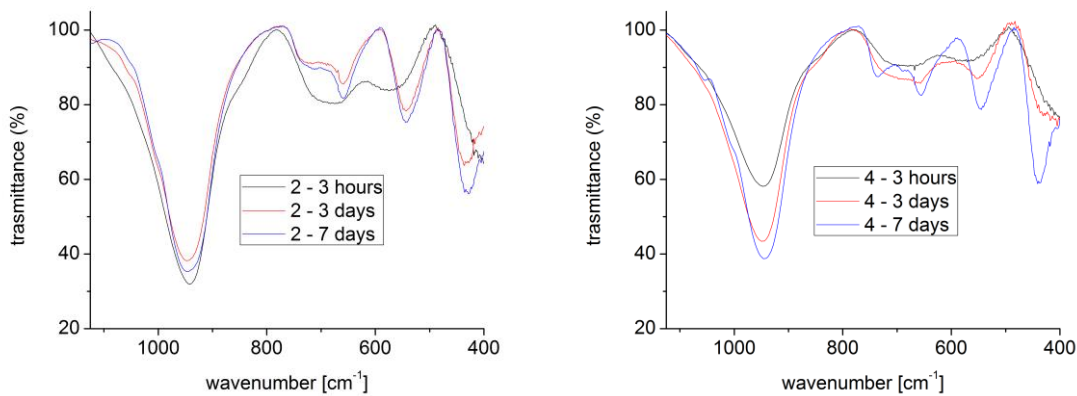


Figure 6.18 ATR-FTIR spectra for the GP seeded with SiO_2 (left) and mordenite (right), at 3 hours, 3 days and 7 days.

The microstructure of the geopolymers at 3 days (studied on the fractured surfaces) consisted of clustered particulates with relatively large (up to $1\text{ }\mu\text{m}$) interconnected pores; at this time the materials were mainly composed of lumps though it was possible to detect some crystalline zeolites in the pores. At 7 days $5\text{ }\mu\text{m}$ cubic crystals were detected together with smaller octahedral faujasite-X crystals, approximately $0.5\text{ to }1\text{ }\mu\text{m}$ large.

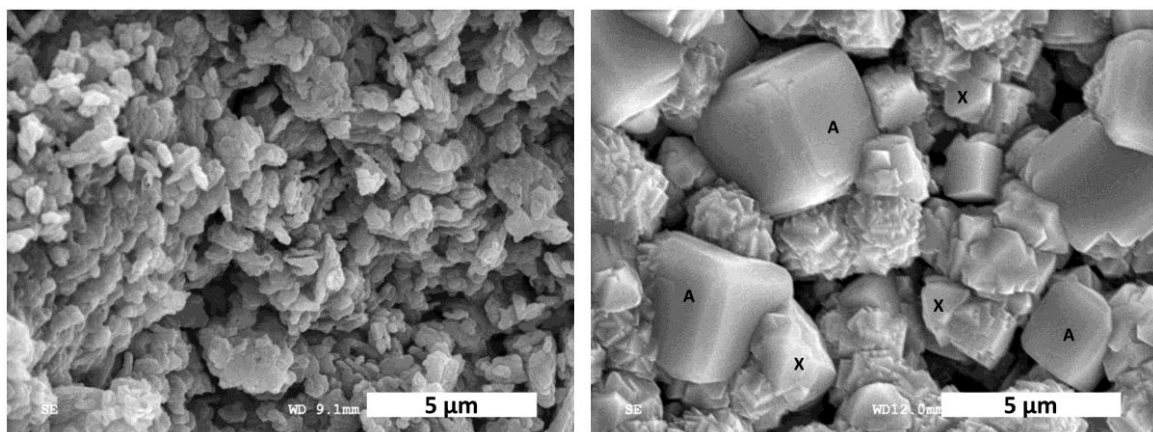


Figure 6.19 SEM images at 3 days (left) and 7 day (right) for the alumina-seeded geopolymer, sample 3. A: zeolite type A; X: zeolite type faujasite-X.

The morphology of the crystallized GPs agreed with the XRD results in Figure 6.17. For example, the microstructure of sample 6 showed 0.5-1 μm faujasite crystals, while sample 7 also contained large cubic LTA crystals, Figure 6.20.

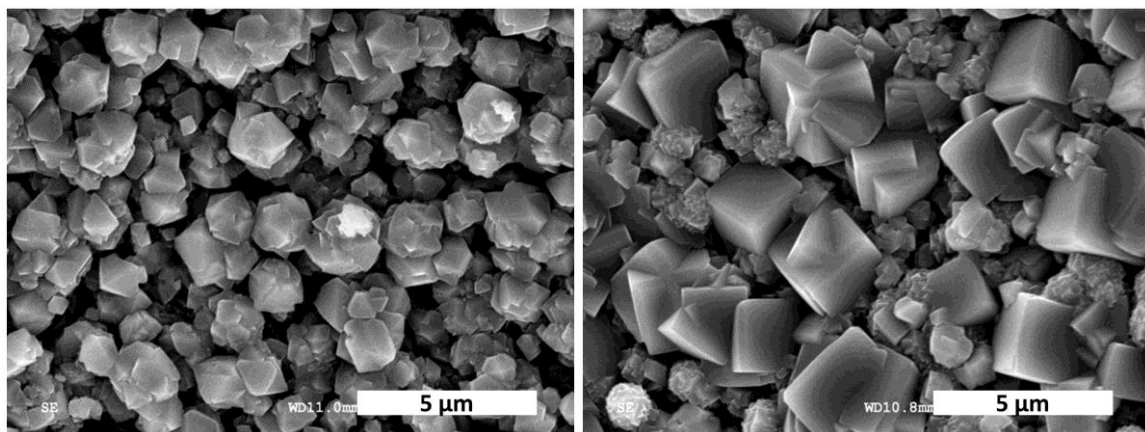


Figure 6.20 SE-SEM images after 7 days curing at 45°C of GP with FAU-Na seeds (sample 6, left) and milled-FAU-Na seeds (sample 7, right).

6.2.2. Effect of synthetic zeolites seeds

6.2.2.1. Seeded-GP synthesis and analyses

Using the same preparation method adopted in the previous Section, GPs with composition 1.0-0.9-1.8-11.3 were cast, cured at 45° for 24 hours and used as a baseline. Fresh synthetic GIS-NaP1 zeolite crystals prepared as previously described in Section 6.1.3.1 were added to the activating solution and mixed for 2 minutes with a magnetic stirrer before addition of MK. Three different additional curing treatments were selected to determine the effect of residual moisture and temperature on the GP properties: curing at 45° for 24 hours at RH=0%, curing at 125°C for 6 hours at RH=0%, curing at 125°C and 30psi for 6 hours at RH=100% (autoclave treatment).

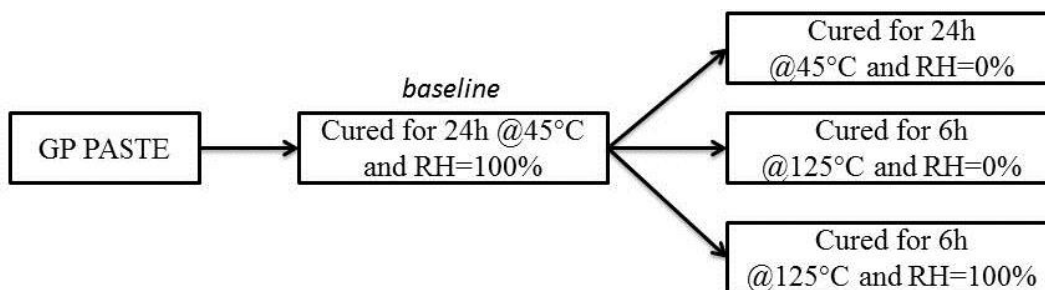


Figure 6.21 Curing procedures of the unseeded and seeded geopolymers.

The 8 GPs were tested for compressive strength and crystallinity using QXRD. More details on the XRD analysis with internal standard and Rietveld refinement can be found in Section 8.3.2.

6.2.2.2. GPs physical and mechanical properties

The bulk density of the unseeded and seeded GPs after 20 hours of curing at 40°C in RH=100% were respectively 1.62 ± 0.04 and 1.62 ± 0.02 g cm⁻³. Thus, the differences observed for the compressive strength cannot be attributed to the difference in density which may have resulted from different mixing, casting, degassing and curing conditions. The density of the GPs dried at 40°C for 24 hours at RH≈0% were 1.22 ± 0.01 and 1.21 ± 0.01 g cm⁻³, where the water lost upon drying corresponded to $25 \pm 1\%$ of the initial GPs weight. The initial H₂O

content was 43%, thus 18% of the dried GP was still water. These values were in agreement with the results obtained previously for similar GPs (refer to Section 6.2.1.2). The residual water probably represented the zeolitic water in the GP which requires higher temperatures to be removed. In fact, crystalline faujasite-X $\text{Na}_{86}(\text{Al}_{86}\text{Si}_{106}\text{O}_{384})(\text{H}_2\text{O})_{265}$ (ICSD 155683), zeolite type A $\text{Na}_{12}\text{Al}_{12}\text{Si}_{12}\text{O}_{48}(\text{H}_2\text{O})_{27}$ (ICSD 24901), hydrosodalite $\text{Na}_6(\text{AlSiO}_4)_6(\text{H}_2\text{O})_8$ (ICSD 413494) have respectively 26%, 22% and 14% of water by weight.

The values of unconfined compressive strength reported in Table 6.3 are the averages of nine tests on 1-inch cubes GPs. T-test were performed to determine if a statistically significant difference occurred between the samples. The additional curing treatments increased the UCS of the GPs: 24 hours at 45°C and RH=0% increased the strength of the GP by approximately 45%, 8 hours at 125°C increased it by 150%. The relative humidity at high temperatures did not have a statistical effect on the UCS. Zeolite-P1 seeds slightly decreased the compressive strength of the GP when cured at 45°C, but had no effect at higher curing temperatures. Possibly, the amorphous GP gels interacted poorly with the seeds which acted as defects and discontinuities in the binding matrix. After curing at 125°C the interlocking of GP crystals enclosed the pre-existing crystals.

Table 6.3 Unconfined compressive strength of unseeded GP and seeded with synthetic zeolite type P at different curing conditions.

Unconfined compressive strength [MPa]				
GP	none	additional curing (after 20 h at 45°C)		
		24h at 45°C (RH≈0%)	8h at 125°C (RH≈0%)	8h at 125°C (RH=100%)
unseeded	7.0±0.9	9.1±1.6	16±2	15.1±1.6
seeded	5.5±0.5	8.01±1.4	14±3	17.0±1.7

6.2.2.3. Structural characterization of the GPs

Both the seeded and unseeded GPs cured at 45°C for 24 hours were completely amorphous as determined by XRD. Increasing the curing time or temperature promoted crystallization of the GP gel, regardless of the relative humidity RH. Since crystallization occurred also when RH=0%, it did not occur via a solution-mediated mechanism but through solid state reactions. The main phases detected were zeolite type A, X and P (also named respectively LTA, faujasite and gismondine). Selected diffractograms are shown in Figure 6.22.

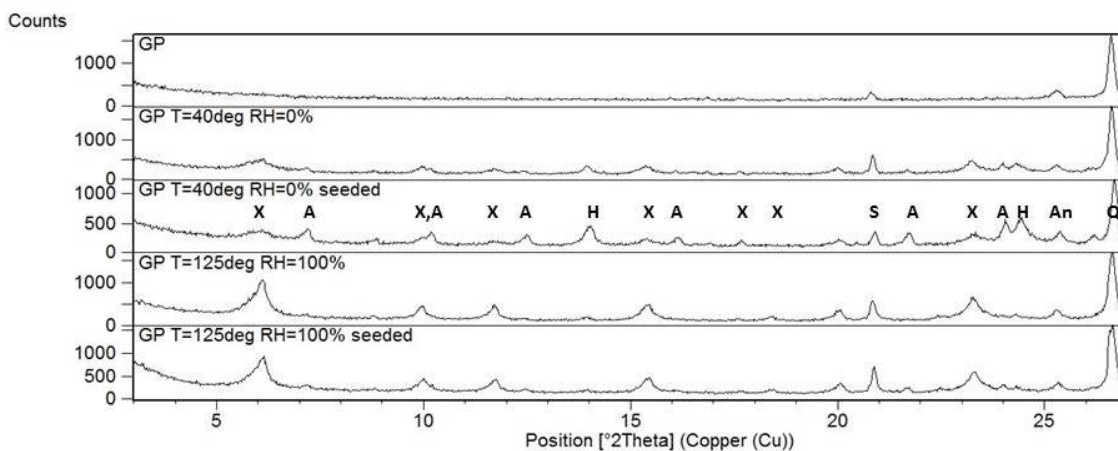


Figure 6.22 Selected X-Ray diffractograms of the seeded and unseeded GPs with different curing conditions. Letters indicate the peak position of faujasite (X), zeolite type A (A), hydrosodalite (H), silica (S), and Anatase (An).

The QXRD results, Table 6.4, show that GP cured at RH=100% had negligible content of hydrosodalite HS, while GPs cured at RH=0% have a significant amount of HS, especially at T=125°C. Zeolite type A was found prevalently in seeded GP cure at 45°C, while faujasite was detected in large amount in all samples, especially in the autoclaved GP. These observations suggest that LTA zeolites were converted into HS at higher temperatures and lower RH: the water loss induced a collapse of the aluminosilicate framework which increased its framework density FD from 12.9 to 17.2 tetrahedra/Å³. The LTA-to-HS transformation is commonly observed for LTA [148] but not for zeolite type X, probably due to a different Si/Al ratio and different atoms in the cages and channels. Whether the GPs

contain LTA or HS depends on the curing and post-curing procedure: if the GPs are dried prior to the XRD analysis the LTA cannot be detected as it converts in HS.

The addition of zeolite-P seeds did not induce the formation of this phase within the GPs, but increased the LTA content and decreased the FAU-X content. Thus, zeolite type P can favour the formation of LTA zeolite in NaOH/MK-based GP which probably heterogeneously nucleates on the seed surface. This hypothesis could not be confirmed by direct observation using SEM (Figure 6.23), thus further studies are required. A possible alternative is that the seeds altered the activating solution chemistry in which the homogeneous nucleation of zeolite type A occurs.

The NaOH/MK-based GPs studied in Chapter 5 contained only zeolite type A, while the GP studied in this Chapter were predominantly made of faujasite-X. The higher value of Na/Al may be responsible for this difference. The maximum amount of zeolite in GPs was only 30% because of the impurities contained in the MK and amorphous water present in the GP. These considerations will be taken in account in Chapter 8 wherein a detailed multifactorial analysis of the GP crystallization was conducted.

Table 6.4 Zeolite weight % of different GPs as determined by QXRD using internal TiO₂ standard. LTA: zeolite type A. FAU: zeolite type X. HS: hydroxysodalite.

phase	zeolite weight %							
	additional curing (after 20 hours at 45°C)							
	none		24h at 45°C (RH≈0%)		24h at 125°C (RH≈0%)		24h at 125°C (RH=100%)	
	GP	seeded GP	GP	seeded GP	GP	seeded GP	GP	seeded GP
LTA	0	0	5	12	1	2	2	5
FAU	0	0	17	10	17	12	30	25
HS	0	0	3	8	10	11	2	1

The SEM images of the seeded and unseeded GP cured for additional 24 hours at 45°C and RH=0% are shown in Figure 6.23. The microstructures were similar, as suggested by their

close values of compressive strength. Amorphous gel lumps and submicron zeolite crystal were detected in both GPs and the non-continuity of the matrix explains the relatively low value of UCS, i.e. 9MPa.

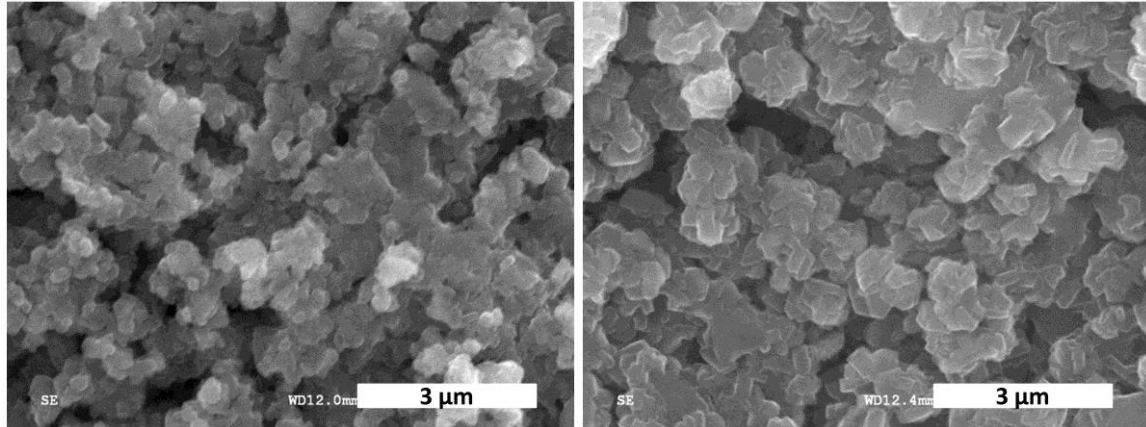


Figure 6.23 SE-SEM images of the unseeded (left) and zeolite-P1-seeded (right) GPs cured for additional 24 hours at 45°C and RH=0%.

6.2.3. Discussion: strength of interlocked GP crystals

In this Chapter we report research wherein small amount (2 wt%) of different seeds gave different results, in particular the ratio of zeolite type A and zeolite type X. The values of UCS and GPs durability indicates that the higher the zeolite A (LTA) content, the poorer the performance of the GP. The decrease in strength appears due to the cubic crystals of LTA, which cannot properly interlock with each other. On the contrary, smaller octahedral faujasite crystals have higher contact area and thus can better distribute the stress within the matrix. In granular physics research particles shapes are known to have an effect on the stiffness and yielding of a particulate material: octahedral objects showed higher values than cubes [255].

By using different seeds and by mechanically activating the seeds different outcomes could be obtained. Milled faujasite seeds probably dissolved in the activating solution, they modified its chemistry and increased the nucleation and growth of zeolite LTA in the GPs. With the exception of SiO₂ seeds, the other seed particles did not dissolve and acted as nuclei

for heterogeneous nucleation of faujasite-X. Seeding with synthetic zeolite type P also favors the formation of zeolite type A. Increasing the amount of faujasite can also be obtained by changing the GP composition, i.e. increasing Na/Al, and the amount of LTA can be decreased by drying, inducing a LTA-to-HS transformation.

Although different method to increase the UCS of NaOH/MK-based GPs were found in this work, their values remained too low to be used as cementitious material, i.e. generally $UCS < 17 \text{ MPa}$. The reason for this low strength probably relates to the rigid crystalline nature of these GPs as compared with the more flexible amorphous gel of WG-based GPs. The same crystals that provided advanced functionality to the GPs are the reasons of their poor performance as constructional cements.

6.2.4. Summary

In this work the role of silica, alumina and zeolites seeds on the geopolymerization of metakaolin based system were studied. The seeding had no evident effects on the short term properties of the geopolymers. In particular the different samples had a similar setting time of about 75 minutes, no crystalline phases (XRD) and no definite zeolitic ring vibrations (FTIR) were detected after 3 hours. The setting reactions appear to correspond with the dissolution of metakaolin and the precipitation of amorphous geopolymer lumps with the characteristic FTIR band at 950 cm^{-1} .

The structural reorganization that occurs between 3 and 7 days results in an increase in crystalline zeolite content detectable both in XRD diffractograms, ATR-FTIR spectra and SEM images and as an increase in compressive strength. The seeds, with the exception of SiO_2 and milled-faujasite-Na seeds, showed an enhancement in the structural reorganization compared with the non-seeded geopolymer.

The geopolymers seeded with zeolites had higher compressive strength, crystallinity and durability. In particular the best result for compressive strength was obtained using milled-mordenite which gives a 92% increase of UCS in comparison with the non-seeded geopolymers at 7 days of setting. Certain seeds can enhance the durability and the UCS of GPs by promoting the crystallization of better interconnected octahedral faujasite crystals over the isolated cubic LTA crystals. Zeolite type A decreased the durability of the GP and it

can decompose in hydrosodalite upon drying. Although the polycrystalline GP displays better mechanical properties compared with colloidal amorphous lumps, their strength is not comparable with amorphous GP obtained using soluble silicate or with the semicrystalline colloidal precipitate of calcium-silicate-hydrate present in Ordinary Portland Cement.

7. Rheology and reaction kinetics of GPs

7.1. Introduction and hypothesis

The description of the overall kinetics of geopolymerization can be quite challenging both because the reaction mechanism and kinetics of some individual steps reactions are not well studied and because the products of one reaction step are often the reagents of the following steps [33]. An extensive discussion on this topic can be found in Section 2.2.4. During geopolymerization of MK-based GP the following reaction steps occur [114], [119], [256]:

1. wetting of the metakaolin by the activating solution;
2. dissolution of metakaolin and release of aluminosilicate species into solution (hydrolysis catalyzed by alkali);
3. condensation between aluminosilicate species to give an amorphous gel;
4. gel reorganization;
5. crystallization of zeolites from the amorphous gel.

Both step 3 and step 5 are associated with nucleation and growth of gel and zeolite respectively, and the nucleation may be associated with an induction period. Step 3 can also affect step 2 depending on the nucleation mechanism: if homogeneous nucleation occurs step 3 can accelerate step 2 by decreasing the concentration of aluminosilicate in solution, but if gel nucleation occurs on the metakaolin surface this can passivate the metakaolin and slow the reaction [150]. Reorganization of the gel (step 4) can also have an influence on the metakaolin passivation layer.

In Chapter 5 we reported on the research wherein MK dissolved only to a certain extent when soluble silicates were added to the activating solution. In particular there were several unreacted aggregates of clay, Figure 5.9. It has been hypothesized that the growing geopolymer gel passivates the surface of the MK [114], [150]. No one has ever investigated the effects of the activating solution chemistry on the wettability of metakaolin. It would be difficult for a solution to penetrate between the MK aggregates and break them apart if such solution has a large contact angle. Moreover, differences in the contact area between the activating solution and the metakaolin can result in different reaction kinetics, as can be seen

in EQ. 2.12 and EQ. 2.14. On the other hand, if the MK is fully wettable than the passivation theory is the most plausible explanation for the unreacted MK. Unfortunately clear experimental observations of the passivation layer have not been obtained yet.

Although geopolymerization includes multistep reactions, the overall kinetics can be approximated by using the assumption of a single rate limiting step [121]. It is not clear which of the aforementioned stage of reactions is controlling the overall process and if this stage is common for all types of geopolymers or it varies based on the type of activating solution, i.e. sodium hydroxides and sodium silicates. The determination of the rate limiting mechanism in heterogeneous reaction by seeding is a widely adopted method. It has been used both for inorganic [156], [157], [257], [258] and organic [155], [158] heterogeneous reactions. The method consists of measuring the kinetics of reactions with and without seeds. If the seeds accelerate the kinetics, then the precipitation of the products is considered to be the rate limiting step, Figure 7.1. If seeds have no effect, than it is concluded that the dissolution of reagents controls the overall transformation.

Since the geopolymerization reactions induce an increase in the material viscosity [259], rheological analysis was performed in this work to study the kinetics of reaction and evaluate the effect of seeding.

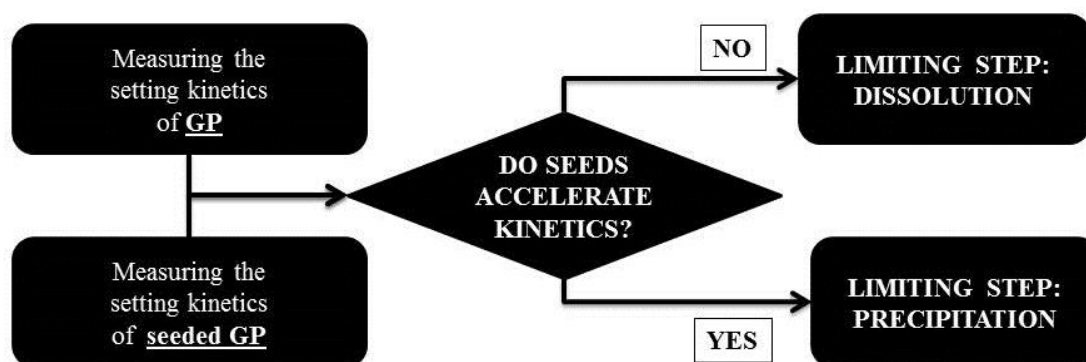


Figure 7.1 Schematic of the method to determine the rate limiting step by seeding.

Assuming the reaction kinetics is controlled by a single reaction step, it can be expressed as a pseudo-first order reaction [132] with reaction constant k and extent of reaction α , EQ. 7.1. The reaction constant k varies with temperature with Arrhenius dependence. The activation

energy can be calculated from an Arrhenius plot, i.e. logarithm of reaction kinetics k versus the reaction temperature. It is thus possible to quantify the effect of different seeds on the geopolymerization reactions based on the decrease in activation energy.

$$\alpha = 1 - e^{-kt} \quad \text{EQ. 7.1}$$

7.2. Metakaolin wettability in activating solution

7.2.1. Contact angle measurement

Sessile drop and captive bubble experiments to determine the contact angle cannot be performed on powders but they need flat and clean surfaces, possibly without porosity, thus pellets made of metakaolin had to be prepared. Dry pressing these pellets was prepared and the pressure needed during uniaxial compaction of the metakaolin powder determined by trial and error [260]. The die was composed of a Rockwell 58C steel cylinder with a 15.8mm diameter hole and two Rockwell 58C steel with a 15.8 mm diameter. Pressure of approximately 5 metric tons was applied using a Carver Laboratory Press to 0.6g of MK. Pressure was held for 2 minutes and reapplied for 3 times. The steel rods were cleaned with acetone and no lubricant was used to minimize surface contaminations. Few pellets were coated in gold and observed with SE-SEM to determine the surface roughness and porosity. The adopted preparation procedure was optimized to minimize surface features (in the order of 5-10 microns due to the die surface morphology) and porosity (pores size of maximum 500 nm diameter), Figure 7.2.

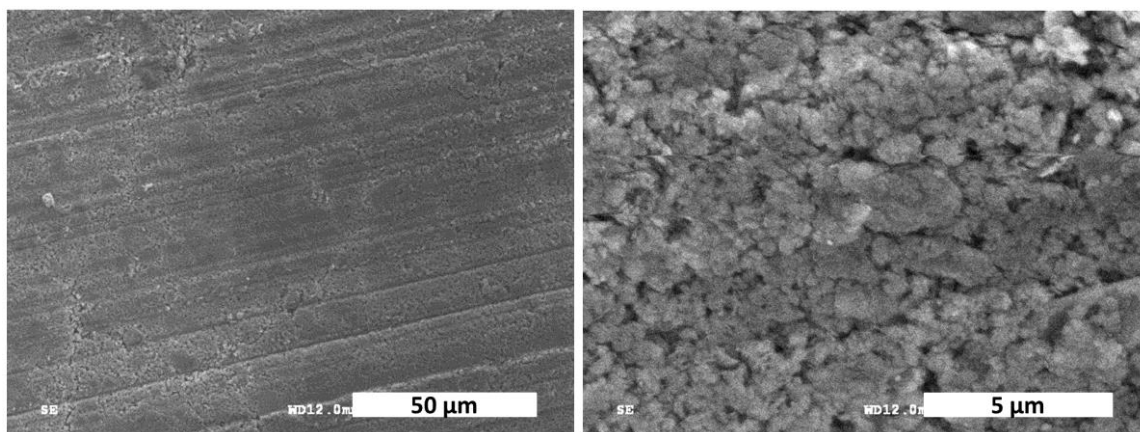


Figure 7.2 SE-SEM images of the surface of the metakaolin pellet.

Two methods can be used to determine the contact angle: sessile drop or captive bubble [218]. Sessile drop involves producing a droplet of the testing fluid and placing it on top of a substrate where the contact angle is then measured. Different trials were made with 1, 5 and 10 M NaOH solutions and soluble silicate type N ($M_s=3.22$) and type D ($M_s=2.0$). It was not possible to measure the contact angles as the solutions were immediately absorbed by the pellet: this is typical of highly wettable surfaces. The bubble penetration was so fast that it was not possible to determine the dynamic contact angles. The captive bubble method was also performed to obtain quantifiable results. According to this method the pellet was immersed in the testing fluid and an air bubble was placed underneath the submerged substrate and the contact angle is measured, Figure 7.3.

Each contact angle was the average of three values each obtained on a new pellet freshly immersed in a new solution. The image acquisition started approximately 30 seconds after the pellet immersion in the activating solution, thus the dynamic contact angle could not be measured. Every contact angle value was the average of 200 images acquired over time (≈ 1 minute) on a 3 μL bubble of air dispensed from the needle. Each image was analyzed with the software and the bubble shape fitted using the Young Laplace fit [218].

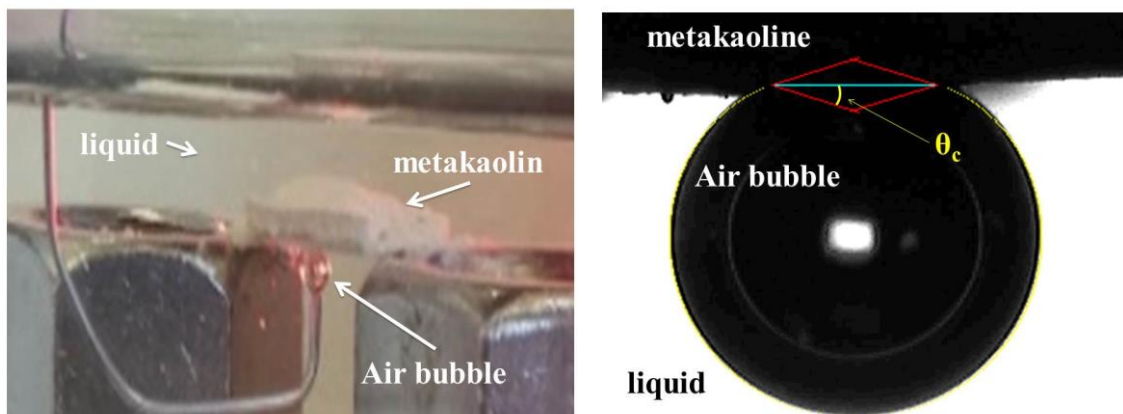


Figure 7.3 Left: photo of the MK pellet immersed in the liquid and the needle dispensing an air bubble. Right: image of the contact angle θ_c measured by the software; in yellow the Young-Laplace fitting of the bubble shape.

7.2.2. Result and discussion

The contact angle measurement could not be performed on the activating solution used in the research reported in Chapter 5 for two different reasons. Metakaolin pellet disintegrated when in contact with concentrated NaOH solution, i.e. $[\text{NaOH}] > 3\text{M}$. On the other hand concentrate soluble silicates, i.e. WG type N and WG type D, are too opaque and the camera could not successfully focus on the air bubble attached to the MK pellet. For these reasons we studied NaOH and waterglass solutions with different degrees of dilution. The results are plotted in Figure 7.4. A weak trend for both sodium hydroxide and sodium silicate was found: the more concentrated the solutions the lower the contact angles. It is therefore reasonable to assume that the contact angle of the activating solutions commonly used for geopolymers (i.e 10 molar sodium hydroxides and non-diluted sodium silicate type D) is well below 40° . Contact angles below 90° denotes wettable surface and the value of 30° is usually adopted to distinguish low and high contact angles [218].

These results suggested that both types of activating solutions can penetrate quite easily between the metakaolin platelets due to the high wettability, as observed during the sessile drop experiments. The platelets will likely break apart and fully disperse in the activating solutions for both sodium hydroxide based geopolymer and sodium silicate based

geopolymers. In fact soluble silicates are well known dispersants for kaolinite and other oxide particles [101]. Both contact angles are in the 30°-40° range, thus differences in the reaction kinetics of these two classes of geopolymer [25] are not due to different contact areas but different interfacial rates of reaction. A rheological method was developed to study these reaction rates as reported in the following Sections 7.3-7.5.

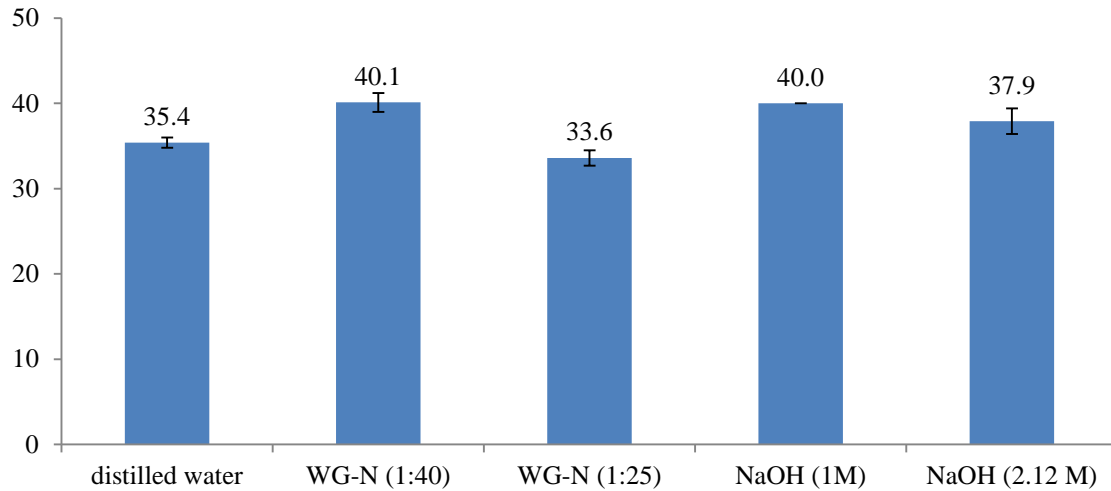


Figure 7.4 Contact angles between different solutions and metakaolin. WG-N stands for soluble silicate type N, in bracket the water dilution.

7.3. Rheology of MK-based GP

7.3.1. Introduction to concentrate suspensions and clays materials

The rheology of suspensions, i.e. solid dispersed in liquid, is an important field of study as the preparation, stability and application of these materials depends on their flow characteristics [209]. In particular rheological techniques can provide important information on the nature, interaction and stability of colloidal materials.

One of their most important parameters is the volume fraction Φ of solid which differentiates the various types of suspensions. A dilute suspension has a viscous response to the applied stress, as the particles have largely independent translational motions (Brownian motion) and

their properties are time-independent [209]. In concentrated suspensions movement of the particles is smaller than their dimension (or vibration range) and their properties are time-independent. At intermediate volume fractions the suspension is defined as concentrated, interparticle distance is similar to their size and hydrodynamic interactions and interparticle forces are more important than Brownian motion forces [209]. The combination of Van der Waals attraction forces, steric interactions and double layer repulsion forces can induce ordering of the solid particles in the liquid. To initiate the flow this structure needs to be disrupted and the material displays Bingham behaviour, Figure 4.3. On the contrary dilute and solid suspensions have respectively Newtonian and Hookean responses. The volume fraction has a direct impact on the suspension viscosity as shown in the Dougherty-Krieger equation, EQ. 5.7 [209].

The maximum packing factor Φ_m for monosized spherical particles is $\Phi_m=0.64$ and concentrated solutions usually have $\Phi>0.5$ [209]. The rheology of concentrated suspensions not only depends on the volume fraction of solids, but also on their particle size distribution, particle shape [261] and particle size [209]. The presence of the double layer can result in an effective volume fraction $\Phi_{EFF} \gg \Phi$ when the double layer thickness approaches the size of the particles. For this reason smaller GP precursor particles often need a higher amount of water to obtain similar flowability. Thus, the reduction of particle size (i.e. below 10 μm , depending on the system) causes a decrease in Φ_m and decrease in the volume fraction Φ at which viscoelasticity is observed. Also, flocculation of the suspension, i.e. aggregation of particles to form larger clusters [209], produces an increase in viscosity due to the lower efficiency of particle packing, i.e. lower the Φ_m . The maximum volume fraction can thus be considered as an indicator of the actual structure of the suspension and can also depend on time and shear history [261]. For fly ashes spheres with average size of 12 μm the maximum packing factor is $\Phi_m=0.49$ [262]. Based on the results presented in Section 5.2.1 we estimate even lower $\Phi_m=0.35-0.40$ for MK-based GP, due to the platelet structure of the calcined clay [261].

The interparticle forces arising from the surface charges have a pronounced effect on the suspension rheology. These charges are due to ionization of surface groups, differential dissolution of ions from the surface, isomorphous substitution, specific ion adsorption and

charged crystal surface [263]. There is a direct relationship between the surface charge and the zeta potential of the particles and the yield stress of the Bingham suspension [264]: when the zeta potential approaches zero, the suspension flocculates and the yield stress increases. Since the dielectric constant and the ionic strength of the solvent influence the double layer thickness, they also influence the suspension rheological responses.

Most concentrate suspensions, also referred to as structured liquids, are thixotropic: the material response depends on its shear history and it is time dependent [209]. Shear partially destroys the ordered structure of such “structured liquid”, thus its viscosity decreases; once shear is removed both the viscosity and the yield stress increase due to the rebuild of the structure. Thixotropy can be exploited to improve performance of cementitious materials. For example the addition of clay to OPC increases the cement stability, reduces aggregates segregation and reduces pressure on formworks [212].

The rheological response of MK-based GP is complicated by the platelets shape of the MK particles. Moreover the structure of clay particles, such as kaolinite, is known to be quite peculiar due to their unique surface properties: the face of kaolinite clay is always negatively charged due to aluminum substitution, while the charge at the edge depends on the pH. As a result the edges could be attracted by the faces of the platelets forming a “house of card structure” [265], Figure 7.5.



Figure 7.5 House of card structure observed in kaolinite suspension (from [265]).

For MK-based GP there are other complications, that is the high solids concentration of MK, the high electrolyte concentration in the activating solution and the complex nature of the

MK surface [124]. Furthermore, as the geopolymerization reaction takes place, both the solution and the solid surfaces change over time. Increasing the temperature is known to increase the reaction kinetics, but the viscosity of the activating solution also decreases, with Arrhenius dependence.

Albeit difficult to model, this complex dependence of the rheological properties on the physical and chemical properties of the materials makes rheological measurement an interesting probe to monitor microstructural changes, the effect of additives, and the reactions kinetics [212]. In the following Section we report on the studies of rheological behaviour of NaOH/MK-based GP, by following the evolution over time of viscoelastic parameters during oscillation time sweep tests. We have also assessed the effects of temperature and seeds on the evolution of the viscoelastic parameters and finally determined the rate limiting step for two MK-based GPs based on sodium hydroxide and sodium silicate respectively.

7.3.2. Flow curve and thixotropy of NaOH/MK-based GP

A NaOH/MK based GP was prepared according to the procedure described in Section 4.1.2, adopting a 10.3M NaOH solution, ratio solution/MK=1.16 and ratio H₂O/solids=0.69. The chemical formula of this GP can therefore be written as 1.00.1.00-2.00-10.90. This composition was chosen as it had low solution/MK ratio that allowed the GP to flow within the narrow gaps of the rheometer. The paste was poured in a Haake Rotovisco vt550 rotational rheometer using coaxial cylinder geometry. The grooved cylinders were 2 mm gap apart and the rheometer was operated in control rate mode, i.e. the strain rate was imposed and the shear stress was measured. The GP was subjected to a strain rate of 2 s⁻¹ for 30 seconds in order to eliminate residual stresses before the test began. The flow curve was measured from 0 to 2 s⁻¹ with intervals of 0.017 s⁻¹; these shear rates represented the real values inside a concrete truck mixer[266], although the shear rates experienced by the binder can be orders of magnitude higher when sand and other aggregates are present [266], [267]. For each data point a 2 seconds waiting time was adopted to favor the steady state. The total measurement time was 4 minutes and all the data were acquired within 10 minutes from the initial contact between activating solution and MK. A longer waiting time would not have

provided more accurate results as the increase in viscosity due to the reaction kinetics changed the material viscosity.

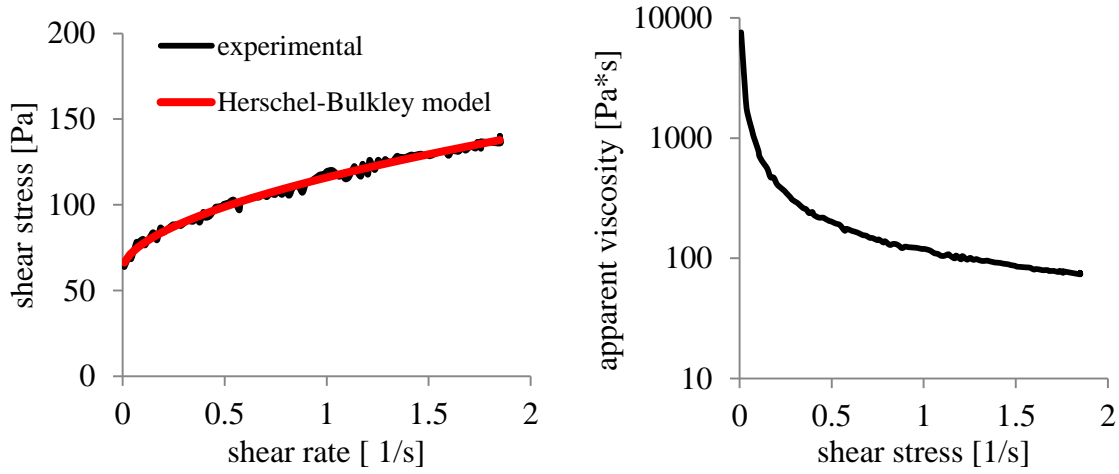


Figure 7.6 Flow curve (left) and apparent viscosity (right) of a NaOH/MK-based GP.

The flow curve of the GP is displayed in Figure 7.6 and the yield stress typical of a concentrated suspension was observed. The data could be fitted using the Herschel-Bulkley equation, EQ. 4.3, providing yield stress $\tau_0=62.6$ Pa, consistency $k=53.4 \text{ Pa}\cdot\text{s}^{0.56}$ and flow index $n=0.56$ (i.e. exhibiting shear thinning behaviour). The NaOH/MK-based GP can thus be described as a pseudoplastic suspension with yield stress. Depending on the particle size and water content of cements, Ordinary Portland cement has yield stress $\tau_0\approx 50$ Pa and consistency $k\approx 1 \text{ Pa}\cdot\text{s}$ [268]. The higher consistency of the MK-based GP may be due to the platelet shape of the MK which increased the energy dissipation due to viscous flow. Romagnoli [170] also obtained lower values for the consistency of a WG/MK-based GP as he measured a more diluted GP compared with the materials tested in this work. Cements with a yield stress values of 120 Pa failed to fill properly the formwork [269] but a cement with $\tau_0=60$ Pa could; thus the rheology of the GP adopted in this work is satisfactory for casting operations.

Following the same GP synthesis procedure the thixotropy of the MK-based GP was tested using a hysteresis loop, Figure 7.7. The curves indicated the thixotropic nature of the geopolymer: the shear stresses measured from 2s^{-1} to 0s^{-1} are lower than the ones measured

from 0s^{-1} to 2s^{-1} . In particular the shear stress exceeded 100 Pa when the material was tested after a period of rest, i.e. 1 minute. The shear stress peak in the up-curve was associated with the thixotropic nature of the GP paste: the shear stress dropped as a result of the destruction of the local structure. It is thus strongly recommended to keep the GP under constant shear stress until the casting operation, otherwise its yield stress and apparent viscosity increase compromising the casting operations.

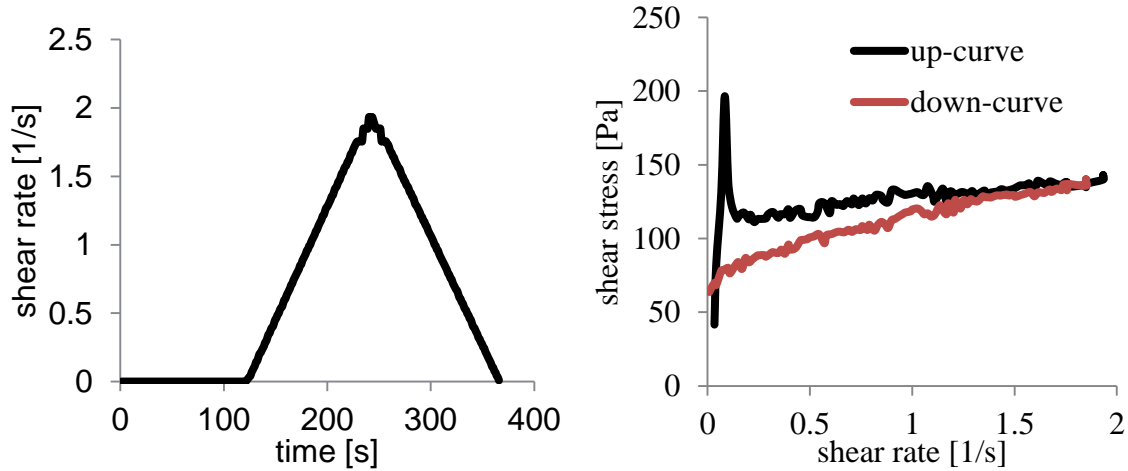


Figure 7.7 Hysteresis loop of a NaOH/MK-based GP. Left: shear rate program. Right: experimental hysteresis loop.

7.4. Dynamic rheology and crossover time

Dynamic rheology has been widely used to study the liquid-to-solid transformation for polymers, inorganic cements (including geopolymers) and hydrogels [259], [270]–[275]. By using this technique it is possible to separate the elastic from the viscous contribution of the viscosity. The storage modulus G' represents the energy elastically stored in the materials during a cycle, while the loss modulus G'' represents the energy dissipated during the viscous flow of the suspension. During time sweep experiments two plates controlled by the rheometer apply a sinusoidal shear to the material with a fixed frequency and maximum strain amplitude. The transition from a liquid to a solid is usually called gel point and it occurs when $G'=G''$: before the gel point the material is mostly viscous ($G''>G'$) and after

the material behaves more like a solid ($G' > G''$) [270]. The time at which the gel point occurs is also referred to as crossover time. Using dynamic rheology is also possible to follow the development of other rheological parameters of the setting geopolymer, such as the complex viscosity over time.

7.4.1. Materials and experimental set-up

A NaOH/MK based GP with composition 1.00.1.14-2.28-12.05 was prepared according to the procedure described in Section 4.1.2, adopting a 9.4M NaOH solution, ratio solution/MK=1.08 and ratio H₂O/solid=0.68. The geopolymerization reactions were studied at different curing temperatures, i.e. $T=20, 30, 40$ and 50°C . As reactions at 50°C occurred pretty fast, the reaction kinetics needed to be reduced. Thus we selected NaOH concentration smaller than the one adopted for the GP used in steady state experiments, i.e. 10.3 M NaOH.

The time sweep measurements at different temperatures were first carried on the unseeded GP, i.e. to provide a baseline. Then the same tests were performed to evaluate the effects of 2 wt% of the mass of MK of different seeds. The seeds investigated included Al₂O₃, faujasite, mordenite and fully stabilized zirconia ZrO₂ (more information on these seeds is available in Section 6.1.2). The seeds were dispersed in the activating solution for 30 seconds by vigorous hand-shaking before the MK was added.

Time sweep tests were performed using a Anthon Paar Rheometer mcr 502 equipped with a Peltier heater. Disposable aluminum bottom plates (Item: EMS/TEK 500/600) and 25mm aluminum top plates (Item: D-PP25/AL/S07) were coated with a glossy black all-purpose spray paint to avoid reaction between the plate and the alkaline solution. Without coating the aluminum was oxidized and produced hydrogen gas (see EQ. 7.2) at the interface causing wall slip, especially at higher temperatures. Nonetheless the coatings strength also represented the limit of this experimental set-up: at moderate GP viscosity, i.e. $\eta=1000-2000$ Pa·s, the shear stress experienced by the coating caused its detachment and the end of the experiment.



Immediately after mixing the GP, it was transferred to the rheometer and the top plate was lowered a 1mm from the bottom plate, excess geopolymer was scraped away and mineral oil was applied around the circumference of the top plate to limit water evaporation, Figure 7.8. The gap between the plates was kept at 1mm, the oscillation frequency at 1 Hz and the strain at 3% for all the test, following the procedure adopted by [273] to determine the gel point of crosslinkable hydrogels.

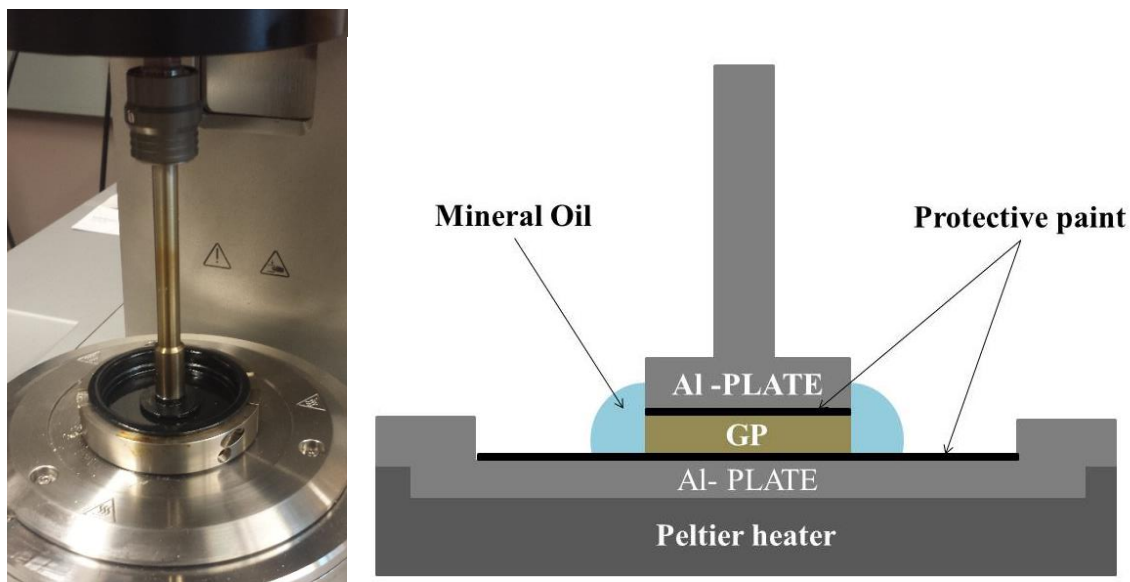


Figure 7.8 Left: picture of the rheometer. Left: schematic of the parallel plate geometry.

7.4.2. Results and discussion

The storage modulus G' , dynamic modulus G'' ; and the complex viscosity η^* for an unseeded GP at 30°C are displayed in Figure 7.9. An initial decay of moduli and viscosity was detected for all suspensions and it was due to the thixotropic breakdown until an equilibrium between flocculation and deflocculation was reached [276]. The MK dissolution could not be responsible of the viscosity decrease as delayed experiments, Figure 7.9 right, also displayed a similar drop in viscosity. The GP suspension reached a viscosity minimum $\eta \approx 50\text{-}100\text{Pa}\cdot\text{s}$ similar to the values obtained during steady state experiments, Figure 7.6 right.

Initially G'' values were larger than G' values and constant until the geopolymerization reaction induced an increase in G' , G'' and η^* .

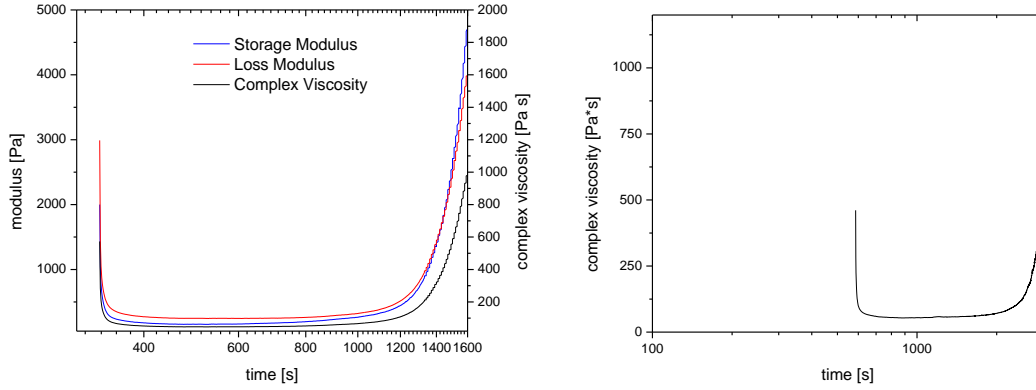


Figure 7.9 Left: moduli and complex viscosity measured during a time sweep test for the unseeded GP at 30°C. Right: complex viscosity for an unseeded GP at 30 °C measured during a delayed time sweep test.

There can be many phenomena occurring during geopolymerization reactions which could explain the increase in viscosity. For example, according to Krieger-Dougherty (EQ. 5.7) the viscosity of the suspension can increase due to the changes in chemistry of the solution or water consumption, which leads to an increase in viscosity η_0 . Flocculation of MK or geopolymer gel can also increase the viscosity by reducing the maximum packing factor Φ_m .

$$\eta = \eta_0 \left[1 - \left(\frac{\Phi}{\Phi_m} \right) \right]^{-[\eta]\Phi_m} \quad \text{EQ. 7.3}$$

As expected, temperature had a dramatic effect on the GP reaction kinetics [119], [120]. In Figure 7.10 the storage modulus, loss modulus and complex viscosity for different GPs are shown. At higher temperatures there was a decrease in time at which the moduli and the viscosity started to increase. A similar but smaller effect was also obtained by seeding the GP while keeping the temperature constant.

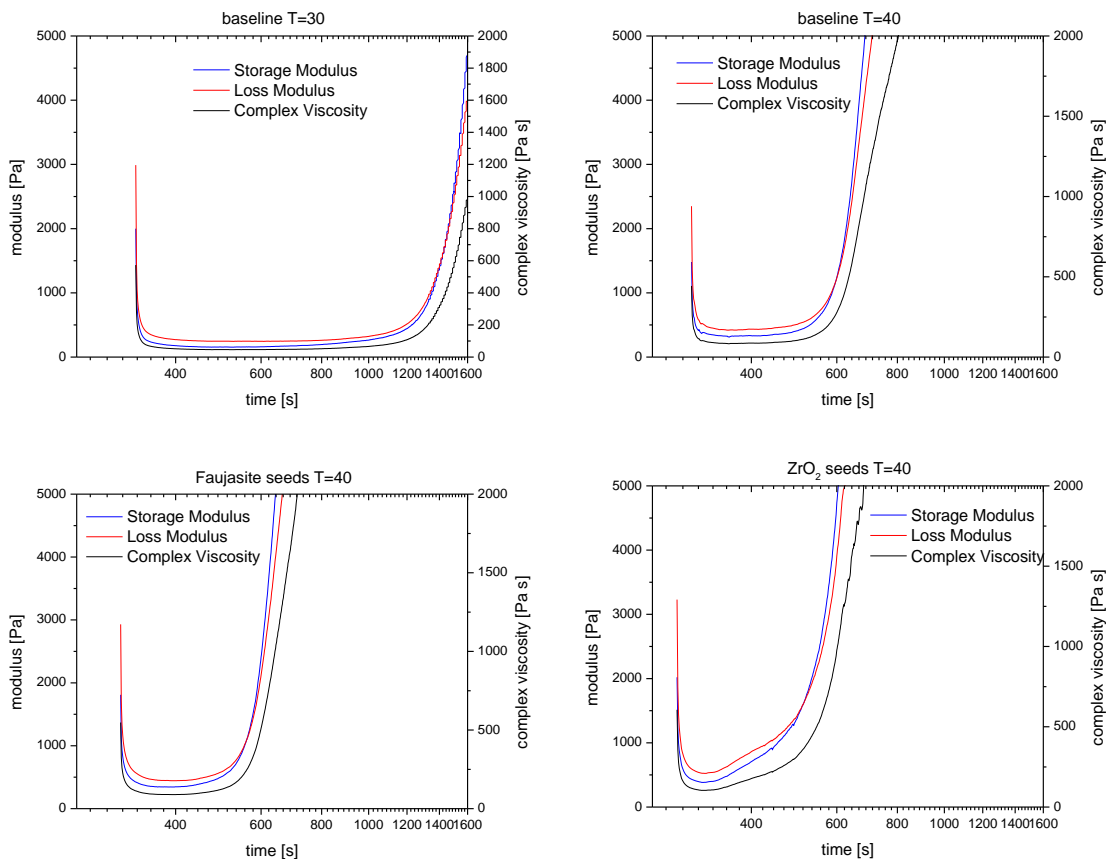


Figure 7.10 Time sweep tests for unseeded GP at 30°C (top left), unseeded GP at 40°C (top right), faujasite seeded GP at 40°C (bottom left) and zirconia seeded GP at 40°C (bottom right).

While qualitative information could be obtained by the visual inspection of these rheograms, the crossover time could quantify the effect of temperature and seeding on the geopolymerization reactions. Crossover point was measured at the point in which the loss tangent $\tan\delta = G''/G' = 1$. The precision of the method was tested by replicating the time sweep test for unseeded GP cured at 40°C, Figure 7.11. The absolute values of the moduli were slightly different but the crossover points were similar: 599 and 595 seconds.

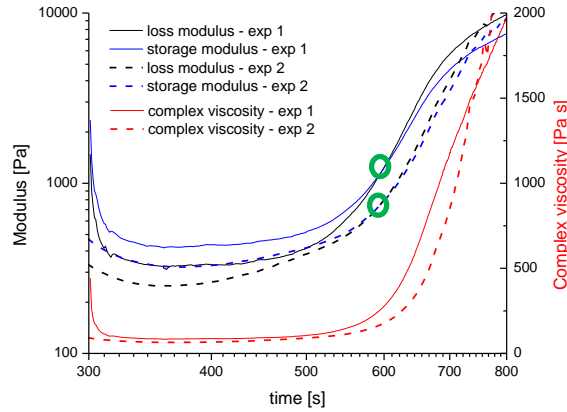


Figure 7.11 Repeated time sweep test for unseeded GP cured at $T=40^{\circ}\text{C}$ to assess the reproducibility of the method to determine the crossover point. Crossover points are marked in green.

By plotting the crossover times at different temperatures is it possible to calculate the activation energy of the reaction. The difficulties in describing the kinetics and activation energy of heterogeneous reactions were already reviewed in Section 2.2.4.2. “Geopolymerization is clearly a complex multistep process and so the calculation of a single activation energy for the entire process is a gross simplification. However, ... knowledge of the global activation energy may be of some value in analysing the kinetics of this process...” [146]. In this case we perceive the value of the calculation of the global activation energy as helpful in the quantification of the seeding effect on the reaction kinetics.

In Figure 7.12 the Arrhenius plot, with the Least Squares Fitting (LSF) lines are shown. EQ. 7.4 was used in the LSF and we assumed the crossover time to be inversely proportional to the overall geopolymerization constant rate. The correlation coefficients R^2 were close to $R^2=1$ for all GP except for the GP seeded with faujasite. This lower value could be due to experimental error or due to different rate limiting steps occurring at different temperatures as previously explained in Section 2.2.4.2.1.

$$t_{\text{Crossover}} \approx \frac{1}{k} = \frac{e^{(E_{\text{act}}/RT)}}{A} \quad \text{EQ. 7.4}$$

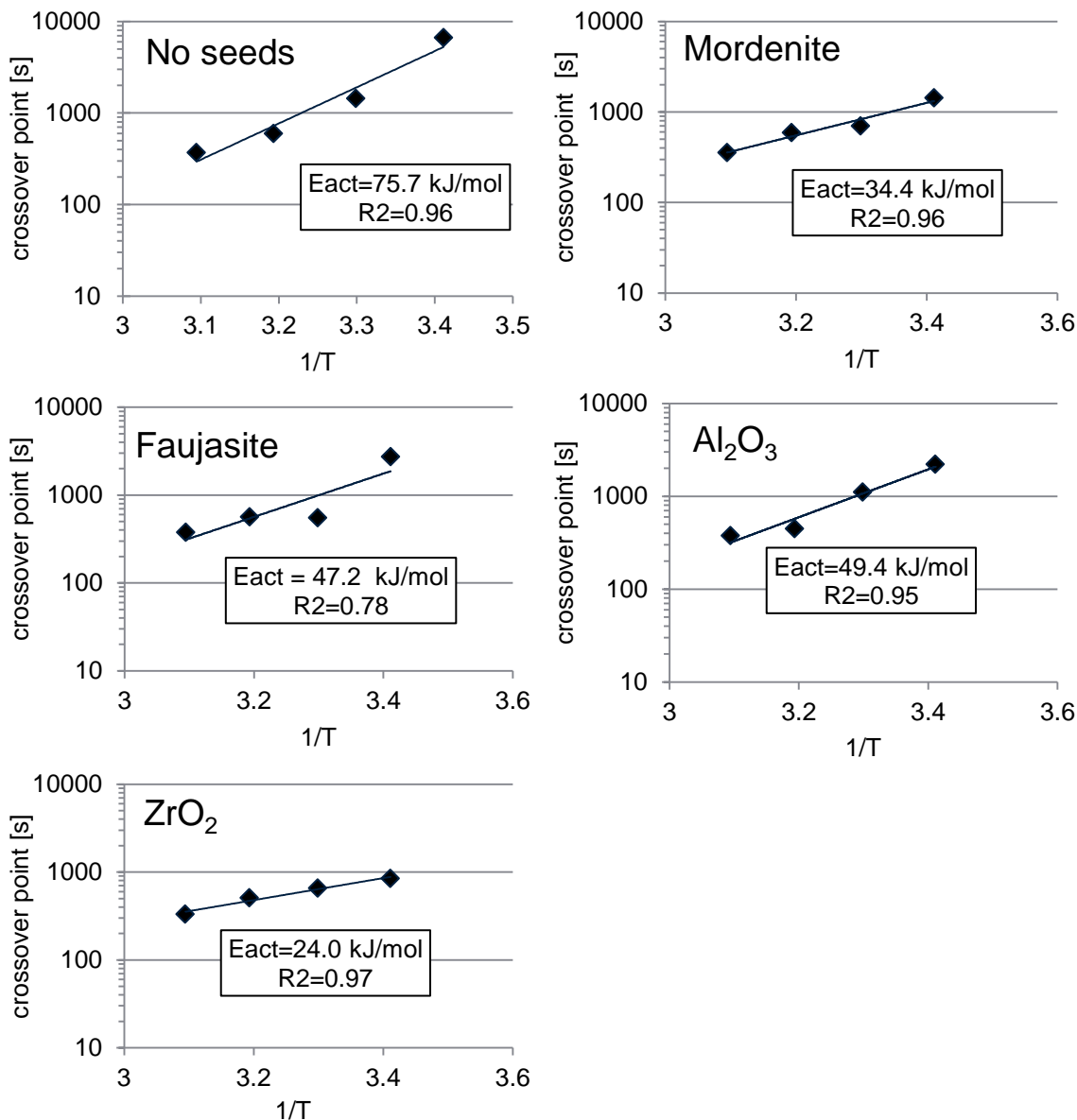


Figure 7.12 Arrhenius plot of the crossover times at different temperatures for seeded and non-seeded GP.

The activation energies for the unseeded and seeded GP are shown in Figure 7.13. The value $E_{act}=75.7$ kJ/mol obtained for the NaOH/MK based GP was in agreement with literature values obtained during similar rheological tests [259]; MK-based GP had $E_{act}=74.5$ kJ/mol when reacted with sodium silicates and $E_{act}=64.8$ kJ/mol when reacted with potassium silicates. Energy-dispersive X-ray Diffractometry tests performed on a GP based on metakaolin and potassium silicate found a smaller value: $E_{act}=31.5$ kJ/mol [146]. A value of

E_{act} =86.2 kJ/mol instead was obtained by microcalorimetry on a fly ash based geopolymer [277]. To the best of our knowledge no literature values are however available for NaOH-based GP. The crystallization of zeolite LTA from a suspension of MK in NaOH measured by XRD had an activation energy of E_{act} =34.6 kJ/mol [148].

In summary, the activation energies obtained by the time sweep tests are comparable with the values available in literature. It is possible to lower the activation energy of the geopolymerization reaction by using different type of seeds in small quantities, i.e. 2 wt% over the MK mass. The lowest value was obtained by using nanosized ZrO_2 . The decrease in activation energy can be explained in term of nucleation of the geopolymer gel: the homogenous nucleation of gel had a higher activation energy compared with the heterogeneous nucleation and growth of the GP gel on the seeds surfaces.

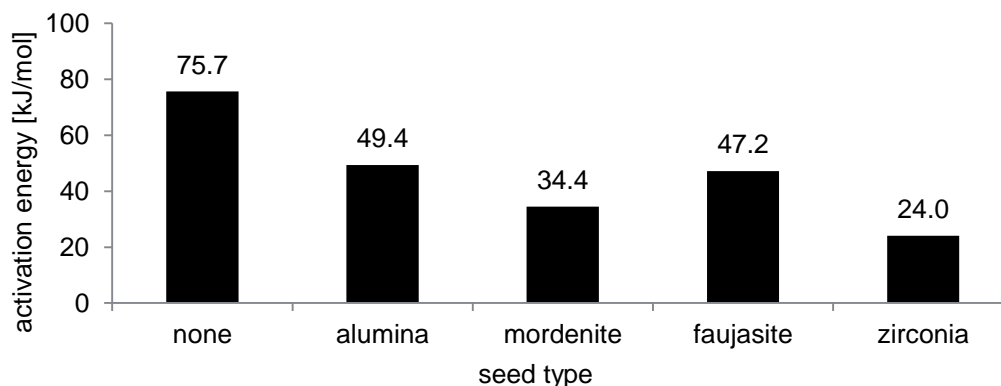


Figure 7.13 Geopolymer activation energies for unseeded and seeded GPs obtained from the Arrhenius plot of the crossover points in time sweep experiments.

7.5. Dynamic rheology and rate limiting steps

In the previous Chapters we observed how hydroxide and silicate activated geopolymers are different in terms of their crystallinity, compressive strength, compositional degrees of freedom. Other studies have shown that their reaction molecular mechanisms are also different [114]. In NaOH-based GP the homogeneous nucleation of the gel occurs only when enough monomers and oligomers had detached from MK. For a WG-based GP the nucleation

is immediate due to the pre-existing silicates in solution. In another study silicates were suggested to have a templating function in the nucleation and growth of the GP gel [203].

Time sweep tests were performed on hydroxide and silicate activated geopolymers GP, both unseeded and seeded, in order to determine if they have the same rate limiting step, Figure 7.1. We expected the seed to have negligible effect on the WG-based GP as in this system the silicate acts already as nucleation sites.

7.5.1. Materials and experimental set-up

Two different GPs were prepared, one based on soluble silicate (GP-WG) and one based on sodium hydroxide (GP-NaOH). GP-WG had a formula 1.00-1.00-3.35-13.68, $H_2O/solid=0.60$ and $solution/solid=1.43$, while GP-NaOH had a formula 1.00-1.00-2.00-15.20, $H_2O/solid=0.84$ and $solution/solid=1.27$. For both GPs the effect of nanocrystalline colloidal faujasite seeds was studied; 2 wt% of faujasite (over the mass of MK) was adopted for all experiments. A different Anton Paar Rheometer mcr 502 equipped with a Peltier heater was used in this study. The selected curing temperatures were $T=25, 30, 35$ and $40^\circ C$ and all the other parameters were kept the same as in the experiment described in the previous Section.

7.5.2. Results and discussion

The complex viscosities obtained for the 16 time sweep tests are shown in Figure 7.14. All GPs display an initial decrease in viscosity due to thixotropic breakdown. As previously observed, higher curing temperatures resulted in faster reaction kinetics.

During the initial stages of geopolymerization of unseeded NaOH-based GP the viscosity remained constant, followed by a non-linear growth. The onset of growth was probably due to the nucleation and growth of the geopolymer gel. Seeding had two effects on the NaOH based GP: the induction time (time at constant viscosity) was shorter; the increase in viscosity was steeper. Thus presence of seeds promoted nucleation and growth of the gel and improved the dissolution of metakaolin.

WG-based GP had a different behaviour: the increase in viscosity was linear throughout the time sweep experiment. As the monomers detached from the MK, they immediately reacted with the silicate in solution to increase the gel molecular weight and interconnectivity [114]. The colloidal faujasite seeds had no evident effect on the reaction kinetics: since the soluble silicates have a seeding effect, the addition of other seeding agent is superfluous.

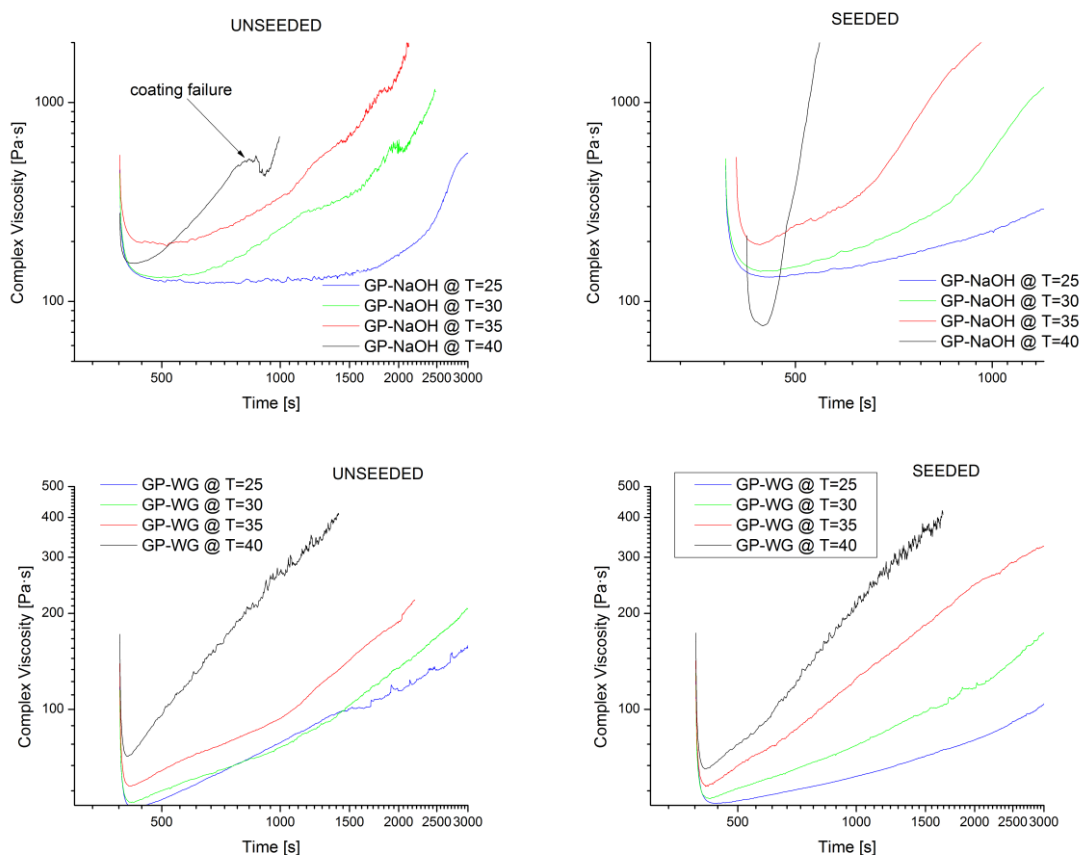


Figure 7.14 Complex viscosity measured during time sweep tests for unseeded NaOH-based GP (top left), faujasite seeded NaOH-based GP (top right, note different scale), unseeded WG-based-GP (bottom left) and faujasite seeded WG-based GP (bottom right).

Although the qualitative inspection of the rheograms already provided important insight on the GP reactions, a model was implemented in order to quantify the effect of seeding and curing temperature. NLSF using the Avrami equation could not properly represent the observed data. Papo [276] studied the hydration of Portland cement at different water-to-

cement ratios using dynamic rheology and time sweep test. The model in EQ. 7.5 was used to fit the evolution of complex viscosity η^* over time t .

$$\eta^* = \eta_0^* + (1000 - \eta_0^*) \left(\frac{t}{t_R} \right)^N \quad \text{EQ. 7.5}$$

where η_0^* is the initial complex viscosity, t_R is the setting time and N is the kinetics factor. The setting time corresponded to the time the geopolymers assumed viscosity $\eta^*(t_R)=1000$ Pa·s. This value did not represent the real setting time, as the viscosity at the setting time (as determined by Vicat needle test) is at least two orders of magnitude higher [272]. Vicat needle test is mostly a measurement of the development of yield stress rather than viscosity. The value $\eta^*(t_R)=1000$ Pa·s simply represented an arbitrary reference point in which the cement was highly viscous. We adopted this value because it was already used by Papo [276] and because we could not measure viscosity higher than $\eta^*=1000\text{-}2000$ Pa·s due to the rupture of the plate protective coatings. Papo model could successfully describe all the rheograms, Figure 7.15, and the results of the NLSF are shown in Table 7.1.

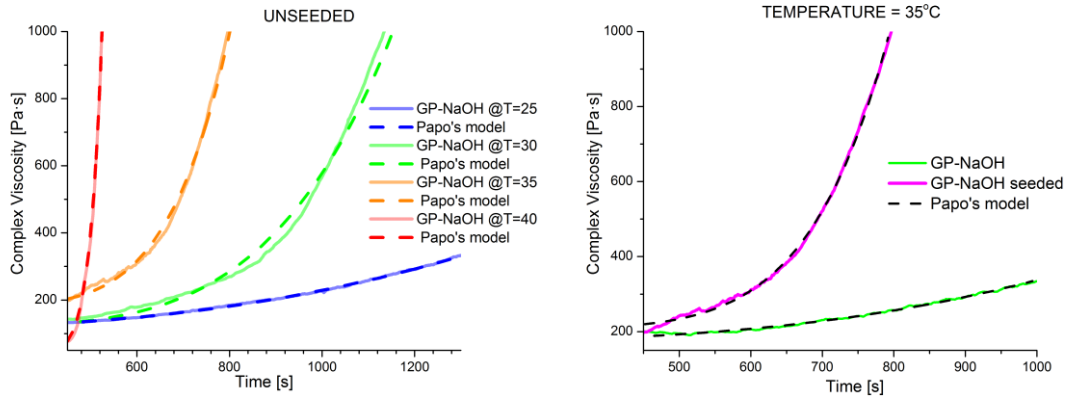


Figure 7.15 Time sweep tests performed on GPs. Solid lines represent the measured viscosity, dashed lines represent the NLSF using Papo's model. Left: effect of temperature on unseeded NaOH-based GP. Right: effect of faujasite seeding on NaOH-based GP cured at 35°C.

Table 7.1 Parameters of Papo's model obtained by NLSF of the complex viscosities for different GP pastes.

		temperature [°C]	n_0 [Pa·s]	t_r [s]	N
GP-NaOH	unseed	25	125	3801	4.60
		30	113	2008	2.92
		35	177	1652	3.26
		40	111	980	3.74
	seeded	25	116	2323	2.44
		30	120	1153	4.58
		35	180	800	6.20
		40	33	524	20.00
GP-WG	unseed	25	13	36487	0.75
		30	43	10180	1.45
		35	52	5657	1.77
		40	1	2420	1.47
	seeded	25	49	23961	1.37
		30	45	15704	1.24
		35	12	7634	1.07
		40	26	2400	1.88

Papo's model parameters obtained by NLSF, Figure 7.16, clearly show the effects of temperature and seeding for the different GPs. The setting times t_R were shorter at higher temperatures and in general NaOH-based GP set faster than WG-based GP, in accordance with literature reports [25]. Seeding had an evident accelerating effect on NaOH-based-GP, but no clear effect on the WG-based-GP. Interesting observations can be made on the kinetic factors N . For WG-based GP the kinetic factor of $N \approx 1-2$, did not change significantly with temperature or seeding. Unseeded NaOH-based GPs had higher kinetic factors compared with WG-based GP. Seeding of NaOH-based GPs had a pronounced effect, especially at elevated temperatures $T=35$ and 40°C .

The explanation of these trends can be ascribed to the reaction mechanisms. The rate limiting step for a WG-based GP was the dissolution of MK. As the silicate solutions are known to act as buffers, the pH during initial dissolution was approximately constant and so was the metakaolin dissolution. Nucleation could not be the rate limiting step as soluble silicates in solution immediately reacted with the monomers in the solutions. For NaOH-based GPs

cured at $T > 35^\circ\text{C}$ the dissolution of MK in the highly caustic activating solution was extremely fast and the rate limiting step was the nucleation and growth of the geopolymer gel; in this case seeding caused a large increase in the kinetic factor, from $N=2.44$ to 20. At lower temperatures the effect of seeding on NaOH-based GP was relatively smaller, thus the rate limiting step was once again the dissolution of MK. Similar results were observed for other GP systems [163], [165], [166], [177]: seeding had an clear effect only when the activating solution was an metal hydroxide, but had negligible effect when soluble silicate were used.

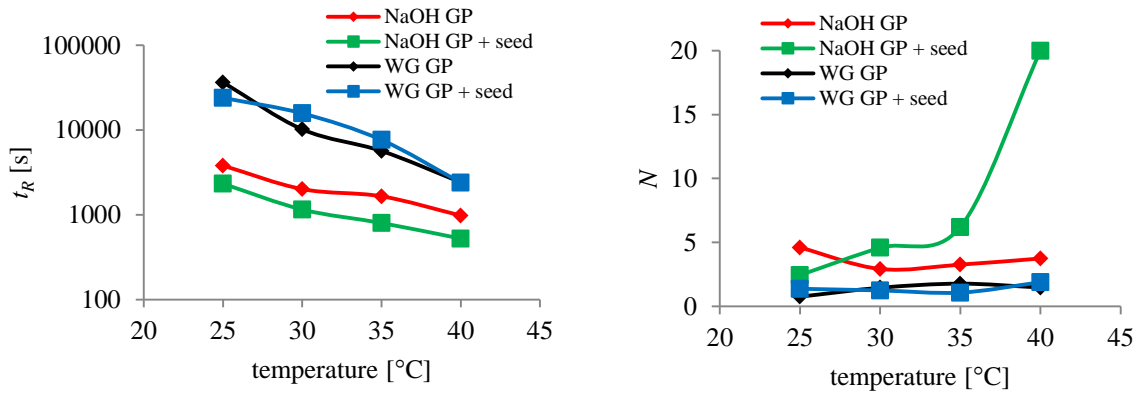


Figure 7.16 Setting times t_r (left) and kinetic factors N (right) obtained by NLSF of the rheograms using Papo's model.

7.6. Summary and conclusions

In this Chapter the wettability and rheological properties of MK based geopolymers were measured using contact angle and time sweep tests to determine the geopolymerization rate limiting step and to obtain more experimental evidences on the molecular mechanisms involved. It was determined that NaOH/MK-based GPs are thixotropic pseudoplastic suspensions with a yield stress and their behaviour can be described by Herschel-Bulkley equation, with yield stress $\tau_0=63$ Pa, consistency $K=53$ Pa·s and flow index 0.56.

Both crossover time and NLSF of complex viscosity could provide important information on the transformation from liquid slurry to solid materials. Geopolymerization is a thermally activated reaction with the overall energy of activation of $E_{act}=75.7$ kJ/mol. The addition of 2 wt% of inorganic seeds (calculated over MK mass) could decrease the activation energy and accelerate the reaction kinetics. A more detailed analysis in the temperature range 25-30°C revealed that the rate limiting step for NaOH/MK-based GP is the dissolution of MK, while at $T>30^{\circ}\text{C}$ the rate limiting step is the nucleation and growth of the geopolymer gel. Soluble silicates instead facilitate the nucleation and growth of the geopolymer, thus the rate limiting step for WG/MK-based GP is the MK dissolution even at $T>30^{\circ}\text{C}$.

The slower reaction kinetics of WG-based GP is due to the slower dissolution of MK in the activating solution as the other causes were ruled out: contact angle measurements suggested that soluble silicate can easily wet and penetrate between the MK particles; dynamic rheology tests showed that nucleation and growth of the gel is instantaneous.

In conclusion, seeding can be an effective method to accelerate the consolidation kinetics of NaOH/MK-based GP cured at mild temperatures, but it is less effective in low temperature curing or for any WG/MK based GPs. The largest accelerating effect was induced by zirconia nanoseeds, which lowered the activation energy to $E_{act}=24$ kJ/mol.

8. Geopolymer phase transformations and crystal engineering

8.1. Rationale

Among the different precursor materials, metakaolin MK [7] and aluminosilicate glasses [198] have the least amount of contaminants and no heavy metals impurities. Moreover, their homogeneous distribution of alumina and silica species results in a more predictable geopolymerization reaction as compared to fly ash based GP. Since MK-based GPs are relatively cheaper than synthetic aluminosilicate glasses, they are the favorite candidates to produce functional geopolymer for advanced applications.

Most studies on MK-based GPs focused on increasing the mechanical strength of the binders, mainly by increasing the Si/Al ratio using alkaline silicate [62]. Sodium silicates modify the overall Si/Al and decrease the H₂O/solid ratio, but they also act as templates for aluminates assembly [203]. Fewer studies have focused on the crystallization of zeolites in metakaolin-based geopolymer, usually LTA-type zeolite, NaX-type zeolite (faujasite) and hydroxodalite. Only Zhang [203] quantified their crystallinity and nobody has ever tried to control the type and amount of zeolite obtained. Increasing the amount of sodium silicate usually decreases the crystallinity and when activating solution has a SiO₂/Na₂O > 0.8 the geopolymer is generally completely amorphous [73]. The degree of crystallinity and reaction kinetics increase by increasing the molarity of the solution and temperature [119], and increasing the Si/Al by replacing metakaolin with fly ashes seems to increase the faujasite in highly diluted condition [204].

In Section 2.2.4.6 and 6.2 and in Chapter 7 we introduced and tested the effects of seeds in the geopolymerization reactions and on the final geopolymer structure. Since few works have dealt with zeolite crystallization within functional geopolymer, this Chapter 8 provides new evidences on the factors affecting the mechanisms and the final structure of this phase transformation. It is beyond the scope of this work to implement these findings into empirical geopolymerization models. Here we studied the reaction kinetics and the degree of crystallization of metakaolin-based functional geopolymers seeded with nanocrystalline colloidal faujasite, thus avoiding seeds agglomeration and amorphization through grinding.

We used a multifactorial design and analysis of the variance (ANOVA) to determine the most influential factors for the conversion of metakaolin-NaOH-based geopolymer into zeolite and to identify synergistic or competitive effects between the variables. The effects of the DOE factors on each response are individually described in the Sections 8.4 and the most significant of them are further discussed in Section 8.5.

8.2. Design of experiments

The kinetics of geopolymerization depends mainly on: (i) the concentration of the activating solution and the presence of silicate species, which control the precursors dissolution and aluminosilicates condensation reactions; (ii) the presence of seeds, which can modify the nucleation rate of solid product. The compositional parameters under investigation in this work included the ratios Na/Al and H₂O/solid; the processing factors included the curing time and temperature, and the seeds included synthetic nanocrystalline colloidal faujasite and small quantities of sodium silicate. Soluble silicate concentrations were chosen to match the silica modulus in the colloidal faujasite solutions, refer to Table 8.2. The responses were obtained from the deconvolution of the FTIR-spectra and Rietveld refinement with internal standard. Setting times were measured according with ASTM C807 [217] and SEM microstructural analyses were also performed to verify the QXRD results.

In total 180 geopolymers structures were characterized by varying three compositional parameters (i.e. Na/Al, H₂O/solid, and seeding type) and two curing parameters (i.e. temperature and time), Table 8.2. The parameter Na/Al was chosen because it was already determined to be an important factor which influences the crystallinity of the geopolymer [203], the central point for this parameter was selected at Na/Al=1 as suggested by many [38], [62], [73]. By changing this parameter we indirectly also varied the alkalinity of the activating solution. The other compositional parameter investigated here was the H₂O/solid in order to understand the effects of dilution and porosity on the geopolymer setting kinetics and conversion to zeolite. Preliminary SEM analyses reported in Section 5.2.1 suggested that geopolymer crystallinity was enhanced by porosity. This observation suggested that a volume change may be associated with the crystallization and it may explain why some GPs

remain amorphous (i.e. adding silicate reduces the GP porosity). Unfortunately the framework density FD of the amorphous gel is unknown, while faujasite, LTA and sodalite have respectively a FD of 12.7, 12.9 and 17.2 tetrahedra/Å³ [24].

The H₂O/solids factor is also important because it differentiates geopolymer materials from aluminosilicate gels and zeolites [199]. Since it indirectly also influences the ratio solid/solution, it is one of the main parameters affecting the rheological properties, and thus the processability, of MK-based geopolymers [170]. We have chosen the values H₂O/solid=0.66 and 1.02 because the former represents the minimum achievable value of solution/solid to produce an initial homogeneous paste, as determined by the previous experiments.

Samples coding with letters A, B, C, D, E, Figure 8.1 and Table 8.1, reflects the variation of the parameters Na/Al and H₂O/solid between two levels with central points, i.e. GP type E. The compositions were varied so that samples A, D and E have similar concentration of the sodium activating solution (7.5M NaOH), while B and C have respectively low and high molarities, Figure 8.1 and Table 8.2. The difference between samples A, D and E consisted in the ratio solution/MK. Similar NaOH concentrations have similar solvation conditions of the sodium ions and thus similar ion-pairing. NaOH concentration of 7.5M is equivalent to a H₂O/Na₂O ratio of 15.2 where the Na⁺ and the OH⁻ ions are poorly solvated. Complete solvation occurs at H₂O/Na₂O>33, which correspond to 4.7 M NaOH (Section 2.2.3).

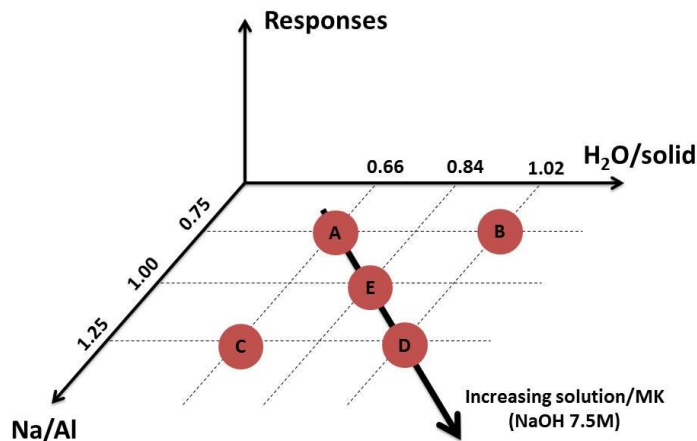


Figure 8.1 Representation of the GP compositions and GP codes in the adopted 2^2 factorial design with a central point.

Table 8.1 Geopolymers formulas for samples A, B, C, D and E.

code	GEOPOLYMER FORMULA			
	Na ₂ O	Al ₂ O ₃	SiO ₂	H ₂ O
A	1.00	1.33	2.67	15.21
B	1.00	1.33	2.67	23.41
C	1.00	0.80	1.60	10.04
D	1.00	0.80	1.60	15.44
E	1.00	1.00	2.00	15.20

We conducted two different ANOVA analyses on samples A, B, C, D and samples A, D, E because a single analysis could not be performed: ANOVA requires the factors to be independent of each other, which is not the case for Na/Al, H₂O/solid and solution/MK, see Section 5.1.1 and Table 8.2 for further details. By performing two distinct analyses we could decouple the effects of NaOH concentration, Na/Al, solution/MK and H₂O/solid, Table 8.7. If an effect of the Na/Al factor is detected for a particular response at constant H₂O/solid, this can be due to an increase in Na/Al or an indirect increase in NaOH concentration. We can discern these two contributions by looking at the response for different levels of the factor solution/MK, in which NaOH molarity is fixed and Na/Al changes. If we detect a statistically

significant effect of the factor solution/MK, then molarity does not play a fundamental role in the response while Na/Al does. If ANOVA analysis suggests there is no effect of the factor solution/MK, then the effect of Na/Al is probably an indirect consequence of the increasing NaOH concentration. These considerations are valid especially when the effect of H₂O/solid is negligible, i.e. p -value>0.05, Table 8.5.

Beside the unseeded GP, we used two different seed types: 2wt% of nanocrystalline faujasite calculated vs the total MK content of the geopolymer formulation (these samples have postfix “s” after the letter code, Tab. 19) and sodium silicate (with postfix “w” after the letter code in Tab. 19). Sodium silicate were included in the experimental design because it has a templating role in the geopolymer synthesis [203] and different Si/Al may change the final crystalline phases [204]. Moreover, samples seeded with waterglass were the baseline of zeolite-seeded geopolymer since they could separate the role of crystalline zeolite from the sodium silicate solution in which those nanocrystals were dispersed (see Section 6.1.3.2 for details on the seeds). The silica concentration, expressed in term of silica modulus of the activating solution $M_s=0.11$, was kept below the value of 0.80, above which the geopolymer is usually completely amorphous [73]. Samples without seeds have a Si/Al=1, while seeded GP have a Si/Al \approx 1.05; the silicon belonging to quartz and halloysite impurities was ignored when calculating the GP chemical formula.

Temperature and time were also determined to be an important factor both in terms of reaction extent and the final degree of crystallinity [119], [203]. By including these two factors we could also study the effects of GP composition and seeding on the reaction kinetics. The curing temperatures and times are suffixes in the geopolymer code, Table 8.2. For example, Bs-40-4 represents a geopolymer with H₂O/solid=1.02, Na/Al=0.75, 2% nanocrystalline faujasite seed, cured at 40°C for 4 days.

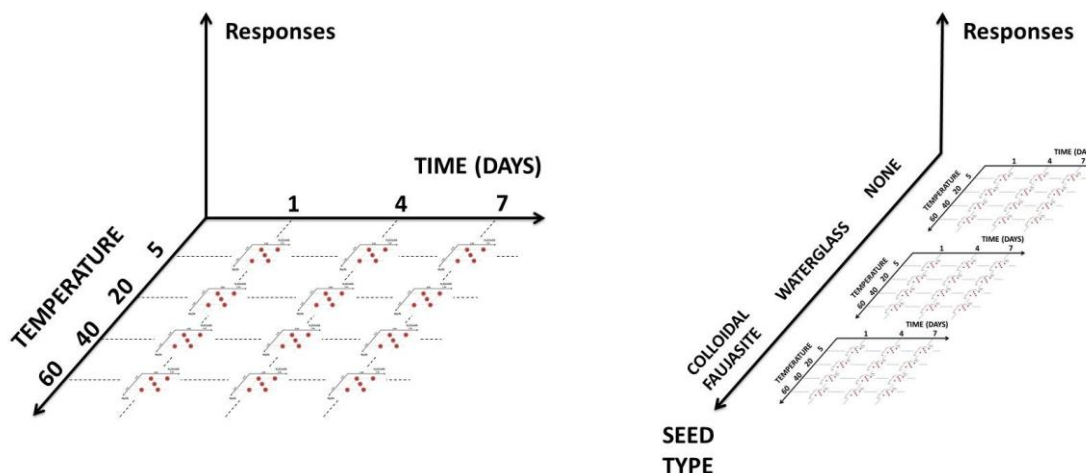


Figure 8.2 Representation of the 180 characterized GPs: 5 compositions, 4 temperatures and 3 curing times (left), and 3 seeding conditions (right; each of the three systems in this graph is the time-temperature system copied from the left figure).

Table 8.2 List of all geopolymer compositions used in this study. Geopolymer parameters are fixed and derived ratios calculated based on the real metakaolin content in Powerpozz. MK stands for metakaolin, WG-N for sodium silicate type N, WG-Ms for molar ratio $\text{SiO}_2/\text{Na}_2\text{O}$ of the activating solution

CODE	GEOPOLYMER PARAMETERS					MIXING PROPORTIONS					ACTIVATING SOLUTION		
	H ₂ O/ solid	Na/ Al	H ₂ O/ Na ₂ O	solution/ solid	Si/ Al	MK	Coll zeol	NaOH (20.45M)	WG-N	H ₂ O	NaOH		WG
											wt%	mol	Ms
A	0.66	0.75	15.2	0.95	1.00	51.2	0.0	22.1	0.0	26.7	23.8	7.5	0.00
B	1.02	0.75	23.4	1.37	1.00	42.2	0.0	18.2	0.0	39.7	15.7	4.6	0.00
C	0.66	1.25	10.0	1.15	1.00	46.6	0.0	33.4	0.0	20.0	32.9	11.2	0.00
D	1.02	1.25	15.4	1.61	1.00	38.3	0.0	27.5	0.0	34.1	23.5	7.4	0.00
E	0.84	1.00	15.2	1.27	1.00	44.1	0.0	25.3	0.0	30.6	23.8	7.5	0.00
As	0.66	0.75	15.7	0.98	1.04	49.6	9.4	18.5	0.0	22.5	-	-	0.11
Bs	1.02	0.75	24.2	1.40	1.04	40.8	7.8	15.2	0.0	36.2	-	-	0.11
Cs	0.66	1.25	10.4	1.19	1.07	44.8	8.5	29.1	1.9	15.6	-	-	0.11
Ds	1.02	1.25	16.0	1.66	1.07	36.9	7.0	24.0	1.6	30.5	-	-	0.11
Es	0.84	1.00	15.8	1.31	1.05	42.5	8.1	21.7	0.9	26.7	-	-	0.11
Aw	0.66	0.75	15.5	0.98	1.04	50.4	0.0	21.0	3.2	25.3	-	-	0.11
Bw	1.02	0.75	23.8	1.41	1.04	41.5	0.0	17.3	2.7	38.5	-	-	0.11
Cw	0.66	1.25	10.3	1.20	1.07	45.5	0.0	31.6	4.9	18.1	-	-	0.11
Dw	1.02	1.25	15.8	1.67	1.07	37.5	0.0	26.0	4.0	32.5	-	-	0.11
Ew	0.84	1.00	15.5	1.31	1.05	43.2	0.0	24.0	3.7	29.1	-	-	0.11

The activating solutions were prepared starting from a 20.45M NaOH master batch. Two days before casting NaOH was diluted in water and soluble sodium silicate (waterglass type N, PQ corp®) was added and continuously mixed using magnetic stirrer. Then the colloidal zeolite dispersion was added to the activating solution, mixed for 1 minute and immediately added to the metakaolin. The geopolymer pastes were prepared according to the procedure described in Section 4.1.2, poured in different airtight HDPE containers and placed at their respective curing temperatures in hot or cooling baths: 5°C, 20°C, 40°C and 60°C. The samples were periodically tested using a Vicat needle to determine their setting times according with ASTM C807 [217].

By looking in detail into the variables effects during the different stages of geopolymerization, i.e. setting, evolution of geopolymer gel, and gel conversion into zeolite - we aimed to improve the current knowledge about geopolymerization reaction pathways and rate limiting step, and to provide practical guidelines for enhancing the performance of metakaolin-base functional geopolymers.

8.3. Response quantification

The determination of the statistically significant factors for the geopolymerization reaction and the final crystalline structure using ANOVA required quantifiable responses, and these are included in Table 8.3. The details of the methods to measure and calculate these responses are presented in the following Sections.

Table 8.3 List of quantifiable responses (obtained from the deconvolved ATR-FTIR spectra and QXRD) and the main information they carry.

RESPONSE	FROM	FORMULA		MAIN INFORMATION
GP%	FTIR	$\frac{Area_{\approx 955cm^{-1}}}{Area_{1070cm^{-1}} + Area_{1187cm^{-1}} + Area_{\approx 955cm^{-1}}} * 100$	EQ. 8.1	MK dissolution extent
GP peak position	FTIR	obtained from deconvolution		type of GP gel
GP peak FWHM	FTIR	obtained from deconvolution		local order of GP gel
peak area ratio solid/H ₂ O	FTIR	$\frac{Area_{\approx 3300cm^{-1}}}{Area_{1070cm^{-1}} + Area_{1187cm^{-1}} + Area_{\approx 955cm^{-1}}}$	EQ. 8.2	water content
zeolite conversion %	QXRD	$\frac{(\%wt_{LTA} + \%wt_{FAU-X})}{100\% - \%wt_{H_2O} - \%wt_{MK-impurities}} * 100$	EQ. 8.3	normalized geopolymer crystallization
LTA% (zeolite)	QXRD	$\frac{\%wt_{LTA}}{\%wt_{LTA} + \%wt_{FAU-X}} * 100$	EQ. 8.4	zeolite type

The response “GP%” (EQ. 8.1) was obtained from the deconvolved ATR-FTIR spectra conveyed information on the metakaolin alkalination and dissolution and GP gel formation [119], [120], [278]. The “GP peak position” depended on the nature of the gel: Si/Al ratio, deprotonation degree, ion-pairing, and connectivity [55], [254], [279]–[284]. Moreover, zeolites with same structure and Si/Al but different charge balancing cations had different FTIR peak positions, refer to Figure 6.3. A smaller “GP peak FWHM” indicated a narrower

distribution of bond length and angle, thus a more organized and homogeneous structure at the nanoscale [247]. The response “peak area ratio solid/H₂O” provided two important pieces of information: 1) if free water was consumed or regenerated due to the dissolution and polymerization reactions, EQ. 2.18, EQ. 2.24 and EQ. 2.26; 2) if water was lost during curing operations. This last aspect was particularly important because the crystallinity of the GP needed to be normalized considering the different levels of impurities carried by the MK and the different water content of the different GP compositions, EQ. 8.3. Since water contributes to the amorphous content in the XRD, increasing water content artificially “decreases” the GP crystallinity. On the other hand, the loss of water during curing operation artificially “increases” the GP crystallinity. These artifacts were eliminated by using EQ. 8.3. Finally, “LTA%” indicated the percentage of zeolite type LTA over the total amount of zeolites and, since the other main detected zeolite is faujasite type X, the formula can be expressed as EQ. 8.4. These last two responses were the most important to engineer the crystalline structure of GP towards the development of functional MK-based GP (i.e. with controlled amount of specific-type zeolite) for advanced applications, such as membranes or encapsulation.

8.3.1. ATR-FTIR spectra deconvolution

The FTIR spectra were collected using a PerkinElmer 100 series equipped with a universal ATR accessory, acquisition range 4000-450cm⁻¹, 1 cm⁻¹ resolution and averaging 25 scans. ATR-FTIR configuration was chosen to quickly analyze the geopolymers removed from the environment of the respective curing temperature without affecting their water content, which would occur if transmission geometry using KBr pellets was adopted. Baseline and ATR corrections were done using the “PerkinElmer Spectrum” software to remove sample scattering effects and the depth of penetration dependence [227]. The transmittance data were then converted into absorbance (EQ. 4.22 and EQ. 4.23) and the spectra normalized based on the maximum peak intensity in the 850-1300cm⁻¹ range.

The spectra of the metakaolin was deconvolved using a nonlinear least-square fitting (NLSF) adapting the method described by Kemmer [285]. Two Gaussian curves were used to

represent the region between 1400 cm^{-1} and 975 cm^{-1} . The obtained peak positions were 1070.13 cm^{-1} and 1197.3 cm^{-1} and peak area ratio 10.5 (Figure 8.3, top left). The peak positions were comparable with other studies [84]: 1080 cm^{-1} and 1204 cm^{-1} assigned respectively to Si-O-Al and Si-O-Si asymmetric stretching.

The geopolymer spectra in the region of major interest, $1400\text{-}800\text{cm}^{-1}$ were deconvolved using the same method [285] and adopting two Gaussian peaks for the metakaolin and one Gaussian peak for the geopolymer (Figure 8.3, top right). The peak positions and intensity ratio between the two metakaolin peaks were kept constant for all the geopolymer spectra deconvolution. Areas, positions and the FWHMs of the Gaussian peaks representing the geopolymers were all variables of the NLSF. Although ATR-FTIR spectra could be better modelled by more Gaussian peaks, this would only destabilize the NLSF procedure. For example Zhang [119] used two Gaussian peaks at $\approx 1000\text{cm}^{-1}$ and 950cm^{-1} to describe respectively the Si-O-T and the Si-O-Na bonds. Silicate anions with different connectivities, aluminum substitutions and ion-paired cations have different vibration frequencies (Figure 8.3, top right) but these frequencies cannot be properly resolved using FTIR [97]. Moreover the structure and FTIR spectrum of the metakaolin is still not fully understood. For these reasons we adopted only three Gaussian peaks to quantify the dissolution of metakaolin and formation of geopolymer over time. The peak at 3300cm^{-1} associated with free water was also modelled by a Gaussian peak to determine if water was consumed or generated during the geopolymerization reaction (Figure 8.3, bottom left and right).

The geopolymerization conversion can thus be approximated by the area percentage of the main geopolymer peak over the metakaolin and geopolymer peaks: $\text{GP}/(\text{GP}+\text{MK})\times 100$. A similar approach was used by Provis [100], where the extent of geopolymerization was defined as $(\text{P}+\text{G}+\text{N}+\text{Z})/(\text{M}+\text{P}+\text{G}+\text{N}+\text{Z})$. M, P, G, N and Z were respectively the concentration of metakaolin, aluminosilicate polymer and gel, zeolite nuclei and zeolite crystals. The FTIR geopolymer peak area contained P, G, N and Z since they all contribute to the geopolymer FTIR peak.

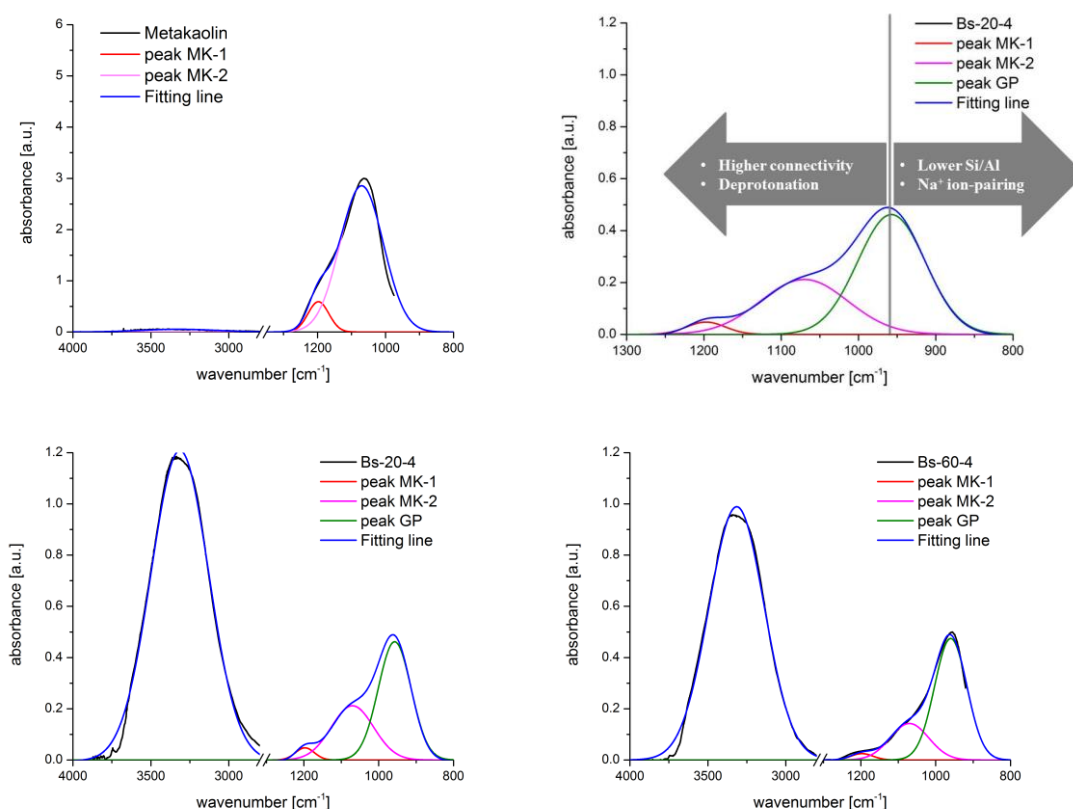


Figure 8.3 ATR-FTIR measured spectra (in black) and NLSF fitting lines (in blue) of the metakaolin and selected geopolymer samples: sample Bs cured at 20°C for 4 day and sample Bs cured at 60°C for 4 days. Deconvolved peaks of the metakaolin are in red and fuchsia, deconvolved peak of geopolymer is in green.

8.3.1.1. Precision and accuracy

The pure errors of the responses (i.e. precision) were estimated by repeating five casting, data acquisition and elaboration for the sample C_40_4. This sample was selected since it is the central point in terms of the composition, curing temperatures and times of the samples under consideration. The standard errors associated with the FTIR peak position was 1.6 cm^{-1} , 1.2% for the GP%, 1.8% for the FWHM of the geopolymer peak and 9% for the peak area ratio $\text{H}_2\text{O}/\text{solid}$. These errors were a combination of both intrinsic error in the materials processing (e.g. inaccuracy during casting, material inhomogeneity) and error due to the data elaboration (e.g. FTIR background subtraction and peak deconvolution).

To determine the accuracy of the method two different samples were analyzed four times with ATR-FTIR and deconvolved in order to verify the relation between concentration of components and absorbance peak area: a mixture composed of 66.6% MK and 33% synthetic sodium faujasite (Alfa Aesar), and a mixture of 33.3% MK and 66.6% synthetic sodium faujasite (Alfa Aesar). The peak areas associated with faujasite were respectively $27.6\% \pm 1.3\%$ and $56.6\% \pm 1.2\%$. Thus, the peak area percentages underestimated the actual weight percentage, or geopolymerization percentage. This may explain why none of the geopolymers reached 100% of geopolymerization, Figure 8.12.

The underestimation could be due to several reasons: the data correction and normalization, preferential contact of the platelet-like metakaolin with the ATR crystal, the use of Gaussian peaks, and/or the fitting method that ignore the shoulder of zeolites at higher wavelength, Figure 6.3. Also the weight percentages of MK and GP gel differed from their molar concentration of Si-O-Al and Si-O-Si bonds: while MK is completely made of Si, Al and O atoms, geopolymer and zeolites also have Na and H atoms. GPs and zeolites have less Si-O-Al and Si-O-Si bonds than MK on a weight basis. We did not attempt to include these considerations on the quantification of GP% due to its complexity which will require approximations and ultimately elaboration artifacts of the final data. The fact that the highest GP% values were obtained for the highest Na/Al ratios (Section 8.4.3.2) suggested that these corrections were negligible compared to the factor effects. For these reasons, the values GP% must be considered as only semi-quantitative, nonetheless they still provided important information and new insight into studies of the effects of different factors on GP processing and properties.

8.3.2. QXRD and Rietveld refinement

The X-ray diffractograms were acquired using a MultiFlex Rigaku X-Ray Diffractometer in Bragg Brentano geometry in theta-theta mode, using a Cu-K α source at 40kV and 40 mA, 1 cm receiving slit, 1° soller slit, 0.3° divergence slit and a graphite monochromator. Rietveld refinement were performed using the “X’pert highscore plus” software.

Due to the large amount of QXRD runs performed (180 analyses) the alumina NIST standard SRM 676a for quantitative analysis was replaced by a rutile (TiO_2) standard, which has already been used in quantitative Rietveld analysis of cements and clinkers [286]. It is also not soluble in alkaline medium, thus it did not affect the solution chemistry of not fully reacted geopolymer, and its peaks were not overlapping with the main zeolites and metakaolin impurities phases. We adopted a 25% spike of rutile as indicated by Pamela [286] and similar to the 20% value used in another work [203].

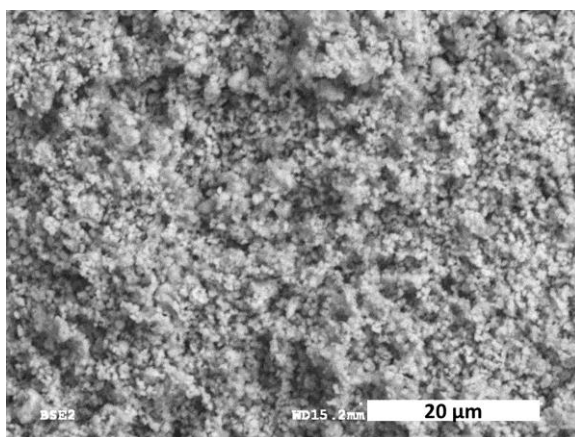


Figure 8.4 SEM image of the XRD internal standard rutile. Particles are below 2 μm providing a good standard for QXRD in term of count statistic.

The amorphous content of the rutile was determined by two methods: a) performing a QXRD using the SRM 676a as an internal standard, b) considering the area of the broad low angle peak as representative of the amorphous material (analysis performed by an independent external laboratory). The two amorphous content values obtained were respectively 16.4 % and 12%. To calculate the amorphous content of the metakaolin and to quantify the phases in the GP samples we used the value 16.4% since we considered the internal standard method more reliable. The phase ICSD-34372 was selected to refine this phase. 25% of rutile was added on the geopolymer samples and gently mixed using an agate and mortar pestle.

The diffractograms of the spiked geopolymers were collected from 3° to 45° , at 2 θ step of 0.02° , collection speed $1^\circ/2\theta/\text{s}$ and the total measuring time of 43 minutes. The scan speed and range were a compromise between good count statistic and scan range to perform Rietveld analysis, and the total measuring time. Since zeolites have a prompt response to

changes in moisture, we kept the scan time at a minimum to limit water evaporation which can affect the peak intensity at low angle [251]. By analyzing wet GPs and minimizing water evaporation the LTA-to-HS transformation observed as reported in Section 6.2.2.3 was avoided. Pseudo-Voigt functions were used to model the peak profiles and the refinement strategy for the spiked GPs included: polynomial background, sample displacement, unit cells parameters and scale factors for all phases, W parameter for the FWHM, peak asymmetry and preferential orientation of the quartz phase in the 101 direction [222].

The model phases used to refine the geopolymer diffractograms included (i) zeolite NaX ICSD-155683 (as faujasite type X), (ii) zeolite LTA ICSD-24901 (as zeolite type A), (iii) quartz low ICSD-90145 (as silica), (iv) anatase ICSD-63711, (v) hydrosodalite ICSD-413494, (vi) zeolite ZK-5 ICSD-22054. All these phase were detected by Belviso [204]. Although LTA and NaX were the best models available to describe the zeolite peaks of these two phases, discrepancies between the intensities of these phases and the diffractograms were obvious, especially at low angle. This is a common problem when analysing zeolites, since small variation in channel content and water content can strongly affect the peak intensities, especially at low angles [251]. In fact the ASTM D3906 method to quantify zeolite type material uses only 8 peaks in the range 15°-35°. For this reason we excluded the zeolite peaks under 2 θ =8°, but we included the range 8°-15° since it contained diffraction peaks of hydrosodalite and ZK-5. The occupancies of non-framework elements in LTA [287] and NaX [288] were refined on two selected diffractograms, each containing a single zeolite phase. The respective GOF (goodness of fit) values improved respectively from 11.9 to 5.7 and from 7.5 to 5.6. The element position and occupancy can be found in Table A.1 in Refinement of LTA and FAU-X crystal structures. The diffractograms and the Rietveld refinements can be found in Figure A.1, Figure A.2 and Table A.1 in Refinement of LTA and FAU-X crystal structures.

Since kaolinite deposits without silica and other impurities are extremely rare, most MKs carry those extra crystalline phases. Although these unwanted minerals are often acknowledged, in the geopolymer community the real metakaolin content is rarely determined and its value used when preparing the geopolymer formulation. Therefore in

this work a Rietveld refinement was performed on the Powerpozz metakaolin using 25% rutile as internal standard. We determined the total of 16% of impurities: 10% of silica, 2% of anatase and 4% of halloysite (all by weight). Thus only 84% of Powerpozz is actual reactive metakaolin, a material similar to the one used by Rahier in his studies which contained 85% of amorphous phase [71].

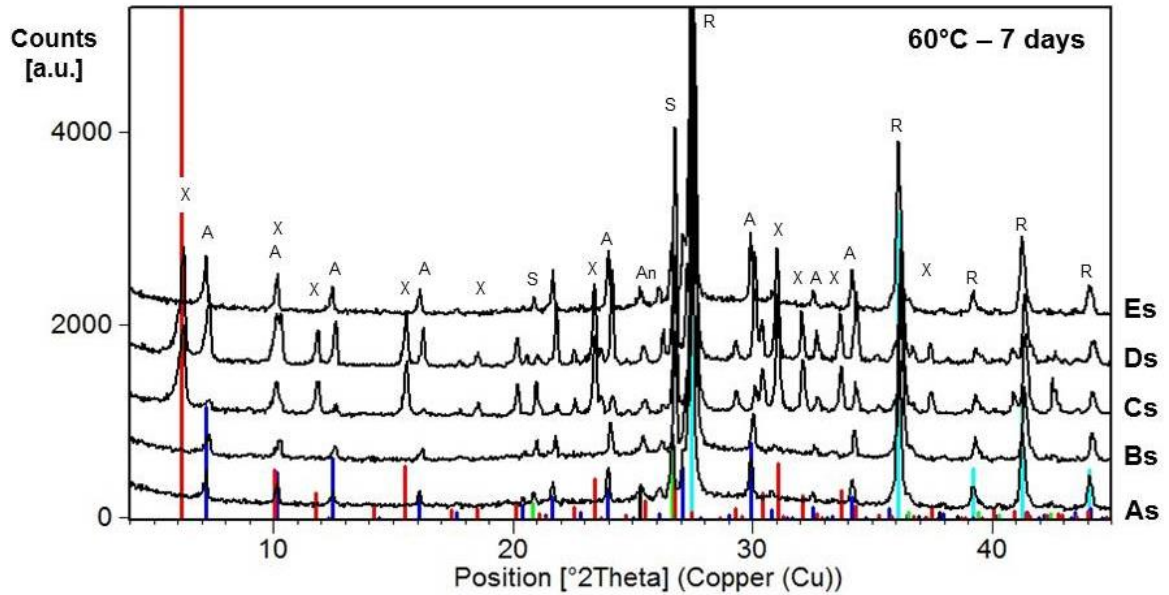


Figure 8.5 Measured diffraction patterns of selected geopolymers seeded with colloidal faujasite, and cured for 7 days at 60°C. Symbols in the image represents the position of the more intense peak zeolite type LTA (A), zeolite type X (X), rutile (R), silica (S), anatase (An).

8.3.2.1. Precision and accuracy

The pure errors of the responses were estimated by repeating five casting, data acquisition and elaboration for the sample C_40_4. The standard deviation for the zeolite conversion % as determined by QXRD was 0.9% and we estimated the standard deviation of LTA% by error propagation to be approximately 1.4% (max 2%). These errors were a combination of errors in the sample preparation and in data elaboration: weighting and mixing the QXRD internal standard with the geopolymer, Rietveld errors, and others.

To determine the accuracy of the method we performed QXRD on two samples: 100% faujasite-Na (Alfa Aesar) and a mixture made of 33% faujasite-Na (Alfa Aesar) and 66% metakaolin. We obtained the underestimated values of 79.8% and 29.2% respectively. This discrepancy can depend on the differences between this pure high-silica faujasite and the faujasite that crystallize in the geopolymer used to refine the model (refer to Refinement of LTA and FAU-X crystal structures). In fact XRD peaks at $2\theta=15.8$, 20.4 and 23.8 were all more intense than in the geopolymer samples, thus the calculated XRD pattern underrepresented those peaks.

A general underestimation of the zeolite crystalline phase was probably occurring throughout this work. Although we could not exclude systematic errors, the method remains sufficiently precise (i.e. with overall error less than 1%) and its robustness allowed the determination of the factors main effects and the interactions on the two responses: “zeolite conversion %” and “LTA%”.

8.4. Results

8.4.1. Setting time

The most important factors affecting the setting time were determined to be temperature, followed by $H_2O/solid$ ratio and then NaOH concentration: the higher temperature, higher [NaOH] and lower $H_2O/solid$ decreased the setting times. The geopolymer composition became less important at higher temperatures, nonetheless a combination of high water content and low Na/Al could delay the setting times even at high temperatures. Seeding had no detectable effects on the setting time, probably due to the low precision of the method as the percentage error was estimated to be approximately 20%. In fact it was observed in the research reported in Chapter 7 that the addition of colloidal faujasite seeds increased the setting reactions kinetics. However, even if a seeding effect existed, it was negligible compared with the other factors listed above. In conclusion, $H_2O/solid$ was more important at low temperatures and NaOH concentration had a major effect at high temperatures, Table 8.4 and Figure 8.6.

Table 8.4 Setting time of GPs type A, B, C, D, E (refer to Table 8.1 for their compositions) vs curing temperature

TEMPERATURE	SETTING TIMES [minutes]				
	A	B	C	D	E
5°C	360	>10080	2880	5760	4320
20°C	300	1800	300	1800	300
40°C	150	1200	60	150	60
60°C	60	600	30	60	30

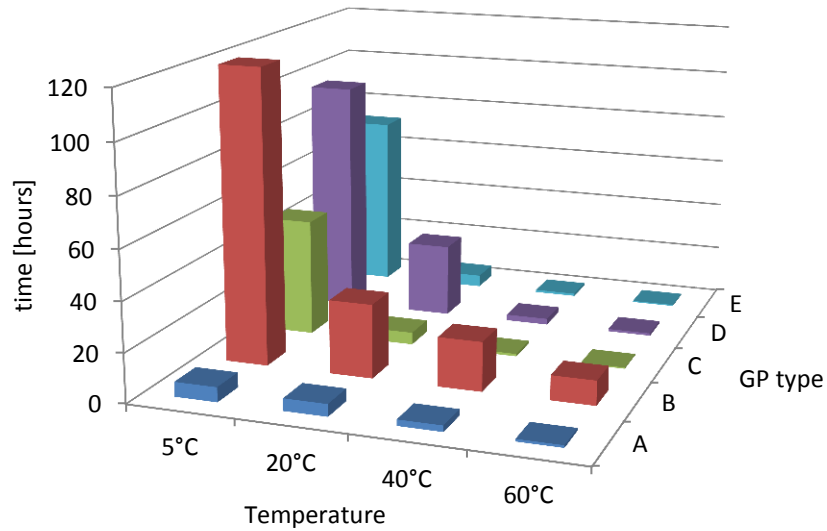


Figure 8.6 GPs setting time measured according with ASTM C807.

8.4.2. ANOVA analysis

In this Section the results of the multifactorial design and the ANOVA analyses are presented and summarized in Table 8.5, Table 8.6. The ANOVA analyses allowed the identification of the most influencing factors for each response, without dealing with each particular treatment but looking at their average effect across all the other factors. The analyses were performed ignoring the high-terms interactions when they were found to be statistically non-significant, i.e. p -values > 0.05 . The 5°C level for the factor temperature was also ignored since many

samples were still corrosive due to the unreacted sodium hydroxide and could not be analyzed by FTIR. An unequal number of observations would have led to an unbalanced design of experiments [229]. Some representative ATR-FTIR spectra were collected and will be discussed in Section 8.5.1. Similarly, the 20°C level for the factor “temperature” was ignored for the response LTA% since no crystalline zeolites were detected at this temperature.

Table 8.5 The *p*-values obtained from the Analysis of Variance (ANOVA) of GP samples A,B,C and D (see Table 8.2)

Responses	QXRD zeolite conversion %	QXRD LTA% (zeolite)	FTIR GP%	FTIR position	FTIR FWHM	FTIR solid/H ₂ O from area
excluded data	5°C	5°C, 20°C, 1 day	5°C	5°C	5°C	5°C
interactions	3FI	2FI	2FI	2FI	2FI	2FI
α -seeds	0.0001	0.0001	0.004	0.0068	0.326	0.0508
β -temperature	0.0001	0.0005	0.0001	0.5858	0.0131	0.0272
γ -time	0.0001	0.3972	0.0001	0.063	0.0879	0.0072
δ -H ₂ O/SOLID	0.9951	0.0001	0.0568	0.0002	0.2878	0.0009
ϵ -Na/Al	0.0001	0.0001	0.0001	0.0001	0.0001	0.044
$\alpha \beta$	0.0027	0.5597	0.0013	0.2109	0.9324	0.5344
$\alpha \gamma$	0.0541	0.9562	0.1498	0.0001	0.1384	0.0397
$\alpha \delta$	0.6005	0.1163	0.7013	0.8257	0.0384	0.1088
$\alpha \epsilon$	0.4683	0.0001	0.2771	0.7006	0.0196	0.2406
$\beta \gamma$	0.0001	0.2762	0.0003	0.354	0.0773	0.1934
$\beta \delta$	0.7903	0.8741	0.0183	0.7641	0.3977	0.0431
$\beta \epsilon$	0.0026	0.0011	0.0244	0.3988	0.5461	0.0224
$\gamma \delta$	0.7175	0.3592	0.1994	0.7741	0.785	0.2927
$\gamma \epsilon$	0.0124	0.6209	0.7837	0.9842	0.7258	0.1869
$\delta \epsilon$	0.0272	0.0001	0.0707	0.9401	0.6749	0.7408
$\alpha \beta \gamma$	0.0001					
$\alpha \beta \delta$	0.6804					
$\alpha \beta \epsilon$	0.3788					
$\alpha \gamma \delta$	0.8914					
$\alpha \gamma \epsilon$	0.6391					
$\alpha \delta \epsilon$	0.7154					
$\beta \gamma \delta$	0.8677					
$\beta \gamma \epsilon$	0.0434					
$\beta \delta \epsilon$	0.2449					
$\gamma \delta \epsilon$	0.4876					

Table 8.6 The *p*-values obtained from the Analysis of Variance (ANOVA) of GP samples A, E and D. (see Table 8.2)

Responses	QXRD zeolite conversion %	QXRD LTA% (zeolite)	FTIR GP%	FTIR position	FTIR FWHM	FTIR solid/H ₂ O from area
excluded data	5°C	5°C, 20°C, 1 day	5°C	5°C	5°C	5°C
interactions	3FI	2FI	2FI	2FI	2FI	2FI
α -seeds	0.0002	0.0002	0.0016	0.8626	0.234	0.843
β -temperature	0.0001	0.0326	0.0001	0.5737	0.6461	0.0031
γ -time	0.0001	0.5499	0.0001	0.1412	0.0542	0.0451
χ -solution/MK	0.0214	0.0001	0.0001	0.0001	0.0001	0.0002
$\alpha \beta$	0.0223	0.2694	0.0037	0.0148	0.2214	0.5839
$\alpha \gamma$	0.3662	0.7352	0.0023	0.0002	0.002	0.1444
$\alpha \chi$	0.6489	0.0001	0.1053	0.5705	0.7526	0.0276
$\beta \gamma$	0.0001	0.4997	0.0001	0.2169	0.2767	0.201
$\beta \chi$	0.3906	0.0118	0.0144	0.4416	0.1736	0.1951
$\gamma \chi$	0.4966	0.4197	0.8126	0.7185	0.9361	0.2515

The effect plots for all statistically significant parameters can be found in DOE effects plots. In the following Sections the factors and interactions with $p < 0.05$ on the responses were analyzed in details, and the effect across different responses compared in order to extract more information on the geopolymerization reactions. The absence of statistically significant effects could also convey important information: e.g. if the factor H₂O/solid has no effect on the crystallization kinetics, then the crystallization is probably a solid-state rather than a solution-mediated transformation.

Finally, as previously anticipated in Section 8.2 , by comparing the *p*-values of the factors Na/Al, solution/MK and H₂O/solid from the two separated ANOVA analyses it was possible to partially isolate the effects of the interdependent variables: Na/Al, H₂O/solid and [NaOH] (refer to Table 8.7). In the DOE involving sample A, B C and D (Table 8.5) the factors Na/Al and H₂O/solid varied independently, but the NaOH concentration in the activating solution [NaOH] varied with each of them (Table 8.2 and Figure 8.1). An increase in Na/Al meant an increase in [NaOH], while an increase in H₂O/solid caused a decrease in [NaOH]. Instead, in the DOE involving samples A, E and D (Table 8.6) the NaOH concentrations were fixed at [NaOH]≈7.4M while the ratios Na/Al and H₂O/solid varied with the factor solution/MK.

For example, in this paragraph the response Zeolite_conversion_% as determined by QXRD is examined in detail. In the first ANOVA (samples A, B C and D) the factor Na/Al had *p*-

value<0.0001 but H₂O/solid had no effect, i.e. p-value=0.99. The response Zeolite_conversion_% could have increased due to the increase of Na/Al or due to the indirect increase in [NaOH]. In the second ANOVA at constant [NaOH] (samples A, E and D) the factor solution/MK had a p-value<0.05, thus the Zeolite_conversion_% increased when Na/Al increased and H₂O/solid decreased. The first ANOVA revealed that H₂O/solid had no effect, thus Na/Al had a “pure effect” on the Zeolite_conversion_%.

The same method, i.e. comparing the p-values of Na/Al, H₂O/solid and solution/MK, was used for all the other responses. The responses FTIR_GP% and FTIR_FWHM had the same behaviour as response Zeolite_conversion_%: factor H₂O/solid had no effect while factor Na/Al had a “pure effect”. Finally every single factor had an effect on the response LTA%.

Table 8.7 Attribution of the response variation to the appropriate factor (Na/Al, H₂O/solid or [NaOH]) by comparing the p-values of Na/Al, H₂O/solid and solution/MK.

sample A,B,C,D		samples A,E,D	effect attributable to
p-value: Na/Al	p-value: H ₂ O/solid	p-value: solution/MK	
<0.05	>0.05	<0.05	Na/Al
<0.05	<0.05	<0.05	all factors
>0.05	<0.05	<0.05	H ₂ O/solid

It must be emphasized that all these considerations are valid within the range of the factors under examination which were chosen to represent MK-based geopolymers. Different results may be obtained for different compositions or curing conditions: e.g. if H₂O/solid>>1 then this factor may have a detrimental effect on the GP% as the NaOH concentration is highly reduced.

The discussion of the results of this multifactorial design in the following Sections 8.4.3 and 8.4.4 focuses on the individual responses and analysis of the effect of each factor and factor interaction FI. Additionally we look into each factor and its effect on the different responses to obtain more detailed information on the possible reaction mechanisms and transformations occurring during geopolymerization, refer to Section 8.5.

8.4.3. FTIR

8.4.3.1. FTIR: GP peak position

The most important factors affecting the peak position were: (i) Na/Al followed by (ii) solution/MK and (iii) H₂O/solid (see Table 8.5, Table 8.6 and Figure C.3). By increasing Na/Al and solution/MK the peak position shifted to lower values, likely due the ion-pairing between the aluminosilicate anions and the sodium cations. By decreasing the water content a peak shift to lower wavenumbers was observed. This shift could also be explained in terms of ion pairing: sodium ions could be better solvated in presence of excess water, while sodium preferred to form an ion-pair with the aluminosilicate anions when water is limited.

With time the peak positions seemed to shift to higher wavenumbers but a p -value=0.063 made this result less certain. A weaker effect was detected for the factor “seed” (higher wavelength for the unseeded sample peak), and an interaction for “seed” and “time”. The peak positions did not vary substantially for the samples containing FAU seeds and WG seeds.

The peak position for the unseeded samples was located at lower wavenumbers at 1 day compared with the seeded samples and at higher wavenumbers at 4 and 7 days. Since there were no interactions with Na/Al and H₂O/Al factors, we can assume the peak shift was not due to ion-pairing differences but in the changing Si/Al ratio of the gel. At shorter curing times the unseeded samples are richer in alumina (lower wavenumbers), while the gel that forms at longer times is richer in silica. Both the incongruent dissolution of metakaolin and the preferential Si-O-Al condensation can account for the abovementioned phenomenon. This pendular motion has already been observed and reported in the literature [168].

In seeded samples this phenomenon was not observed due to the presence of initial silica in solution and also this was previously seen in fly ash geopolymer [168]. The fact that the peak position of the seeded sample was lower at longer curing times was probably due to the passivation effect, refer to Section 8.5.2 for further discussion of this possibility.

8.4.3.2. FTIR: GP%

The factors with major effect on the geopolymer conversion percentage “GP%” were: (i) Na/Al, (ii) solution/MK, (iii) temperature and (iv) time (see Table 8.5, Table 8.6 and Figure C.4). Increasing any of these parameters increased the GP%, in particular due to the strongest factor Na/Al. The GP% saturated at approximately 4 days, depending on temperature. The factor “seeds” had a relatively smaller effect and the unseeded samples had higher GP%.

The factor “temperature” interacted with most of the other factors, Figure C.5. At 40°C and 60°C the GP% almost reached saturation after only 1 day of curing, while at 20°C the MK needed longer time to be transformed into geopolymer gel. Moreover, at 20°C the GP% for higher H₂O/solid was smaller, but at higher temperatures it was comparable with lower levels of H₂O/solid (the *p*-value of the main factor H₂O/solid was 0.057). Similarly the effect of Na/Al was more pronounced at lower temperatures.

This suggests that increasing the curing temperature to 40°C or above made the GP% less susceptible to other parameters, or in other words the factors “time” and “H₂O/solid” were important especially at lower curing temperatures. This confirmed the conclusion drawn from the setting time measurements, wherein the detrimental effect of higher water content was worse at lower temperatures.

8.4.3.3. FTIR: GP peak FWHM

The ratios Na/Al and solution/MK had the biggest impact on the FWHM of the geopolymer peak: the higher these ratios were the larger the FWHM. Temperature had a minor effect and in opposite direction: the higher temperatures were associated with smaller FWHM. Since the FWHM could be associated with the variability of the geopolymer gel (in terms of connectivity, Si/Al ratio and ion-pairing) higher Na/Al and lower temperatures were associated with less homogeneous geopolymer gels, Figure C.6.

The effect of Na/Al was higher for the unseeded sample and the factor interaction between “seed” and “Na/Al” had a p -value=0.02. Similarly there was a relatively small effect of H₂O/solid for the unseeded samples. It seems that the effect of the geopolymer composition on the FWHM was less severe when seeds were used (Figure C.7), probably because the initial silicate presence in solution compensates for the initial preferential dissolution of alumina (which produced an initial alumina-rich gel and a secondary silica-rich gel). Nonetheless this could also be an artifact due the adoption of a single Gaussian peak to represent the different bonds in the GP gel: higher Na/Al increases the intensity of the Si-O-Na band and thus it increases the FWHM.

8.4.3.4. FTIR: peak area ratio solid/H₂O

The main factor having a statistically significant effect on the response “FTIR peak area ratio solid/H₂O” was the factor H₂O/solid as expected, Figure C.8. This result confirmed that no water was lost during the curing of the geopolymer, which was important in order to have reliable results during the QXRD analyses.

8.4.4. QXRD

8.4.4.1. XRD: zeolite conversion %

All main factors besides H₂O/solid have a statistically significant effect on the zeolite %. High temperatures were required for the zeolite crystallization: no zeolites were detected for samples cured at 5°C and 20°C and the amount of zeolite increased from 40°C to 60°C. Similarly longer curing times, higher Na/Al and higher solution/MK increased the zeolite content. The factor “seed” also had an effect: the zeolite conversion % of the GP gel was higher for the unseeded sample, followed by the waterglass seeded geopolymer. Nonetheless, the analysis of the factors interactions revealed that this last finding was probably an artifact of adopted DOE, as explained in the next paragraphs.

A clear 2 factor interaction “2-FI” exists between the curing time and temperature: at 20°C the curing time had no effect, at 40°C the crystallization started around the 4th day and

continued through the 7th day, and at 60°C the crystallization had reached saturation already at the 4th day. The zeolite contents obtained by curing at 40°C for 7 days (i.e. 43% for geopolymer C-40-7) were smaller than the saturation value (i.e. 58% for geopolymer C-60-7) obtained for the samples at 60°C. Depending on the GP compositions, curing time longer than 7 days may be needed to obtain the maximum achievable zeolite for $T=40^{\circ}\text{C}$, as already observed by Zhang [119]. Interaction occurred also between the Na/Al and temperature, and Na/Al and time. Higher temperatures and longer curing times enhanced the effect of Na/Al: the higher the Na/Al the more zeolite% was present in the geopolymer.

Beside these three 2-FI there was also a 3-FI between time, temperature and Na/Al: at 4 days of curing at 40°C there was zeolite only for the samples at higher Na/Al (see Figure C.10 in DOE effects plots). Another interesting 3-FI occurred between “seed”, “time” and “temperature”. In geopolymer seeded with waterglass or colloidal faujasite the crystallization seemed delayed for samples cured at 40°C and 60°C. Generally at 40°C the unseeded samples reached saturation at 4 days, while seeded samples had zeolite ($\approx 10\%$) only at 7 days. Similarly, at 60°C the crystallization started already after 24 hours for unseeded samples but the seeded samples had no zeolite at such early curing time. Thus the seeds retarded the zeolite crystallization, although the final zeolite contents were comparable (see interactions in Figure C.11 in DOE effects plots). Since this experimental design focused on the early stages of crystallization and the seeds delayed the crystallization, the overall effect of seed addition was determined to be detrimental for the geopolymer crystallinity. The crystallization delay observed in samples seeded with zeolites was due to the presence of soluble silicates in the seeding colloidal solution. The presence of zeolite did not accelerate or delay the crystallization compared with the GPs seeded with waterglass.

8.4.4.2. XRD: LTA%

The main factors that increased the faujasite% and decreased the LTA% were: seeding the geopolymer with waterglass or colloidal faujasite, lower temperature, decreasing the $\text{H}_2\text{O}/\text{solid}$ ratio. These effects were observed only at high values of Na/Al and solution/MK: low Na/Al always produces 100% of zeolite type LTA. Thus in order to have more faujasite

it was necessary to have high Na/Al, but the LTA% can be further decreased by increasing temperature, using seeds or lowering H₂O/solid (see Figure C.12 in DOE effects plots) .

Since the value LTA% referred to the total zeolite percentage and not to the total geopolymer, this value taken by itself did not specify if the LTA or the NaX decreased or increased over time. For instance, if the LTA in the geopolymer increased from 20% to 40% over time and the NaX increased from 0% to 40% over time, the LTA% decreased over time from 100% to 50%. In this regards it is important to notice that time was not an important factor for the response LTA% but it was for the zeolite conversion %. This mean that the ratio between these two phases remained approximately the same, there was no inter-zeolite transformation but only zeolite nucleation and growth from the amorphous gel.

8.4.4.3. Long term stability: Oswald rule of successive transformations

QXRD were repeated after 1 year for selected samples in order to determine the long term stability of the zeolite. In particular the residual excess NaOH present in the samples could have destroyed the zeolite structure. Alternatively, the zeolite framework could have transformed to a denser structure, i.e. sodalite, according with the Oswald rule of successive transformations. The rule states that a system evolves from the initially metastable state to a more thermodynamically stable state. Also, system with different zeolite types could reduce their energy by reducing the interfacial energies between the different phases in contact (e.g. Figure 5.3) by becoming monophasic. The QXRD results are presented in Table 8.8.

Table 8.8 QXRD results of 1 year old samples compared with their initial phase content. The selected samples were the unseeded GP with composition A, E and D cured at 60deg for 7 days.

	Amorphous wt%		LTA wt%		FAU wt%	
	7 days	1 year	7 days	1 year	7 days	1 year
A-60°C	80	77	14	14	0	0
E-60°C	57	38	39	55	0	0
D-60°C	24	25	67	65	6	7

For samples A-60-7 and D-60-7 (refer to Section 8.2 and Table 8.1 for the compositions of these samples) the amorphous and zeolite contents did not vary compared with their initial respective values. However, samples E-60-7 showed a substantial decrease in the amorphous content and proportional increase in zeolite type A content. This change could be due to a further slow growth of the zeolite at the expense of the amorphous gel, i.e. through the process of the amorphous phase crystallization. Also the weight percentage of the impurities increased from 4% to 7%, and the FTIR peak area ratio solid/H₂O increased. Thus it is more likely that the increase in crystallinity was associated with water evaporation from the sample.

The pre-existing faujasite did not transform into zeolite type LTA over time, or vice versa. After curing for 1 year no other zeolite phases were detected, such as sodalite, zeolite type P, analcime and cancrinite [253]. Thus it is concluded that the Ostwald's process of successive transformation was not occurring in the MK-based GPs under investigation.

8.4.5. SEM images

Five different samples were dried overnight in a vacuum desiccator at room temperature, coated with carbon and observed in high-vacuum using secondary electron SEM, Figure 8.7. In order to study the effects of the different factors, the sample C_60_4 was chosen as the baseline, i.e. unseeded geopolymer with Na/Al=1.25, H₂O/solid=0.66, cured at 60°C for 4 days. The microstructure of this geopolymer was porous and several cubic crystals of zeolite LTA with size of 1 to 2 µm were observed.

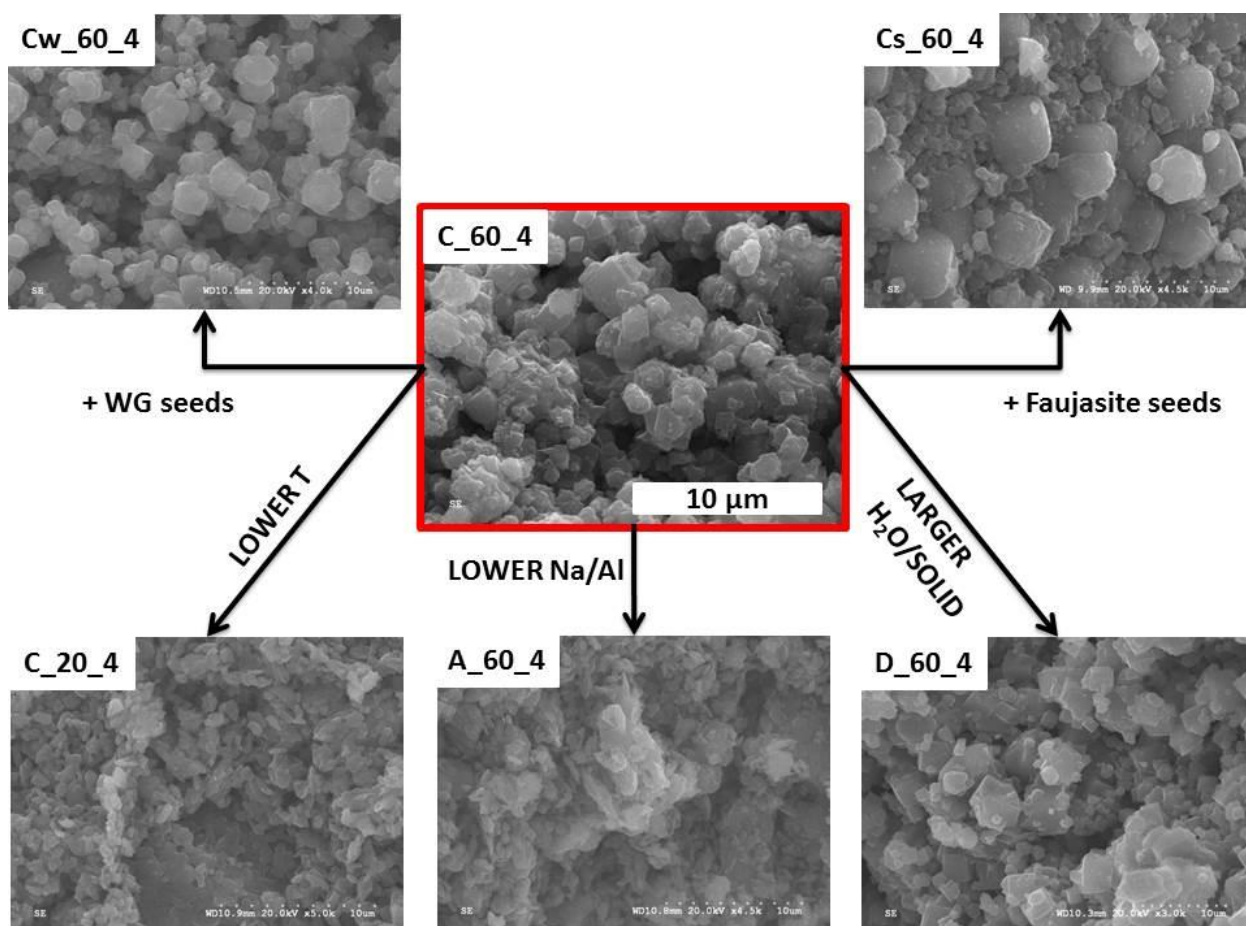


Figure 8.7 SEM images showing the effects of the different compositional, seeding and curing factors on the geopolymer morphology. Sample C_60_4 is taken as baseline.

Increasing the $H_2O/solid$ had no major effects on the crystallinity of the product, confirming the data in Table 8.5. Zeolite crystals were replaced by amorphous gel lumps when the Na/Al was reduced, and the same effect could be seen when the curing temperature was lowered to $20^\circ C$. These observations were also in agreement with the QXRD results, Table 8.9.

Table 8.9 Results of the QXRD for the different geopolymers analyzed with SEM. “Saturation” refers to the zeolite content of the geopolymers compared to the values obtained for the same geopolymers at 7 days curing.

sample code	zeolite conversion % [wt%]	LTA% _{zeolite} [wt%]	saturation
C_60_4	59	85	yes
Cw_60_4	43	17	yes
Cs_60_4	48	10	yes
D_60_4	50	92	no
A_60_4	12	100	no
C_20_4	0	n/a	n/a

The effect of the different seed can be seen in Cw_60_4 and Cs_60_4 (Figure 8.7). Both seeded and unseeded GP contained large numbers of crystals, but they had different crystal sizes and shapes. The main differences can be seen at higher magnification in Figure 8.8: most crystals in the unseeded sample were cubic while most crystals in the waterglass-seeded samples were octahedral. This was in agreement with the respective crystal morphologies of LTA and NaX zeolite [204], thus the SEM confirmed the results obtained by QXRD. Moreover a distinct morphology characteristic of ZK-5 zeolite was observed in the sample C_60_4; a 2% of ZK-5 on the total geopolymer was previously determined by QXRD, Table B.1.

Although the materials coded Cw_60_4 and Cs_60_4 (refer to Section 8.2 and Table 8.1 for their content) had similar zeolite compositions, the morphologies of these phases were different: the sample seeded with the colloidal zeolite had a bi-modal size distribution with some bigger crystals almost 5 μm large (Figure 8.7). Those could potentially be the crystals which grew from the original colloidal faujasite. Those big particles had surface patterns which resemble the crystal growth mechanism mediated by screw dislocations already observed in LTA [289], Figure 8.8.

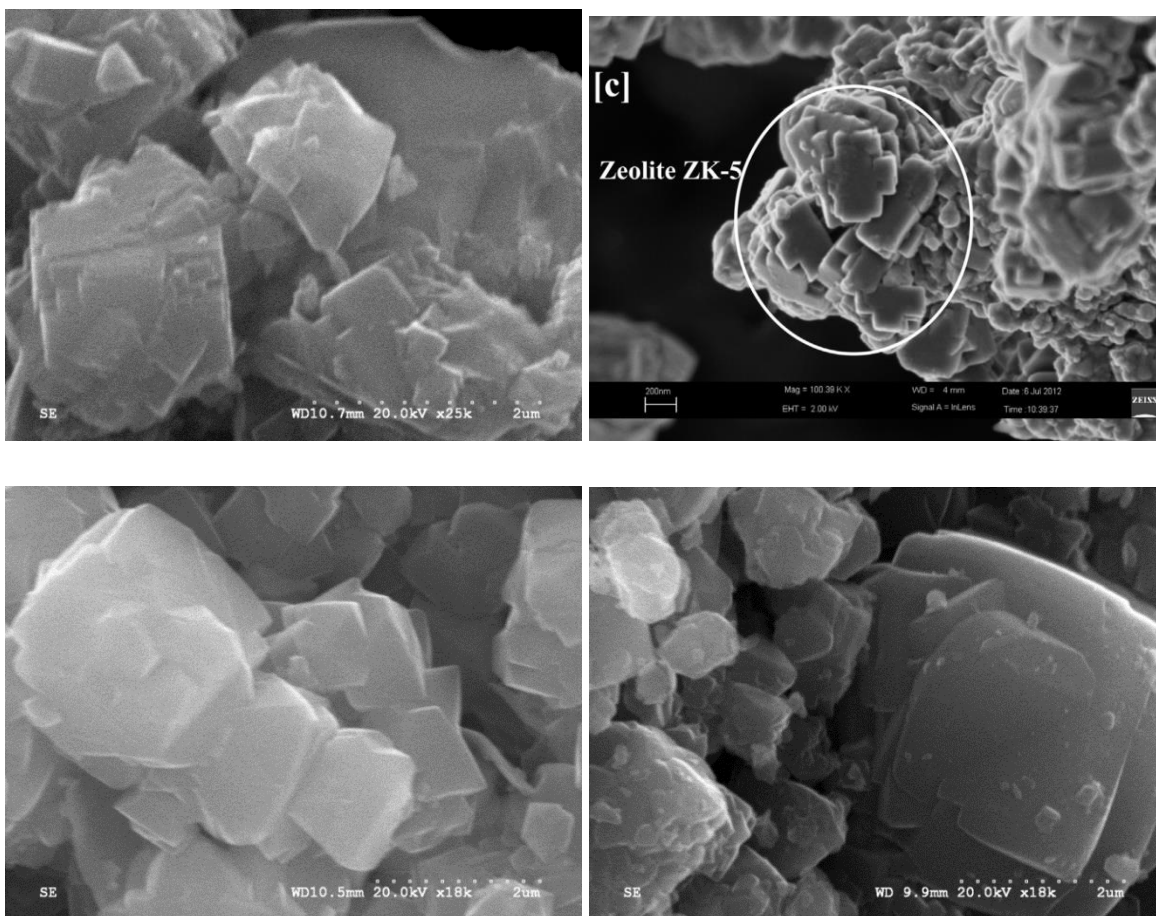


Figure 8.8 SEM images of C_{60_4} (top-left) and Belviso's GP [204] (top-right) showing the ZK-5 zeolite. Octahedral crystals observed in the Cw_{60_4} (bottom left). Crystal growth of a FAU-X and LTA crystals in Cs_{60_4} (bottom-right).

8.5. Discussion

8.5.1. Reaction extent and kinetics

By comparing the setting time and the crystallization kinetics it was clear that zeolite nucleation and growth did not take place during the consolidation reaction, but in fact occurred only after the material had set. The onset of crystallization depended on the GP composition and curing temperature and it was within 1 and 7 days, in agreement with [203]. More importantly the crystallization commences when all the geopolymer gel had already formed, as determined by the response GP% obtained by FTIR, Figure 8.9. Thus, the

nucleation and growth of amorphous gel and zeolite were sequential reactions and not parallel reaction as described in the kinetic model in Figure 2.11 [100]. This was also in agreement with the calorimetry study performed by Zhang [119]; the setting of the GPs depended on the dissolution and condensation reactions that produced the amorphous geopolymer gel that bonded the remaining particles together.

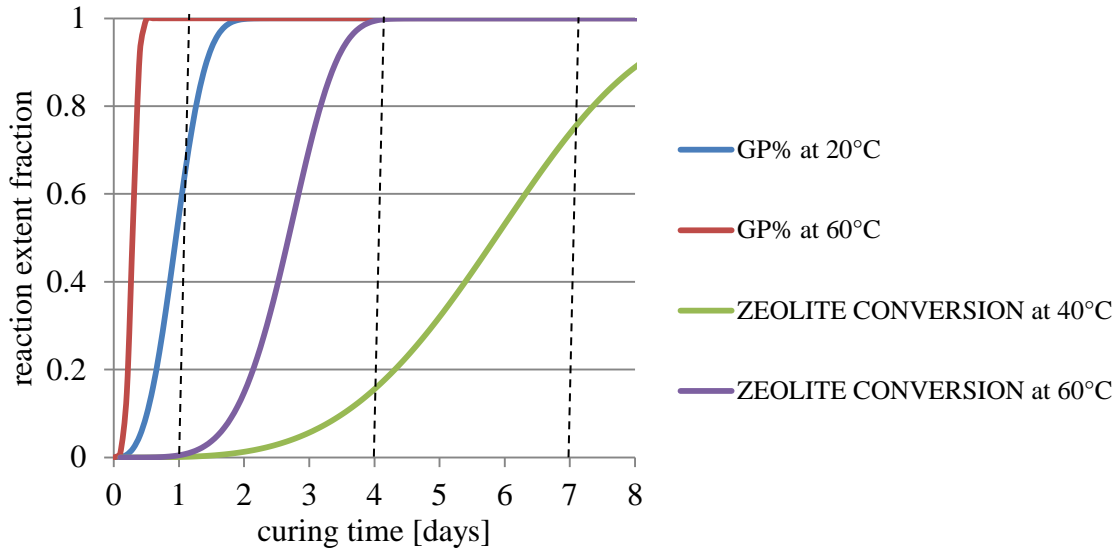


Figure 8.9 Simplified representation of the kinetics of the geopolymer formation and zeolite conversion at different curing temperatures using an Avrami-type expression [146]. Dashed lines represent the times when the responses were collected.

Through data presented in Table 8.7 we have also determined that the ratio Na/Al was more important than the NaOH concentration for the precipitation of geopolymer gel and the crystallization of zeolites. For the geopolymer gel formation this is particularly valid when $\text{Na/Al} \leq 1$ since there was not enough NaOH to react with all the MK, Figure 8.10 left. On the other hand an increase in Na/Al greatly enhanced the zeolite crystallization, even when $\text{Na/Al} \geq 1$, Figure 8.10 right. More NaOH in the geopolymer, even in excess, allowed a better reorganization of the geopolymer gel in which zeolites could nucleate and grow. This was more likely connected to a higher solubility of the amorphous gel in alkaline conditions compared to crystalline zeolite. North have found that the exchange of silicate in cyclic aluminosilicate (such as zeolite) was slower than in linear aluminosilicate (initial amorphous GP gel) [115]. Without the extra NaOH, the bonds in the amorphous gel were relatively stable and the growth of zeolite from this “frozen” gel was reduced. In a geopolymer gel with

$\text{Na}/\text{Al} \leq 1$ most of the NaOH was consumed by the metakaolin dissolution, e.g. refer to EQ. 2.17, thus there was little free NaOH left which could promote the gel reorganization.

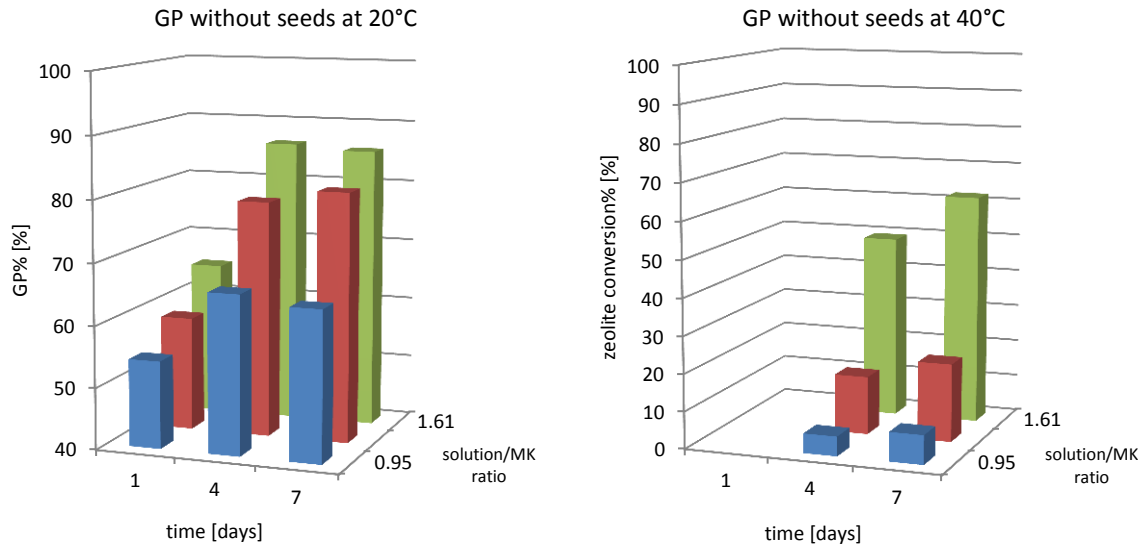


Figure 8.10 Effect of solution/MK on GP% (left) and on zeolite conversion% (right) for unseeded GPs. The central values (red bars) represents a GP with $\text{Na}/\text{Al}=1$, i.e. GP type E.

Comparing the GP% with the setting time provided information on the amount of gel needed for the binder to set. Figure 8.11 presents GP% after curing for 7 days at different temperatures (5°C to 60°C). At 5°C and low Na/Al the GP% was approximately 45%, however only the sample with low $\text{H}_2\text{O}/\text{solid}$ had set. Thus, for larger $\text{H}_2\text{O}/\text{solid}$ ratio, more gel was needed in order to bridge the unreacted particles. When curing at elevated temperatures more geopolymer gel formed, thus the $\text{H}_2\text{O}/\text{solid}$ factor became less important. Also, higher Na/Al ratio meant more and faster MK dissolution, thus more geopolymer gel formation.

Increasing the curing temperature also increased the geopolymerization kinetic, but had a relatively small effect on the total extent of reaction when $\text{Na}/\text{Al} \geq 1$. When cured at 20°C, the GP% for $\text{Na}/\text{Al} \geq 1.25$ was close to saturation, i.e. $\text{GP}\% \approx 85\%$, Figure 8.11. This was however not the case for geopolymers with $\text{Na}/\text{Al}=0.75$. These trends were also observed using calorimetry for similar MK-based GPs [119], where a maximum extent of reaction of

40% was obtained. The difference may be due to a more reactive metakaolin used in this study. In order to assure that GP% was not overestimated by our method we further compared the amount of zeolite conversion % with the GP% for all the samples under consideration, Figure 8.12. The percentage of gel that crystallized was between 0% and 95%, which supported the rigor of the adopted methodology.

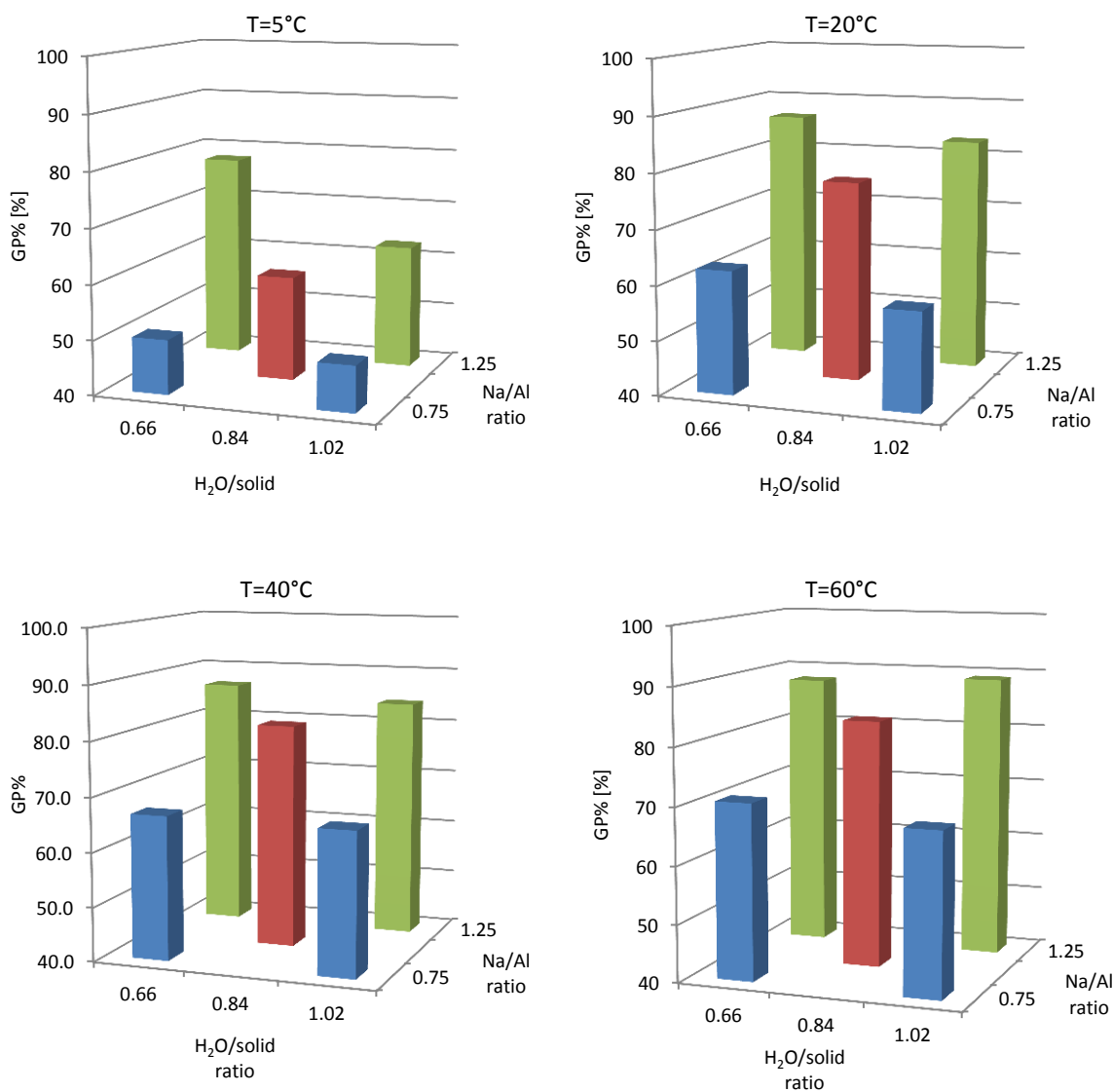


Figure 8.11 GP% responses obtained from ATR-FTIR deconvoluted spectra of GP seeded with colloidal faujasite after 7 days of curing. Samples cured at 5°C (top left), 20°C (top right), 40°C (bottom left) and 60°C (bottom right).

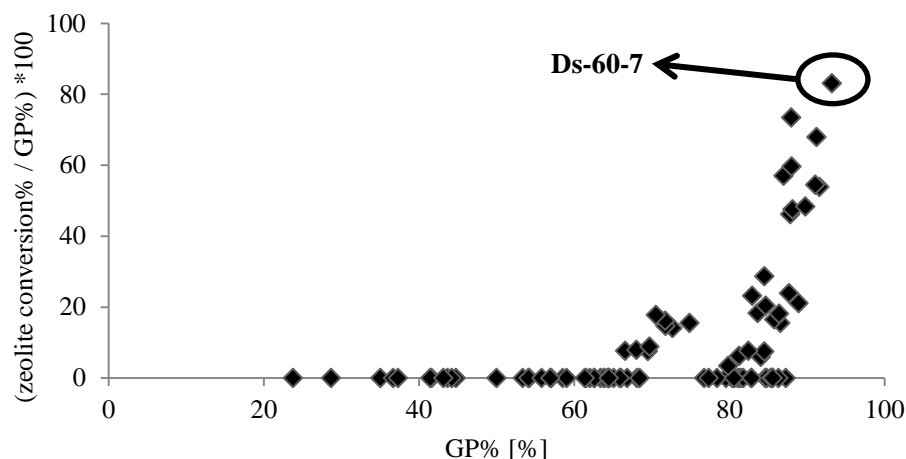


Figure 8.12 Percentage of the geopolymer gel that was converted in crystalline zeolite for all the crystallized GPs. The maximum value of 94.7% was obtained for a GP seeded with colloidal faujasite seeds Ds-60-7.

The ratio $H_2O/solution$ had effect neither on the kinetics and extent of gel formation nor on zeolite conversion, especially at $T > 20^\circ C$, as seen in Figure 8.11 and. Thus this factor can be modified to optimize other important properties of the GP - such as rheology, porosity and strength - without modifying the reaction kinetics and yield.

Seeding had a significant effect on the crystallinity and also a minor role on GP%. In particular the unseeded GPs had larger values for these responses compared with waterglass or colloidal faujasite seeded GPs. This was partially an effect of the chosen times under investigation, i.e. from 1 to 7 days, at relatively low temperatures, combined with the retarding effect of the waterglass. Samples containing waterglass always had smaller zeolite content. On the other hand colloidal faujasite solutions, which also contained soluble silicates, had smaller zeolite content at early times and low temperatures, but after seven days curing at $60^\circ C$ they had the highest amount of zeolite detected for all samples (Figure 8.13): zeolite conversion of 84.3% and ratio $\frac{zeolite\ conversion\ \%}{GP\ \%} = 94.7\%$. The preexisting faujasite nanoseeds in similar amorphous geopolymer gel can thus substantially increase the final crystallinity of the geopolymer. This original observation generated through present research may open up new avenues for processing of novel GPs for functional applications such as membranes and impurities encapsulation.

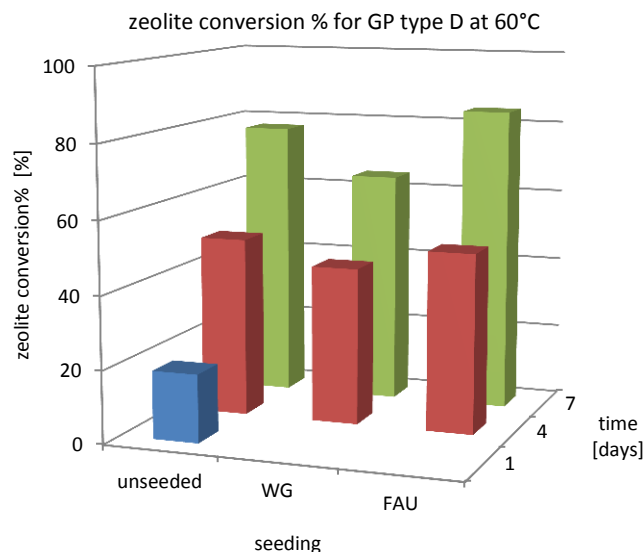


Figure 8.13 Effect of seeding on the zeolite conversion % for GP with $\text{Na}/\text{Al}=1.25$, $\text{H}_2\text{O}/\text{solid}=1.06$ and curing temperature 60°C .

8.5.2. Geopolymer gel nature and reorganization

The retarding effect of waterglass on the GP crystallization observed in Figure 8.13 can be associated with the nature of the amorphous gel. On the contrary, the amount of geopolymer gel had no direct effect on crystallization; it only indicated the maximum amount of crystallinity achievable for a particular geopolymer since the crystals grew consuming the amorphous gel, Figure 8.12. Although the GP% value was almost saturated after 1 day at $T \geq 40^\circ\text{C}$, (Figure C.5) the FTIR peak position associated with the GP shifted, Figure 8.14, and this can be attributed to structural reorganization of the amorphous gel.

As already mentioned, the peak position of the main GP band decreased when increasing Na/Al and decreasing $\text{H}_2\text{O}/\text{solid}$ due to different concentration of $\text{Si}-\text{O}-\text{Na}$ ion pairs, Figure C.3. When these two factors were constant the peak position reveals information on the Si/Al ratio of the geopolymer gel: the higher this ratio the higher the wavenumber.

In unseeded GPs there was an initial aluminum rich gel that was slowly transformed into a silica rich gel. This effect was also observed in fly-ash based geopolymer [164]. Since the

total GP% did not change, it is unlikely that this was due the siliceous remains of the metakaolin that dissolved slowly. Instead, it is more likely that in the initial depolymerized gel most of the Al-O⁻ bonds undergo condensation with the Si-OH bonds (peak at $\approx 945\text{cm}^{-1}$). These condensation reactions were responsible for the initial setting of the geopolymer. The remaining Si-OH and Si-O⁻ bonds would then react over time increasing the gel connectivity (peak at $\approx 965\text{cm}^{-1}$, Figure 8.14). Thus the silica was already present in the gel, but complete condensations took longer [115], [144]. This explanation was proposed for the first time by Provis and Bernal [290] to explain the two stages of gel evolution in the alkali activation of fly ash.

For the waterglass seeded geopolymers this reorganization was not observed but the peak fluctuate around 955cm^{-1} , Figure 8.14. The higher initial value was associated with a higher content of Si-O-Si bonds due to the additional silicate present in the gel. Strangely the peak position did not increase as for the unseeded samples, the final peak position was at lower wavenumber and thus the GP had a lower Si/Al. The initial silica rich gel likely precipitated on the unreacted metakaolin as already proven [114]. North and Swaddle [115] demonstrated that the aluminosilicate rearrangement (i.e. bonds rupture and formation) in linear aluminosilicate is slower in Si-rich oligomers. An Al-rich gel precipitating on the MK surface can eventually break down and expose the MK; instead a silica rich gel would likely cover the MK surface for longer time. It is also possible that the silicates in the initial solution quickly reacted with the Al(IV) centers on the MK surface before dissolution can occur [199].

Even small amount of waterglass could form a more stable passivation barrier that hindered the complete dissolution of MK and this may explain the unreacted MK detected in WG-based GPs, Figure 5.9. This statement was also supported by the GP% in Figure 8.14 (right). Although this effect was small, i.e. 87% vs 82%, the amount of waterglass used was also small and the effect was observed across all compositions; the factor “seeding” had a *p*-value of 0.003, thus a statistically significant effect. Similar considerations were valid for the peak position, Figure 8.14 (left) and Figure C.3 (bottom right). This slower rearrangement of the initially silica rich gel could also explain the crystallization delay in the seeded geopolymer as seen in Figure 8.13. The decrease of the peak position at 4 days of curing for the GP

seeded with colloidal faujasite was more difficult to explain. In fly ash based-geopolymer Rees [164] found that seeds could grow nuclei of an Al-rich gel, but this was probably not the case here where silicates were already in the solution.

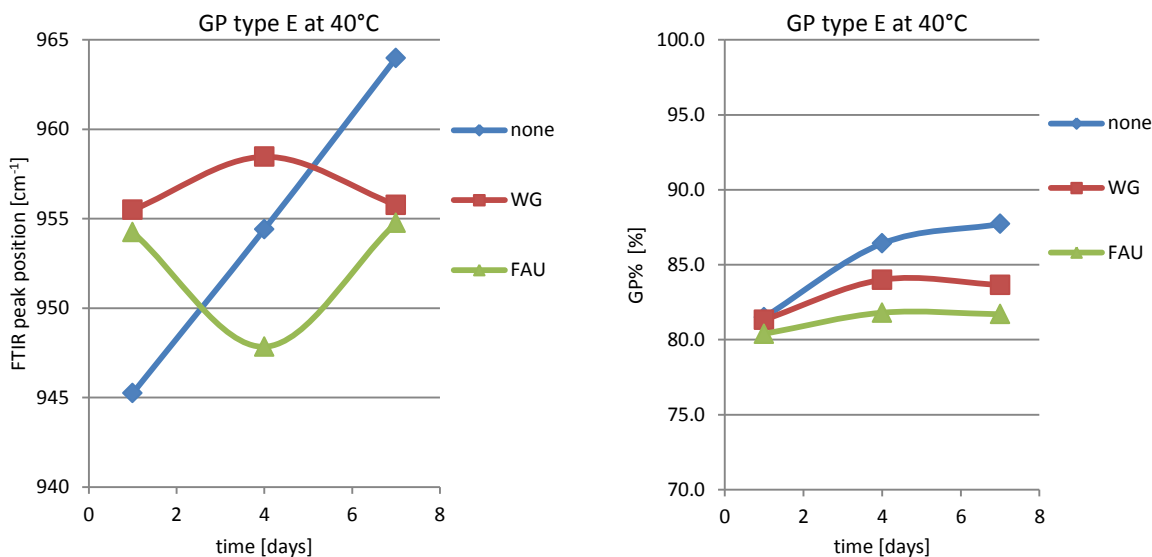


Figure 8.14 Effect of seeding on the GP peak position (left) and GP% (right) for a geopolymer with $\text{Na/Al}=1$ and $\text{H}_2\text{O/solid}=0.84$ cured at 40°C .

8.5.3. Crystallinity and crystal engineering

In Section 8.5.1 we already introduced the importance of the factors including Na/Al , temperature and time to increase the geopolymer crystallinity. According to crystallization diagrams of zeolite LTA and faujasite [174], [185], [253], it is possible to obtain the former when $\text{Si/Al}=1$ and the latter when $\text{Si/Al}>1$, with a small interval of coexistence of both when $\text{Si/Al}\approx 1$ (Figure 2.16). Instead, the main factor affecting GP crystallization in this study was the Na/Al ratio, which has never been reported before for geopolymers. The importance of alkalinity to direct crystal structures has been studied for zeolite synthesis from metakaolin and metal hydroxides in dilute condition ($\text{H}_2\text{O/solid}\approx 10$) and elevated temperature ($T>80^\circ\text{C}$). Nonetheless it was found that only higher Si/Al ratio could favour the faujasite over the zeolite LTA structure [291]. This was probably due to the crystallization mechanism differences in geopolymer and conventional zeolite synthesis. When $\text{Na/Al}\leq 1$ the only phase

that forms was zeolite type A, no matter if extra silica was added or faujasite seeds were included. When $\text{Na}/\text{Al} > 1$ a small amount of faujasite is detected for the unseeded GP, but its percentages increased dramatically when WG or FAU seeds are used. This could be observed in Figure 8.15 in which the LTA% is presented for samples A, E and D: solution/MK of 0.95, 1.27 and 1.61 which correspond to Na/Al ratios of 0.75, 1 and 1.25 (Table 8.2). For GP with $\text{Na}/\text{Al}=1.25$ the factor $\text{H}_2\text{O}/\text{solid}$ had also an effect, in particular a decrease in water content increased even further the percentage of faujasite, Figure 8.15 right. A similar trend was observed in the FTIR peak position, as described in Section 8.4.3.1, which could be explained in terms of ions pairing as previously demonstrated in Figure 6.3 (Section 6.1.1).

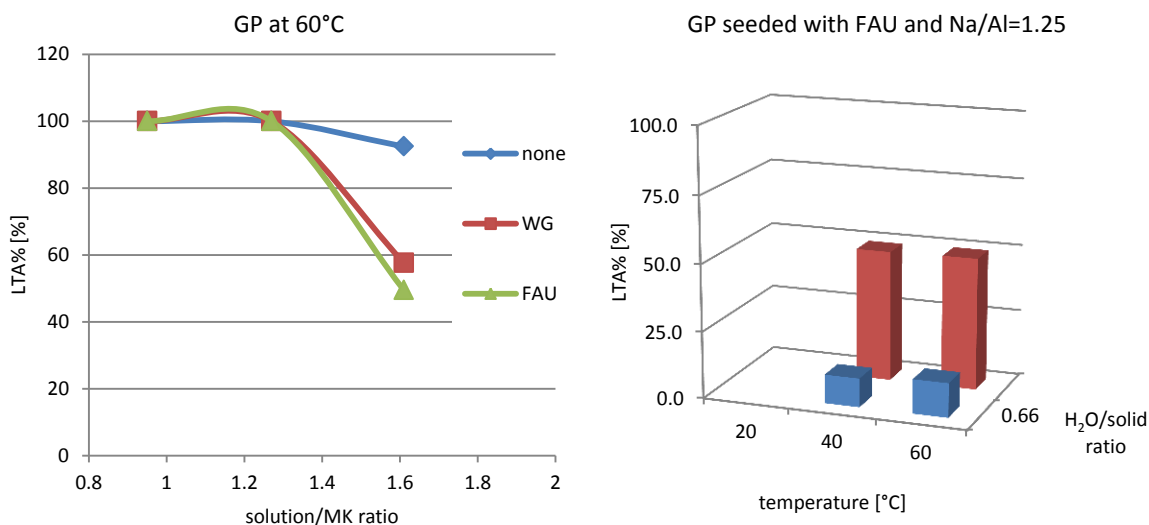


Figure 8.15 Left: effect of solution/MK, and indirectly of Na/Al , on the LTA% for GP cured at 60°C with different seeding type. Right: effect of temperature and $\text{H}_2\text{O}/\text{solid}$ on the LTA% for GP with $\text{Na}/\text{Al}=1.25$ seeded with colloidal FAU.

To explain this crystallization behavior we propose the formation of co-crystal of NaOH and faujasite, where the NaOH fills the faujasite cages and channels and thus becomes indistinguishable from the other charge balancing cations. Since the faujasite has a more open structure compared with LTA, it is easier to accommodate the extra NaOH in its channels or cages [24], Figure 2.15. By reducing water content, NaOH in excess has even less water to interact with. In order to minimize its energy it is possible that it prefers to stay

within the zeolite structure and thus it favors a more open framework. On the contrary if $\text{H}_2\text{O}/\text{solid}$ increases, only zeolite LTA can crystallize at low Si/Al ratios [291]. The existence of co-crystal is not new in zeolite science, for example NaCl and NaOH can form co-crystals with sodalites: $\text{NaCl}-\text{Na}_6[\text{Al}_6\text{Si}_6\text{O}_{24}]$ and $\text{Na}_8(\text{OH})_2\text{Na}_6[\text{Al}_6\text{Si}_6\text{O}_{24}]$ [162].

This is partially in agreement with the work of Zhang [203] on the crystallization of metakaolin based geopolymer. For $\text{Na}/\text{Al}<1$ only zeolite type A was detected, but for $\text{Na}/\text{Al}=1$ a small quantity of zeolite type X was also detected. The value of Na/Al was probably underestimated in that work: the compositions were not corrected for the impurities of the metakaolin, thus the total alumina content in the geopolymer gel was possibly overestimated. This is a common mistake in many studies reported in literature and it can explain the different ratio FAU/LTA obtained using different metakaolin sources. In the same work [197] Zhang prepared GP with $\text{Na}/\text{Al}=1.5$, but only zeolite type A and sodium carbonate were detected by XRD. The samples were stored in plastic bags and not in airtight containers as in the current (our) study, thus CO_2 may have reacted with the excess of NaOH before the onset of crystallization. No sodium carbonate was detected by XRD in our samples. Different extent of carbonation could also explain the different FAU/LTA ratio observed in literature when an excess of NaOH was used [197].

Temperature seems to also have an effect on LTA%, in particular lower temperature seems to further increase the faujasite content. Nonetheless those samples were mostly amorphous, and since faujasite usually nucleated and grew sooner than LTA, at 40°C the zeolite type A had not had the time to form yet. Still, if the crystallization of zeolite type A needs to be avoided, reducing curing temperature and time can be a solution.

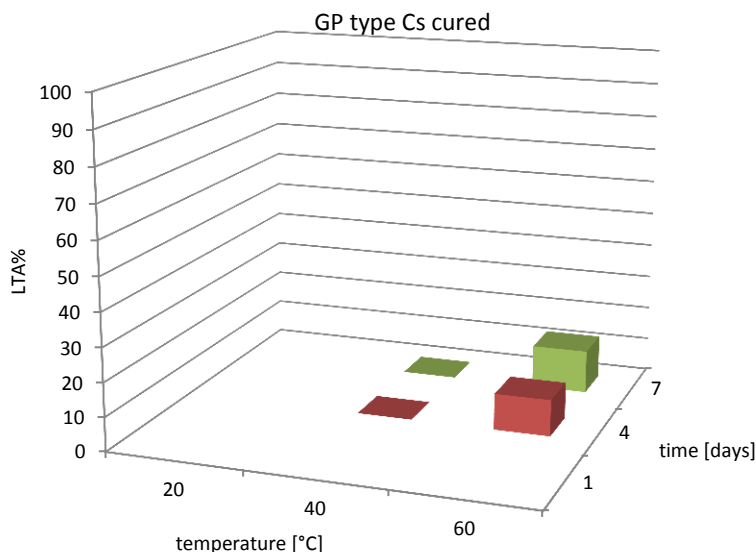


Figure 8.16 Effect of curing time and temperature on the LTA% of a GP with Na/Al=1.25, H₂O/solid=0.66 seeded with colloidal FAU.

Besides a small delay in the crystallization of zeolite type A at certain conditions (i.e. sample Cw cured at 40°C), the factor “time” had no effect on the response LTA%. Examining in detail the QXRD responses presented in Table B.1 revealed that both faujasite and LTA weight percentage always increased over time. This means that there was no inter-zeolite transformation and the zeolite only consumed the amorphous geopolymer gel. The Ostwald’s law of successive transformation and other studies [148], [199] suggest that the initial metastable zeolites will convert into more stable structures, which often correspond to a more dense structures. If this is true we should initially obtain faujasite (FD=12.7 tetrahedra/Å³), which will then convert into zeolite type A (FD=12.9 tetrahedra/Å³) and finally sodalite (FD=17.2 tetrahedra/Å³). However these transformations were not observed neither after 7 days nor after 1 year, Table 8.8. Thus, functional MK-based geopolymers can retain their initial zeolitic properties over time.

Colloidal faujasite seeds did not have a significant effect on LTA%, when compared with WG seeds. We expected the FAU seeds to further decrease the LTA%, while increasing the crystallinity. Epitaxial nucleation on zeolite seeds is not exclusive: the same seed can

promote the crystallization of different species. This is the case for FAU and LTA: since their structure is similar it is possible that one nucleates on the surface of the other [162].

8.6. Summary

In this Chapter a multifactorial design including GP composition, seed type, curing time and temperature was performed and the properties of the GPs were quantified by ATR-FTIR deconvolution and QXRD. Analysis of Variance allowed the determination of the main factors and factors interactions affecting the geopolymerization kinetics expressed in terms of gel precipitation, gel reorganization and zeolite crystallization. Detailed analysis of these factors improved the overall understanding of the transformation that occurs in metakaolin-based geopolymers intended for functional applications.

The analysis revealed that gel formation and zeolite nucleation and growth are not parallel but sequential reactions, and the setting of GP depends only on the former. By decreasing the H₂O/solid ratio it is possible to reduce the setting time at relatively low curing temperatures (5°C to 20°C); a similar effect can be obtained at higher temperatures (40°C to 60°C) by increasing the NaOH concentration. The initial geopolymer gel is richer in alumina, but when small amount of waterglass is added, the initial gel is richer in silica and can form a passivation layer around the unreacted MK.

Higher temperature and higher geopolymer Na/Al ratio increased the GP crystallinity. Longer curing times are needed if soluble silicates are added to the activating solution and this is due to a slower gel rearrangement associated with the Si-rich gel. The addition of colloidal zeolite does not seem to increase the kinetics or extent of gel formation, but the seeds increase its conversion to crystalline zeolite. The crystallization of zeolite from the amorphous gel is a solid state reaction and the Ostwald's - type successive transformation has not been observed for samples aged up to one year.

In conclusion, functional MK-based geopolymer which requires zeolitic properties typical of LTA can be prepared using Na/Al \leq 1, $T=40^\circ$ and curing time $t\geq 7$ days or $T=60^\circ\text{C}$ and $t\approx 4$ days. GP with faujasite functionality can be obtained by using an excess of NaOH (which

likely forms co-crystals), low water content and small amount of waterglass. Attention should be paid to determine the actual content of reactive alumina in the MK and to avoid carbonation of the samples before crystallization has occurred.

9. Conclusions and future work

This work investigated geopolymerization reactions in MK-based GP. We have varied the processing parameters both in terms of the chemical composition (Na/Al, H₂O/solid, Si/Al, solution/solid, addition of seeds) and curing conditions (curing time, temperature and relative humidity). Flow table, Vicat needle, steady state and dynamic rheology were adapted to study the flowability, viscosity and setting time of the GPs viscoelastic suspensions. Structural changes within the GP were followed by quantitative X-ray diffractions (Rietveld refinement with internal standard) and by deconvoluted ATR-FTIR spectra. Unconfined compressive tests and microstructural characterization using SEM were also performed. The goal of this work was to provide new experimental evidences on the differences between NaOH and water-glass (WG) metakaolin-based GPs and to contribute to a comprehensive understanding of the transformations that lead to zeolite crystallization. A deeper understanding of the geopolymerization of metakaolin in NaOH solutions finally allows the optimization of the GP structure to prepare functional materials for environmental applications. The extensive experimental observations and analysis across different GP compositions and using different seeding agents lead to the following conclusions:

- Geopolymerization is a thermally activated reaction and the setting time can be reduced to just few hours when the GPs are cured at $T \geq 35^{\circ}\text{C}$. Nonetheless 24 hours of curing at 40°C are not enough to achieve the maximum strength and longer curing time and/or temperatures (e.g. 40° for 7 days or 125°C for 6 hours) are recommended.
 - The setting reactions correspond to MK dissolution and amorphous gel precipitation, but the nucleation and growth of zeolite is a result of a structural reorganization that occurs once the material has already set. Seeding cannot induce immediate growth of zeolites, thus gel formation is a necessary intermediate step for crystallization. In particular setting occurs when the formed gel can bridge the unreacted particles and it depends both on Na/Al (reaction kinetics) and H₂O/solid (interparticle distance). For GP with low

water content, i.e. $H_2O/solid \approx 0.7$, a geopolymer conversion of approximately 45% is needed for setting to occur.

- Nucleation and growth of zeolite occurs only after prolonged curing at $T \geq 40^\circ C$ (depending on the Si/Al and Na/Al of the amorphous gel). It is a solid state transformation that does not require water to occur. Zeolites detected in this work were mainly zeolite type A, faujasite and hydrosodalite. Ostwald rule of successive transformation was not observed, nonetheless zeolite LTA can transform into hydrosodalite upon drying.
- NaOH/MK based GPs are thixotropic pseudoplastic suspensions with a yield stress and their flow can be described by Herschel-Bulkley equation. They can be used and processed as regular cement (e.g OPC) but the paste needs to be kept in constant shear as the material is highly thixotropic. This behaviour can be exploited in 3D printing of geopolymers, self-supporting membranes and chemically bonded ceramics.
 - The rate limiting steps for the type of GP studied in this work seems to depend on curing temperature, in terms of dissolution of MK at lower temperatures and the growth of gel at higher temperatures, i.e. $T \geq 35^\circ C$. The activation energy of the overall reaction was determined to be about 76 kJ/mol, and it can be reduced to the range of 25 to 50 kJ/mol by using 2 wt% of seeds such as mordenite, faujasite and ZrO_2 and Al_2O_3 . Silica seeds had no effect on the activation energy.
 - The effect of seeding on the setting time, although useful from a scientific standpoint, remains marginal compared with other processing factors such as temperature, Na/Al and $H_2O/solid$.

- Different seeds had different effects on the gel reorganization and crystallization reactions. In particular some seeds induced the formation of zeolite LTA while others favored faujasite. More studies are required in this field. The mechanical properties and durability of NaOH/MK-based GP depends on the crystalline structure formed: octahedral faujasites provide better crystal interlocking and lower solubility. The maximum compressive strength achievable for this crystalline material is $\approx 20\text{MPa}$; consequently this material cannot compete with Ordinary Portland Cement as construction cement but it is suitable for self-sustaining membrane production and encapsulation of hazardous materials.
- The actual Na/Al ratio in NaOH/MK-based GP regulates the reaction kinetics, the total extent of reaction and the type of zeolite formed. Thus, the quantification of the impurities and reactive metakaolin in the solid precursor is of paramount importance. The geopolymer conversion increases dramatically up to Na/Al=1, although small increments were observed also at Na/Al>1. The amorphous gel structural reorganization depends on Na/Al and the crystallization reaction rate and yield increase with this ratio also at Na/Al>1. The formation of NaOH/faujasite co-crystals can favour the faujasite structure when Na/Al>1, although this phenomenon can be reduced at higher H₂O/solid.
- Water in the geopolymers studied in this work not only controlled their rheological properties but had an effect on setting time, ion-pairing and their final crystalline structure. When preparing and testing GPs, it was essential to control the relative humidity throughout the whole process.
- Now that it is possible to control the crystallization in geopolymers, more studies are needed to assess the effects of zeolite type and amount in water purification and heavy metal and radioactive element encapsulation. More

studies are also needed to identify other post-synthesis modification of the crystalline geopolymers to further enhance their performance.

- WG/MK based GPs have an extra degree of freedom compared with NaOH/based GP due to the presence of silica in the activating solution. The silicates in solution have the strongest impact on the geopolymerization reaction steps:
 - soluble silicates increase the mechanical strength of the GP in two ways: by producing a stronger gel (at $\text{Si/Al} \leq 1.35$) and by reducing the $\text{H}_2\text{O/solid}$ required to produce a flowable paste (for $\text{Si/Al} > 1$).
 - by increasing Si/Al we also decrease the dissolution rate and yield of the metakaolin (MK). This effect cannot be ascribed to difference in MK wettability but on the pH of the activating solution and the formation of passivation layers on the surface of MK. For this reason WG/MK based GPs should be considered as a composite material: an amorphous geopolymer matrix with clay fillers. Compressive strength of 40 MPa can be achieved for such composites and thus the material can be used as constructional cement.
 - The passivation layer consists in a relatively stable and dense amorphous gel with high Si/Al that once precipitated on the MK surface and cannot be dissolved. This provides GP with higher compressive strength but, as a consequence, slower gel reorganization leads to slower or totally absent crystallization, depending on the Si/Al , Na/Al and temperature. When autoclaved, new amorphous fibrous structures were observed in the studied GP systems; further studies are needed to identify these phases and investigate the possibility to prepare in-situ fibers-composite geopolymers in autoclaves.
 - At intermediate $\text{Si/Al} \approx 1.35$ the activating solution contains crystalline colloidal sodium metasilicate hydrates. These nanocrystals can possibly act as

seeding agents and therefore they need to be included in future geopolymerization models.

- Since the dissolving monomers and oligomers quickly react with the silicates in solution, the rate limiting step in WG/MK-based GP is the dissolution of MK even at $T \geq 35^\circ\text{C}$. Thus, seeding the GPs with other types of seeds has no effect on the geopolymerization kinetics.
- Small amount of soluble silicate (for geopolymer with $\text{Si}/\text{Al}=1.08$) can promote the formation of faujasite in GP, especially when $\text{Na}/\text{Al}>1$. To compensate for the slower gel rearrangement, higher crystallization temperatures and times are needed.

References

- [1] V. Smil, *Making the Modern World : Materials and Dematerialization*. Hoboken, NJ, USA: Wiley, 2013.
- [2] D. Bonchev and D. H. Rouvray, Eds., *Complexity in Chemistry, Biology, and Ecology*. Boston, MA: Springer US, 2005.
- [3] C. B. Carter and M. G. Norton, *Ceramic Materials*. New York, NY: Springer New York, 2013.
- [4] J. L. Provis and J. S. J. van Deventer, Eds., *Alkali Activated Materials*, vol. 13. Dordrecht: Springer Netherlands, 2014.
- [5] M. Alshaaer, B. El-Eswed, R. I. Yousef, F. Khalili, and H. Rahier, “Development of functional geopolymers for water purification, and construction purposes,” *J. Saudi Chem. Soc.*, vol. 20, pp. S85–S92, 2016.
- [6] T. Luukkonen, M. Sarkkinen, K. Kemppainen, J. Rämö, and U. Lassi, “Metakaolin geopolymer characterization and application for ammonium removal from model solutions and landfill leachate,” *Appl. Clay Sci.*, vol. 119, pp. 266–276, 2016.
- [7] J. Zhang, Y. He, Y. P. Wang, J. Mao, and X. M. Cui, “Synthesis of a self-Supporting faujasite zeolite membrane using geopolymer gel for separation of alcohol/water mixture,” *Mater. Lett.*, vol. 116, pp. 167–170, 2014.
- [8] E. Gartner, “Industrially interesting approaches to ‘low-CO₂’ cements,” *Cem. Concr. Res.*, vol. 34, no. 9, pp. 1489–1498, Sep. 2004.
- [9] A. R. Sakulich, “Reinforced geopolymer composites for enhanced material greenness and durability,” *Sustain. Cities Soc.*, vol. 1, no. 4, pp. 195–210, Dec. 2011.
- [10] M. C. G. Juenger, F. Winnefeld, J. L. Provis, and J. H. Ideker, “Advances in alternative cementitious binders,” *Cem. Concr. Res.*, vol. 41, no. 12, pp. 1232–1243, 2011.

- [11] E. M. Gartner and D. E. Macphee, “A physico-chemical basis for novel cementitious binders,” *Cem. Concr. Res.*, vol. 41, no. 7, pp. 736–749, Jul. 2011.
- [12] U.S. Geological Survey, “Mineral Commodities Summaries,” 2016.
- [13] S. Sorel, “On a new magnesium cement,” *CR Acad Sci*, vol. 65, pp. 102–104, 1867.
- [14] S. A. Walling and J. L. Provis, “Magnesia-Based Cements: A Journey of 150 Years, and Cements for the Future?,” *Chemical Reviews*, vol. 116, no. 7, pp. 4170–4204, 2016.
- [15] J. Skibsted and C. Hall, “Characterization of cement minerals, cements and their reaction products at the atomic and nano scale,” *Cem. Concr. Res.*, vol. 38, no. 2, pp. 205–225, 2008.
- [16] J. Aspdin, “An Improvement in the Modes of Producing an Artificial Stone,” BP 5022, 1824.
- [17] H. Taylor, *Cement chemistry*. T. Telford, 1997.
- [18] K. L. Scrivener and A. Nonat, “Hydration of cementitious materials, present and future,” *Cem. Concr. Res.*, vol. 41, no. 7, pp. 651–665, Jul. 2011.
- [19] A. S. Wagh, *Chemically Bonded Phosphate Ceramics. 21st century materials with diverse applications*. Oxford, UK: Elsevier, 2004.
- [20] A. S. Wagh and A. S., “Recent Progress in Chemically Bonded Phosphate Ceramics,” *ISRN Ceram.*, vol. 2013, pp. 1–20, 2013.
- [21] J. Davidovits, “Structural characterization of geopolymeric materials with X-ray diffractometry and MAS NMR spectroscopy,” *Geopolymer '88 Proc.*, pp. 149–166, 1988.
- [22] J. Davidovits, “Geopolymers and geopolymeric materials,” *J. Therm. Anal.*, vol. 35, no. 2, pp. 429–441, Mar. 1989.
- [23] J. Davidovits, “Geopolymers,” *J. Therm. Anal.*, vol. 37, no. 8, pp. 1633–1656, 1991.

- [24] J. M. Newsam, "Zeolites," in *Solid state chemistry: compounds*, A. K. Cheerthan and P. Day, Eds. Claretton Press, Oxford, 1992, p. 304.
- [25] P. De Silva, K. Sagoe-Crenstil, and V. Sirivivatnanon, "Kinetics of geopolymerization: Role of Al₂O₃ and SiO₂," *Cem. Concr. Res.*, vol. 37, no. 4, pp. 512–518, Apr. 2007.
- [26] C. Ruiz-Santaquiteria, a. Fernández-Jiménez, J. Skibsted, and a. Palomo, "Clay reactivity: Production of alkali activated cements," *Appl. Clay Sci.*, vol. 73, pp. 11–16, Mar. 2013.
- [27] P. Duxson and J. L. Provis, "Designing Precursors for Geopolymer Cements," *J. Am. Ceram. Soc.*, vol. 91, no. 12, pp. 3864–3869, Dec. 2008.
- [28] V. Glukhovskiy, "Soil silicates," *Gostroiizdat Publ. Kiev, USSR*, 1959.
- [29] P. Duxson, A. Fernández-Jiménez, J. L. Provis, G. C. Lukey, A. Palomo, and J. S. J. Van Deventer, "Geopolymer technology: The current state of the art," *J. Mater. Sci.*, vol. 42, no. 9, pp. 2917–2933, 2007.
- [30] J. L. Provis and J. S. J. van Deventer, *Geopolymers: Structures, Processing, Properties And Industrial Applications*. Cambridge, UK: Woodhead, 2009.
- [31] D. Davidovits, "The Poly(sialate) terminology : a very useful and simple model for the promotion and understanding of green-chemistry," in *Geopolymer, Green Chemistry and Sustainable Development Solutions: Proceedings of the World Congress Geopolymer*, Saint Quentin, France, 2005, pp. 9–15.
- [32] P. Duxson, J. L. Provis, G. C. Lukey, and J. S. J. van Deventer, "The role of inorganic polymer technology in the development of 'green concrete,'" *Cem. Concr. Res.*, vol. 37, no. 12, pp. 1590–1597, Dec. 2007.
- [33] P. Duxson, a. Fernández-Jiménez, J. L. Provis, G. C. Lukey, a. Palomo, and J. S. J. Deventer, "Geopolymer technology: the current state of the art," *J. Mater. Sci.*, vol. 42, no. 9, pp. 2917–2933, Dec. 2006.

- [34] F. Pacheco-Torgal, J. Castro-Gomes, and S. Jalali, "Alkali-activated binders: A review," *Constr. Build. Mater.*, vol. 22, no. 7, pp. 1305–1314, Jul. 2008.
- [35] J. Davidovits, "Mineral polymers and methods of making them," US 4349386, 1982.
- [36] J. Davidovits, "Geopolymer Chemistry and Properties," in *1st International Conference on Geopolymer*, 1988, pp. 25–48.
- [37] "Geopolymer Institute." [Online]. Available: <https://www.geopolymer.org/>. [Accessed: 10-Jun-2017].
- [38] J. Davidovits, *Geopolymer Chemistry and Applications, 3rd Ed.* Saint Quentin, France: Institut Géopolymère, 2011.
- [39] H. Xu and J. S. J. Van Deventer, "The geopolymerisation of alumino-silicate minerals," *Int. J. Miner. Process.*, vol. 59, no. 3, pp. 247–266, Jun. 2000.
- [40] A. Autef, E. Joussein, G. Gasgnier, and S. Rossignol, "Role of the silica source on the geopolymerization rate: A thermal analysis study," *J. Non. Cryst. Solids*, vol. 366, no. 1, pp. 13–21, 2013.
- [41] M. W. Munthali, M. A. Elsheikh, E. Johan, and N. Matsue, "Proton adsorption selectivity of zeolites in aqueous media: Effect of Si/Al ratio of zeolites," *Molecules*, vol. 19, no. 12, pp. 20468–20481, 2014.
- [42] D. M. Roy and D. M., "Alkali-activated cements Opportunities and challenges," *Cem. Concr. Res.*, vol. 29, no. 2, pp. 249–254, Feb. 1999.
- [43] F. Pacheco-Torgal, J. Castro-Gomes, and S. Jalali, "Alkali-activated binders: A review. Part 2. About materials and binders manufacture," *Constr. Build. Mater.*, vol. 22, no. 7, pp. 1315–1322, Jul. 2008.
- [44] C. Li, H. Sun, and L. Li, "A review: The comparison between alkali-activated slag (Si+Ca) and metakaolin (Si+Al) cements," *Cem. Concr. Res.*, vol. 40, no. 9, pp. 1341–1349, Sep. 2010.
- [45] C. Shi, A. F. Jiménez, and A. Palomo, "New cements for the 21st century: The pursuit

- of an alternative to Portland cement,” *Cem. Concr. Res.*, vol. 41, no. 7, pp. 750–763, Jul. 2011.
- [46] J. L. Provis, A. Palomo, and C. Shi, “Advances in understanding alkali-activated materials,” *Cem. Concr. Res.*, vol. 78, pp. 110–125, Dec. 2015.
 - [47] J. Davidovits, “Geopolymer Cement Based on Fly Ash and Harmless to Use,” US 8202362B2, 2012.
 - [48] J. Davidovits, “30 years of successes and failures in geopolymer applications. Market trends and potential breakthroughs,” *Keynote Conf. Geopolymer Conf.*, pp. 1–16, 2002.
 - [49] M. Davidovits, N. Davidovits, and J. Davidovits, “Process for obtaining a geopolymeric alumino-silicate and products thus obtained,” US 5342595, 1994.
 - [50] S. Ahmari, L. Zhang, and J. Zhang, “Effects of activator type/concentration and curing temperature on alkali-activated binder based on copper mine tailings,” *J. Mater. Sci.*, vol. 47, no. 16, pp. 5933–5945, Apr. 2012.
 - [51] O. Peyronnard and M. Benzaazoua, “Estimation of the cementitious properties of various industrial by-products for applications requiring low mechanical strength,” *Resour. Conserv. Recycl.*, vol. 56, no. 1, pp. 22–33, 2011.
 - [52] O. Peyronnard and M. Benzaazoua, “Alternative by-product based binders for cemented mine backfill: Recipes optimisation using Taguchi method,” *Miner. Eng.*, vol. 29, pp. 28–38, 2012.
 - [53] T. T. Le, S. a. Austin, S. Lim, R. a. Buswell, a. G. F. Gibb, and T. Thorpe, “Mix design and fresh properties for high-performance printing concrete,” *Mater. Struct.*, vol. 45, no. 8, pp. 1221–1232, Aug. 2012.
 - [54] M. Xia and J. Sanjayan, “Method of formulating geopolymer for 3D printing for construction applications,” *Mater. Des.*, vol. 110, pp. 382–390, 2016.
 - [55] E. Prud’Homme, P. Michaud, E. Joussein, J. M. Clacens, and S. Rossignol, “Role of

- alkaline cations and water content on geomaterial foams: Monitoring during formation,” *J. Non. Cryst. Solids*, vol. 357, no. 4, pp. 1270–1278, 2011.
- [56] C. Bai *et al.*, “High-porosity geopolymer foams with tailored porosity for thermal insulation and wastewater treatment,” *J. Mater. Res.*, vol. 32, no. 17, pp. 3251–3259, Sep. 2017.
- [57] M. Steveson and K. Sagoe-Crentsil, “Relationships between composition, structure and strength of inorganic polymers,” *J. Mater. Sci.*, vol. 40, no. 8, pp. 2023–2036, Apr. 2005.
- [58] P. Duxson, J. L. Provis, G. C. Lukey, S. W. Mallicoat, W. M. Kriven, and J. S. J. van Deventer, “Understanding the relationship between geopolymer composition, microstructure and mechanical properties,” *Colloids Surfaces A Physicochem. Eng. Asp.*, vol. 269, no. 1–3, pp. 47–58, Nov. 2005.
- [59] H. Yan, C. Xue-Min, M. Jin, L. P. Liu, X. D. Liu, and J. Y. Chen, “The hydrothermal transformation of solid geopolymers into zeolites,” *Microporous Mesoporous Mater.*, vol. 161, pp. 187–192, 2012.
- [60] S. A. Bernal, E. D. Rodríguez, R. Mejía de Gutiérrez, M. Gordillo, and J. L. Provis, “Mechanical and thermal characterisation of geopolymers based on silicate-activated metakaolin/slag blends,” *J. Mater. Sci.*, vol. 46, no. 16, pp. 5477–5486, Aug. 2011.
- [61] A. Palomo, M. T. Blanco-Varela, M. L. Granizo, F. Puertas, T. Vazquez, and M. W. Grutzeck, “Chemical stability of cementitious materials based on metakaolin,” *Cem. Concr. Res.*, vol. 29, no. 7, pp. 997–1004, 1999.
- [62] M. Rowles and B. O’Connor, “Chemical optimisation of the compressive strength of aluminosilicate geopolymers synthesised by sodium silicate activation of metakaolinite,” *J. Mater. Chem.*, vol. 13, no. 5, pp. 1161–1165, Apr. 2003.
- [63] J. L. Provis, P. Duxson, and J. S. J. van Deventer, “The role of particle technology in developing sustainable construction materials,” *Advanced Powder Technology*, vol. 21, no. 1, pp. 2–7, 2010.

- [64] T. F. W. Greig, J. W., Barth, "The system $\text{Na}_2\text{O} \cdot \text{Al}_2\text{O}_3 \cdot 2\text{SiO}_2$ (nepheline, carnegietite)- $\text{Na}_2\text{O} \cdot \text{Al}_2\text{O}_3 \cdot 6\text{SiO}_2$ (albite)," *Amer. J. Sci.*, vol. 5, pp. 93–112, 1938.
- [65] A. Purdon, "The action of alkalis on blast-furnace slag," *J Soc Chem Ind*, vol. 59, pp. 3–4, 1940.
- [66] R. Snellings, G. Mertens, and J. Elsen, "Supplementary Cementitious Materials," *Rev. Mineral. Geochemistry*, vol. 74, no. 1, 2012.
- [67] J. Dalle, "Process of manufacturing panels composed of units in, for example, ceramic, assembled by a thermoplastic material," US 4000027A, 1976.
- [68] J. Davidovits and J. J. Legrand, "Process for agglomerating compressible mineral substances under the form of powder, particles or fibres," US 4028454, 1977.
- [69] J. Wastiels, X. Wu, S. Faignet, and G. Patfoort, "Mineral polymer based on fly ash," *J. Resour. Manag. Technol.*, vol. 22, no. 3, pp. 135–141, 1994.
- [70] A. Palomo and F. P. Glasser, "Chemically-bonded cementitious materials based on metakaolin," *Br. Ceram. Trans. J.*, vol. 91, pp. 107–112, 1992.
- [71] H. Rahier, B. Van Mele, M. Biesemans, J. Wastiels, and X. Wu, "Low-temperature synthesized aluminosilicate glasses Part I low-temperature reaction stoichiometry and structure of a model compound," *J. Mater. Sci.*, vol. 31, no. 1, pp. 71–79, 1996.
- [72] H. Rahier, B. Van Mele, and J. Wastiels, "Low-temperature synthesized aluminosilicate glasses Part II rheological transformations during low-temperature cure and high-temperature properties of a model compound," *J. Mater. Sci.*, vol. 31, no. 1, pp. 80–85, 1996.
- [73] H. Rahier, W. Simons, B. Van Mele, and M. Biesemans, "Low-temperature synthesized aluminosilicate glasses Part III influence of the composition of the silicate solution on production, structure and properties," *J. Mater. Sci.*, vol. 32, no. 9, pp. 2237–2247, 1997.
- [74] H. Rahier, J. F. Denayer, and B. Van Mele, "Low-temperature synthesized

- aluminosilicate glasses: Part IV. Modulated DSC study on the effect of particle size of metakaolinite on the production of inorganic polymer glasses,” *J. Mater. Sci.*, vol. 38, no. 14, pp. 3131–3136, 2003.
- [75] M. L. Granizo and M. T. Blanco, “Alkaline Activation of Metakaolin An Isothermal Conduction Calorimetry Study,” *J. Therm. Anal. Calorim.*, vol. 52, no. 3, pp. 957–965, 1998.
- [76] V. F. . Barbosa, K. J. . MacKenzie, and C. Thaumaturgo, “Synthesis and characterisation of materials based on inorganic polymers of alumina and silica: sodium polysialate polymers,” *Int. J. Inorg. Mater.*, vol. 2, no. 4, pp. 309–317, Sep. 2000.
- [77] V. F. F. Barbosa and K. J. D. MacKenzie, “Thermal behaviour of inorganic geopolymers and composites derived from sodium polysialate,” *Mater. Res. Bull.*, vol. 38, no. 2, pp. 319–331, Jan. 2003.
- [78] V. F. F. Barbosa and K. J. D. MacKenzie, “Synthesis and Thermal Behaviour of Potassium Silate Geopolymers,” *Mater. Lett.*, vol. 57, pp. 1477–1482, 2003.
- [79] W. M. Kriven, J. L. Bell, and M. Gordon, “Microstructure and Microchemistry of Fully-Reacted Geopolymers and Geopolymer Matrix Composites,” in *Advances in Ceramic Matrix Composites IX*, Hoboken, NJ, USA: John Wiley & Sons, Inc., 2012, pp. 227–250.
- [80] D. C. Comrie and W. M. Kriven, “Composite cold ceramic geopolymer in a refractory application,” in *Advances in Ceramic Matrix Composites IX*, 2004, vol. 153, pp. 211–225.
- [81] H. Xu and J. S. J. Van Deventer, “Geopolymerisation of multiple minerals,” *Miner. Eng.*, vol. 15, no. 12, pp. 1131–1139, 2002.
- [82] H. Xu and J. S. J. Van Deventer, “The effect of alkali metals on the formation of geopolymeric gels from alkali-feldspars,” *Colloids Surfaces A Physicochem. Eng. Asp.*, vol. 216, no. 1–3, pp. 27–44, 2003.

- [83] B. Fabbri, S. Gualtieri, and C. Leonardi, "Modifications induced by the thermal treatment of kaolin and determination of reactivity of metakaolin," *Appl. Clay Sci.*, vol. 73, pp. 2–10, Mar. 2013.
- [84] P. Ptáček, F. Šoukal, T. Opravil, M. Nosková, J. Havlica, and J. Brandštetr, "Mid-infrared spectroscopic study of crystallization of cubic spinel phase from metakaolin," *J. Solid State Chem.*, vol. 184, no. 10, pp. 2661–2667, Oct. 2011.
- [85] I. W. M. BROWN, K. J. D. MacKENZIE, M. E. BOWDEN, and R. H. MEINHOLD, "Outstanding Problems in the Kaolinite-Mullite Reaction Sequence Investigated by ^{29}Si and ^{27}Al Solid-state Nuclear Magnetic Resonance: 11, High-Temperature Transformations of Metakaolinite," *J. Am. Ceram. Soc.*, vol. 68, no. 6, pp. 298–301, Jun. 1985.
- [86] K. J. D. MacKenzie, M. E. Bowden, and R. H. Meinholt, "The structure and thermal transformations of allophanes studied by ^{29}Si and ^{27}Al high resolution solid-state NMR," *Clays Clay Miner.*, vol. 39, no. 4, pp. 337–346, 1991.
- [87] Y. He, L. Liu, L. He, and X. Cui, "Characterization of chemosynthetic $\text{H}_3\text{PO}_4\text{-Al}_2\text{O}_3\text{-2SiO}_2$ geopolymers," *Ceram. Int.*, vol. 42, no. 9, pp. 10908–10912, 2016.
- [88] C. R. D. E. Kimpe and R. Rivard, "Hydrothermal formation of a kaolinite-like product from noncrystalline aluminosilicate gels," *Clays Clay Miner.*, vol. 29, no. 6, pp. 446–450, 1981.
- [89] Y. L. Tsai, J. V. Hanna, Y. L. Lee, M. E. Smith, and J. C. C. Chan, "Solid-state NMR study of geopolymer prepared by sol-gel chemistry," *J. Solid State Chem.*, vol. 183, no. 12, pp. 3017–3022, 2010.
- [90] P. Duxson, S. W. Mallicoat, G. C. Lukey, W. M. Kriven, and J. S. J. van Deventer, "The effect of alkali and Si/Al ratio on the development of mechanical properties of metakaolin-based geopolymers," *Colloids Surfaces A Physicochem. Eng. Asp.*, vol. 292, no. 1, pp. 8–20, Jan. 2007.
- [91] K. Lu, J. L. Bell, and W. M. Kriven, *Advances in synthesis, processing, and*

applications of nanostructures, vol. 165. Wiley, 2012.

- [92] J. Burgess, “Ions in Solution: Basic Principles of Chemical Interactions,” *Woodhead Publishing; 1st edition*, vol. 78, no. 4. Horwood Pub, pp. 15–61, 1999.
- [93] “C. F. Baes and R. S. Mesmer: The Hydrolysis of Cations. John Wiley & Sons, New York, London, Sydney, Toronto 1976. 489 Seiten, Preis: £ 18.60,” *Berichte der Bunsengesellschaft für Phys. Chemie*, vol. 81, no. 2, pp. 245–246, Feb. 1977.
- [94] J. Mähler and I. Persson, “A Study of the Hydration of the Alkali Metal Ions in Aqueous Solution,” *Inorg. Chem.*, vol. 51, no. 1, pp. 425–438, Jan. 2012.
- [95] T. Megyes, S. Bálint, T. Grósz, T. Radnai, I. Bakó, and P. Sipos, “The structure of aqueous sodium hydroxide solutions: a combined solution x-ray diffraction and simulation study,” *J. Chem. Phys.*, vol. 128, no. 4, p. 44501, Jan. 2008.
- [96] G. Busca, *Heterogeneous Catalytic Materials: Solid State Chemistry, Surface Chemistry and Catalytic Behaviour*. 2014.
- [97] I. Halasz, M. Agarwal, R. Li, and N. Miller, “What can vibrational spectroscopy tell about the structure of dissolved sodium silicates?,” *Microporous Mesoporous Mater.*, vol. 135, no. 1–3, pp. 74–81, Nov. 2010.
- [98] J. L. Provis, G. C. Lukey, and D. C. Shallcross, “Modeling Multicomponent Ion Exchange: Application of the Single-Parameter Binary System Model,” *Ind. Eng. Chem. Res.*, vol. 44, no. 7, pp. 2250–2257, 2005.
- [99] J. L. Provis, P. Duxson, G. C. Lukey, F. Separovic, W. M. Kriven, and J. S. J. Van Deventer, “Modeling speciation in highly concentrated alkaline silicate solutions,” *Ind. Eng. Chem. Res.*, vol. 44, no. 23, pp. 8899–8908, 2005.
- [100] J. L. Provis and J. S. J. van Deventer, “Geopolymerisation kinetics. 2. Reaction kinetic modelling,” *Chem. Eng. Sci.*, vol. 62, no. 9, pp. 2318–2329, May 2007.
- [101] J. G. Vail, *Soluble Silicates: Chemistry*. Reinhold, 1952.
- [102] E. Engelhardt, G. Hoebbel, D. Tarmak, M. Samoson, A. and Lippmaa, “²⁹Si-NMR-

Untersuchungen zur Anionenstruktur von kristallinen Tetramethylammonium-alumosilicaten und -alumosilicatlösungen,” *Zeitschrift für Anorg. und Allg. Chemie*, vol. 484, no. 1, pp. 22–32, 1982.

- [103] H. Maekawa, T. Maekawa, K. Kawamura, and T. Yokokawa, “The structural groups of alkali silicate glasses determined from ^{29}Si MAS-NMR,” *J. Non. Cryst. Solids*, vol. 127, no. 1, pp. 53–64, Jan. 1991.
- [104] D. Papias, I. P. Giannopoulou, and T. Perraki, “Effect of synthesis parameters on the mechanical properties of fly ash-based geopolymers,” *Colloids Surfaces A Physicochem. Eng. Asp.*, vol. 301, no. 1–3, pp. 246–254, Jul. 2007.
- [105] D. Matson, S. Sharma, and J. Philpotts, “The structure of high-silica alkali-silicate glasses. A Raman spectroscopic investigation,” *J. Non. Cryst. Solids*, no. 416, p. 7771, 1983.
- [106] I. L. Svensson, S. Sjöberg, and L.-O. Ohman, “Polysilicate equilibria in concentrated sodium silicate solutions,” *J. Chem. Soc. Faraday Trans. 1*, vol. 82, no. 12, p. 3635, 1986.
- [107] I. Halasz, M. Agarwal, R. Li, and N. Miller, “What can vibrational spectroscopy tell about the structure of dissolved sodium silicates?,” *Microporous Mesoporous Mater.*, vol. 135, no. 1–3, pp. 74–81, 2010.
- [108] J. Nordström *et al.*, “Concentration- and pH-dependence of highly alkaline sodium silicate solutions,” *J. Colloid Interface Sci.*, vol. 356, no. 1, pp. 37–45, Apr. 2011.
- [109] P. B. Jamieson and L. S. D. Glasser, “Sodium Silicate Hydrates. I. Crystallographic Data,” *Acta Cryst.*, vol. 20, no. 373, pp. 2–5, 1966.
- [110] T. W. Swaddle, J. Salerno, and P. A. Tregloan, “Aqueous aluminates, silicates, and aluminosilicates,” *Chem. Soc. Rev.*, vol. 23, no. 5, p. 319, 1994.
- [111] T. Swaddle, “Silicate complexes of aluminum(III) in aqueous systems,” *Coord. Chem. Rev.*, vol. 219–221, pp. 665–686, Oct. 2001.

- [112] C. S. Cundy and P. A. Cox, "The hydrothermal synthesis of zeolites: Precursors, intermediates and reaction mechanism," *Microporous and Mesoporous Materials*, vol. 82, no. 1–2, pp. 1–78, 2005.
- [113] L. Weng and K. Sagoe-Crentsil, "Dissolution processes, hydrolysis and condensation reactions during geopolymer synthesis: Part I—Low Si/Al ratio systems," *J. Mater. Sci.*, vol. 42, no. 9, pp. 2997–3006, Jan. 2007.
- [114] C. E. White, J. L. Provis, T. Proffen, and J. S. J. van Deventer, "Molecular mechanisms responsible for the structural changes occurring during geopolymerization: Multiscale simulation," *AIChE J.*, vol. 58, no. 7, pp. 2241–2253, Jul. 2012.
- [115] M. R. North and T. W. Swaddle, "Kinetics of silicate exchange in alkaline aluminosilicate solutions.," *Inorg. Chem.*, vol. 39, no. 12, pp. 2661–5, Jun. 2000.
- [116] A. Bauer and G. Berger, "Kaolinite and smectite dissolution rate in high molar KOH solutions at 35° and 80°C," *Appl. Geochemistry*, vol. 13, no. 7, pp. 905–916, Sep. 1998.
- [117] A. M. Buckley and M. Greenblatt, "The Sol-Gel Preparation of Silica Gels," *J. Chem. Educ.*, vol. 71, no. 7, p. 599, Jul. 1994.
- [118] K. Sagoe-Crentsil and L. Weng, "Dissolution processes, hydrolysis and condensation reactions during geopolymer synthesis: Part II. High Si/Al ratio systems," *J. Mater. Sci.*, vol. 42, no. 9, pp. 3007–3014, Dec. 2006.
- [119] Z. Zhang, H. Wang, J. L. Provis, F. Bullen, A. Reid, and Y. Zhu, "Quantitative kinetic and structural analysis of geopolymers. Part 1. The activation of metakaolin with sodium hydroxide," *Thermochim. Acta*, vol. 539, pp. 23–33, Jul. 2012.
- [120] Z. Zhang, J. L. Provis, H. Wang, F. Bullen, and A. Reid, "Quantitative kinetic and structural analysis of geopolymers. Part 2. Thermodynamics of sodium silicate activation of metakaolin," *Thermochim. Acta*, vol. 565, pp. 163–171, Aug. 2013.
- [121] S. L. Brantley, J. D. Kubicki, and A. F. White, *Kinetics of water-rock interaction*.

Springer, 2008.

- [122] S. K. Upadhyay, *Chemical kinetics and reaction dynamics*. Springer, 2006.
- [123] F. Bellmann, D. Damidot, B. Möser, and J. Skibsted, “Improved evidence for the existence of an intermediate phase during hydration of tricalcium silicate,” *Cem. Concr. Res.*, vol. 40, no. 6, pp. 875–884, 2010.
- [124] C. E. White, J. L. Provis, T. Proffen, D. P. Riley, and J. S. J. van Deventer, “Density functional modeling of the local structure of kaolinite subjected to thermal dehydroxylation,” *J. Phys. Chem. A*, vol. 114, no. 14, pp. 4988–4996, 2010.
- [125] L. Valentini, M. Favero, M. C. Dalconi, V. Russo, G. Ferrari, and G. Artioli, “Kinetic Model of Calcium-Silicate Hydrate Nucleation and Growth in the Presence of PCE Superplasticizers,” *Cryst. Growth Des.*, vol. 16, no. 2, pp. 646–654, 2016.
- [126] Z. X. Xie and J. V Walther, “Incongruent Dissolution and Surface-Area of Kaolinite,” *Geochim. Cosmochim. Acta*, vol. 56, no. 9, pp. 3357–3363, 1992.
- [127] E. H. Oelkers, J. Schott, and J.-L. Devidal, “The effect of aluminum, pH, and chemical affinity on the rates of aluminosilicate dissolution reactions,” *Geochim. Cosmochim. Acta*, vol. 58, no. 9, pp. 2011–2024, 1994.
- [128] R. Snellings, “Solution-controlled dissolution of supplementary cementitious material glasses at pH 13: The effect of solution composition on glass dissolution rates,” *J. Am. Ceram. Soc.*, vol. 96, no. 8, pp. 2467–2475, 2013.
- [129] W. L. Bourcier, “Affinity functions for modeling glass dissolution rates,” *U.S. DOE Rep. UCRL-JC-131186 Prep. At. Energy Commission, Val. due Rhone Summer Work. Glas. Sci. Res. High Perform. Contain. Jeannes-le-Clap, Fr.*
- [130] A. Bauer, B. Velde, and G. Berger, “Kaolinite transformation in high molar KOH solutions,” *Appl. Geochemistry*, vol. 13, no. 5, pp. 619–629, Jul. 1998.
- [131] N. Granizo, A. Palomo, and A. Fernandez-Jiménez, “Effect of temperature and alkaline concentration on metakaolin leaching kinetics,” *Ceram. Int.*, vol. 40, no. 7

PART A, pp. 8975–8985, 2014.

- [132] J. L. Provis, “Modelling the formation of geopolymers,” The University of Melbourne, 2006.
- [133] M. B. Ogundiran and S. Kumar, “Synthesis and characterisation of geopolymer from Nigerian Clay,” *Appl. Clay Sci.*, vol. 108, pp. 173–181, May 2015.
- [134] P. Duxson, G. C. Lukey, F. Separovic, and J. S. J. van Deventer, “Effect of Alkali Cations on Aluminum Incorporation in Geopolymeric Gels,” *Ind. Eng. Chem. Res.*, vol. 44, no. 4, pp. 832–839, Feb. 2005.
- [135] R. P. Williams, R. D. Hart, and A. van Riessen, “Quantification of the Extent of Reaction of Metakaolin-Based Geopolymers Using X-Ray Diffraction, Scanning Electron Microscopy, and Energy-Dispersive Spectroscopy,” *J. Am. Ceram. Soc.*, vol. 94, no. 8, pp. 2663–2670, Aug. 2011.
- [136] U. Schubert, “Chemistry and Fundamentals of the Sol-Gel Process,” in *The Sol-Gel Handbook*, vol. 1–3, 2015, pp. 1–28.
- [137] A. V. McCormick, A. T. Bell, and C. J. Radke, “Evidence from alkali-metal NMR spectroscopy for ion pairing in alkaline silicate solutions,” *J. Phys. Chem.*, vol. 93, no. 5, pp. 1733–1737, Mar. 1989.
- [138] P. Sipos, “The structure of Al(III) in strongly alkaline aluminate solutions - A review,” *J. Mol. Liq.*, vol. 146, no. 1–2, pp. 1–14, 2009.
- [139] J. Šefčík and A. V. McCormick, “Thermochemistry of aqueous silicate solution precursors to ceramics,” *Sol-Gel Wet Chem. Synth.*, vol. 43, no. 11A, pp. 2773–2784, 1997.
- [140] C. E. White, J. L. Provis, T. Proffen, and J. S. J. Van Deventer, “Quantitative mechanistic modeling of silica solubility and precipitation during the initial period of zeolite synthesis,” *J. Phys. Chem. C*, vol. 115, no. 20, pp. 9879–9888, 2011.
- [141] M. J. Mora-Fonz, C. R. A. Catlow, and D. W. Lewis, “Oligomerization and

cyclization processes in the nucleation of microporous silicas,” *Angew. Chemie - Int. Ed.*, vol. 44, no. 20, pp. 3082–3086, 2005.

- [142] C. a Rees, J. L. Provis, G. C. Lukey, and J. S. J. van Deventer, “In situ ATR-FTIR study of the early stages of fly ash geopolymer gel formation,” *Langmuir*, vol. 23, no. 17, pp. 9076–82, Aug. 2007.
- [143] M. J. Mora-Fonz, C. R. A. Catlow, and D. W. Lewis, “Modeling aqueous silica chemistry in Alkali media,” *J. Phys. Chem. C*, vol. 111, no. 49, pp. 18155–18158, 2007.
- [144] C. E. White, J. L. Provis, G. J. Kearley, D. P. Riley, and J. S. J. van Deventer, “Density functional modelling of silicate and aluminosilicate dimerisation solution chemistry,” *Dalt. Trans.*, vol. 40, no. 6, pp. 1348–1355, 2011.
- [145] J. L. Provis, P. Duxson, J. S. J. Van Deventer, and G. C. Lukey, “The Role of Mathematical Modelling and Gel Chemistry in Advancing Geopolymer Technology,” *Chem. Eng. Res. Des.*, vol. 83, no. 7, pp. 853–860, Jul. 2005.
- [146] J. L. Provis and J. S. J. van Deventer, “Geopolymerisation kinetics. 1. In situ energy-dispersive X-ray diffractometry,” *Chem. Eng. Sci.*, vol. 62, no. 9, pp. 2309–2317, May 2007.
- [147] J. Faimon, “Oscillatory silicon and aluminum aqueous concentrations during experimental aluminosilicate weathering,” *Geochim. Cosmochim. Acta*, vol. 60, no. 15, pp. 2901–2907, Aug. 1996.
- [148] A. Gualtieri, P. Norby, G. Artioli, and J. Hanson, “Kinetics of formation of zeolite Na-A [LTA] from natural kaolinites,” *Phys. Chem. Miner.*, vol. 24, no. 3, pp. 191–199, Apr. 1997.
- [149] G. Kemmer and S. Keller, “Nonlinear least-squares data fitting in Excel spreadsheets,” *Nat. Protoc.*, vol. 5, no. 2, pp. 267–281, Feb. 2010.
- [150] K. Yang and C. E. White, “Modeling the Formation of Alkali Aluminosilicate Gels at the Mesoscale Using Coarse-Grained Monte Carlo,” *Langmuir*, vol. 32, no. 44, pp.

11580–11590, 2016.

- [151] C. E. White, K. Page, N. J. Henson, and J. L. Provis, “In situ synchrotron X-ray pair distribution function analysis of the early stages of gel formation in metakaolin-based geopolymers,” *Appl. Clay Sci.*, vol. 73, pp. 17–25, Mar. 2013.
- [152] G. Artioli and J. W. Bullard, “Cement hydration: the role of adsorption and crystal growth,” *Cryst. Res. Technol.*, vol. 48, no. 10, pp. 903–918, Oct. 2013.
- [153] R. Alizadeh, L. Raki, J. M. Makar, J. J. Beaudoin, and I. Moudrakovski, “Hydration of tricalcium silicate in the presence of synthetic calcium–silicate–hydrate,” *J. Mater. Chem.*, vol. 19, no. 42, p. 7937, 2009.
- [154] J. J. Thomas, H. M. Jennings, and J. J. Chen, “Influence of Nucleation Seeding on the Hydration Mechanisms of Tricalcium Silicate and Cement,” *J. Phys. Chem. C*, vol. 113, no. 11, pp. 4327–4334, Mar. 2009.
- [155] J. B. Presores *et al.*, “Solution-mediated phase transformation of uric acid dihydrate,” *CrystEngComm*, vol. 16, no. 31, p. 7278, May 2014.
- [156] D. E. Giammar, R. G. Bruant, and C. A. Peters, “Forsterite dissolution and magnesite precipitation at conditions relevant for deep saline aquifer storage and sequestration of carbon dioxide,” *Chem. Geol.*, vol. 217, no. 3–4 SPEC. ISS., pp. 257–276, 2005.
- [157] P. W. Brown and M. Fulmer, “Kinetics of Hydroxyapatite Formation at Low Temperature,” *J. Am. Ceram. Soc.*, vol. 74, no. 5, pp. 934–940, May 1991.
- [158] H. Ecroyd *et al.*, “Dissociation from the oligomeric state is the rate-limiting step in fibril formation by κ -casein,” *J. Biol. Chem.*, vol. 283, no. 14, pp. 9012–9022, 2008.
- [159] P. K. Dutta and J. Bronic, “Mechanism of Zeolite Formation - Seed Gel Interaction,” *Zeolites*, vol. 14, no. 4, pp. 250–255, 1994.
- [160] R. D. Edelman, D. V. Kudalkar, T. Ong, J. Warzywoda, and R. W. Thompson, “Crystallization phenomena in seeded zeolite syntheses,” *Zeolites*, vol. 9, no. 6, pp. 496–502, Nov. 1989.

- [161] J. Warzywoda and R. W. Thompson, "Synthesis of zeolite A in the Na/K system and the effect of seeding," *Zeolites*, vol. 11, no. 6, pp. 577–582, 1991.
- [162] D. L. Dorset, "Nascent zeolite frameworks grown from amorphous gels - Identification and prospects for crystal engineering," *Zeitschrift fur Krist.*, vol. 226, no. 1, pp. 18–31, 2011.
- [163] J. W. Phair, J. S. J. Van Deventer, and J. D. Smith, "Mechanism of Polysialation in the Incorporation of Zirconia into Fly Ash-Based Geopolymers," *Society*, vol. 39, no. 8, pp. 2925–2934, 2000.
- [164] C. a. Rees, J. L. Provis, G. C. Lukey, and J. S. J. van Deventer, "The mechanism of geopolymer gel formation investigated through seeded nucleation," *Colloids Surfaces A Physicochem. Eng. Asp.*, vol. 318, no. 1–3, pp. 97–105, Apr. 2008.
- [165] S. Riahi and A. Nazari, "The effects of nanoparticles on early age compressive strength of ash-based geopolymers," *Ceram. Int.*, vol. 38, no. 6, pp. 4467–4476, Aug. 2012.
- [166] A. Hajimohammadi, J. L. Provis, and J. S. J. van Deventer, "Time-resolved and spatially-resolved infrared spectroscopic observation of seeded nucleation controlling geopolymer gel formation.," *J. Colloid Interface Sci.*, vol. 357, no. 2, pp. 384–92, May 2011.
- [167] Z. Zuhua, Y. Xiao, Z. Huajun, and C. Yue, "Role of water in the synthesis of calcined kaolin-based geopolymer," *Appl. Clay Sci.*, vol. 43, no. 2, pp. 218–223, 2009.
- [168] M. Criado, a. Fernández-Jiménez, and a. Palomo, "Alkali activation of fly ash: Effect of the SiO₂/Na₂O ratio," *Microporous Mesoporous Mater.*, vol. 106, no. 1–3, pp. 180–191, Nov. 2007.
- [169] C. Ferone *et al.*, "Application-oriented chemical optimization of a metakaolin based geopolymer," *Materials (Basel).*, vol. 6, no. 5, pp. 1920–1939, 2013.
- [170] M. Romagnoli, C. Leonelli, E. Kamse, and M. Lassinantti Gualtieri, "Rheology of geopolymer by DOE approach," *Constr. Build. Mater.*, vol. 36, pp. 251–258, Nov.

2012.

- [171] J. D. Sherman, "Synthetic zeolites and other microporous oxide molecular sieves.," *Proc. Natl. Acad. Sci. U. S. A.*, vol. 96, no. 7, pp. 3471–8, Mar. 1999.
- [172] "International Zeolite Association." [Online]. Available: www.iza-online.org. [Accessed: 10-Jun-2017].
- [173] M. a Zwijnenburg and S. T. Bromley, "Zeolite synthesis: an energetic perspective.," *Phys. Chem. Chem. Phys.*, vol. 12, no. 43, pp. 14579–14584, 2010.
- [174] J. Šefčík and A. V. McCormick, "Prediction of crystallization diagrams for synthesis of zeolites," *Chem. Eng. Sci.*, vol. 54, no. 15–16, pp. 3513–3519, 1999.
- [175] H. Ghobarkar, O. Schäf, and U. Guth, "Zeolites—from kitchen to space," *Prog. Solid State Chem.*, vol. 27, no. 2–4, pp. 29–73, Jan. 1999.
- [176] W. Wagner and a. Pruss, "International Equations for the Saturation Properties of Ordinary Water Substance. Revised According to the International Temperature Scale of 1990. Addendum to J. Phys. Chem. Ref. Data 16, 893 (1987)," *J. Phys. Chem. Ref. Data*, vol. 22, no. 3, p. 783, 1993.
- [177] C. A. Rees, J. L. Provis, G. C. Lukey, and J. S. J. van Deventer, "The mechanism of geopolymer gel formation investigated through seeded nucleation," *Colloids Surfaces A Physicochem. Eng. Asp.*, vol. 318, no. 1–3, pp. 97–105, Apr. 2008.
- [178] J. S. J. van Deventer, G. C. Lukey, and H. Xu, "Effect of Curing Temperature and Silicate Concentration on Fly-Ash-Based Geopolymerization," *Ind. Eng. Chem. Res.*, vol. 45, no. 10, pp. 3559–3568, May 2006.
- [179] I. Lancellotti, M. Catauro, C. Ponzoni, F. Bollino, and C. Leonelli, "Inorganic polymers from alkali activation of metakaolin: Effect of setting and curing on structure," *J. Solid State Chem.*, vol. 200, pp. 341–348, Apr. 2013.
- [180] J. Warzywoda, R. D. Edelman, and R. W. Thompson, "Thoughts on the induction time in zeolite crystallization," *Zeolites*, vol. 9, no. 3, pp. 187–192, 1989.

- [181] B. Subotic, T. Antić, and J. Bronić, “02-P-24 - Population balance: a powerful tool for the study of critical processes of zeolite crystallization,” 2001, p. 191.
- [182] J. Warzywoda and R. W. Thompson, “Analysis of zeolite crystallization with autocatalytic nucleation,” *Zeolites*, vol. 9, no. 4, pp. 341–345, 1989.
- [183] A. Katović, B. Subotić, I. Šmit, and L. A. Despotović, “Crystallization of tetragonal (B8) and cubic (B1) modifications of zeolite NaP from freshly prepared gel. Part 1. Mechanism of the crystallization,” *Zeolites*, vol. 9, no. 1, pp. 45–53, Jan. 1989.
- [184] A. Palčić, J. Bronić, Đ. Brlek, and B. Subotić, “New insights on the autocatalytic nucleation in zeolite A synthesis,” *CrystEngComm*, vol. 13, no. 4, p. 1215, 2011.
- [185] D. W. Breck, *Zeolite molecular sieves: structure, chemistry, and use*. Wiley, 1973.
- [186] L. Heller-Kallai and I. Lapides, “Reactions of kaolinites and metakaolinites with NaOH—comparison of different samples (Part 1),” *Appl. Clay Sci.*, vol. 35, no. 1–2, pp. 99–107, Jan. 2007.
- [187] C. A. Ríos, C. D. Williams, and M. A. Fullen, “Nucleation and growth history of zeolite LTA synthesized from kaolinite by two different methods,” *Appl. Clay Sci.*, vol. 42, no. 3–4, pp. 446–454, 2009.
- [188] a. Madani, J. Sanz, and J. M. Serratosa, “²⁹Si and ²⁷Al NMR Study of Zeolite Formation from Alkali-Leached Kaolinites. Influence of Thermal Preactivation,” *J. Phys. Chem.*, vol. 94, no. 5, pp. 760–765, 1990.
- [189] H. Youssef, D. Ibrahim, and S. Komarneni, “Microwave-assisted versus conventional synthesis of zeolite A from metakaolinite,” *Microporous Mesoporous Mater.*, vol. 115, no. 3, pp. 527–534, 2008.
- [190] C. A. R. Reyes, C. Williams, and O. M. C. Alarcón, “Nucleation and growth process of sodalite and cancrinite from kaolinite-rich clay under low-temperature hydrothermal conditions,” *Mater. Res.*, vol. 16, no. 2, pp. 424–438, 2013.
- [191] I. Lapides and L. Heller-Kallai, “Reactions of metakaolinite with NaOH and colloidal

silica - Comparison of different samples (part 2),” *Appl. Clay Sci.*, vol. 35, no. 1–2, pp. 94–98, 2007.

- [192] D. Sabatino, B. Di Sabatino, D. Gimeno, and C. Pace, “Synthesis and characterization of Na-X, Na-A and Na-P zeolites and hydroxysodalite from metakaolinite,” *Clay Miner.*, vol. 46, no. 3, pp. 339–354, 2011.
- [193] J. Rocha, J. Klinowski, and J. M. Adams, “Synthesis of zeolite Na-A from metakaolinite revisited,” *J. Chem. Soc. Faraday Trans.*, vol. 87, no. 18, p. 3091, 1991.
- [194] E. Prud’Homme, P. Michaud, E. Joussein, and S. Rossignol, “Influence of raw materials and potassium and silicon concentrations on the formation of a zeolite phase in a geopolymer network during thermal treatment,” *J. Non. Cryst. Solids*, vol. 358, no. 16, pp. 1908–1916, 2012.
- [195] W. M. Kriven, “Refractory composite comprising a geopolymer and method of making a refractory composite,” US 20160304402A1, 2015.
- [196] T. W. Cheng, M. L. Lee, M. S. Ko, T. H. Ueng, and S. F. Yang, “The heavy metal adsorption characteristics on metakaolin-based geopolymer,” *Appl. Clay Sci.*, vol. 56, pp. 90–96, 2012.
- [197] S. Andrejković *et al.*, “The effect of natural zeolite on microstructure, mechanical and heavy metals adsorption properties of metakaolin based geopolymers,” *Appl. Clay Sci.*, vol. 126, pp. 141–152, 2016.
- [198] Y. He, X. min Cui, X. dong Liu, Y. pin Wang, J. Zhang, and K. Liu, “Preparation of self-supporting NaA zeolite membranes using geopolymers,” *J. Memb. Sci.*, vol. 447, pp. 66–72, 2013.
- [199] J. L. Provis, G. C. Lukey, and J. S. J. van Deventer, “Do Geopolymers Actually Contain Nanocrystalline Zeolites? A Reexamination of Existing Results,” *Chem. Mater.*, vol. 17, no. 12, pp. 3075–3085, Jun. 2005.
- [200] H. H. Weldes and K. R. Lange, “PROPERTIES OF SOLUBLE SILICATES,” *Ind. Eng. Chem.*, vol. 61, no. 4, pp. 29–44, Apr. 1969.

- [201] Y. M. Liew *et al.*, “Optimization of solids-to-liquid and alkali activator ratios of calcined kaolin geopolymeric powder,” *Constr. Build. Mater.*, vol. 37, pp. 440–451, Dec. 2012.
- [202] P. De Silva and K. Sagoe-Crenstil, “Medium-term phase stability of Na₂O–Al₂O₃–SiO₂–H₂O geopolymer systems,” *Cem. Concr. Res.*, vol. 38, no. 6, pp. 870–876, Jun. 2008.
- [203] B. Zhang, K. J. D. MacKenzie, and I. W. M. Brown, “Crystalline phase formation in metakaolinite geopolymers activated with NaOH and sodium silicate,” *J. Mater. Sci.*, vol. 44, no. 17, pp. 4668–4676, Jul. 2009.
- [204] C. Belviso, L. C. Giannossa, F. J. Huertas, A. Lettino, A. Mangone, and S. Fiore, “Synthesis of zeolites at low temperatures in fly ash-kaolinite mixtures,” *Microporous Mesoporous Mater.*, vol. 212, no. August, pp. 35–47, 2015.
- [205] Z. Li, T. Ohnuki, and K. Ikeda, “Development of Paper Sludge Ash-Based Geopolymer and Application to Treatment of Hazardous Water Contaminated with Radioisotopes,” *Materials (Basel)*, vol. 9, no. 8, p. 633, Jul. 2016.
- [206] M. Gordon, J. L. Bell, and W. M. Kriven, “Comparison of naturally and synthetically-derived, potassium-based geopolymers,” in *Ceramic Transactions*, 2005, vol. 165, pp. 95–106.
- [207] A. M. Rashad, “Metakaolin as cementitious material: History, scours, production and composition – A comprehensive overview,” *Constr. Build. Mater.*, vol. 41, pp. 303–318, Apr. 2013.
- [208] R. L. Frost, “Fourier transform Raman spectroscopy of Kaolinite, dickite and halloysite,” *Clays Clay Miner.*, vol. 43, no. 2, pp. 191–195, 1995.
- [209] T. F. Tadros, “Correlation of viscoelastic properties of stable and flocculated suspensions with their interparticle interactions,” *Adv. Colloid Interface Sci.*, vol. 68, pp. 97–200, 1996.
- [210] X. Yang, W. Zhu, and Q. Yang, “The Viscosity Properties of Sodium Silicate

- Solutions,” *J. Solution Chem.*, vol. 37, no. 1, pp. 73–83, Jan. 2008.
- [211] R. W. Whorlow, *Rheological techniques*. E. Horwood, 1980.
- [212] G. H. Tattersall and P. F. G. Banfill, *The rheology of fresh concrete*. Pitman Advanced Publishing Program, 1983.
- [213] “Instruction manual software HAAKE RheoWin 3.” Fisher Scientific Bioblock.
- [214] P. F. G. Banfill, British Society of Rheology., and E. International Conference on Rheology of Fresh Cement and Concrete (1990 : Liverpool, *Rheology of fresh cement and concrete : proceedings of the international conference organized by the British Society of Rheology, University of Liverpool, UK, March 26-29, 1990*. E. & F.N. Spon, 1991.
- [215] C. F. Ferraris, “Measurement of the rheological properties of high performance concrete: State of the art report,” *J. Res. Natl. Inst. Stand. Technol.*, vol. 104, no. 5, p. 461, Sep. 1999.
- [216] ASTM:C1437-07, “Standard Test Method for Flow of Hydraulic Cement Mortar,” *Annu. B. ASTM Stand.*, vol. C 1437, no. 07 Standard, pp. 1–2, 2007.
- [217] ASTM International, “ASTM C807-05 - Standard Test Methods for Time of Setting of Hydraulic Cement Mortar by Modified Vicat Needle,” *B. Stand. Vol. 04.01*, pp. 1–3, 2005.
- [218] Y. Yuan and T. R. Lee, “Contact Angle and Wetting Properties,” in *Surface Science Techniques*, vol. 51, no. 1, 2013, pp. 3–5.
- [219] J. Schultz and M. Nardin, “Determination of the surface energy of solids by the two-liquid-phase method,” *Mod. Approaches Wettability*, pp. 73–100, 1992.
- [220] C. Giacovazzo, *Fundamentals of crystallography*. Oxford University Press, 2002.
- [221] H. M. Rietveld and IUCr, “Line profiles of neutron powder-diffraction peaks for structure refinement,” *Acta Crystallogr.*, vol. 22, no. 1, pp. 151–152, Jan. 1967.

- [222] L. B. McCusker, R. B. Von Dreele, D. E. Cox, D. Louër, and P. Scardi, “Rietveld refinement guidelines,” *J. Appl. Crystallogr.*, vol. 32, no. 1, pp. 36–50, 1999.
- [223] A. F. Gualtieri, “Accuracy of XRPD QPA using the combined Rietveld-RIR method,” *J. Appl. Crystallogr.*, vol. 33, no. 2, pp. 267–278, 2000.
- [224] B. H. Toby, “R factors in Rietveld analysis: How good is good enough?,” *Powder Diffraction*, vol. 21, no. 1, pp. 67–70, 2006.
- [225] M. Tamer, “Quantitative Phase Analysis Based on Rietveld Structure Refinement for Carbonate Rocks,” *J. Mod. Phys.*, vol. 4, no. 8, pp. 1149–1157, Aug. 2013.
- [226] P. W. Atkins and J. C. N.-Q. . . A. 2014b De Paula, *Physical chemistry*. W.H. Freeman, 2014.
- [227] B. C. Smith, *Fundamentals of Fourier transform infrared spectroscopy*. CRC Press, 2011.
- [228] H. J. Seltman, “Experimental Design and Analysis,” 2015.
- [229] S. Kraber, P. Whitcomb, and M. Anderson, *Handbook for Experimenters Version 06.8*. 2005.
- [230] I. M. Krieger and T. J. Dougherty, “A Mechanism for Non- Newtonian Flow in Suspensions of Rigid Spheres,” *Trans. Soc. Rheol.*, vol. 3, no. 1, pp. 137–152, Mar. 1959.
- [231] G. A. Rao, “Generalization of Abrams’ law for cement mortars,” *Cem. Concr. Res.*, vol. 31, no. 3, pp. 495–502, Mar. 2001.
- [232] W. H. Taylor, *Concrete technology and practice*. American Elsevier Pub. Co, 1965.
- [233] S. B. Singh, P. Munjal, and N. Thammishetti, “Role of water/cement ratio on strength development of cement mortar,” *J. Build. Eng.*, vol. 4, pp. 94–100, Dec. 2015.
- [234] “PQ Corporation.” [Online]. Available: <http://www.pqcorp.com>. [Accessed: 10-Jun-2017].

- [235] P. B. Jamieson and L. S. D. Glasser, "Sodium silicate hydrates. II. The crystal structure of $\text{Na}_2\text{O} \cdot \text{SiO}_2 \cdot 9\text{H}_2\text{O}$," *Acta Crystallogr.*, vol. 20, no. 5, pp. 688–693, 1966.
- [236] P. B. Jamieson, L. S. D. Glasser, and IUCr, "Sodium silicate hydrates. III. The crystal structure of $\text{Na}_2\text{O} \cdot \text{SiO}_2 \cdot 6\text{H}_2\text{O}$ and of the isostructural $\text{Na}_2\text{O} \cdot \text{FeO}_2 \cdot 6\text{H}_2\text{O}$," *Acta Crystallogr.*, vol. 22, no. 4, pp. 507–522, Apr. 1967.
- [237] H. Koller, G. Engelhardt, and J. Felsche, " ^{29}Si NMR studies of the transformation of silicate anions in the system $\text{Na}_2\text{O} \cdot \text{SiO}_2 \cdot n\text{H}_2\text{O}$ ($n=9,5$) in crystals, melts, and solution," *J. Chem. Soc., Chem. Commun.*, no. 5, pp. 371–372, 1990.
- [238] J. L. Provis, A. Kilcullen, P. Duxson, D. G. Brice, and J. S. J. Van Deventer, "Stabilization of low-modulus sodium silicate solutions by alkali substitution," *Ind. Eng. Chem. Res.*, vol. 51, no. 5, pp. 2483–2486, 2012.
- [239] S. K. Nath, S. Maitra, S. Mukherjee, and S. Kumar, "Microstructural and morphological evolution of fly ash based geopolymers," *Constr. Build. Mater.*, vol. 111, pp. 758–765, 2016.
- [240] W. E. Morris, J. H., Perkins, P. G., Rose, A. E. A., Smith, "The chemistry and binding properties of aluminium phosphates," *Chem. Soc. Rev.*, vol. 6, pp. 173–194, 1977.
- [241] G. A. Parks, "The Isoelectric Points of Solid Oxides, Solid Hydroxides, and Aqueous Hydroxo Complex Systems," *Chem. Rev.*, vol. 65, no. 2, pp. 177–198, 1965.
- [242] M. Kosmulski, E. Maczka, and J. B. Rosenholm, "Isoelectric points of metal oxides at high ionic strengths," *J. Phys. Chem. B*, vol. 106, no. 11, pp. 2918–2921, 2002.
- [243] A. Hajimohammadi, J. L. Provis, and J. S. J. van Deventer, "One-Part Geopolymer Mixes from Geothermal Silica and Sodium Aluminate," *Ind. Eng. Chem. Res.*, vol. 47, no. 23, pp. 9396–9405, Dec. 2008.
- [244] B. Nic, M., Jirat, J., Kosata, "IUPAC Compendium of Chemical Terminology," *Blackwell Sci. Publ. Oxford*, p. 1670, 2014.

- [245] J. Xie and S. Kaliaguine, “Zeolite ball milling as a means of enhancing the selectivity for base catalyzed reactions,” *Appl. Catal. A Gen.*, vol. 148, no. 2, pp. 415–423, 1997.
- [246] G. Majano, L. Borchardt, S. Mitchell, V. Valtchev, and J. Pérez-Ramírez, “Rediscovering zeolite mechanochemistry-A pathway beyond current synthesis and modification boundaries,” *Microporous and Mesoporous Materials*, vol. 194, pp. 106–114, 2014.
- [247] W. Mozgawa and J. Deja, “Spectroscopic studies of alkaline activated slag geopolymers,” *J. Mol. Struct.*, vol. 924–926, no. C, pp. 434–441, 2009.
- [248] C. J. R. D. M. Ginter, A. T. Bell, “The chemistry of NaY crystallization from sodium-silicate solution,” in *Symposium on Synthesis of Microporous Materials*, 1992, pp. 6–30.
- [249] S. Mintova, J.-P. Gilson, and V. Valtchev, “Advances in nanosized zeolites,” *Nanoscale*, vol. 5, no. 15, p. 6693, 2013.
- [250] H. Awala *et al.*, “Template-free nanosized faujasite-type zeolites,” *Nat. Mater.*, vol. 14, no. 4, pp. 447–451, 2015.
- [251] F. H. Chung and D. K. (Deane K. Smith, *Industrial applications of X-ray diffraction*. Marcel Dekker, 2000.
- [252] S. Kawashima, J.-W. T. Seo, D. Corr, M. C. Hersam, and S. P. Shah, “Dispersion of CaCO₃ nanoparticles by sonication and surfactant treatment for application in fly ash–cement systems,” *Mater. Struct.*, vol. 47, no. 6, pp. 1011–1023, 2014.
- [253] M. Maldonado, M. D. Oleksiak, S. Chinta, and J. D. Rimer, “Controlling crystal polymorphism in organic-free synthesis of na-zeolites,” *J. Am. Chem. Soc.*, vol. 135, no. 7, pp. 2641–2652, 2013.
- [254] W. Mozgawa, M. Król, K. Barczyk, and M. Science, “FT-IR studies of zeolites from different structural groups,” no. 7, pp. 671–674, 2011.
- [255] A. G. Athanassiadis *et al.*, “Particle shape effects on the stress response of granular

- packings,” *Soft Matter*, vol. 10, no. 1, pp. 48–59, 2014.
- [256] X. Yao, Z. Zhang, H. Zhu, and Y. Chen, “Geopolymerization process of alkali–metakaolinite characterized by isothermal calorimetry,” *Thermochim. Acta*, vol. 493, no. 1–2, pp. 49–54, Sep. 2009.
- [257] R. M. Cornell and R. Giovanoli, “Transformation of hausmanite into birnessite in alkaline media,” *Clays Clay Miner.*, vol. 36, no. 3, pp. 249–257, 1988.
- [258] E. Pustovgar *et al.*, “Understanding silicate hydration from quantitative analyses of hydrating tricalcium silicates,” *Nat. Commun.*, vol. 7, p. 10952, 2016.
- [259] a. Poulesquen, F. Frizon, and D. Lambertin, “Rheological behavior of alkali-activated metakaolin during geopolymerization,” *J. Non. Cryst. Solids*, vol. 357, no. 21, pp. 3565–3571, Nov. 2011.
- [260] D. Bortzmeyer, “Dry pressing of ceramic powders,” in *Ceramic Processing*, Dordrecht: Springer Netherlands, 1995, pp. 102–146.
- [261] J. Z. Q. Zhou, P. H. T. Uhlherr, and F. T. Luo, “Yield stress and maximum packing fraction of concentrated suspensions,” *Rheol. Acta*, vol. 34, no. 6, pp. 544–561, 1995.
- [262] M. Romagnoli, P. Sassatelli, M. L. Gualtieri, and G. Tari, “Rheological characterization of fly ash-based suspensions,” *Constr. Build. Mater.*, vol. 65, pp. 526–534, 2014.
- [263] T. Cosgrove, *Colloid Science: Principles, Methods and Applications*. John Wiley & Sons, 2010.
- [264] S. B. Johnson, A. S. Russell, and P. J. Scales, “Volume fraction effects in shear rheology and electroacoustic studies of concentrated alumina and kaolin suspensions,” vol. 141, pp. 119–130, 1998.
- [265] P. B. Laxton and J. C. Berg, “Relating clay yield stress to colloidal parameters,” *J. Colloid Interface Sci.*, vol. 296, no. 2, pp. 749–55, Apr. 2006.
- [266] J. E. Wallevik and O. H. Wallevik, “Analysis of shear rate inside a concrete truck

- mixer,” *Cem. Concr. Res.*, vol. 95, pp. 9–17, May 2017.
- [267] N. Roussel, “A thixotropy model for fresh fluid concretes: Theory, validation and applications,” *Cem. Concr. Res.*, vol. 36, no. 10, pp. 1797–1806, Oct. 2006.
- [268] D. P. Bentz, C. F. Ferraris, M. A. Galler, A. S. Hansen, and J. M. Gynn, “Influence of particle size distributions on yield stress and viscosity of cement-fly ash pastes,” *Cem. Concr. Res.*, vol. 42, no. 2, pp. 404–409, 2012.
- [269] N. Roussel, “Rheology of fresh concrete: from measurements to predictions of casting processes,” *Mater. Struct.*, vol. 40, no. 10, pp. 1001–1012, 2007.
- [270] H. Murata, “Rheology - Theory and Application to Biomaterials,” in *Polymerization*, InTech, 2012.
- [271] J. M. Zuidema, C. J. Rivet, R. J. Gilbert, and F. A. Morrison, “A protocol for rheological characterization of hydrogels for tissue engineering strategies,” *J. Biomed. Mater. Res. - Part B Appl. Biomater.*, vol. 102, no. 5, pp. 1063–1073, 2014.
- [272] L. Nachbaur, J. C. Mutin, a. Nonat, and L. Choplin, “Dynamic mode rheology of cement and tricalcium silicate pastes from mixing to setting,” *Cem. Concr. Res.*, vol. 31, no. 2, pp. 183–192, 2001.
- [273] L. Weng, X. Chen, and W. Chen, “Rheological characterization of in situ crosslinkable hydrogels formulated from oxidized dextran and N-carboxyethyl chitosan,” *Biomacromolecules*, vol. 8, no. 4, pp. 1109–1115, 2007.
- [274] P. Steins, A. Poulesquen, O. Diat, and F. Frizon, “Structural Evolution during Geopolymerization from an Early Age to Consolidated Material,” *Langmuir*, vol. 28, no. 22, pp. 8502–8510, Jun. 2012.
- [275] V. Benavent *et al.*, “Impact of aluminum on the structure of geopolymers from the early stages to consolidated material,” *Cem. Concr. Res.*, vol. 90, pp. 27–35, Dec. 2016.
- [276] a. Papo and B. Caufin, “A study of the hydration process of cement pastes by means

- of oscillatory rheological techniques,” *Cem. Concr. Res.*, vol. 21, no. 6, pp. 1111–1117, 1991.
- [277] F. Skvára, L. Kopecký, V. Smilauer, and Z. Bittnar, “Material and structural characterization of alkali activated low-calcium brown coal fly ash,” *J. Hazard. Mater.*, vol. 168, no. 2–3, pp. 711–20, Sep. 2009.
- [278] M. Irfan Khan, K. Azizli, S. Sufian, and Z. Man, “Sodium silicate-free geopolymers as coating materials: Effects of Na/Al and water/solid ratios on adhesion strength,” *Ceram. Int.*, vol. 41, no. 2, pp. 2794–2805, 2015.
- [279] I. Halasz, M. Agarwal, R. Li, and N. Miller, “Vibrational spectra and dissociation of aqueous Na₂SiO₃ solutions,” *Catal. Letters*, vol. 117, no. 1–2, pp. 34–42, 2007.
- [280] J. L. Bass and G. Turner, “Anion distributions in sodium silicate solutions. Characterization by ²⁹Si NMR and infrared spectroscopies, and vapor phase osmometry,” *J. Phys. Chem. B*, vol. 101, no. 50, pp. 10638–10644, 1997.
- [281] M. T. Tognonvi, S. Rossignol, and J. P. Bonnet, “Effect of alkali cation on irreversible gel formation in basic medium,” *J. Non. Cryst. Solids*, vol. 357, no. 1, pp. 43–49, 2011.
- [282] M. T. Tognonvi, J. Soro, J. L. Gelet, and S. Rossignol, “Physico-chemistry of silica / Na silicate interactions during consolidation. Part 2: Effect of pH,” *J. Non. Cryst. Solids*, vol. 358, no. 3, pp. 492–501, 2012.
- [283] I. García-Lodeiro, A. Fernández-Jiménez, M. T. Blanco, and A. Palomo, “FTIR study of the sol-gel synthesis of cementitious gels: C-S-H and N-A-S-H,” *J. Sol-Gel Sci. Technol.*, vol. 45, no. 1, pp. 63–72, 2008.
- [284] A. Autef *et al.*, “Influence of metakaolin purities on potassium geopolymer formulation: The existence of several networks,” *J. Colloid Interface Sci.*, vol. 408, no. 1, pp. 43–53, 2013.
- [285] G. Kemmer and S. Keller, “Nonlinear least-squares data fitting in Excel spreadsheets,” *Nat. Protoc.*, vol. 5, no. 2, pp. 267–281, Feb. 2010.

- [286] P. S. Whitfield and L. D. Mitchell, "Quantitative Rietveld analysis of the amorphous content in cements and clinkers," *J. Mater. Sci.*, vol. 38, no. 21, pp. 4415–4421, 2003.
- [287] V. Gramlich and W. M. Meier, "The crystal structure of hydrated NaA: A detailed refinement of a pseudosymmetric zeolite structure," *Zeitschrift fur Krist. - New Cryst. Struct.*, vol. 133, no. 133, pp. 134–149, Jan. 1971.
- [288] B. Beagley, J. Dwyer, N. P. Evmerides, A. I. F. Hawa, and T. K. Ibrahim, "On the structures of X- and Y- type zeolites. II. Non-framework structural disorder and variability in hydrated Na-X," *Zeolites*, vol. 2, no. 3, pp. 167–174, 1982.
- [289] S. Dumrul, S. Bazzana, J. Warzywoda, R. R. Biederman, and A. Sacco, "Imaging of crystal growth-induced fine surface features in zeolite A by atomic force microscopy," *Microporous Mesoporous Mater.*, vol. 54, no. 1–2, pp. 79–88, Jul. 2002.
- [290] J. L. Provis and S. A. Bernal, "Geopolymers and Related Alkali-Activated Materials," *Annu. Rev. Mater. Res.*, vol. 44, no. 1, pp. 299–327, 2014.
- [291] R. M. Barrer and D. E. Mainwaring, "Chemistry of soil minerals. Part XIII. Reactions of metakaolinite with single and mixed bases," *J. Chem. Soc. Dalt. Trans.*, no. 22, p. 2534, 1972.

Appendices

Appendix A: Refinement of LTA and FAU-X crystal structures

The refined structures in this appendix were used in Chapter 8, Section 8.3.2.

Table A.1 Fractional coordinates, isotropic thermal parameters (100\AA^2), occupancies, unit cell parameters, for the refined LTA [287] ICSD 24901 and NaX [288] - ICSD 15568 phases using respectively the diffractograms E-60-7 and Cs-40-7.

ATOM	X	Y	Z	U	Occupancy	Wyckoff position	refined?
FAUJASITE							
F d -3 m, a=25.0463							
NA1	0.1760	0.2500	0.4260	0.5	0.1809	96h	yes
AL1	0.9465	0.0359	0.1247	0.5	0.4480	192i	
O1	0.0000	0.1071	0.8929	0.5	1.0000	96h	
O2	0.9969	0.9969	0.1444	0.5	1.0000	96g	
O3	0.0734	0.0734	0.9678	0.5	1.0000	96g	
O4	0.0736	0.0736	0.3225	0.5	1.0000	96g	
NA2	0.0000	0.0000	0.0000	0.5	0.8590	16c	yes
NA3	0.0660	0.0660	0.0660	0.5	0.2964	32e	yes
NA4	0.1680	0.1680	0.1680	0.5	0.1900	32e	
O5	0.1680	0.1680	0.1680	0.5	0.5600	32e	
O6	0.1150	0.1350	0.0530	0.5	0.3022	96g	yes
NA5	0.2480	0.2480	0.2480	0.5	0.3400	32e	
SI1	0.9465	0.0359	0.1247	0.5	0.5520	192i	
O7	0.2650	0.2650	0.3410	0.5	0.3503	96g	yes
O8	0.1620	0.1620	0.4160	0.5	0.2778	96g	yes
NA6	0.1620	0.1620	0.4160	0.5	0.2100	96g	
O9	0.2090	0.3790	0.4740	0.5	0.1134	192i	yes
NA7	0.4030	0.4030	0.4030	0.5	0.0300	32e	
O10	0.4030	0.4030	0.4030	0.5	0.2048	32e	yes
NA8	0.5000	0.5000	0.5000	0.5	0.0070	16d	
O11	0.5000	0.5000	0.5000	0.5	0.1200	16d	
NA9	0.4500	0.4500	0.4500	0.5	0.0070	32e	
O12	0.4500	0.4500	0.4500	0.5	0.1200	32e	
O13	0.2800	0.2800	0.2800	0.5	0.0900	32e	
O13	0.2800	0.2800	0.2800	0.5	0.0900	32e	
LTA							
F m -3 c, a=24.6072							
O1	0.0200	0.0300	0.0640	0.5	0.1478	192j	yes
NA1	0.0410	0.2100	0.2350	0.5	0.1991	192j	yes
NA2	0.2100	0.0410	0.2350	0.5	0.0630	192j	
NA3	0.2500	0.2500	0.2500	0.5	0.1267	8a	yes
AL1	0.0000	0.1864	0.0902	0.5	1.0000	96i	
SI1	0.0000	0.0929	0.1844	0.5	1.0000	96i	
O2	0.0000	0.1116	0.2473	0.5	1.0000	96i	
NA4	0.1064	0.1064	0.1064	0.5	1.0000	64g	
O3	0.0538	0.0583	0.1704	0.5	1.0000	192j	
O4	0.0300	0.0200	0.0640	0.5	0.1882	192j	yes
O5	0.1598	0.1598	0.1598	0.5	0.1250	64g	
O6	0.1155	0.1670	0.2620	0.5	0.4150	192j	
O7	0.1670	0.1155	0.2620	0.5	0.4150	192j	
O8	0.0410	0.2100	0.2350	0.5	0.0210	192j	

O9	0.2100	0.0410	0.2350	0.5	0.0210	192j
O10	0.7500	0.7500	0.7500	0.5	1.0000	8a
O11	0.0000	0.1463	0.1476	0.5	1.0000	96i

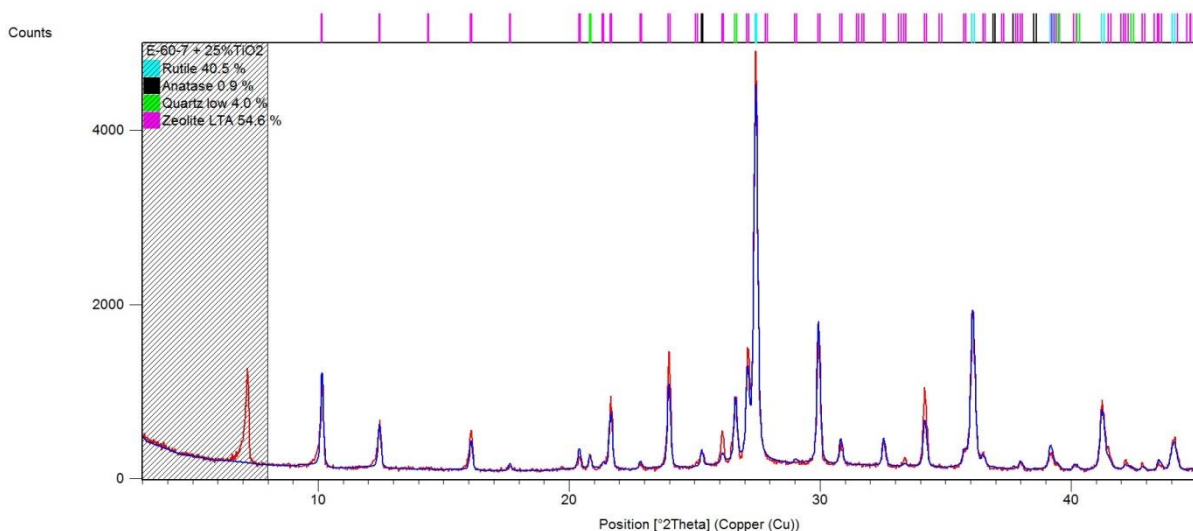


Figure A.1: Observed (in red) and calculated (in blue) diffraction pattern of the sample E-60-7 with 25% of rutile as internal standard. On top of the diffractograms peak positions: rutile ICSD 34372 as aqua bars, anatase ICSD 63711 as black bars, quartz ICSD 90145 as green bars, zeolite LTA ICSD 24901 as fuchsia bars. GOF=6.0.

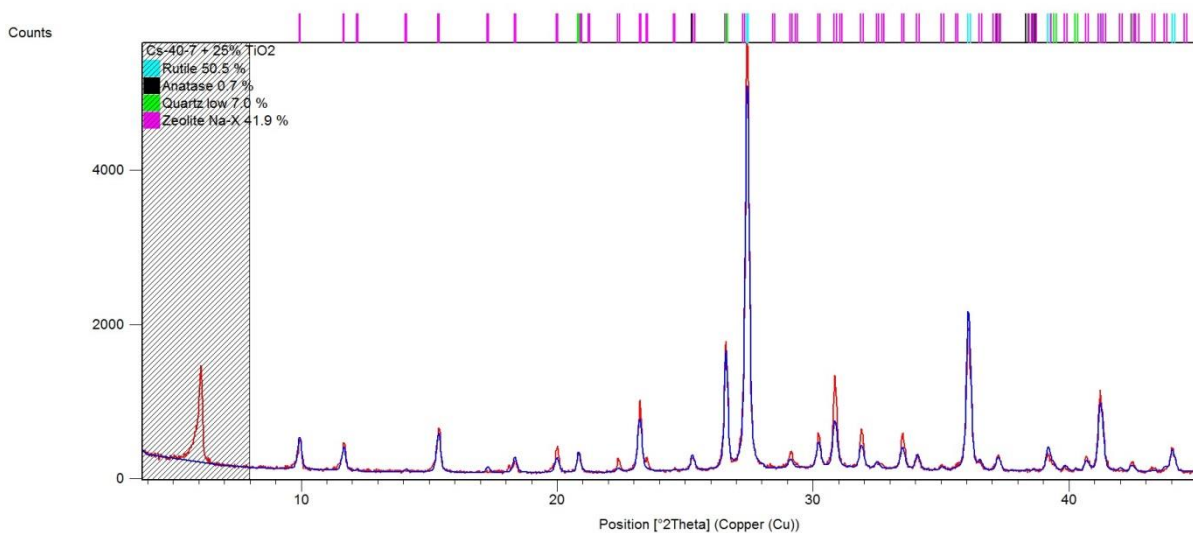


Figure A.2: Observed (in red) and calculated (in blue) diffraction pattern of the sample Cs-40-7 with 25% of rutile as internal standard. On top of the diffractograms peak positions: rutile ICSD 34372 as aqua bars, anatase ICSD 63711 as black bars, quartz ICSD 90145 as green bars, zeolite NaX ICSD 155683 as fuchsia bars. GOF=5.1.

Appendix B: DOE responses

In this Appendix the DOE responses of Chapter 8 are collected, Section 8.4.2. These are the results from the deconvolutions of the ATR-FTIR spectra and from the QXRD using Rietveld refinements on the geopolymer samples.

“GP peak” represents the peak position of the main geopolymer band around 960 cm^{-1} ; “GP%” represents the area percentage of the main geopolymer peak over the metakaolin and geopolymer peaks; “solid/H₂O” represents the area ratio between the sum of metakaolin and geopolymer peaks over the water peak located at 3300 cm^{-1} ; “FWHM” represents the FWHM of the main geopolymer peak.

“GOF” is the Goodness of Fit obtained for each Rietveld refinement; “% amorphous” and other zeolite percentages are calculated based on the internal standard, “% conversion” is calculated by normalizing the total percentage of zeolite based on the impurities coming from the metakaolin which do not contribute in the geopolymerization reactions.

QXRD were performed on all samples: blank cell means no zeolite detected. Some ATR-FTIR data are missing, especially for samples that have not set in order to avoid damage to the ATR-FTIR instrument. Some “GP/MK” are marked as “small” when the geopolymer band was too weak for the deconvolution to be successful.

Table B.1 Responses obtained from the multifactorial design in Chapter 8.

code	ATR-FTIR DECONVOLUTION				QXRD (RIETVELD REFINEMENT)								
	GP peak [cm ⁻¹]	GP%	solid/ H ₂ O	FWHM [cm ⁻¹]	GOF	% AMORPH	% LTA	% NaX	% Hs	% KZ-5	TOTAL % ZEOL	% LTA (over NaX)	% CONVERSION
A-5-1	/	/	/	/	/	/	0.0	0.0	0.0	0.0	0.0	/	6.0
A-20-1	950.1	54.2	0.2	43.4	/	/	0.0	0.0	0.0	0.0	0.0	/	6.0
A-40-1	953.1	63.4	0.2	42.8	/	/	0.0	0.0	0.0	0.0	0.0	/	6.0
A-60-1	950.8	69.7	0.2	43.1	2.4	89.8	5.6	0.0	0.0	0.0	5.6	100.0	6.1
B-5-1	/	17.7	/	/	/	/	0.0	0.0	0.0	0.0	0.0	/	6.0
B-20-1	954.6	44.5	0.2	48.2	/	/	0.0	0.0	0.0	0.0	0.0	/	6.0
B-40-1	952.9	54.7	0.2	43.2	/	/	0.0	0.0	0.0	0.0	0.0	/	6.0
B-60-1	958.8	68.1	0.1	39.9	2.7	81.1	12.7	0.0	0.0	0.0	12.7	100.0	13.6
C-5-1	/	/	/	/	/	/	0.0	0.0	0.0	0.0	0.0	/	6.0
C-20-1	934.3	65.4	0.1	47.1	/	/	0.0	0.0	0.0	0.0	0.0	/	6.0
C-40-1	937.6	88.0	0.2	45.1	/	/	0.0	0.0	0.0	0.0	0.0	/	6.0
C-60-1	948.8	90.2	0.2	42.9	5.1	45.9	43.8	6.1	0.0	1.2	51.1	87.9	55.1
D-5-1	/	23.8	/	/	/	/	0.0	0.0	0.0	0.0	0.0	/	6.0
D-20-1	946.2	65.1	0.1	44.1	/	/	0.0	0.0	0.0	0.0	0.0	/	6.0
D-40-1	/	/	/	/	/	/	0.0	0.0	0.0	0.0	0.0	/	6.0
D-60-1	947.3	88.9	0.2	44.0	3.5	76.8	17.6	0.0	0.0	0.0	17.6	100.0	18.7
E-5-1	/	/	/	/	/	/	0.0	0.0	0.0	0.0	0.0	/	6.0
E-20-1	949.0	58.5	0.2	43.9	/	/	0.0	0.0	0.0	0.0	0.0	/	6.0
E-40-1	945.2	81.5	0.1	44.4	/	/	0.0	0.0	0.0	0.0	0.0	/	6.0
E-60-1	945.2	82.4	0.1	43.4	2.6	88.6	5.9	0.0	0.0	0.0	5.9	100.0	6.3
As-5-1	/	/	/	/	/	/	0.0	0.0	0.0	0.0	0.0	/	0.0
As-20-1	957.1	57.1	0.1	41.5	/	/	0.0	0.0	0.0	0.0	0.0	/	0.0

As-40-1	959.1	64.5	0.1	42.0	/	/	0.0	0.0	0.0	0.0	0.0	/	0.0
As-60-1	959.7	68.1	0.1	42.5	/	/	0.0	0.0	0.0	0.0	0.0	/	0.0
Bs-5-1	/	/	/	/	/	/	0.0	0.0	0.0	0.0	0.0	/	0.0
Bs-20-1	/	/	/	/	/	/	0.0	0.0	0.0	0.0	0.0	/	0.0
Bs-40-1	960.9	61.6	0.1	41.7	/	/	0.0	0.0	0.0	0.0	0.0	/	0.0
Bs-60-1	971.7	65.4	0.1	42.1	/	/	0.0	0.0	0.0	0.0	0.0	/	0.0
Cs-5-1	/	/	/	/	/	/	0.0	0.0	0.0	0.0	0.0	/	0.0
Cs-20-1	/	73.8	/	/	/	/	0.0	0.0	0.0	0.0	0.0	/	0.0
Cs-40-1	940.2	86.6	0.2	46.8	/	/	0.0	0.0	0.0	0.0	0.0	/	0.0
Cs-60-1	944.2	85.0	0.3	46.4	/	/	0.0	0.0	0.0	0.0	0.0	/	0.0
Ds-5-1	/	/	/	/	/	/	0.0	0.0	0.0	0.0	0.0	/	0.0
Ds-20-1	/	/	/	/	/	/	0.0	0.0	0.0	0.0	0.0	/	0.0
Ds-40-1	946.8	85.5	0.2	45.3	/	/	0.0	0.0	0.0	0.0	0.0	/	0.0
Ds-60-1	950.6	84.6	0.2	45.4	/	/	0.0	0.0	0.0	0.0	0.0	/	0.0
Es-5-1	/	/	/	/	/	/	0.0	0.0	0.0	0.0	0.0	/	0.0
Es-20-1	955.2	66.0	0.1	43.1	/	/	0.0	0.0	0.0	0.0	0.0	/	0.0
Es-40-1	954.2	80.4	0.1	43.1	/	/	0.0	0.0	0.0	0.0	0.0	/	0.0
Es-60-1	956.9	81.1	0.1	44.3	/	/	0.0	0.0	0.0	0.0	0.0	/	0.0
Aw-5-1	/	/	/	/	/	/	0.0	0.0	0.0	0.0	0.0	/	0.0
Aw-20-1	959.4	53.4	0.2	47.0	/	/	0.0	0.0	0.0	0.0	0.0	/	0.0
Aw-40-1	952.3	61.5	0.2	43.7	/	/	0.0	0.0	0.0	0.0	0.0	/	0.0
Aw-60-1	960.4	64.5	0.1	43.4	/	/	0.0	0.0	0.0	0.0	0.0	/	0.0
Bw-5-1	/	/	/	/	/	/	0.0	0.0	0.0	0.0	0.0	/	0.0
Bw-20-1	/	/	/	/	/	/	0.0	0.0	0.0	0.0	0.0	/	0.0
Bw-40-1	/	/	/	/	/	/	0.0	0.0	0.0	0.0	0.0	/	0.0
Bw-60-1	959.7	64.4	0.1	43.4	2.3	84.5	4.9	0.0	0.0	0.0	4.9	100.0	5.3
Cw-5-1	/	/	/	/	/	/	0.0	0.0	0.0	0.0	0.0	/	0.0
Cw-20-1	942.0	75.7	0.2	47.0	/	/	0.0	0.0	0.0	0.0	0.0	/	0.0
Cw-40-1	952.3	87.4	0.1	47.4	/	/	0.0	0.0	0.0	0.0	0.0	/	0.0
Cw-60-1	948.2	86.8	0.2	46.6	2.1	85.9	2.8	8.3	0.0	0.0	11.1	25.5	12.0
Dw-5-1	/	/	/	/	/	/	0.0	0.0	0.0	0.0	0.0	/	0.0
Dw-20-1	/	/	/	/	/	/	0.0	0.0	0.0	0.0	0.0	/	1.0
Dw-40-1	953.2	85.6	0.1	46.4	/	/	0.0	0.0	0.0	0.0	0.0	/	2.0
Dw-60-1	947.8	85.3	0.1	45.6	/	/	0.0	0.0	0.0	0.0	0.0	/	3.0
Ew-5-1	/	/	/	/	/	/	0.0	0.0	0.0	0.0	0.0	/	4.0
Ew-20-1	958.8	66.8	0.1	44.6	/	/	0.0	0.0	0.0	0.0	0.0	/	5.0
Ew-40-1	955.5	81.3	0.1	44.4	/	/	0.0	0.0	0.0	0.0	0.0	/	6.0
Ew-60-1	948.0	79.9	0.1	44.6	2.5	92.8	2.6	0.0	0.0	0.0	2.6	100.0	2.7
A-5-4	950.5	28.7	0.2	47.5	/	/	0.0	0.0	0.0	0.0	0.0	/	6.0
A-20-4	960.9	65.9	0.1	41.5	/	/	0.0	0.0	0.0	0.0	0.0	/	6.0
A-40-4	961.9	69.5	0.2	44.0	2.3	91.2	4.8	0.0	0.0	0.0	4.8	100.0	5.3
A-60-4	960.2	74.9	0.1	43.0	2.9	83.8	10.7	0.0	0.0	0.0	10.7	100.0	11.6
B-5-4	953.1	33.8	0.2	76.5	/	/	0.0	0.0	0.0	0.0	0.0	/	6.0
B-20-4	965.7	49.9	0.1	40.7	/	/	0.0	0.0	0.0	0.0	0.0	/	6.0
B-40-4	973.3	74.5	0.1	40.7	3.2	81.6	13.2	0.0	0.0	0.0	13.2	100.0	14.1
B-60-4	967.0	78.3	0.1	40.2	3.5	72.2	20.5	0.0	0.0	0.0	20.5	100.0	22.0
C-5-4	/	38.6	/	/	/	/	0.0	0.0	0.0	0.0	0.0	/	6.0
C-20-4	947.2	84.7	0.1	48.4	/	/	0.0	0.0	0.0	0.0	0.0	/	6.0
C-40-4	952.9	88.2	0.1	52.3	5.1	53.3	27.8	16.0	0.0	0.0	43.8	63.4	47.2
C-60-4	955.6	89.3	0.1	50.0	5.8	39.6	45.1	7.9	0.0	2.1	55.1	85.0	59.4
D-5-4	945.6	41.5	0.2	54.4	/	/	0.0	0.0	0.0	0.0	0.0	/	6.0
D-20-4	952.5	86.3	0.0	52.2	/	/	0.0	0.0	0.0	0.0	0.0	/	6.0
D-40-4	952.6	91.6	0.1	44.7	18.1	50.3	39.8	6.6	0.0	0.0	46.4	85.7	49.3
D-60-4	954.9	91.1	0.1	47.8	6.8	43.6	42.8	3.9	0.0	0.0	46.7	91.7	49.6
E-5-4	944.3	35.0	0.1	51.8	/	/	0.0	0.0	0.0	0.0	0.0	/	6.0
E-20-4	947.5	78.4	0.1	46.5	/	/	0.0	0.0	0.0	0.0	0.0	/	6.0
E-40-4	954.4	86.4	0.1	44.5	2.8	78.3	14.7	0.0	0.0	0.0	14.7	100.0	15.7
E-60-4	964.7	87.9	0.2	46.9	5.5	44.0	50.9	0.0	0.0	0.0	50.9	100.0	40.5
As-5-4	952.5	54.1	0.2	44.5	/	/	0.0	0.0	0.0	0.0	0.0	/	6.0
As-20-4	961.3	63.9	0.1	42.5	/	/	0.0	0.0	0.0	0.0	0.0	/	6.0
As-40-4	954.3	68.4	0.2	44.4	/	/	0.0	0.0	0.0	0.0	0.0	/	6.0
As-60-4	957.9	72.7	0.2	43.1	2.7	86.8	9.4	0.0	0.0	0.0	9.4	100.0	10.2
Bs-5-4	957.5	45.8	0.2	44.6	/	/	0.0	0.0	0.0	0.0	0.0	/	6.0
Bs-20-4	955.9	60.6	0.1	43.9	/	/	0.0	0.0	0.0	0.0	0.0	/	6.0
Bs-40-4	954.6	67.0	0.2	48.0	/	/	0.0	0.0	0.0	0.0	0.0	/	6.0
Bs-60-4	955.6	71.8	0.2	43.2	2.4	83.4	12.4	0.0	0.0	0.0	12.4	100.0	13.2
Cs-5-4	936.8	65.8	0.2	46.7	/	/	0.0	0.0	0.0	0.0	0.0	/	6.0
Cs-20-4	940.8	86.2	0.1	45.5	/	/	0.0	0.0	0.0	0.0	0.0	/	6.0
Cs-40-4	947.9	83.9	0.1	43.3	1.9	89.1	0.0	4.4	0.0	0.0	4.4	0.0	4.7
Cs-60-4	933.3	86.7	0.2	37.9	6.6	52.7	4.8	39.8	0.0	0.0	44.6	10.8	48.0
Ds-5-4	965.5	62.1	0.0	40.3	/	/	0.0	0.0	0.0	0.0	0.0	/	6.0
Ds-20-4	944.7	82.8	0.1	45.5	/	/	0.0	0.0	0.0	0.0	0.0	/	6.0
Ds-40-4	949.0	84.8	0.1	44.7	/	/	0.0	0.0	0.0	0.0	0.0	/	6.0
Ds-60-4	938.8	87.0	0.2	40.3	5.5	51.1	22.9	23.7	0.0	0.0	46.6	49.1	49.6
Es-5-4	949.4	55.8	0.2	44.4	/	/	0.0	0.0	0.0	0.0	0.0	/	6.0
Es-20-4	951.3	80.7	0.1	41.2	/	/	0.0	0.0	0.0	0.0	0.0	/	6.0
Es-40-4	947.8	81.8	0.2	44.6	2.4	96.2	0.0	0.0	0.0	0.0	0.0	/	0.0
Es-60-4	953.5	85.8	0.1	43.2	4.1	79.9	13.3	0.0	0.0	0.0	13.3	100.0	14.2
Aw-5-4	959.6	41.6	0.2	48.8	/	/	0.0	0.0	0.0	0.0	0.0	/	6.0
Aw-20-4	952.7	63.8	0.1	43.2	/	/	0.0	0.0	0.0	0.0	0.0	/	6.0
Aw-40-4	959.0	64.3	0.2	45.4	/	/	0.0	0.0	0.0	0.0	0.0	/	6.0
Aw-60-4	957.1	71.8	0.2	42.4	2.7	85.1	9.7	0.0	0.0	0.0	9.7	100.0	10.5
Bw-5-4	948.8	15.9	0.1	39.2	/	/	0.0	0.0	0.0	0.0	0.0	/	6.0
Bw-20-4	958.7	56.3	0.1	43.6	/	/	0.0	0.0	0.0	0.0	0.0	/	6.0
Bw-40-4	959.8	63.9	0.1	42.8	/	/	0.0	0.0	0.0	0.0	0.0	/	6.0
Bw-60-4	959.8	72.3	0.1	42.2	3.0	80.1	14.2	0.0	0.0	0.0	14.2	100.0	15.2
Cw-5-4	951.7	50.0	0.1	52.0	/	/	0.0	0.0	0.0	0.0	0.0	/	6.0
Cw-20-4	941.5	83.8	0.2	47.5	/	/	0.0	0.0	0.0	0.0	0.0	/	6.0

Cw-40-4	947.2	87.9	0.1	47.3	3.7	81.4	0.0	17.3	0.0	0.0	17.3	0.0	18.7
Cw-60-4	941.4	88.9	0.2	43.5	5.8	51.7	6.9	33.1	0.0	0.0	40.0	17.3	43.1
Dw-5-4	947.6	44.8	0.2	49.0	/	/	0.0	0.0	0.0	0.0	0.0	/	6.0
Dw-20-4	953.7	87.3	0.1	44.9	/	/	0.0	0.0	0.0	0.0	0.0	/	6.0
Dw-40-4	956.1	86.6	0.1	47.3	3.8	80.4	7.0	5.6	0.0	0.0	12.6	55.4	13.4
Dw-60-4	949.8	89.8	0.1	44.6	5.5	56.2	24.3	16.6	0.0	0.0	40.9	59.4	43.4
Ew-5-4	968.3	43.7	0.1	47.3	/	/	0.0	0.0	0.0	0.0	0.0	/	6.0
Ew-20-4	958.0	79.6	0.1	43.8	/	/	0.0	0.0	0.0	0.0	0.0	/	6.0
Ew-40-4	958.5	84.5	0.1	44.5	2.3	90.7	5.9	0.0	0.0	0.0	5.9	100.0	6.3
Ew-60-4	951.8	84.7	0.1	45.7	3.0	77.4	16.2	0.0	0.0	0.0	16.2	100.0	17.3
A-5-7	944.3	43.2	0.2	45.2	/	/	0.0	0.0	0.0	0.0	0.0	/	6.0
A-20-7	955.4	64.5	0.1	42.7	/	/	0.0	0.0	0.0	0.0	0.0	/	6.0
A-40-7	/	/	/	/	2.4	88.6	7.2	0.0	0.0	0.0	7.2	100.0	7.8
A-60-7	/	/	/	/	2.9	79.8	13.7	0.0	0.0	0.0	13.7	100.0	14.9
B-5-7	952.6	23.1	0.1	43.1	/	/	0.0	0.0	0.0	0.0	0.0	/	6.0
B-20-7	965.6	49.2	0.1	43.1	/	/	0.0	0.0	0.0	0.0	0.0	/	6.0
B-40-7	979.3	71.0	0.2	40.1	3.3	82.6	14.1	0.0	0.0	0.0	14.1	100.0	15.1
B-60-7	963.9	77.8	0.1	38.7	3.4	75.7	19.6	0.0	0.0	0.0	19.6	100.0	21.0
C-5-7	940.8	40.4	0.1	51.1	/	/	0.0	0.0	0.0	0.0	0.0	/	6.0
C-20-7	950.3	85.9	0.1	48.4	/	/	0.0	0.0	0.0	0.0	0.0	/	6.0
C-40-7	957.4	89.8	0.1	48.5	4.8	57.2	18.7	21.5	0.0	0.0	40.2	46.5	43.3
C-60-7	954.1	93.6	0.1	48.7	5.8	42.1	40.0	6.5	4.5	2.9	53.9	86.0	58.1
D-5-7	948.6	37.3	0.1	48.3	/	/	0.0	0.0	0.0	0.0	0.0	/	6.0
D-20-7	947.3	85.6	0.1	44.8	/	/	0.0	0.0	0.0	0.0	0.0	/	6.0
D-40-7	952.0	91.2	0.1	40.7	8.0	38.6	49.9	8.4	0.0	0.0	58.3	85.6	62.0
D-60-7	955.4	93.2	0.1	44.4	9.2	23.7	67.3	5.5	0.0	0.0	72.8	92.4	77.4
E-5-7	949.7	36.7	0.2	48.5	/	/	0.0	0.0	0.0	0.0	0.0	/	6.0
E-20-7	947.2	80.6	0.1	43.4	/	/	0.0	0.0	0.0	0.0	0.0	/	6.0
E-40-7	964.0	87.7	0.1	42.1	3.2	76.1	19.7	0.0	0.0	0.0	19.7	100.0	21.0
E-60-7	958.5	88.2	0.3	42.7	6.0	56.9	39.4	0.0	0.0	0.0	39.4	100.0	41.9
As-5-7	959.2	50.0	0.1	42.2	/	/	0.0	0.0	0.0	0.0	0.0	/	6.0
As-20-7	959.3	62.6	0.1	42.0	/	/	0.0	0.0	0.0	0.0	0.0	/	6.0
As-40-7	952.0	66.6	0.2	42.7	2.9	90.0	4.7	0.0	0.0	0.0	4.7	100.0	5.1
As-60-7	960.4	70.6	0.2	43.2	2.6	85.0	11.5	0.0	0.0	0.0	11.5	100.0	12.5
Bs-5-7	958.7	48.4	0.1	42.2	/	/	0.0	0.0	0.0	0.0	0.0	/	6.0
Bs-20-7	957.2	58.0	0.2	42.8	/	/	0.0	0.0	0.0	0.0	0.0	/	6.0
Bs-40-7	956.3	66.3	0.2	41.9	2.5	85.5	10.2	0.0	0.0	0.0	10.2	100.0	11.0
Bs-60-7	964.6	68.1	0.1	42.9	2.7	83.1	13.0	0.0	0.0	0.0	13.0	100.0	13.9
Cs-5-7	949.1	77.6	0.1	47.0	/	/	0.0	0.0	0.0	0.0	0.0	/	6.0
Cs-20-7	953.6	86.4	0.1	45.4	/	/	0.0	0.0	0.0	0.0	0.0	/	6.0
Cs-40-7	947.9	86.4	0.1	39.9	5.1	68.3	0.0	28.2	0.0	0.0	28.2	0.0	30.4
Cs-60-7	939.0	87.8	0.2	43.0	7.3	51.5	5.5	37.4	0.0	0.0	42.9	12.8	46.2
Ds-5-7	959.6	62.6	0.1	48.0	/	/	0.0	0.0	0.0	0.0	0.0	/	6.0
Ds-20-7	947.0	82.9	0.1	46.2	/	/	0.0	0.0	0.0	0.0	0.0	/	6.0
Ds-40-7	949.0	84.1	0.1	44.7	2.1	91.4	0.0	4.7	0.0	0.0	4.7	0.0	5.0
Ds-60-7	954.7	89.0	0.1	47.2	6.1	18.0	39.3	40.0	0.0	0.0	79.3	49.5	84.3
Es-5-7	957.6	59.0	0.1	44.5	/	/	0.0	0.0	0.0	0.0	0.0	/	6.0
Es-20-7	951.3	76.8	0.1	43.3	/	/	0.0	0.0	0.0	0.0	0.0	/	6.0
Es-40-7	954.8	81.3	0.1	42.8	2.6	87.3	4.7	0.0	0.0	0.0	4.7	100.0	5.0
Es-60-7	961.8	82.9	0.1	45.9	3.5	78.3	18.1	0.0	0.0	0.0	18.1	100.0	19.2
Aw-5-7	957.4	44.2	0.2	45.9	/	/	0.0	0.0	0.0	0.0	0.0	/	6.0
Aw-20-7	961.1	61.4	0.1	42.6	/	/	0.0	0.0	0.0	0.0	0.0	/	6.0
Aw-40-7	954.6	68.0	0.2	42.9	2.2	90.9	5.0	0.0	0.0	0.0	5.0	100.0	5.4
Aw-60-7	955.9	71.7	0.2	42.5	2.7	84.7	10.7	0.0	0.0	0.0	10.7	100.0	11.6
Bw-5-7	967.5	38.3	0.2	49.5	/	/	0.0	0.0	0.0	0.0	0.0	/	6.0
Bw-20-7	953.4	58.5	0.2	43.4	/	/	0.0	0.0	0.0	0.0	0.0	/	6.0
Bw-40-7	963.2	70.0	0.1	41.2	2.7	87.2	8.0	0.0	0.0	0.0	8.0	100.0	8.5
Bw-60-7	964.3	74.5	0.1	41.7	3.2	74.1	18.3	0.0	0.0	0.0	18.3	100.0	19.5
Cw-5-7	949.4	51.9	0.1	48.5	/	/	0.0	0.0	0.0	0.0	0.0	/	6.0
Cw-20-7	953.7	87.7	0.1	48.7	/	/	0.0	0.0	0.0	0.0	0.0	/	6.0
Cw-40-7	938.7	86.3	0.2	40.5	3.8	66.8	3.4	28.0	0.0	0.0	31.4	10.9	33.8
Cw-60-7	937.1	87.5	0.3	42.7	6.1	59.4	5.6	28.7	0.0	0.0	34.3	16.3	37.0
Dw-5-7	/	/	/	/	/	/	0.0	0.0	0.0	0.0	0.0	/	6.0
Dw-20-7	951.2	85.4	0.1	46.0	/	/	0.0	0.0	0.0	0.0	0.0	/	6.0
Dw-40-7	944.6	88.0	0.1	41.8	6.5	47.2	17.5	31.9	0.0	0.0	49.4	35.4	52.5
Dw-60-7	943.8	88.0	0.2	43.7	5.9	36.4	35.0	25.7	0.0	0.0	60.8	57.7	64.6
Ew-5-7	946.9	56.9	0.2	46.6	/	/	0.0	0.0	0.0	0.0	0.0	/	6.0
Ew-20-7	950.3	77.3	0.1	43.8	/	/	0.0	0.0	0.0	0.0	0.0	/	6.0
Ew-40-7	955.8	83.7	0.1	44.4	2.9	79.7	14.4	0.0	0.0	0.0	14.4	100.0	15.3
Ew-60-7	953.4	84.5	0.2	44.0	3.5	74.2	22.8	0.0	0.0	0.0	22.8	100.0	24.2

Appendix C: DOE effects plots

In this Appendix the effects plots for different responses calculated in Chapter 8 (Section 8.4.2) are presented. The models represent the effects of the five different factors - Na/Al, H₂O/solid, seeding, curing time and curing temperature - on each response calculated from the FTIR spectra and QXRD. Here only factors that were determined to be significant by ANOVA analysis are considered.

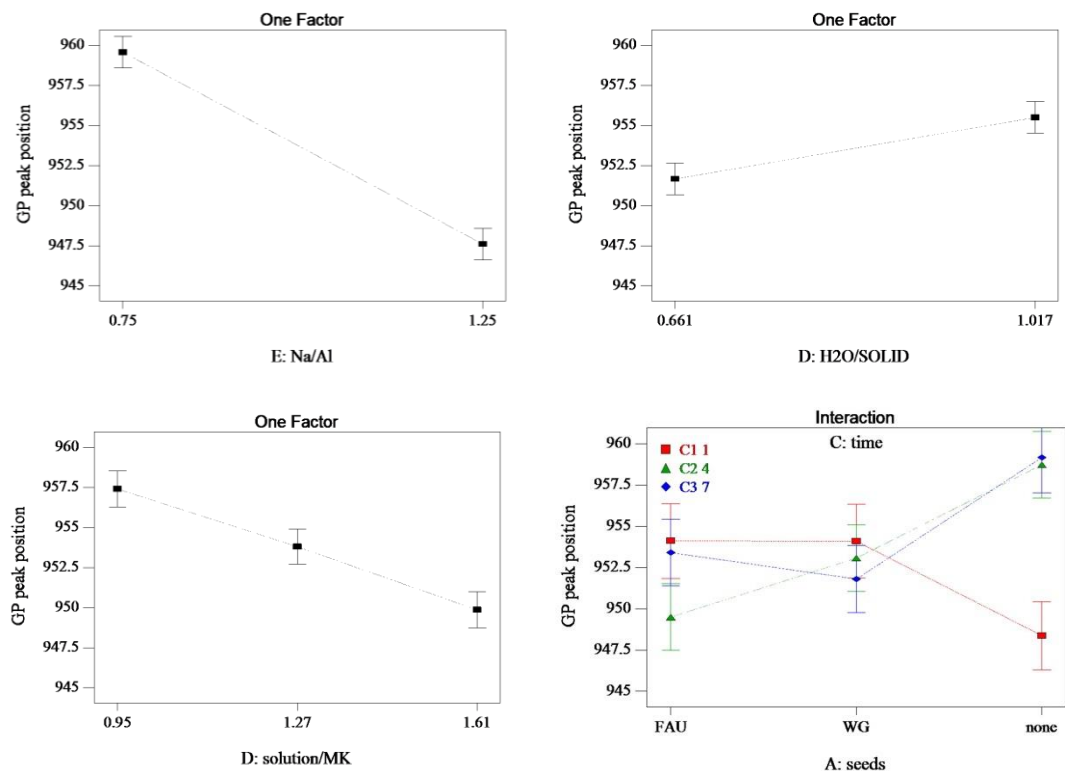


Figure C.3 FTIR peak positions associated with GP: effect of Na/Al (top left), H₂O/solid (top right), solution/MK (bottom left) and interaction between curing time and seeding (bottom right).

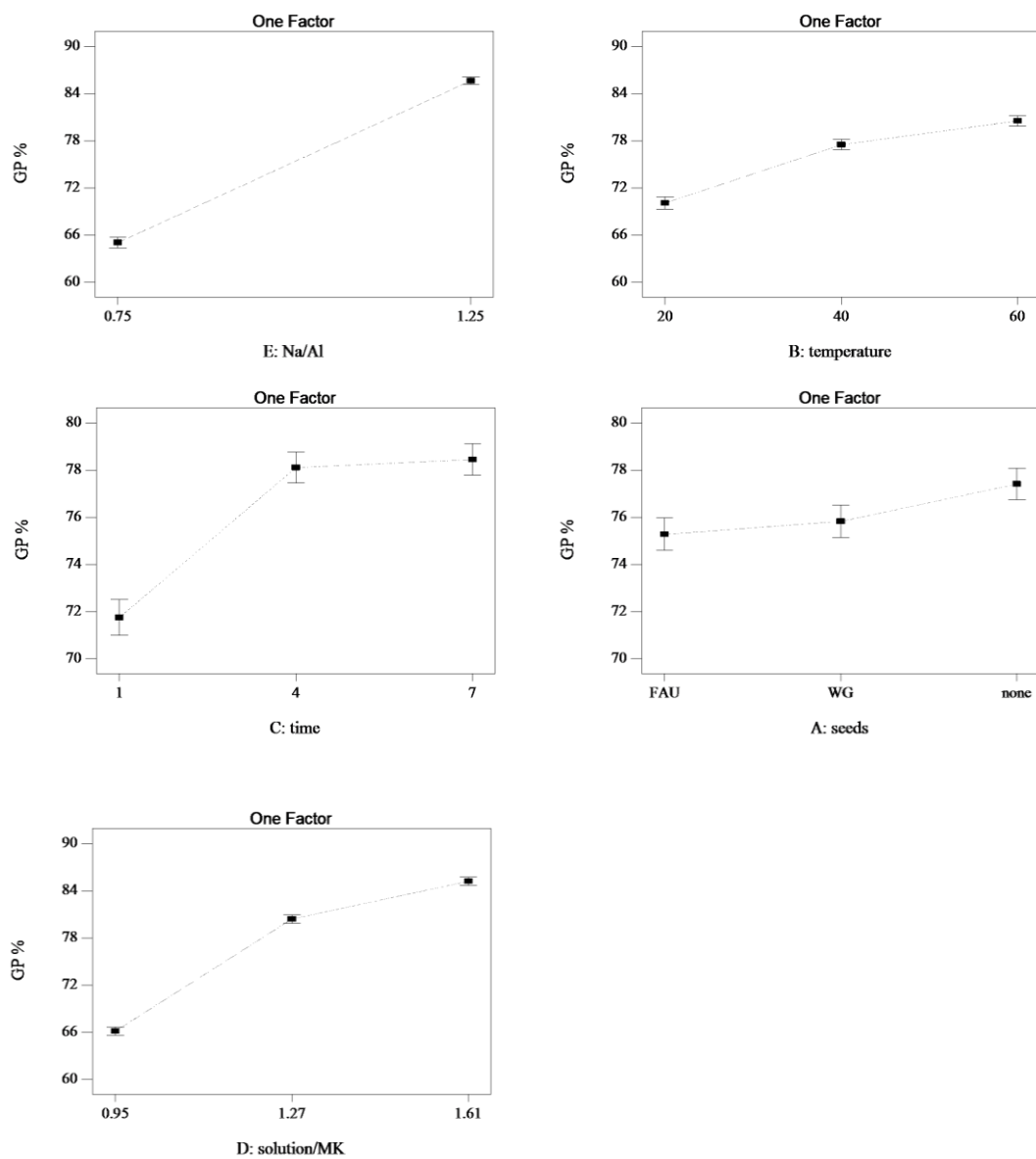


Figure C.4 GP% obtained from the deconvolution of the FTIR spectra: effects of Na/Al (top left), curing temperature (top right), curing time (mid left), seeding (mid right) and solution/MK (bottom)

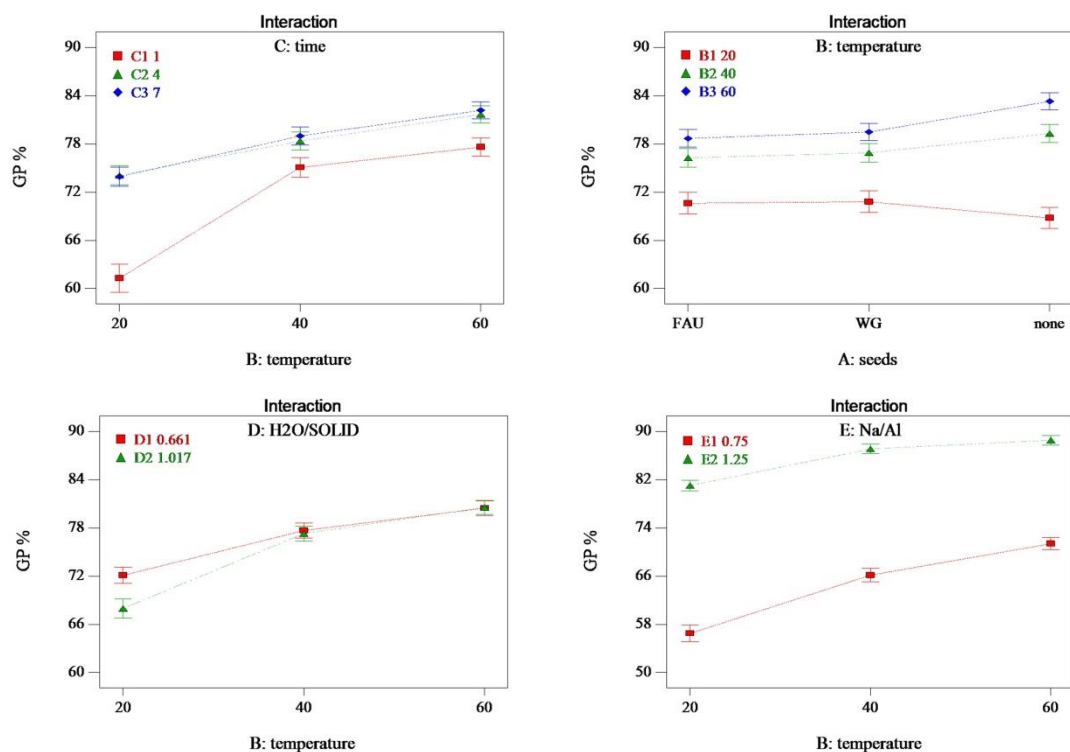


Figure C.5 GP% obtained from the deconvolution of the FTIR spectra: interaction between curing temperature and time (top left), curing temperature and seeding (top right), curing temperature and H₂O/solid (bottom left) and curing temperature and Na/Al (bottom right)

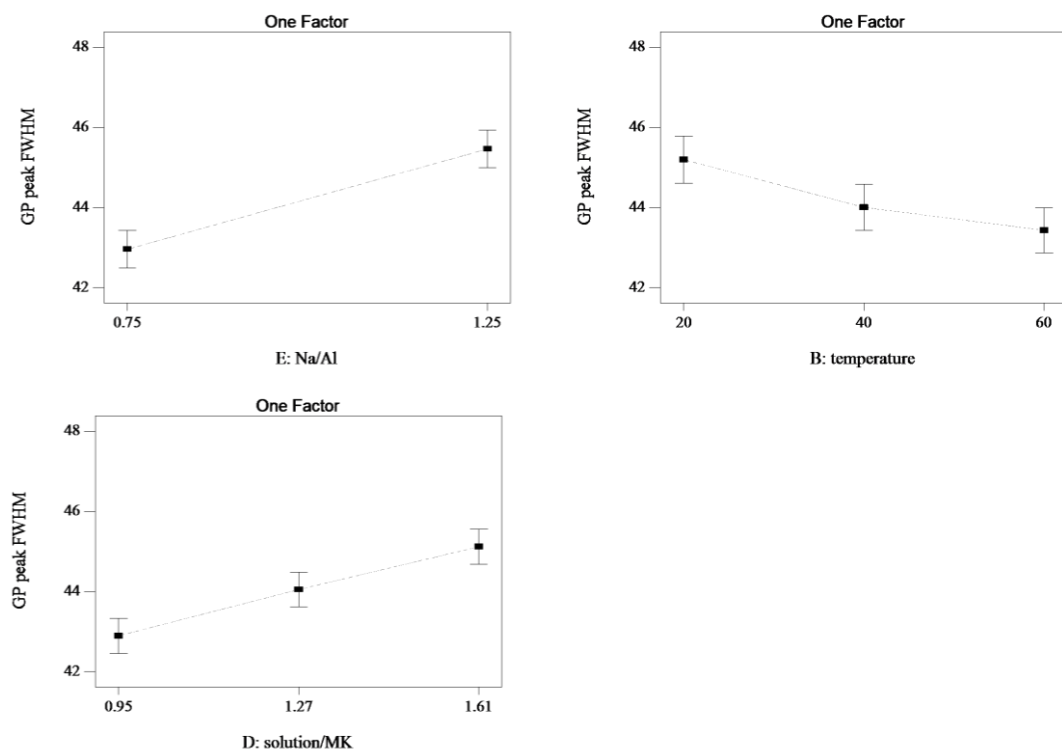


Figure C.6 FWHM of the FTIR peak associated with GP: effects of Na/Al (top left), temperature (top right) and solution/MK (bottom).

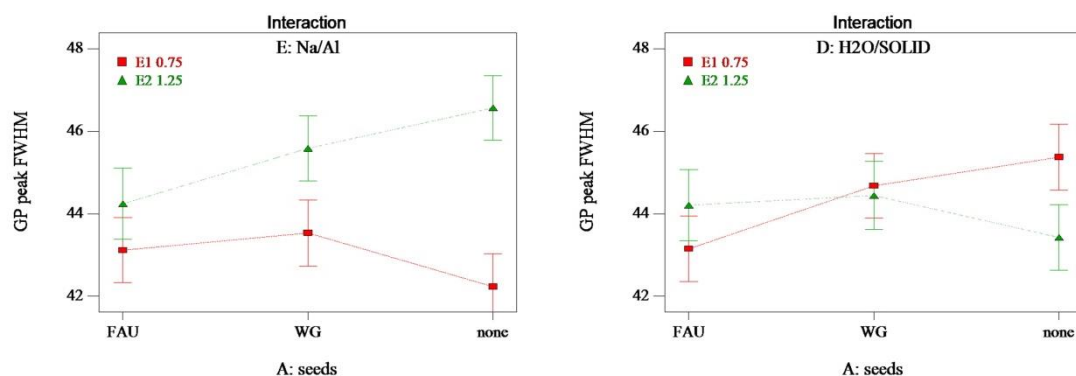


Figure C.7 FWHM of the FTIR peak associated with GP: interaction between Na/Al and seeding (left) and H₂O/solid and seeding (right).

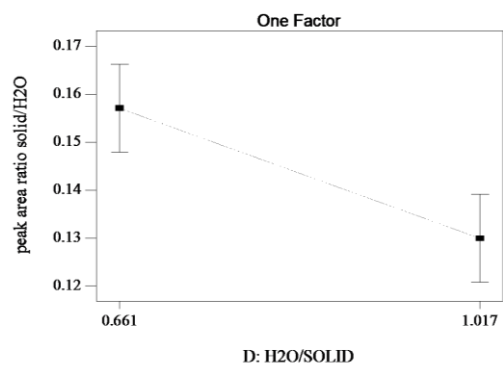


Figure C.8 Area ratio of FTIR peaks associated with solids and H₂O: effect of H₂O/solid.

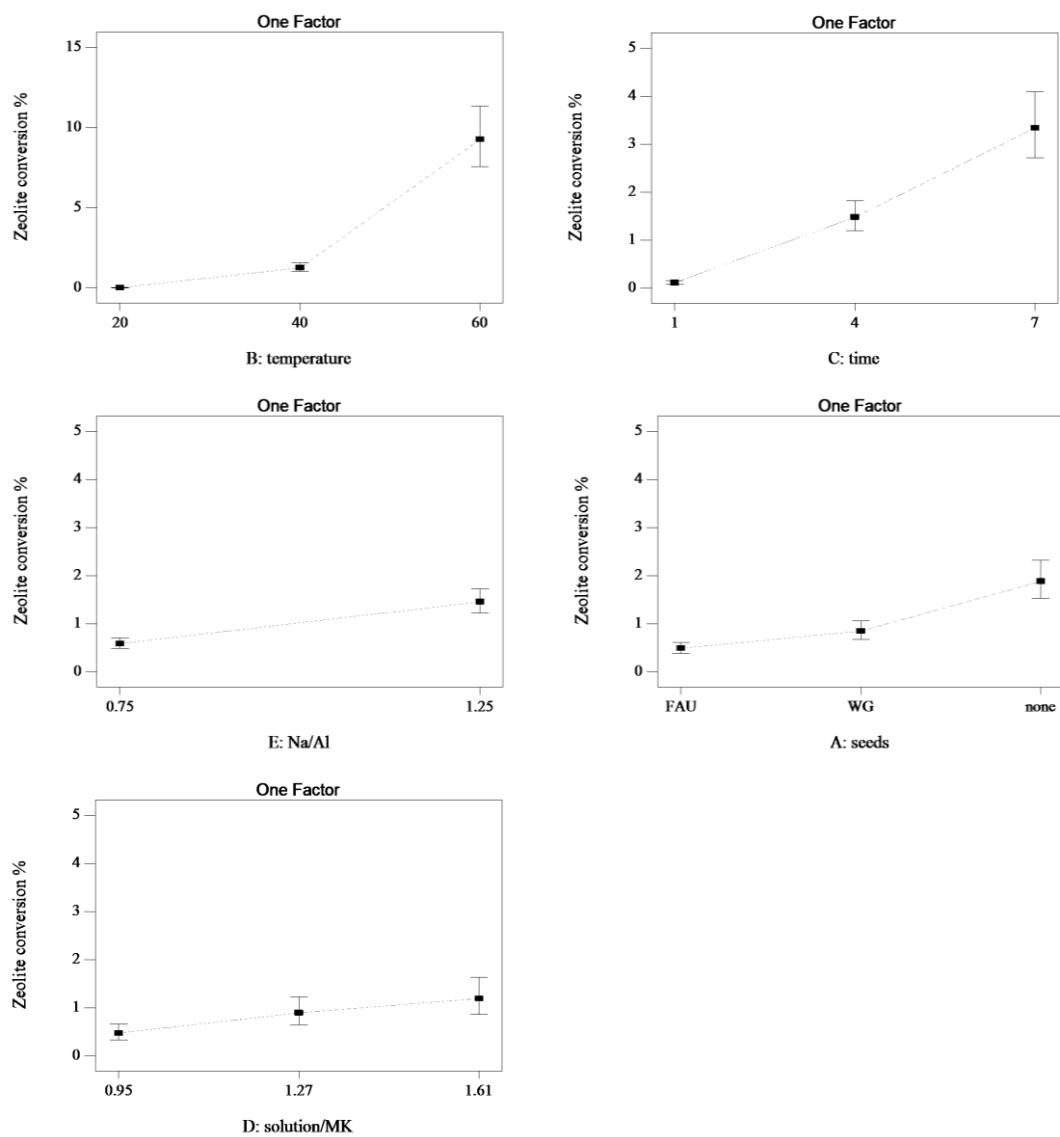


Figure C.9 Zeolite conversion % of GP as determined by QXRD: effects of curing temperature (top left), curing time (top right), Na/Al (mid left), seeding (mid right) and solution/MK (bottom).

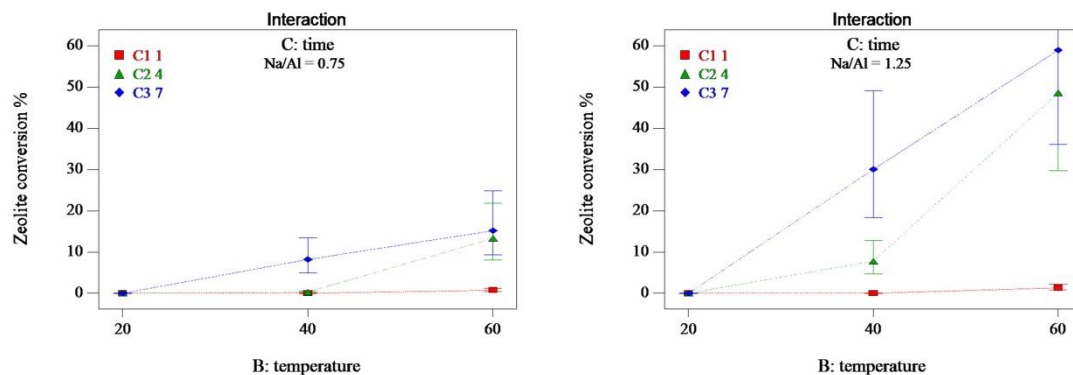


Figure C.10 Zeolite conversion % of GP as determined by QXRD: interaction between curing temperature, curing time and Na/Al. Na/Al=0.75 (left) and Na/Al=1.25 (right).

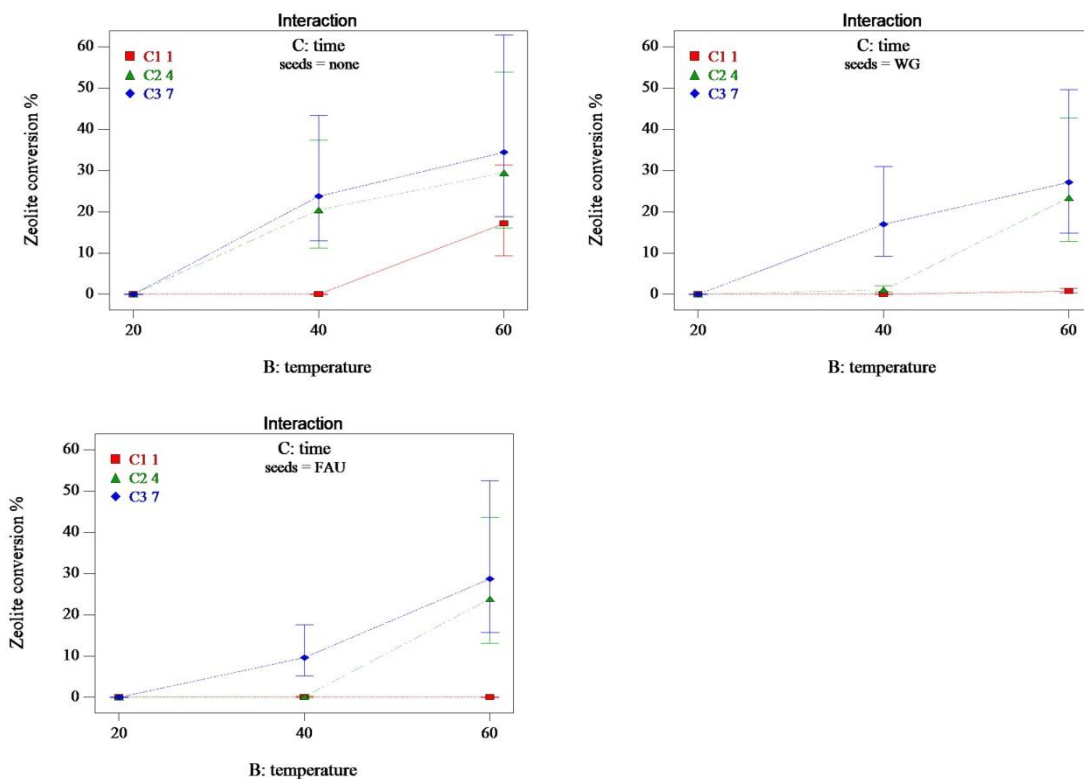


Figure C.11 Zeolite conversion % of GP as determined by QXRD: interaction between curing temperature, curing time and seeding. GP without seeds (top left), GP with waterglass seeds (top right) and GP with colloidal Faujasite (bottom).

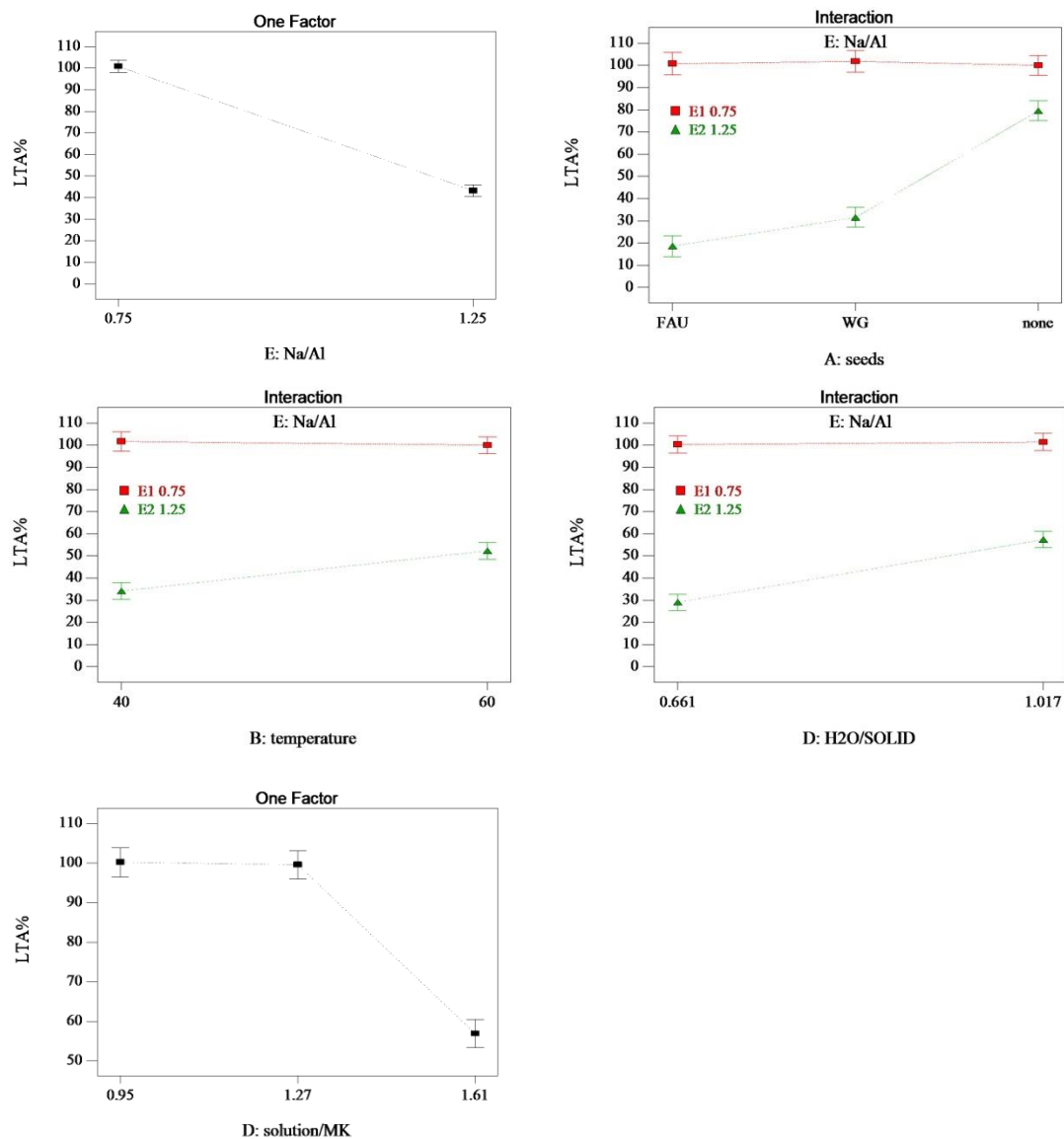


Figure C.12 LTA% of GP as determined by QXRD: effects of Na/Al (left), interaction between seeding and Na/Al (top right), interaction between curing temperature and Na/Al (mid left), interaction between H₂O/solid, seeding (mid right) and effect of solution/MK (bottom).